Micro-morphology and Resorption features of Diamonds from Snap Lake and Ekati Kimberlites (Canada) as an Indicator of Kimberlite Emplacement Conditions

by

Zhuoyuan Li

Submitted in partial fulfilment of the requirements
for the degree of Master of Science

at

Dalhousie University
Halifax, Nova Scotia
August 2017

TABLE OF CONTENTS

LIST OF TABLES

LIST OF FIGURES

ABSTRACT

Volatiles play a significant role in the emplacement mode and the resulting geology of kimberlites, however, the volatile composition and concentrations are poorly constrained. Previous experimental studies have suggested that diamond resorption features are sensitive to the presence and composition of C-O-H fluids. Atomic force microscopy (AFM) can be used to quantify individual features on diamonds to place robust constraints on their resorption conditions and the composition of kimberlitic fluid.

This study examines resorption features on diamonds from kimberlite localities with presumably different fluid and emplacement histories - Snap Lake kimberlite dyke and four kimberlite pipes (Fox, Panda, Koala, Misery) from Ekati Mine. The morphologies of 251 diamonds from Snap Lake were examined and 91 crystals with octahedral or tetrahexahedral forms were selected, which were further divided via optical microscopy and Scanning Electron Microscopy (SEM) into 12 morphological groups based on the resorption features on {111} faces. Related sub-groups were identified based on the edge types. The internal properties (N content and aggregation state) of 82 diamonds selected from different morphological groups were also examined by Fourier Transform Infrared Spectroscopy (FTIR). The lack of correlation between the internal properties of diamonds and resorption morphologies suggests a limited effect of internal factors on resorption morphologies.

Selected diamonds from Snap Lake and Ekati kimberlites were studied with Atomic Force Microscopy (AFM) to provide quantitative data on the geometry of diamond micro-features. The results were compared to the AFM data for diamonds etched in experiments at 0.1 MPa in H_2-CO_2 gas mixture and at 1-3 GPa in CHO fluid with various $CO_2/(H_2O+CO_2)$ ratios. Snap Lake diamonds show widespread development of positive trigons in addition to the common negative trigons, indicating late-stage etching at near-surface conditions superimposed on earlier stage (deeper) etching. Ekati diamonds show only negative trigons implying deeper resorption (at pressures $\geq$ 1 GPa). The AFM data show significant variation in CO_2/H_2O ratio between the volumetrically dominant coherent facies (HKM) and the subordinate phlogopite-rich coherent facies (HKP) in Snap Lake kimberlite, and among the four studied Ekati kimberlites. The differences in the emplacement of Snap Lake dyke and Ekati kimberlite pipes can be explained by variation in fluid composition. The study shows that the new AFM-based method of examining trigonal pits on diamonds can be applied to reconstruct conditions during kimberlite emplacement and the nature of kimberlitic fluids.

LIST OF ABBREVIATIONS AND SYMBOLS USED

General Abbreviations	
Abbreviation	Description
Ol	Olivine
Qtz	Quartz
Prv	Perovskite
Sp	Spinel
P	Pressure
T	Temperature
fO_2	Oxygen fugacity
CCO	Graphite-Oxygen buffer
NNO	Nickle-Nickle Oxide buffer
FMQ	Fayalite-Magnetite-Quartz buffer
WM	Wüstite-Magnetite buffer
IW	Iron-Wüstite buffer
X	Fluid composition in mole fraction
X_{CO2}	$X_{CO2} = CO_2/(CO_2+H_2O)$, mole fraction
SEM	Scanning Electron Microscope
FTIR	Fourier Transform Infrared Spectroscopy
AFM	Atomic Force Microscopy

Kimberlite- and diamond-related Symbols	
Symbols	Description
VK	Volcaniclastic kimberlite
RVK	Resedimented volcaniclastic kimberlite
MVK	Massive volcaniclastic kimberlite
CK	Coherent kimberlite
HKM	Volumetrically dominant coherent kimberlite in Snap Lake dyke
HKP	Subordinate coherent phlogopite-rich kimberlite in Snap Lake dyke
HK1-6	Six sub-lithofacies of HKM and HKP in Snap Lake dyke based on the degree of alteration
THH	Tetrahexahedral diamonds
pos	positive trigon
neg	negative trigon
th	trigon-hexagon
hex	Hexagon
p/b	Point-bottomed
f/b	Flat-bottomed
c/b	Curved-bottomed
L_{100}	Length of trigon sides in positive directions
L_{111}	Length of trigon sides in negative directions
W_{100}	Walls on the sides of positive directions
W_{111}	Walls on the sides of negative directions
$\alpha_{\{111\}}$	Pit wall angle relative to {111}

ACKNOWLEDGEMENTS

I would like to express special thanks to my supervisor, Yana Fedortchouk, for introducing me into this brilliant project, guiding me with patience and knowledge, and encouraging me with her perseverance in work and life.

I am deeply thankful to my awesome thesis committee crew: Yana Fedortchouk, Richard Cox, and Alexandrina Fulop, who have provided valuable contributions to this work. I have learned a lot from them during committee meetings, and thesis writing.

I would like to direct my gratitude to all the people who helped me during this study: Ingrid Chinn for the guidance on my poster for GAC-MAC conference and thesis writing, John Goss for introducing me to geochronology in the course ERTH6400, Nicholas Culshaw for bringing me unforgettable memories of the field trip in course ERTH6350, Patricia Scallion for the assistance with SEM examination of my diamond samples, Rebecca Jamieson and Isabelle Coutand for their great patience and guidance in the course ERTH6300, Ryan Kressall for encouraging me to get through the course of ERTH6300, Thomas Stachel (University of Alberta) for the assistance with FTIR measurements of my diamond samples, and Zhihai Zhang for helping me with diamond cleaning, FTIR measurements, calibration for AFM, and discussion of my thesis.

I would like to thank De Beers Canada Inc. for the financial support and access to diamond parcels; BHP Billiton and Jon Carlson for access to Ekati diamond parcels. The study was supported by NSERC Engage and Discovery grants to Yana Fedortchouk and my scholarship from Cargill Food Technology (Pinghu, China) Co., Ltd and Shell funding.

AFM analyses were funded by a Canada Foundation for Innovation grant to Yana Fedortchouk.

Finally, I would like to dedicate my thesis to my family and friends for their unconditional support during my studies.

CHAPTER 1. INTRODUCTION

1.1 Kimberlites and Diamonds

1.1.1 Role of Volatiles in Kimberlite Magmatism

It is generally believed that the kimberlite magma carries a high concentration of volatiles (mainly CO_2 and H_2O), considering the melt generation process and explosive character of kimberlite eruption (Eggler 1978; Wyllie 1980). The composition of volatile constituents affects the behavior and explosivity of magmas, and the geometry and geology of the kimberlite intrusion due to the differences in the depths of volatile exsolution and character of eruption for CO_2-rich and H_2O-rich magmas (Moussallam et al. 2016; Moussallam et al. 2015; Papale and Polacci 1999; Skinner and Marsh 2004; Sparks et al. 2006). The effects of CO_2 on magma ascent and eruption dynamics are generally opposite to those of H_2O. An increase in CO_2 causes increased overall magma viscosity, larger magma depressurization (due to increased friction at the conduit walls), and lower mass flow rate. An increase in H_2O counteracts the effects of CO_2 and results in decreased magma viscosity, lower depressurization and larger mass flow rate (Papale and Polacci 1999). The exsolution of the volatiles plays an important role in near-surface emplacement and pipe-formation processes. Degassing will exert great effects on the acceleration of the ascent rate of the kimberlite magma due to the enhanced buoyancy, and adiabatic gas expansion is a significant factor on magma cooling (Sparks et al. 2006). The increased melt liquidus temperature combined with the adiabatic cooling due to degassing will lead to sudden crystallization and stalling of the ascending melt, and may result in either fragmentation and pipe initiation or formation of hypabyssal kimberlites (sills and dykes) depending on the capacity of the gas phase to decouple from the melt (Moussallam et al.

2016). Studies on CO_2 and H_2O solubility in low-silicate melts indicate that kimberlite magma can retain a large quantity of volatiles to shallow crustal levels (~3 km depth) where significant degassing will take place, which helps explain the typical depth extent of root zones (2.5-0.5 km) and the widening upward shape of conduits in a bottom-up emplacement model (Moussallam et al. 2016; Moussallam et al. 2015). In addition, in Class 1 kimberlites, the exsolved volatiles may corrode and weaken the country rocks creating zones of weakness that can be exploited later by the rising kimberlite magma (Sparks et al. 2006), or may cause brecciation in the country rocks forming embryonic pipes that are removed after the magma breaches the surface and explosive eruption begins (Clement 1982; Field and Scott Smith 1999). It is also widely believed that volatile exsolution induces fluidization of the magma, which thoroughly mixes the magma with xenoliths and forms the homogenous MVK facies in Class 1 kimberlite (Field and Scott Smith 1999; Mitchell 1986; Skinner and Marsh 2004; Sparks et al. 2006; Walters et al. 2006).

The morphologies of kimberlite pipes are considered to be related to the original CO_2/H_2O ratio. Skinner and Marsh (2004) proposed that Class 1 and 3 kimberlites are H_2O-rich and are likely to crystallize deeper than to Class 2 kimberlite, which is CO_2-rich and can rise to very shallow levels, inducing phreatomagmatic eruption by interacting with groundwater. This is because wet magma has a more depressed solidus than carbonatitic magma (Figure 1.1). Moussallam et al. (2016) concurred that Class 1 kimberlite is H_2O-rich and Class 2 kimberlite is CO_2-rich. However, he interpreted the emplacement differently, suggesting that H_2O-rich kimberlite tends to initiate pipe formation by degassing at greater depth than CO_2-rich kimberlite, which is more likely to ascend to shallower depth and to have phreatomagmatic eruption. This is due to H_2O-rich magma

exsolving CO_2 at greater depth than CO_2-rich magma, as an increase in the H_2O content lowers the CO_2 activity and forces the CO_2 to exsolve at higher pressure.

Despite the important effects of volatiles on kimberlite magmatism, the content of volatiles and the CO_2/H_2O ratio in the kimberlite magma are poorly constrained. One uncertainty is that the composition of primary kimberlite magma remains enigmatic. Kimberlites are commonly contaminated by mantle and crustal xenoliths and xenocrysts, and have generally undergone severe alteration, notably through serpentinization of olivine, which makes it difficult to reconstruct the primitive composition of the magma (Sparks et al. 2009) and also camouflages the original concentration of CO_2 and H_2O. The only well documented kimberlitic lava, in the Igwisi Hills, Tanzania, shows close connection with differentiated or evolved calcite kimberlites and significant crustal contamination, and cannot be used to estimate the composition of primitive kimberlite magma (Mitchell 2008). Studies using aphanitic kimberlites (Kopylova et al. 2007; Price et al. 2000), considered contamination-free with minimal macrocrysts, to estimate the primitive magma composition can be regarded as equivocal since the melt may still have undergone differentiation (Mitchell 2004). Also, melting experiments on possible mantle source or natural kimberlite (Dalton and Presnall 1998; Gudfinnsson 2005; Mitchell 2004) do not agree regarding the origin of the primary kimberlite magma. In addition, there is no direct way to measure the CO_2/H_2O ratio in kimberlite magma due to the loss of volatiles during the eruption.

Alternatively, diamond resorption morphology can be used as a robust proxy to constrain the composition of kimberlitic fluid and emplacement history of kimberlite. Fedortchouk et al. (2007, 2010) showed that the secondary morphology and surface

features of diamonds are sensitive to the presence and composition of the reacting fluid. The different morphologies of Ekati kimberlites were explained by the presence or loss of a free fluid phase in kimberlite magma, which is well recorded by the diamond surface features.

1.1.2 Diamond Resorption Features as a Proxy for Fluid Composition

The morphology of diamond surface features depends on internal factors such as defects in the diamond lattice, and external factors (temperature, pressure, fO_2 and composition of fluid). Defects (e.g. cracks, dislocations, growth imperfections) on diamond surfaces may have faster local etch rates than nearby perfect regions (Harrison and Tolansky, 1964). Etching experiments at low T (< 1000 °C) using KNO_3 or CO_2 revealed that the N content and aggregation state in the diamond lattice may affect sizes and densities of etch pits. (1) Etch pit densities in Type I (N-bearing) regions of diamonds are at least two orders of magnitude higher than those in Type II (N-free) regions (Harrison and Tolansky, 1964). (2) The distribution and size of platelets may affect the density and size of etch pits (Mendelssohn and Milledge 1995). (3) Type II diamonds (N-free, high dislocation density and no platelets) could be more easily deformed than Type I diamonds (N-bearing, low dislocation density and high platelet density), as platelets hinder the movement of dislocations (Mendelssohn and Milledge 1995). Zhang and Fedortchouk (2012) found that the N content and aggregation state in diamonds with similar types of mantle-derived resorption features seem to follow the same isotherms, indicating that one can use N content and aggregation state to distinguish mantle-derived features from kimberlitic resorption features. In addition, Khokhryakov and Palyanov (2006, 2007b)

proposed that etch pits with distinct wall angles, shapes, or distribution are related to certain types of defects. Point-bottomed positive trigons with $\alpha_{\{111\}}$ = 2-8° and straight sides are associated with dislocations, and etch pits with $\alpha_{\{111\}}$ = 11-15° and round shape are associated with larger defects (impurity clusters, microcracks and other surface defects). Linear features bound by etch pits with $\alpha_{\{111\}}$= 2-3° or showing no etch pits are related to single (double) stacking faults or twin lamellae. However, some studies suggested that there is only very limited effect of internal factors on diamond resorption morphology and geometry of etch pits, compared to external conditions (Fedortchouk et al. 2007; Zhang 2016). Thus, the relationship between internal properties and the surface features on diamonds still needs to be constrained.

In the last decade, experimental studies on diamond dissolution (Arima and Kozai 2008; Fedortchouk et al. 2007; Khokhryakov and Pal'yanov 2007a, 2010) examined the dissolution kinetics in different solvents under various T, P and fO_2, and revealed that the secondary morphology and some dissolution features of diamonds are related to T, P and fO_2, as well as the fluid composition in the melt. The presence of fluid in the magma has a very significant effect on diamond morphology and surface features. Diamond dissolution with a free C-H-O fluid present in the melt results in the development of the resorption features most common for natural diamonds, whereas in the absence of fluid, surface graphitization, irregular cavities, and sharp features are produced (Fedortchouk et al. 2007) that are rare on natural diamonds (Tolansky 1968; Wagner 1914). The composition of the fluid was also found to be important for diamond morphology and resorption features (Fedortchouk et al. 2007). Diamonds oxidized in H_2O fluid show transformation of octahedral into hexoctahedral morphology, and six-sided "ditrigonal" {111} faces covered

with only a few flat-bottomed trigons and circular pits are observed. In contrast, diamonds oxidized in CO_2 fluid preserve the primary octahedral shape with trigonal {111} faces covered by lots of trigons with mostly point bottoms and hexagons, no circular pits are observed (Figure 1.2).

The previous experimental studies have laid the foundation for using diamond morphology and dissolution features to interpret fluid and emplacement histories of kimberlites. Many studies have attempted to examine etch pit morphology using optical and Scanning Electron Microscopy (SEM), or double-reflecting interference microscopy (e.g. Arima and Kozai 2008; Khokhryakov and Pal'yanov 2006, 2007b, 2010). The examination methods applied by these studies are able to study the etch pits in 2D images (optical microscopy and SEM) with limited spatial resolution (up to tens or hundreds nanometers for SEM) and may have difficulty determining the morphology of etch pits accurately (e.g. curved-bottomed etch pits, Figure 2.15d), or to reveal some data on the inclination angles of micro-faces (interference microscopy) with errors estimated around ± 5º (Khokhryakov and Pal'yanov 2010). Some more recent studies (Fedortchouk 2015; Fedortchouk et al. 2011; Zhang et al. 2015) have used Atomic Force Microscopy (AFM) to examine the trigonal pits on diamonds, with the advantage of obtaining a three-dimensional view of individual etch pits at magnifications down to nanometer level with precise quantitative measurements. Fedortchouk (2015) found that the geometry of negative trigons is sensitive to the composition of the reacting fluid, and increasing temperature will enlarge the trigon size when diamonds are etched in H_2O fluid, but will mostly affect the shape of trigons when diamonds are etched in CO_2 fluid. Zhang (2015), (2016) showed that point-bottomed trigons evolve into flat-bottomed trigons during

continuous growth, and negative trigons develop truncated corners only when the fluid has bulk $X_{CO2} > 0.5$. Both authors pointed out that the relationship between diameter and depth of negative trigons is an important indicator for fluid composition: trigons on diamonds etched in H_2O fluids have similar diameter with variable depth, whereas trigons on diamonds etched in CO_2 fluid show a strong positive correlation between diameter and depth. The AFM data derived from these studies provided more constraints on fluid compositions and crystallization conditions of Ekati kimberlites.

All the previous studies showed that diamond dissolution morphology is sensitive to the presence and composition of kimberlitic fluids (Fedortchouk 2015; Fedortchouk et al. 2007; Fedortchouk et al. 2011; Fedortchouk et al. 2010; Zhang 2016; Zhang et al. 2015). Diamonds etched in H_2O vs. CO_2 fluid have different resorption features (Fedortchouk et al. 2007). The preliminary AFM investigations by Fedortchouk (2015), Zhang (2016) showed that the geometry of trigonal etch pits is sensitive to the composition of the fluid. However, these studies used only limited number of diamonds and more data are needed to refine the use of using AFM measurements of etch pits to reconstruct emplacement conditions of kimberlite and to understand the nature of kimberlitic fluids.

This thesis is the first systematic study using AFM to examine the morphology of trigonal pits on a large population of diamonds from kimberlites with good geological control. In this thesis, I examined trigons on diamonds from kimberlite pipes of different classes (Fox, Panda, Koala and Misery) and one kimberlite dyke (Snap Lake) with presumably different fluid composition and emplacement histories. I presented AFM data of negative trigons, and particularly positive trigons on natural diamonds for the first time. The results were compared to the AFM data for the positive trigons produced at 0.1 MPa

at and 900-1050 °C in H_2-CO_2 gas mixture (this study) and negative trigons at 1-3 GPa and 1150-1350 °C in CHO fluids (Fedortchouk 2015, Zhang 2016), which helped to better constrain the emplacement conditions of kimberlite magma and the nature of kimberlitic fluids.

1.2 Objectives and Organization of the Thesis

1.2.1 Objectives of the Thesis

The main objectives of this study were:

(1) To clarify whether defects have effects on diamond resorption morphology. In this thesis, I compared the N content and aggregation state of diamonds to the resorption features on {111} and {110} faces (edges).

(2) To develop a systematic method of using AFM measurements on etch pits (positive and negative trigons, trigon-hexagons, hexagons) to reconstruct the emplacement conditions (crystallization temperature, fO_2) and composition of the kimberlitic fluids. I measured and analyzed several informative parameters of the etch pits which are sensitive to the composition of fluid, based on previous studies (Fedortchouk 2015; Fedortchouk et al. 2007; Fedortchouk et al. 2011; Zhang 2016). The parameters include diameter and depth of the pits and the diameter vs. depth relationship, the angles between the micro-faces formed by the pit walls and the {111} faces (reported as $\alpha_{\{111\}}$), the shape of pit bottom and walls, and the degree of negative trigons converted into hexagons (reported as $L_{100}/L_{100}+L_{111}$), calculated as the total length of sides of positive directions divided by the perimeter of the pit. The results of all these measurements were compared to the products

of dissolution experiments under controlled P-T-X conditions by Fedortchouk (2015) and Zhang (2016).

(3) To examine the effect of fluid composition (derived from the study of trigons) on kimberlite emplacement and morphology. I used the inferred fluid composition for four Ekati kimberlite pipes (Fox, Panda, Koala and Misery) that represent two kimberlite classes (Class 1 and 3) and Snap Lake kimberlite dyke to explain their difference in emplacement history.

1.2.2 Organization of the Thesis

In this study, I selected and examined diamonds in two parcels from Snap Lake kimberlite with optical microscopy and SEM to study their general morphological features. The SEM work was assisted by Patricia Scallion. I also measured N content and aggregation state in selcted Snap Lake diamonds by Fourier Transform Infrared Spectroscopy (FITR) with help from Thomas Stachel and Zhihai Zhang. The selection of Snap Lake diamonds for FTIR study was done by myself. I measured etch pits on selected diamonds from Snap Lake kimberlite and four Ekati kimberlites (Fox, Panda, Koala and Misery), and experimental diamond oxidized in H_2-CO_2 mixture at 0.1 MPa by AFM. The selection of Snap Lake and Ekati diamonds for AFM study was done by myself. All the experimental diamonds were from oxidation experiments done my supervisor Yana Fedortchouk. I did all the AFM measurements independently, with help from Zhihai Zhang for calibration of the atomic force microscope.

In Chapter 2, I introduce the geological setting of the Slave Craton, the exploration and mining history, and background geology of Snap Lake and Ekati kimberlites. I also

describe the choice of kimberlites and sample selection, information on diamond oxidation experiments, and the methods used in this study.

In Chapter 3, I describe the octahedral and tetrahexahedral crystals selected from Snap Lake diamonds. The detailed information of diamonds used in oxidation experiments at 0.1 MPa and 900-1150 °C is given. I briefly illustrate the classification of twelve general morphological groups that are defined for Snap Lake diamonds based on resorption features on {111} faces (SG1-SG12) and their related sub-groups based on resorption characters on edges. The results of AFM measurements on positive trigons are reported, which include positive trigons produced by our oxidation experiment and natural trigons on Snap lake diamonds from different lithologies and morphological groups.

In Chapter 4, I first introduce the selected samples from four Ekati kimberlites (Fox, Panda, Koala and Misery), and then give the general description (morphology, colour, surface features) of Snap Lake diamonds. The specific classification of Snap Lake diamonds into twelve morphological groups based on resorption features on {111} faces and the three edge resorption types are demonstrated. The results of FTIR measurements for N content and aggregation state of Snap Lake diamonds are shown to test their relationship with diamond morphology. The results of AFM measurements for negative trigons (trigon-hexagons, hexagons) on Snap Lake diamonds from different lithologies and morphological groups, and negative trigons on diamonds from Fox, Panda, Koala and Misery kimberlites in Ekati Mine are reported.

In Chapter 5, I review the previous experimental data on positive trigons, and determine the origin of positive trigons on Snap Lake diamonds by observing their development pattern and comparing their morphology and size to the experimentally

produced positive trigons by this and other studies. I describe the controlling factors for formation of positive trigons, and address the T, P limits and possible fO_2 and composition of the reacting fluid. Experimental data from previous studies on the relationship between CO_2/H_2O ratio in the fluid and etch pit parameters are reviewed, and the composition of fluids in the four studied Ekati kimberlites and Snap Lake kimberlites are reconstructed by comparing negative trigons on diamonds from each kimberlite to products from experiments in H_2O and CO_2 fluids at 1-3 GPa and 1150-1350 °C by Fedortchouk (2015) and Zhang (2016). The fluid compositions derived from the study of trigons are compared to the geological features of Ekati kimberlites to confirm the results, and the difference in emplacement history of Snap Lake dyke and Ekati kimberlites is explained by the variation of fluid composition based on the model by Skinner and Marsh (2004). The difference of fluid present in HKM and HKP of Snap Lake kimberlite is also discussed by comparing the degree of diamond resorption, presence of resorption groups, and negative trigon parameters in these two facies. I further review the effect of defects on diamond resorption morphology proposed by previous studies and discuss at what stage defects play a role in trigon growth. The inferred evolution of negative and positive trigons as their size increases is illustrated. I review the kink mechanism proposed by Angus and Dyble (1975) for trigon formation, and compare the AFM measurements on negative and positive trigons to the predicted trigon shape and evolution by Angus and Dyble (1975).

In Chapter 6, I summarize the reconstruction of emplacement conditions in Snap Lake and Ekati kimberlites by AFM measurements of trigons, and conclude the contribution of this thesis to understanding kimberlite fluid systems. I also provide suggestions for future studies.

1.3 Terminologies used in This Study

1.3.1 Kimberlite Lithological Types

Kimberlites are hybrid rocks comprising mantle-derived xenocrysts, cryptogenic macrocrysts and primary magmatic minerals (Mitchell 2004). The kimberlite minerals are dominated by olivine phenocrysts (< 0.5-1 mm, Scott Smith et al., 2013), macrocrysts (> 1 mm, Scott Smith et al., 2013) and xenocrysts that are usually replaced by serpentine and other alteration minerals. Other macrocrysts include ilmenite, garnet, phlogopite, diopside, enstatite and chromite, and the groundmass minerals comprise variable proportions of spinel, perovskite, olivine microphenocrysts, calcite, serpentine, phlogopite, monticellite, apatite and melilite (Mitchell 1986; Skinner and Marsh 2004). The kimberlite intrusions are commonly preserved as downward-tapering pipe-like bodies (Figure 1.3 and 1.4). Three types of kimberlite bodies are proposed by Field and Scott Smith (1999), and termed as Class 1, 2 and 3 by Skinner and Marsh (2004). Each type of kimberlite is characterized by different characteristics and geometries in contrasting local environments (Field and Scott Smith 1999; Scott Smith 2008). The nomenclature for kimberlite lithofacies and textures varies in different literature, and this study generally follows the kimberlite nomenclature proposed by Scott Smith et al. (2013).

Class 1 pipes were first defined based on observations from exploration and mining in southern Africa, as in the "South African kimberlite pipe model" (Hawthorne 1975; Mitchell 1986). Kimberlites of Class 1 have steep-sided carrot-like shapes (Figure 1.4a) with great depths (up to 3km) (Skinner and Marsh 2004), and are made up of three zones (Hawthorne 1975). (1) The uppermost crater zone is filled with pyroclastic kimberlite (PK) that is extrusively formed volcaniclastic kimberlite deposited directly into the pipe, but the

crater zones are rarely preserved due to erosion (Field and Scott Smith 1999). (2) The diatreme zone contains massive volcaniclastic kimberlite (MVK) which consists predominantly of pelletal lapilli (sub-spherical clasts with a central fragment, mantled by an extremely fine-grained rim of probable juvenile origin which contains microlitic diopside; Gernon et al, 2012a) in addition to phenocrysts and macrocrysts of serpentinized olivine and abundant relatively unaltered country rock xenoliths set in fine-grained interclast matrices dominated by serpentine. No primary calcite is present (Field and Scott Smith 1999; Skinner and Marsh 2004). The walls of the diatreme zone have steep slopes of around 82° irrespective of the character of the country rock (Hawthorne 1975). (3) The lowermost root zone is filled with coherent kimberlite (CK) formed by the crystallization of the intrusive kimberlite magma, showing a uniform, coherent (non-fragmental) texture, commonly containing fresh olivine and highly altered xenoliths set in a groundmass of primary calcite and serpentine (Field and Scott Smith 1999; Scott Smith 2008). A transitional zone occurs at the interface of the root zone and diatreme zone showing petrographic transition from CK to MVK (Skinner and Marsh 2004). Class 2 and 3 pipes are mostly recognised from Canadian occurrences. Class 2 pipes have shallow (< 500 m) saucer-shaped craters (Figure 1.4b) with pyroclastic kimberlites (PK) as the dominant fill, while no MVK or CK is observed (Field and Scott Smith 1999; Scott Smith 2008). The PK is characterized by discrete olivine grains and juvenile lapilli (olivine grains rimmed by fined-grained coherent kimberlite which is usually free of diopside) and variable mixtures of both constituents set in interclast matrices of serpentine or carbonate (Scott Smith 2008; Skinner and Marsh 2004). The juvenile lapilli are important components of crater fill in Class 2 kimberlites, and can be recognized in some Class 1 and

Class 3 kimberlites (Scott Smith 2008; Sparks et al. 2006). Class 3 (Figure 1.4c) pipes have small, steep-sided shapes and are mainly filled with resedimented volcaniclastic kimberlite (RVK) and minor PK with local CK (Field and Scott Smith 1999; Scott Smith 2008; Skinner and Marsh 2004). The RVK is composed of volcaniclastic kimberlite reworked by sedimentary processes (Field and Scott Smith 1999), containing variable mixtures of discrete olivine grains that are usually fresh and angular, lithic clasts (xenoliths, autoliths and minor magmatic pyroclasts) and wood set in a sedimentary matrix (Scott Smith 2008).

It is suggested that geological setting can be a controlling factor on the types of kimberlite pipes (Field and Scott Smith 1999; Scott Smith 2008), as Class1 pipes usually occur in competent basement rocks, while Class 2 pipes and Class 3 pipes are commonly found in regions where basement rocks are covered by a veneer of poorly consolidated sediments (Scott Smith 2008). However, Skinner and Marsh (2004) argued that it is the composition of volatiles rather than geological setting that affects the emplacement of kimberlite. They used an example of Fox kimberlite pipe in Lac de Gras kimberlite field to demonstrate that different kimberlite classes can occur in the same geological setting. Fox pipe belongs to Class 1 kimberlite containing MVK in the lower portion of the pipe with overlying RVK in the crater zone, whereas the other pipes in the field are Class 3 kimberlites with abundant RVK (e.g. Koala) or CK (e.g. Grizzly and Leslie) (Nowicki et al. 2004).

Kimberlites can also form dykes and sheets, which are intrusive tabular bodies when emplaced in fracture zones, and may occur as regional swarms, precursor dykes to diatremes, and/or intrusions within, and external to, diatremes and vents (Mitchell 1986). Kimberlite dykes are found mostly in the vicinity of Class 1 pipes (e.g. the Snap Lake dyke

near Gahcho Kue and Camsell Lake) or Class 3 pipes occasionally (e.g. narrow dykes near Ekati kimberlites, Nowicki et al. 2004), and are composed of typical CK (e.g. Snap Lake dyke) or CK with a wide variation in macroscopic appearance caused by local processes such as flow differentiation (e.g. Wemindji) (Scott Smith 2008).

1.3.2 Diamond Resorption Studies and Resorption Terminologies

Diamond morphology and surface features, especially the trigonal pits called trigons (i.e. flat or point bottomed triangular depressions on the {111} faces of diamonds), have attracted lots of studies. The trigons were first observed by Fersmann and Goldschmidt (1911) who explained the origin of trigons by etching. This was supported by studies of Evans and Sauter (1961) and Frank et al. (1958), while Halperin (1954) and Varma (1967) argued for a growth origin for the trigons. It is now commonly accepted that most surface features including the trigons of natural diamond result from dissolution in kimberlite or lamproite magmas (Gurney et al. 2004; Moore and Lang 1974; Orlov 1977; Robinson 1979) and/or in the mantle (Khokhryakov and Pal'yanov 2007a, 2010), through the process of carbon oxidation (Arima 1998). Most of the experimental studies focused on the kinetics of diamond etching under different temperatures, pressures, etchants and partial pressure of oxygen (Evans and Phaal 1961; Evans and Sauter 1961; Frank and Puttick 1958). The first comprehensive study on diamond resorption features on natural diamonds was done by Robinson (1979), who examined large populations of diamonds from different facies and kimberlites in South Africa, trying to understand how different resorption features were produced, whether diamonds from different facies with the same pipe show different resorption features, and which resorption features were formed by dissolution in kimberlite magma and which ones resulted from dissolution in the mantle.

However, it remained unknown if any resorption could occur in the kimberlite pipe after kimberlite emplacement.

This study generally follows the work of Robinson (1979) and Tappert and Tappert (2011) for terminologies on diamond morphology and surface features, as summarized below:

Diamond morphology refers to the diamond crystal form that can show various types. (Figure 1.5). Common diamond morphologies are:

(1) **Monocrystalline** diamonds, including three basic geometric forms: octahedrons, cubes, tetrahexahedrons. There are also combinations of the basic forms, aggregates, parallel intergrowths, twins, irregular forms or fragments.

(2) **Fibrous** diamonds consisting of parallel microscopic fibers that are generally oriented in the direction of diamond growth, usually have dull luster.

(3) **Polycrystalline** diamonds comprising numerous microcrystalline to cryptocrystalline diamond crystallites, usually occurring as masses without an apparent crystallographic form.

Shape of {111} faces: A **ditrigonal** {111} face is a six-sided polygon that is trigonal in two different ways on the same axis (Figure 1.6a and 1.6b). A **trigonal** {111} face is an equilateral triangle (Figure 1.6c and 1.6d). Diamond dissolution experiments show that the ditrigonal face is typically produced in the presence of water (Chepurov et al. 1985; Fedortchouk et al. 2007).

Diamond resorption or **dissolution** refers to a loss of volume of diamonds by reaction with fluid or melt accompanied by morphological changes (Figure 1.7), development of various surface features or graphitization. Experimental results show that redox conditions and composition of the C-O-H fluid affect the diamond dissolution morphology.

Three main forms are found (Figure 1.8). (1) In the redox range of HM and CCO buffers, trisoctahedrons are formed, which are 24-sided polyhedrons where all sides are equidimensional. Positive trigons develop on {111} faces. The rounded surfaces show striations or hillocks perpendicular to [110]. (2) Under moderately oxidizing conditions and in the presence of H_2O-CO_2 fluid, ditrigonal faces and negative trigons are formed. (3) Under highly reducing conditions and in the presence of the CH_4-H_2 fluid, polycentric, almost flat-faced, trisoctahedrons are formed, with striations parallel to [110] and low-angle negative trigons (Khokhryakov et al. 2002).

Surface features are used to describe the diverse textures on diamond surfaces. The textures can originate from such processes as growth, plastic deformation, resorption, and /or abrasion during transportation (placer diamonds) (Tappert and Tappert 2011). Most features are restricted to certain crystal faces, i.e., they only develop on octahedral, cubic or tetrahexahedral (THH) faces. Some features, however, are not restricted to certain crystal faces and can occur anywhere on diamonds.

1.3.2.1 Surface features on octahedral {111} faces

Negative trigons are equilateral trigonal pits with vertices pointing in the opposite direction from the octahedral face (Figure 1.9). The pits are usually flat-bottomed or point-bottomed (Robinson 1979), but bottoms of some pits may have intermediate shapes

between flat- and point-bottomed trigons, termed “round-bottomed” (Fedortchouk et al. 2011). Some trigons have stepped walls. Negative trigons are common on natural diamonds and are considered to be produced by etching (Robinson 1979).

Positive trigons are equilateral trigonal pits with sides parallel to the edges of the octahedral face (Figure 1.10). Positive trigons are also considered etch features but are much less common than negative trigons (Robinson 1979).

Hexagons (Figure 1.11) are hexagonal pits (usually flat-bottomed) and may have trigons on their bottoms (Robinson 1979). It has been suggested that the hexagon is a combination of negative and positive trigons (Sunagawa 1984).

Step faces are single or multiple imbricated layers on the {111} faces on diamonds that show a stepped appearance (Figure 1.12). Some authors prefer the term “triangular plates” for the same textures (Robinson 1979; Tappert and Tappert 2011). It is suggested that the step faces can be formed during growth (Sunagawa 1984) or by resorption (Viljoen et al. 1992). This study distinguishes step faces from laminae and striations if it is possible to follow the whole continuation of such a step around the whole {111} face.

Shield-shaped laminae are superimposed laminae that have curved (shield-like) outlines and stepped appearances (Figure 1.13a and 1.13b). They are generally much thinner than step faces. (Robinson 1979).

Serrate laminae occur as superimposed serrate-like layers of progressively diminishing areal extent (Figure 1.13c and 1.13d) (Robinson 1979). In my samples, some diamonds also developed **irregular layers** that differ from shield-shaped and serrate laminae by showing irregular-shaped outlines (Figure 1.13e).

1.3.2.2 Surface features on tetrahexahedral {110} faces

Hillocks are common features on tetrahexahedral/dodecahedral faces and are formed during resorption. Similar to striations, hillocks are usually parallel to the edges of resorbed octahedral diamonds (Figure 1.14a). Hillocks can be divided into **elongated hillocks** (Figure 1.14b), with semi-cylindrical or semi-ellipsoidal forms, and **pyramidal hillocks** (Figure 1.14c) with triangular-pyramidal forms (Robinson 1979).

Striations are concentric ridges or bands that develop around the six-fold axes of tetrahexahedral faces (Figure 1.15). Some authors use "terraces" for the same textures. When octahedral faces are present, the striations are usually along their edges. Striations are interpreted as outcrops of octahedral growth layers that are relatively resistant to resorption (Robinson 1979).

Cavities are pits developed on tetrahexahedral faces with elliptical or irregularly curved outlines (Figure 1.16). Some cavities are deep and have striated bottoms, and are generally referred as **corrosion sculptures**. In other cases, cavities that are shallower and often bigger are termed **shallow depressions** (Robinson 1979; Tappert and Tappert 2011). It is suggested that cavities are formed by late-stage etching that postdates the formation of striations and hillocks Tappert and Tappert (2011).

Circular pits occur on tetrahexahedral or cubic faces as shallow pits with oval to circular outlines (Figure 1.17). It was typically suggested that circular pits result from etching by adhering gas bubbles, such as CO_2 bubbles produced as a reaction product during the resorption of diamond (Robinson 1979). However, the recent experimental study of Zhang et al. (2015) showed that circular pits also develop in experimental runs lacking CO_2. Therefore, what controls the development of circular pits is not yet well known.

1.3.2.3 Surface features on cubic {100} faces and non-restricted surface features

Square pits develop on the {100} faces on diamonds (Figure 1.18). Some authors use "tetragonal pits" for the same textures (Robinson 1979; Tappert and Tappert 2011).

Ruts are deep channels on diamond surfaces and represent planar zones of weakness or cracks widened by resorption or etching (Robinson 1979).

Frosting sometimes covers parts of the diamond or the entire diamond surface and makes the diamond appear dull. Surface frosting can be caused by numerous microscopic hillocks of sharp or rounded shape (Fedortchouk et al. 2010).

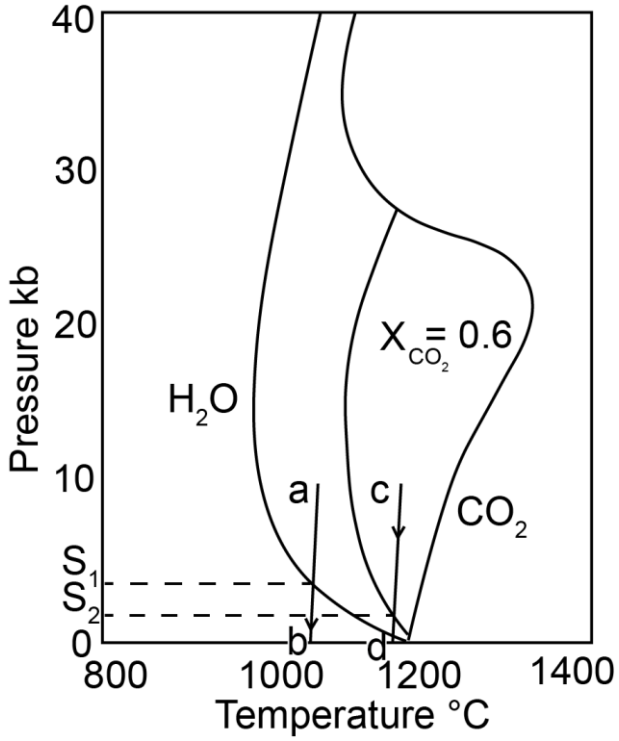

Figure 1.1 Solidus surfaces for peridotite-H_2O and peridotite-CO_2 (X = 1.0 and X = 0.6, mole fraction) after Wyllie (1987). Hypothetical cooling curves ab and cd at similar cooling rates intersect the respective solidi at pressures S1 and S2. Revised from Skinner and Marsh (2004).

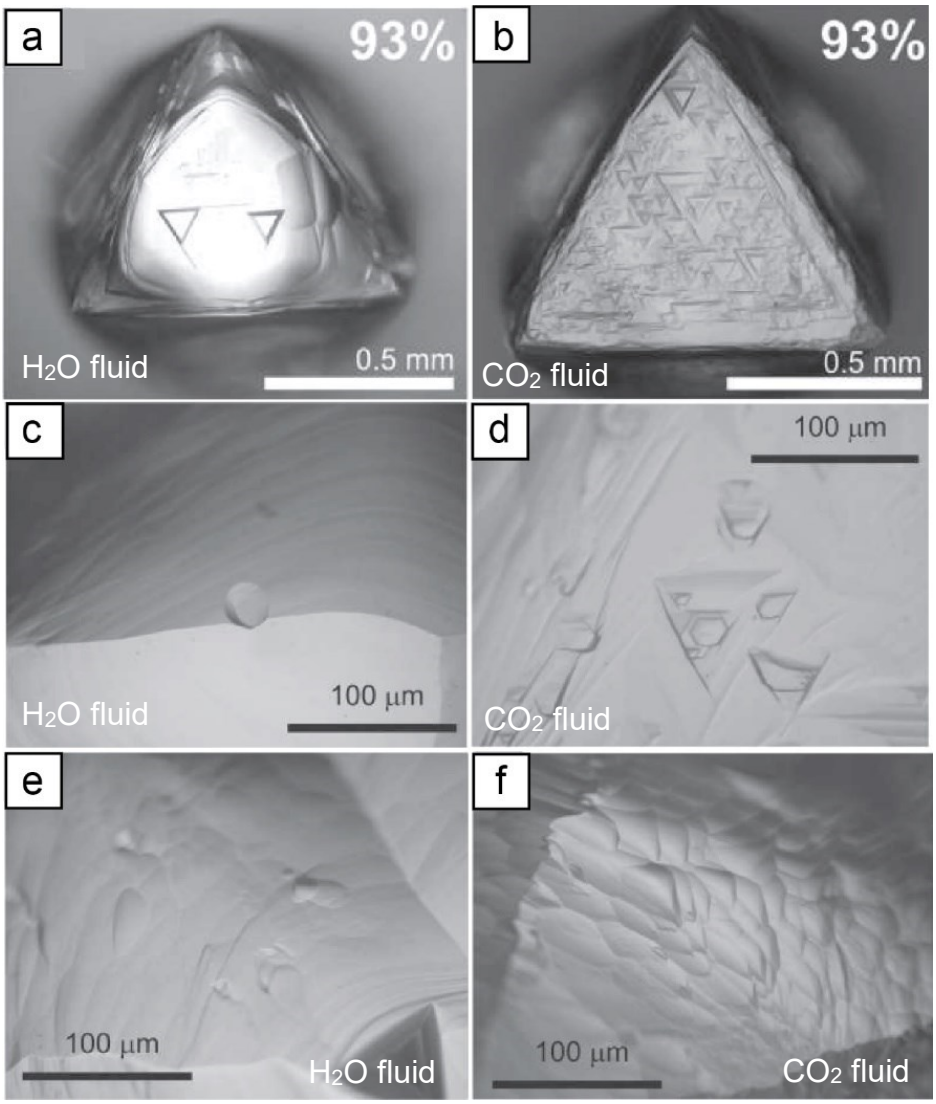

Figure 1.2 (a) Ditrigonal {111} face of diamond oxidized in pure H_2O fluid (93% weight loss). (b) Trigonal {111} face of diamond oxidized in pure CO_2 fluid (93% weight loss). Most common feature produced only in H_2O fluid: (c) Striation and circular cavities on hexoctahedral faces; (e) individual round pyramid-shape hillocks. In CO_2 fluid: (d) Hexagons; (f) Drop-shape hillocks completely covering the surface of hexoctahedrons. All the images are from Fedortchouk et al. (2007).

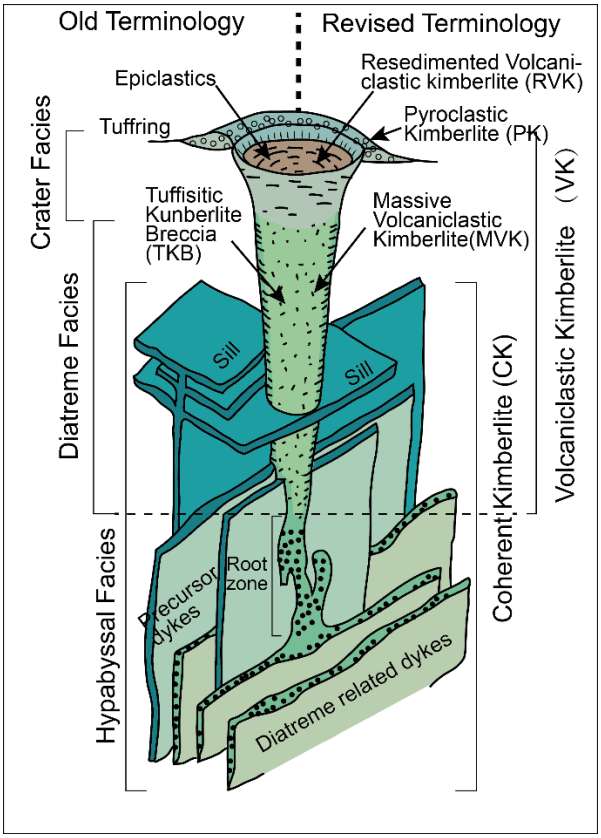

Figure 1.3 The "classic South African model" of a kimberlite pipe (Mitchell 1986) with original nomenclature (left side of figure) and a revised nomenclature system (right side of figure) suggested by Scott Smith et al. (2013), except the term MVK for massive volcaniclastic kimberlite (e.g. Sparks et al., 2006) replacing the original TK. Reproduced from Kjarsgaard (2007).

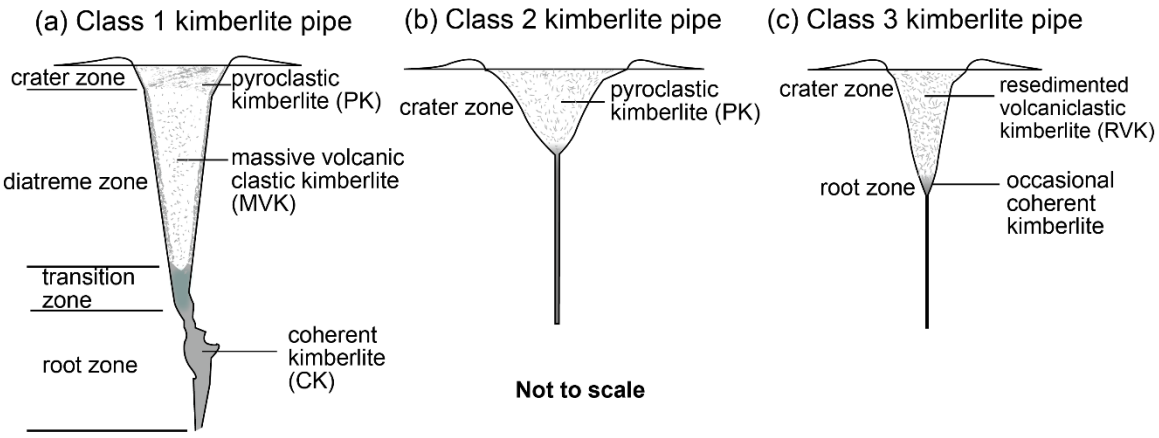

Figure 1.4 Schematic illustration of the three classes of kimberlite pipe reproduced from Walters et al. (2006).

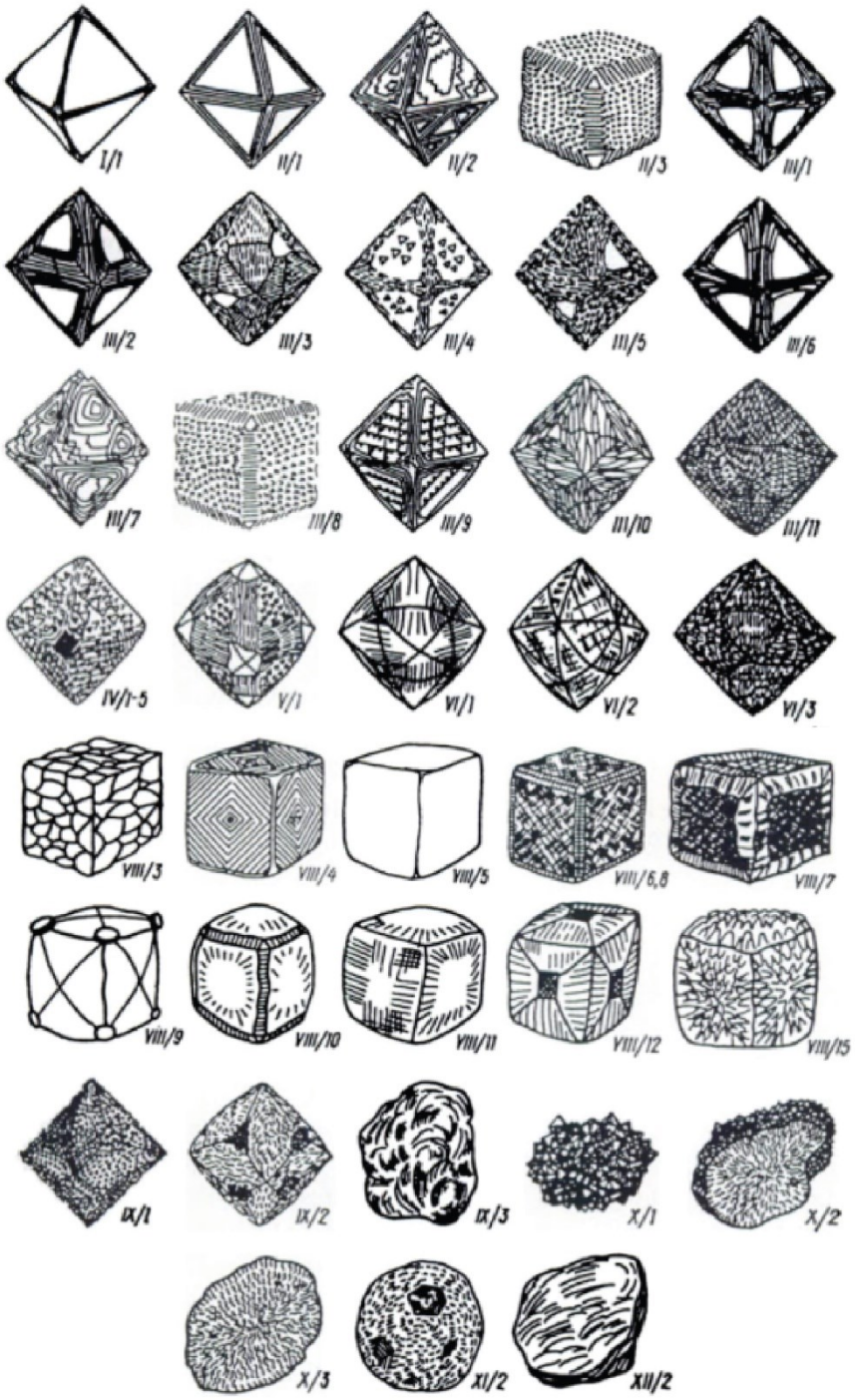

Figure 1.5 Morphological diamond types summarized by Bartoshinsky (1983). Diamonds from different Yukutian kimberlites were classified into 12 groups and 55 types.

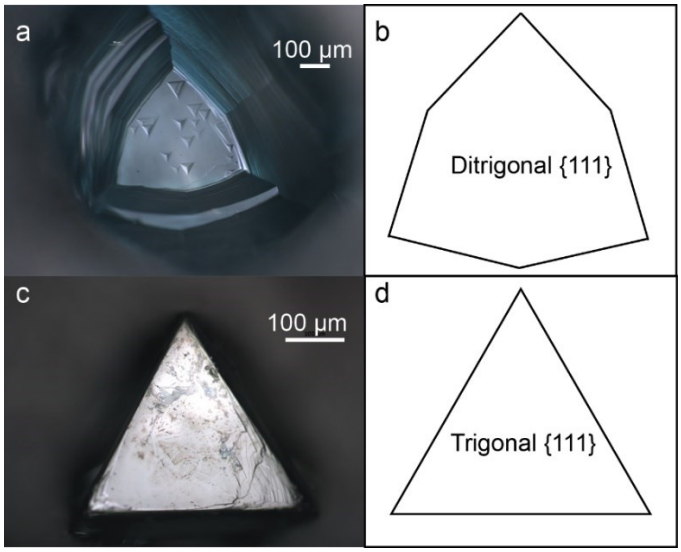

Figure 1.6 Ditrigonal {111} face of natural diamond M95-A3-1 from Misery kimberlite (a) and sketch of a perfect ditrigonal face (b) vs. Trigonal {111} face of natural diamond (c) and sketch of a perfect trigonal face (d).

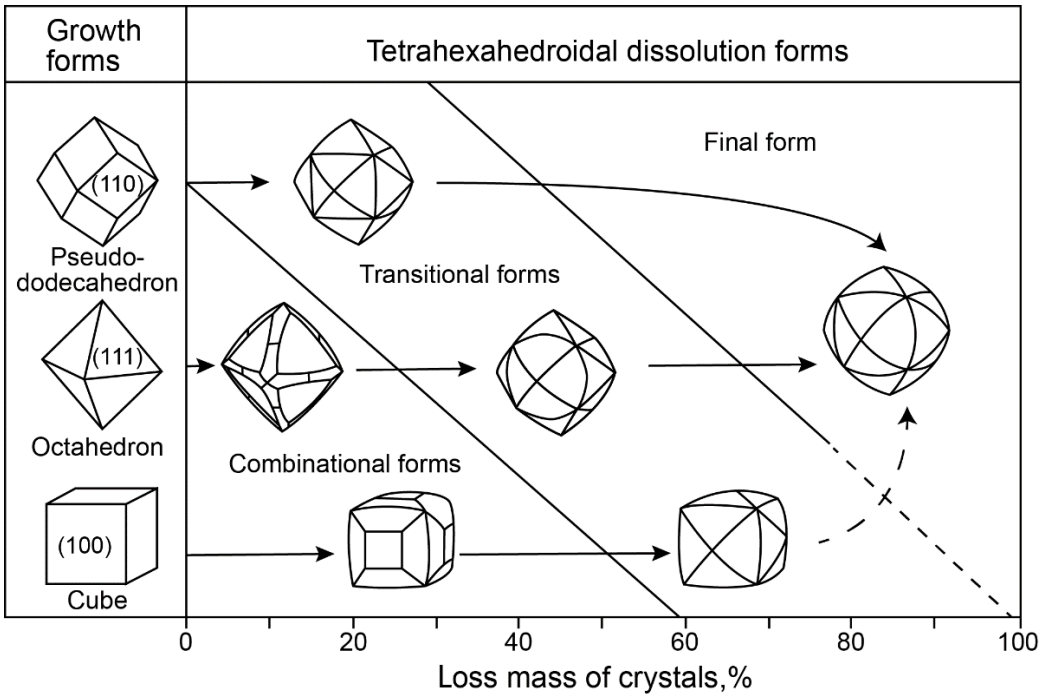

Figure 1.7 Evolution scheme for the morphology of diamond crystals during dissolution in H_2O-containing carbonate and silicate melts, revised from Khokhryakov and Pal'yanov (2007a). Note that pseudo-dodecahedron is defined as a dodecahedron formed by octahedral terracing.

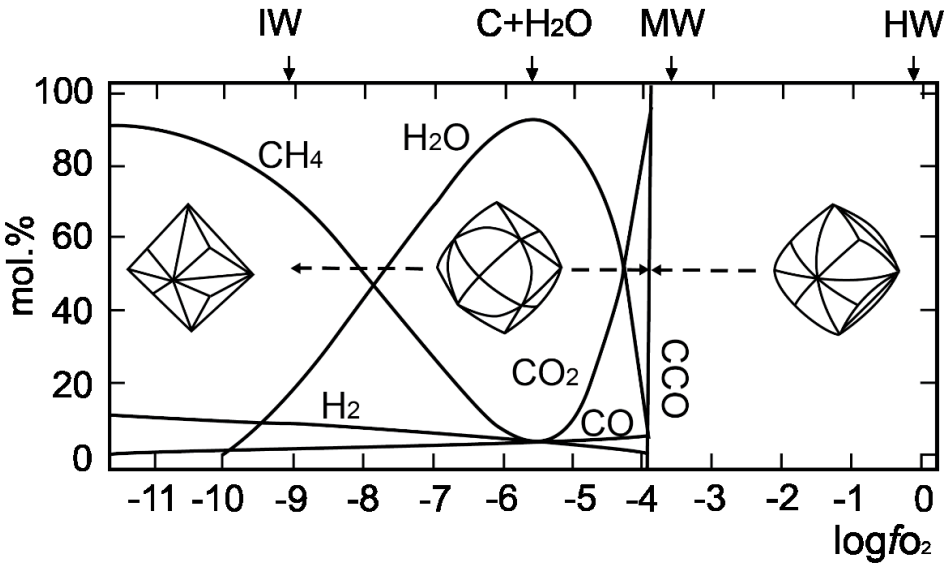

Figure 1.8 The change of diamond dissolution form vs. logfO_2 and composition of C-O-H fluid at 5.7 GPa and 1420 ºC. Composition of the fluid phase in equilibrium with diamond as a function of fO_2 and position relative to the IW, CCO, C+H_2O, HM and MW buffers. Reproduced from Khokhryakov et al. (2002).

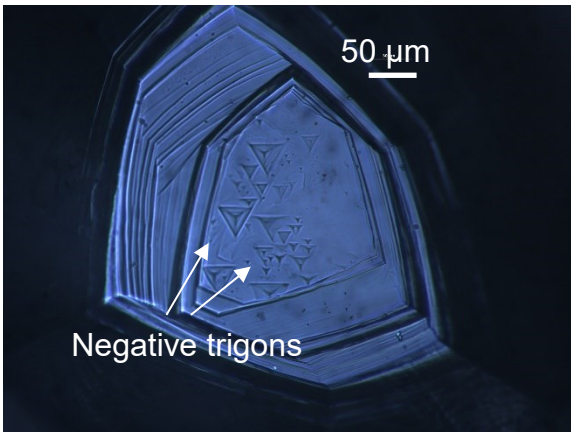

Figure 1.9 Negative trigons on diamond M95-K6 from Misery kimberlite.

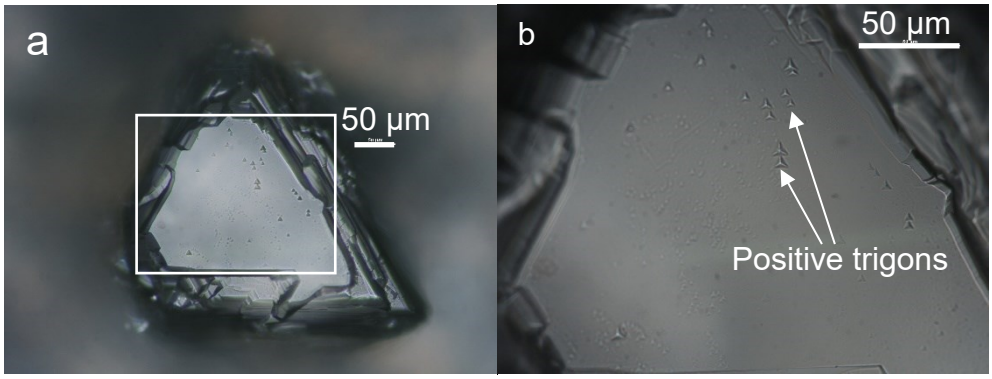

Figure 1.10 Positive trigons on diamond SNP8-9 from Snap Lake kimberlite. Image (b) is a magnified picture of the area marked in (a).

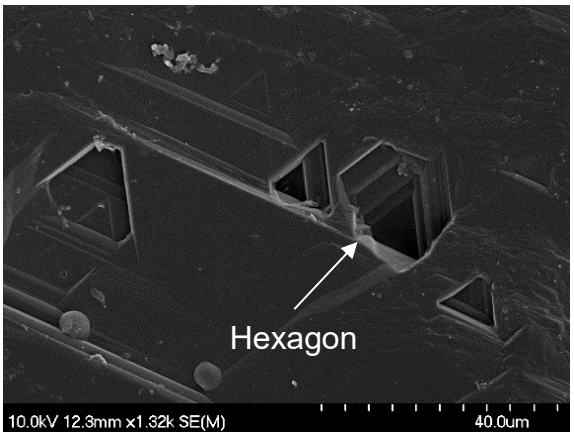

Figure 1.11 Hexagons on diamond 300-38 from A/K15 kimberlite.

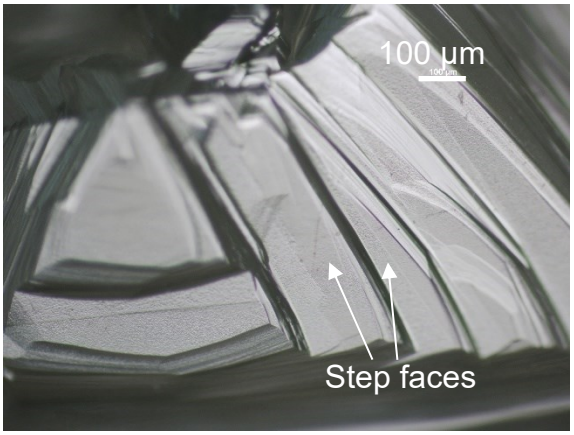

Figure 1.12 Step faces on diamond SNP1-1 from Snap Lake kimberlite.

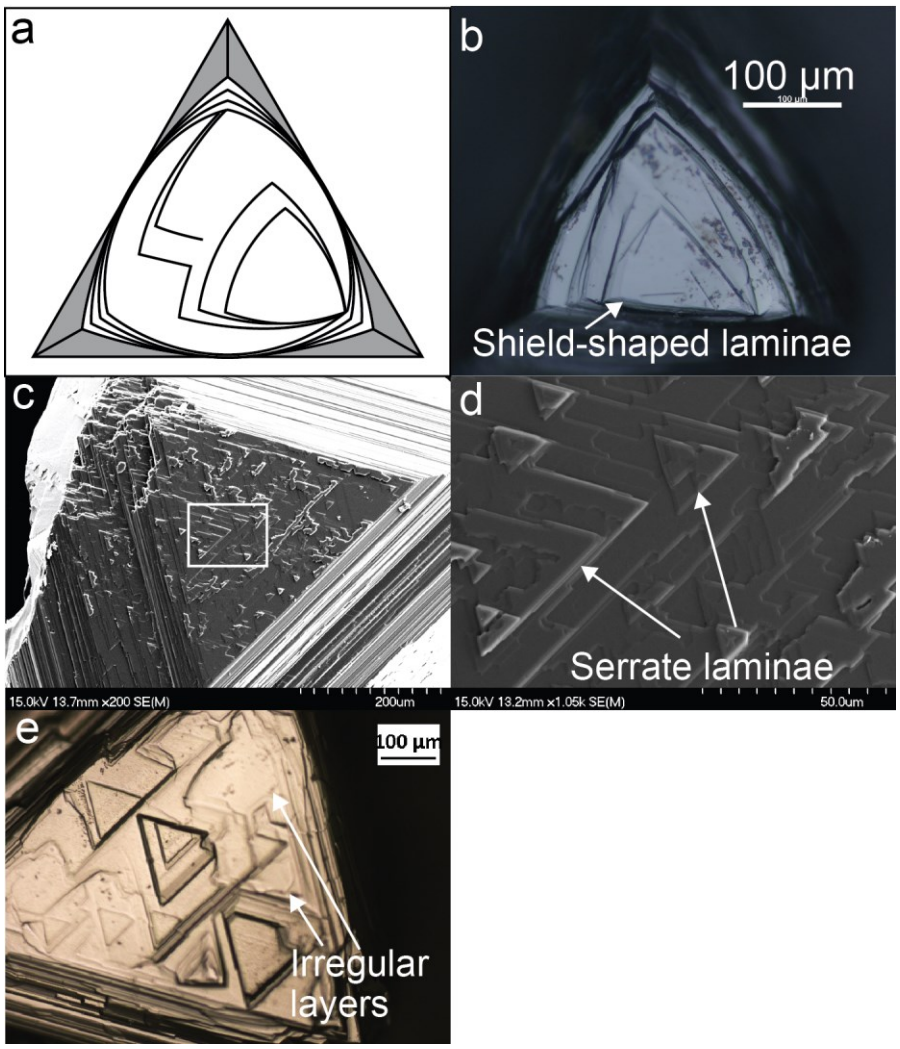

Figure 1.13 (a) Idealized representation of shield-shaped laminae on an octahedral crystal face, reproduced from Tappert and Tappert (2011). (b) Shield-shaped laminae on diamond SNPO12-3 from Snap Lake kimberlite. (c) and (d) Serrate laminae on diamond SNP5-5 from Snap Lake kimberlite. (d) is a magnified image of the area marked in (c); (e) Irregular layers on diamond SNP9-1 from Snap Lake kimberlite.

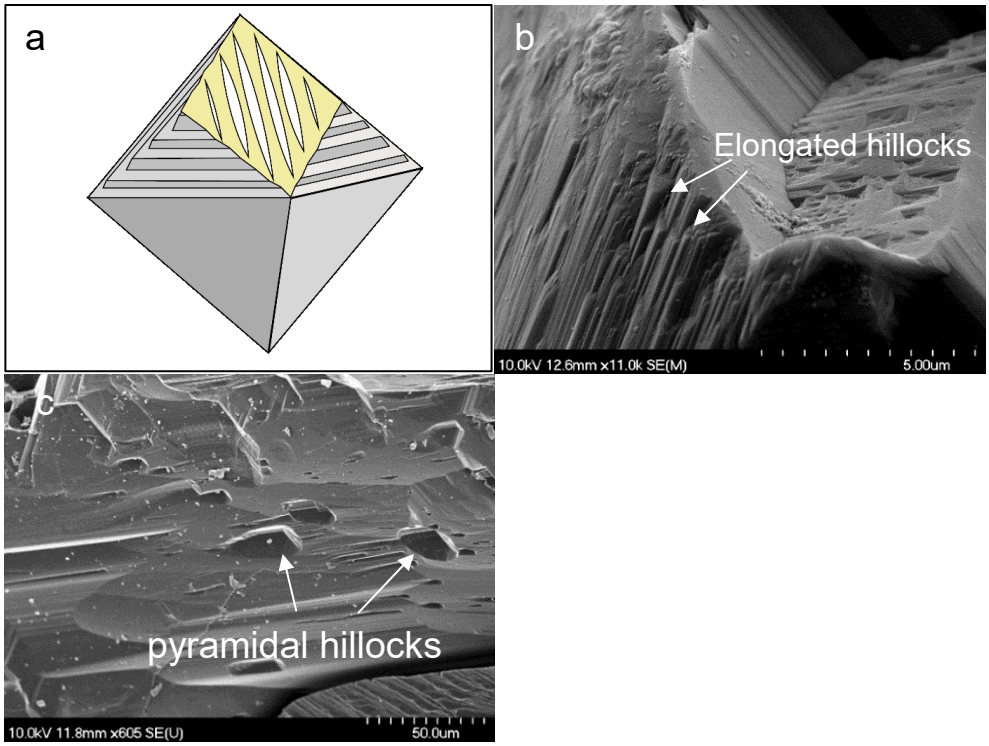

Figure 1.14 (a) Orientation of hillocks (white) with respect to octahedral (grey) and dodecahedral (yellow) crystal faces (Tappert and Tappert 2011). (b) Elongated hillocks (diamond 300-22; AK15 kimberlite). (c) Pyramidal hillocks (diamond 600-16; BK1 kimberlite).

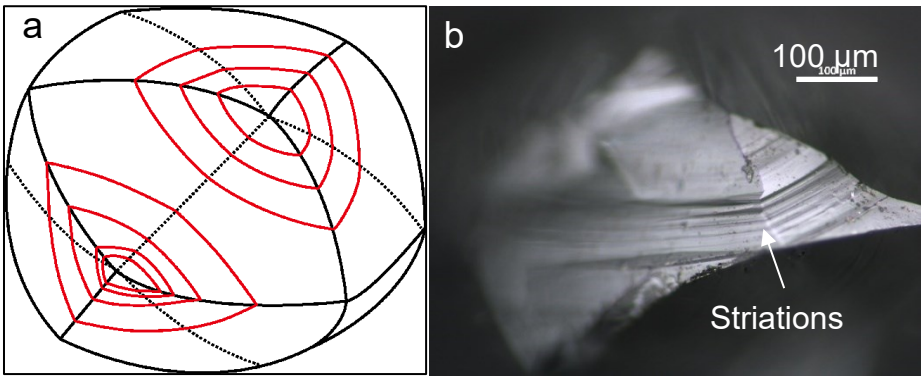

Figure 1.15 (a) Tetrahexahedral crystal form of diamond with striations outlined in red (Tappert and Tappert 2011). (b) Striations on diamond 300-27 from AK15 kimberlite.

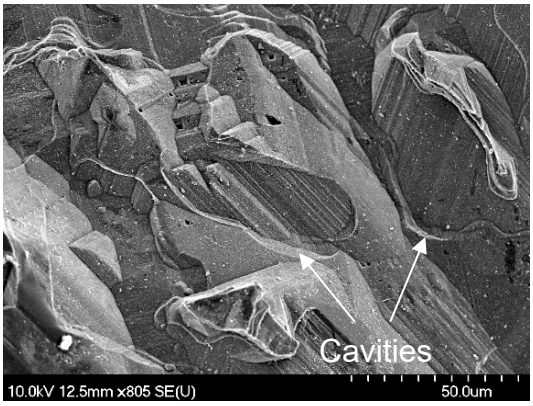

Figure 1.16 Cavities on diamond 600-15 from BK1 kimberlite.

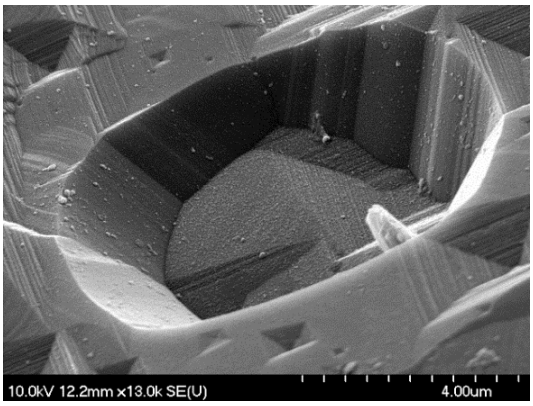

Figure 1.17 A circular pit on diamond 600-15 from BK1 kimberlite.

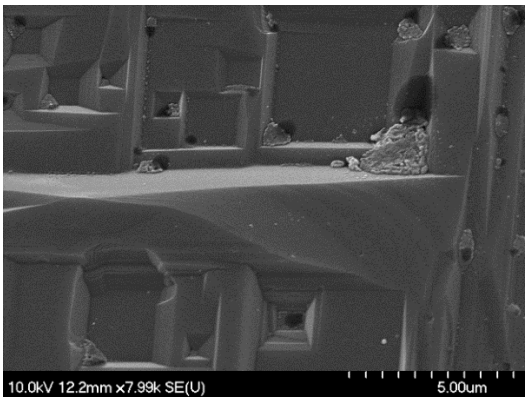

Figure 1.18 Square pits on diamond 600-17 from BK1 kimberlite.

CHAPTER 2. BACKGROUND GEOLOGY AND ANALYTICAL METHODS

2.1 Background Geology of Snap Lake and Ekati Mine Kimberlites

2.1.1 Geological Setting of the Slave Craton

The Snap Lake dyke and the Ekati kimberlites intruded into the Slave Province (Figure 2.1), a relatively small late Archean craton with a surface area of ca. 213000 km^2, one tenth that of the Superior Province (Padgham and Fyson, 1992). The Slave Craton hosts the Acasta gneiss, currently the oldest dated rocks on earth (4.031 ± 0.003 Ga, Bowring and Williams, 1999). The Slave Craton formed by amalgamation of early to late Archean rocks over a billion years (Card and King 1992), and is surrounded by Paleoproterozoic orogenic belts on three sides (Davis and Bleeker 1999). Rocks of the Slave Craton include gneiss, migmatite, granitoid intrusions, metasediments and metavolcanic rocks (Figure 2.2, Padgham and Fyson, 1992). Rocks older than 3.0 Ga are mostly on the western margin of the craton (Figure 2.2, Padgham and Fyson, 1992), including granites, granitoids, gneiss, and migmatite (Padgham and Fyson, 1992; Krogh and Gibbins, 1978). Rocks older than 2.8 Ga (2.8-3.0 Ga), including gneisses and granitoids, are found as inliers in the western and central parts of the Slave Province (Figure 2.2) (Bowring et al. 1989; Frith et al. 1986; Henderson et al. 1987; Lambert and van Breemen 1991).

At least three distinct supracrustal sequences formed in different tectonic-sedimentary environments have been identified (Padgham and Fyson 1992). The most abundant and sequence throughout the Slave Province consists of turbidites (greywacke-

mudstone) formed in a tectonically active environment, with narrow volcanic belts either within or adjacent to the sedimentary rocks. The turbidites and volcanics are underlain by shelf-type quartz arenites and overlain by fluvial conglomerates and sandstones (Padgham and Fyson 1992).

The lithospheric mantle underling the Slave Craton is made up of heterogeneous domains, which differ in architecture, bulk composition, conductivity and seismic anisotropy, but the boundaries of the domains are poorly constrained (Kopylova et al. 2010). Three distinct NE-trending lithospheric domains have been identified (Figure 2.1): the northern, central and southern Slave Province (Grütter et al. 1999). The southern domain is further divided into western and eastern parts based on contrast composition of garnet (Carbno and Canil 2002). The western and eastern parts of the Slave Province are thought to be divided by a 2.7 Ga suture, the location of which is approximated by the Pb isotope line of Thorpe et al. (1992) (Figure 2.1).

The Snap Lake kimberlite and Ekati kimberlites were emplaced into the southeastern and the central domains of Slave Craton respectively (Figure 2.1). The SE domain has a predominantly lherzolitic mantle with subordinate eclogite overlain by 2.70-2.58 Ga crust; harzburgitic garnet xenocrysts with moderate to high Cr_2O_3 content are present (Grütter et al. 1999; Snyder et al. 2014). The SE domain shows WSW-ENE mantle anisotropy (Bank et al. 2000b) and relatively low conductivity (Jones et al. 2001). The central domain shows a two-layered structure (Griffin et al. 1999a). The upper layer contains 3.9-2.85 Ga crust overlying a 3.3-3.0 Ga spinel lherzolitic mantle to 90-110 km depths where an anomalously conductive region occurs (Jones et al. 2001), and a diamondiferous ~3.0 Ga ultradepleted harzburgitic layer to 145 km depth. The lower layer,

between 140 and 210 km depths, shows more uniform seismic anisotropy, velocity, and a refertilized, lherzolitic composition (Snyder et al. 2014). In addition, the central domain has a significantly lower proportion of eclogitic garnet xenocrysts (Grütter et al. 1999) and a different direction of mantle anisotropy (Bank et al. 2000b) (Figure 2.1).

The origin of the layered structure of mantle lithosphere beneath the central Slave Craton is still unknown. The plume subcretion model is supported by diamond inclusions of ultradeep paragenesis, and sulfide inclusions in mantle olivine with age over 3.1 Ga and lower mantle geochemical signatures (Aulbach et al. 2004; Aulbach et al. 2007; Davies et al. 2004; Griffin et al. 1999a; Griffin et al. 2004). In contrast, the "mantle stacking" model is supported by high Cr/Al ratios of garnet inclusions in diamonds, which suggests subduction of oceanic lithosphere and partial melting in the spinel stability field (Canil 2004; Stachel 2003; Tappert et al. 2005).

The host rocks of Snap Lake kimberlite are Archean metavolcanics and granitic rocks in the upper portion of the intrusion, whereas the lower portion of the kimberlite emplaced entirely in granitic rocks (Kopylova et al. 2010). The Ekati kimberlites intruded into Archean granitoids overlapped by greywacke-mudstone turbidites. Late Cretaceous and early Tertiary cover sediments were present at the time of emplacement but are not currently preserved in the region (Nowicki et al. 2004).

2.1.2 Exploration and Mining History of Snap Lake and Ekati Diamond Mines in Northwest Territories, Canada

The Snap Lake Mine was a remote fly-in/fly-out operation, located about 220 km northeast of the city of Yellowknife in the Northwest Territories, Canada (Figure 2.1, Figure 2.3). It was De Beers' first mine outside Africa, and Canada's first completely

underground diamond mine. In 1997, Winspear Diamonds Inc. discovered the Snap Lake kimberlite, and sold the project to De Beers in 2000. The construction and commissioning of the underground crushing and conveying system was completed in 2008. Commercial production began in January 2008. The mine produced 443,000-925,000 carats diamonds annually from 2008-2012, and over 1 million carats annually from 2013-2014, as reported by De Beers. The estimated reserves of the mine were 16.1 million carats and a projected lifetime until 2028 (De Beers Analyst Seminar 2014). De Beers halted the operation and placed the mine into care and maintenance in December 2015, due to a downturn in the market conditions and costly underground water management problems. De Beers put the mine up for sale in 2016 and flooded the underground tunnels of the mine to cut down on costs.

The room-and-pillar method was used for mining the ore. The ore was extracted, creating separate open areas or "rooms" and leaving untouched ore or "pillars" to support the overburden. The ore was crushed underground and then transported to a dense media separation (DMS) plant on the surface for concentration (Robertson 2001).

The Ekati Mine was Canada's first diamond mine, located in the Lac De Gras region of the Northwest Territories, about 300 km northeast of the city of Yellowknife (Figure 2.1). The mine was opened by BHP Billiton in 1998 and was sold to Dominion Diamond Corporation and Archon Minerals in 2013. It occupies a claim block of approximately 1800 km^2 that contains over 150 kimberlite intrusions (Nowicki et al. 2004; Nowicki et al. 2008). Chuck Fipke and Stewart Blusson first discovered the Point Lake kimberlite in Lac De Gras region, which was uneconomic but led to the 1990s diamond rush in the area. In 1993, the Panda kimberlite was confirmed by drilling and production

of the Ekati Mine commenced in 1998 (Dyck et al. 2004). The ore in the Ekati Mine was extracted using both open pit and underground (sub-level caving and sub-level retreat, according to BHP Billiton) methods.

Dominion Diamond Corporation reported that the probable reserves of the Ekati Mine as of January 31, 2017 contain a total of 105.4 million carats, which include 26.0 million carats in the Core Zone of and 79.4 million carats in the Buffer Zone. Cumulative production to January 2017 totaled approximately 67.8 million carats.

2.1.3 Snap Lake Kimberlite

The Snap Lake Mine is located in the southeastern part of the Slave Province (63° 34’ 30” N latitude and 110° 52’ 00” W longitude), about 220 kilometers northeast of the city of Yellowknife (Figure 2.1, Figure 2.3). The size of the mine area is less than 500 hectares. The kimberlite intruded into the Slave Craton in the Cambrian period, determined by Rb-Sr dating of phlogopite (535-523 Ma; Agashev et al. 2001; Heaman et al. 2003, 2004). The country rocks comprise granodiorites, tonalites and granites of the Defeat Pluton Suite (2610-2590 Ma) and metavolcanic rocks including layered amphibolites, metaturbidites and migmatites of the Yellowknife Supergroup (Stubley 2000). There is no evidence of a thermal aureole in country rocks adjacent to the intrusion (Gernon et al. 2012b).

The orebody of the Snap Lake kimberlite (Figure 2.3d) is a segmented hypabyssal dyke flanked by a series of subparallel sheets. It crosses the NNW-SSE-trending contact between the granitoids and metavolanic rocks underground, dipping 5-30º towards the northeast (Gernon et al. 2012b; Kopylova et al. 2010). The orebody is modelled as a

continous discordant dyke on a regional scale, but locally it can be parallel to undulating foliations within the metavolcanic rocks, and a set of subparallel joints within the granitoids (McBean et al. 2003). Where the dyke is exposed as single well-defined intrusion, it is 0.1 to 15 m thick, but typically ranges from 3-5 m. Other parts of the mine have multiple intrusions that are thought to be connected in three dimensions, and can extend over vertical distances of < 30 m in borehole intersections (Gernon et al. 2012b). Between the adjacent dyke segments, there are offsets or "steps" with interconnections or "ramps", and the locations of these offsets and interconnections are related to structural and compositional variability within the country rock (Gernon et al. 2012b). An interpretation from borehole data suggests that the dyke has an 800-m-long NNW-SSE-trending bifurcation with 75 m vertical elevation toward SSE (Kopylova et al. 2010; Mogg et al. 2003). The Snap fault (Figure 2.3c) has been proposed to be a possible candidate as the conduit for the Snap Lake kimberlite, and another WSW-ENE-striking fault may have caused the bifurcation of the intruding kimberlitic magma (Stubley 2000).

The Snap Lake dyke is a coherent kimberlite following the terminology from Scott Smith (2013). Mineralogically the single coherent kimberlite can be divided into two subfacies: a volumetrically dominant coherent kimberlite (HKM) which is olivine-rich and one subordinate coherent kimberlite (HKP) which is both olivine- and phlogopite-abundant (Alexandrina Fulop, personal communication). It was debated if the two sub-facies were generated by two magma batches that co-mingled and intruded almost simultaneously (Field et al. 2009; Gernon et al. 2012b; Ogilvie-Harris et al. 2009), or represent one magma pulse (Kopylova et al. 2010; Mogg et al. 2003) Detailed petrographic and mineralogical studies of Snap Lake kimberlite recognized the importance of country rock contamination

in the magma and recognized six lithologies at Snap Lake based on the degree of alteration: HK1, HK2 and HK5 (former HKM), and HK3, HK4 and HK6 (former HKP) (Alexandrina Fulop, personal communication; Figure 2.3e). The fresh HK1 is dominated by olivine macrocrysts and phenocrysts with minor phlogopite macrocrysts and phenocrysts. The groundmass consists mainly of olivine/monticellite, with phlogopite, spinel and apatite crystals. The slightly altered HK2 is made up of olivine macrocrysts and phenocrysts pseudomorphed by serpentine with local carbonate replacement and shows abundant phlogopite (up to 50% rock volume) in the groundmass. The fresh HK3 comprises olivine macrocrysts and phenocrysts, phlogopite macrocrysts with olivine/monticellite, phlogopite, and spinel as dominant components in groundmass, and apatite and monazite as accessory minerals. The slightly altered HK4 contains olivine macrocrysts and phenocrysts that are pseudomorphed by serpentine and carbonate, with groundmass abundant in both olivine/monticellite and micas, and is more altered than the corresponding HK2. The highly-altered facies HK5 and HK6 both show abundant secondary mineral phases including serpentine, chlorite, mica and carbonate. Although HK5 can be separated from HK6 by the presence of relict poikilitic phlogopite and apatite, the discrimination of HK5 from HK6 is difficult when highly altered. Both slightly and highly altered facies show thin veins filled with serpentine and/or carbonate that crosscut the rock (Alexandrina Fulop, personal communication).

2.1.4 Ekati Mine Kimberlites

The Ekati Mine is located in the central part of the Slave Craton (64° 42’ 49” N latitude and 110° 37’ 10” W longitude, Figure 2.1, Figure 2.4) and occupies a claimed block of ca. 1800 km^2 in the north-central and northeastern part of the Lac de Gras

kimberlite field, consisting of over 150 kimberlites (Nowicki et al. 2004). Ekati kimberlites were emplaced during the Late Cretaceous to Paleogene (ca. 75-45 Ma, Creaser et al. 2005; Lockhart et al. 2004). The country rocks in the Ekati Mine include Archean supracrustal metasediments that were intruded by syn- to post-tectonic plutons (ca. 2.63-2.58 Ga, Kjarsgaard, 2001; Kjarsgaard et al. 1999; van Breemen et al. 1992), mostly granite, granodiorite, and tonalite. Five Proterozoic (ca. 2.23-1.27 Ga, Kjarsgaard, 2001; LeCheminant and van Breemen, 1994) diabase dyke swarms also intruded the area. Generally, the Ekati kimberlites are small (surface area < 3-20 ha, Figure 2.5a), pipe-like bodies (Class 3 kimberlite), with steep (75°-85°) inward-tapering sides, and extend to a depth of 400-1100 m below the surface, with the exception of the Fox pipe that is large and classified as a Class 1 kimberlite (Nowicki et al. 2004; Nowicki et al. 2008). However, the pipe shapes can be complex in detail, as features like outward dipping side walls and elongated and irregular, fault- or joint- controlled pipe geometries are common (Nowicki et al. 2004). In addition, multiple overlapping intrusions such as the Misery kimberlite are found, although most of the kimberlites in the area form discrete, single pipes (Mustafa et al. 2003; Nowicki et al. 2004).

The majority of the Ekati kimberlites are filled with resedimented volcaniclastic kimberlite (RVK) but pyroclastic kimberlite (PK) is present as a minor phase in the lower portions of certain kimberlites, while coherent kimberlite (CK) occurs as minor dykes/sheets (e.g. Anaconda, Koala west, Porpoise), or as volumetrically dominant pipe-infilling components (e.g. Grizzly, Leslie, Pegion) (Nowicki et al. 2004; Nowicki et al. 2008). The CK in Ekati is made up of macrocrystic olivine (mostly fresh or partially serpentinized), phlogopite macrocrysts, and xenocrysts of garnet, Cr-diopside and ilmenite,

set in a fine-grained groundmass of opaque minerals and scattered perovskite. Two broad groups of CK are identified by the TiO_2 and V concentrations (also reflected by MgO, CaO, Nb, Ni contents) together with volatile contents: coherent kimberlites of high Ti and V group have higher total volatile content and higher CO_2/H_2O ratios than those from the low Ti and V group, which entirely comprises pipe-infilling coherent kimberlites (Nowicki et al. 2004; Nowicki et al. 2008). The coherent kimberlites can also be divided into two groups (dolomite- and calcite-bearing) based on groundmass mineralogy and molar ratio of $H_2O/(CO_2+H_2O)$. Kimberlites of the CO_2-rich ($H_2O/(CO_2+H_2O) < 0.5$) dolomite-bearing group are characterized by groundmass spinel, phlogopite, monticellite, apatite, serpentine and dolomite ± perovskite, with dolomite + calcite ± serpentine segregations, represented by Rat, Rattler and Anaconda kimberlites (all are CK as dykes). Kimberlites of the H_2O-rich ($H_2O/(CO_2+H_2O) > 0.5$) calcite-bearing group are characterized by higher modal proportions of groundmass monticellite and ubiquitous perovskite, with high-Sr calcite microphenocrysts, and calcite ± serpentine segregations, represented by Aaron, Pigeon, Porpoise, Koala West, Misery, Misery East, Leslie, Roger and Grizzly kimberlite (Armstrong et al. 2004; Kjarsgaard et al. 2009; Kjarsgaard et al. 2006; Nowicki et al. 2008). The PK from Ekati has abundant juvenile lapilli and the interclast matrix is dominated by serpentine and is compositionally similar to the uncontaminated CK, in terms of a high proportion of juvenile materials (olivine particularly) and abundant of compatible elements such as Cr and Ni. However it is depleted in Ti, V and most incompatible trace elements, and enriched in SiO_2, with much lower LREE/HREE ratios (Nowicki et al. 2004). These features are suggested to be produced by preferential loss of magmatic groundmass components (e.g. chromite, perovskite, Ti-magnetite) during fragmentation and the

associated relative concentration of olivine (Nowicki et al. 2004; Nowicki et al. 2008). The RVK from Ekati consists of commonly broken or angular olivine grains with minor xenoliths, mudstones and wood set in a matrix dominated by dark, very fine-grained, clastic materials, and shows variable but usually prominent enrichment in Al_2O_3, accompanied by a minor increase in SiO_2, TiO_2, V and Nb, compared to CK and PK, which was suggested to be caused by mixing of kimberlitic ash enriched in incompatible elements and surface sediments (Nowicki et al. 2008).

My study selected four Ekati kimberlites representing two types of pipes (Fox, Panda, Koala and Misery, Table 2.1). All four pipes intruded into 2.66-2.58 Ga granitoids between 50-70 Ma: Misery is the oldest pipe emplaced at ~69 Ma and the other three pipes were emplaced at ~53-56 Ma (Carlson et al. 2015; Sarkar et al. 2015). The crystallization temperature was estimated by olivine-spinel geothermometry between 967-1086 °C in Panda and 1053-1138 °C in Misery (Fedortchouk and Canil 2004; Fedortchouk et al. 2005). The fO_2 is ~2-3 log units bellow the Ni-NiO buffer, estimated by olivine-spinel oxygen barometry at a silica activity limited by the presence of monticellite (Fedortchouk et al. 2005). However, fO_2 estimated based on groundmass perovskite ranges from NNO +5.7 in Misery and NNO -2.5 in Panda (Canil and Bellis 2007).

The detailed study of the mineralogy and petrology of Ekati kimberlites (Carlson et al. 2015; Nowicki et al. 2004; Nowicki et al. 2008; Porritt et al. 2008) shows that the selected four pipes represent two kimberlite types (Class 1 and Class 3) and have variable diamond grade. Fox is the largest mined pipe (17 ha at surface, Figure 2.5b) and is a Class 1 kimberlite with a diamond grade of 0.3 ct/t (Carlson et al. 2015). It contains MVK in the lower portion of the pipe and RVK in the crater zone with a sharp contact showing no

intermixing between the two facies. Large granodiorite boulders occur in MVK and at the contact zone (Nowicki et al. 2004). No sign of a root zone is shown in Fox (Nowicki et al. 2004; Porritt et al. 2008). The Fox MVK contains abundant xenoliths, primarily finely disaggregated granodiorite, with serpentinized olivine macrocrysts and pelletal lapilli set in a very fine-grained matrix of clay altered serpentine. Fox RVK is matrix-supported and olivine-poor, with scattered fragments of altered granodiorite and wood with little mud but abundant kimberlitic ash (Nowicki et al. 2004; Nowicki et al. 2008). Panda, Koala and Misery are all Class 3 kimberlites and consist predominantly of RVK, with minor PK and/or CK. Panda (Figure 2.5a) and Koala (Figure 2.5d) are discrete pipes with steep sides, while Misery occurs as multiple overlapping intrusions (Figure 2.5e) (Mustafa et al. 2003; Nowicki et al. 2004). Their diamond grades are 1 (Panda), 0.8 (Koala), and 4.5 (Misery) ct/t (Carlson et al. 2015; Fedortchouk et al. 2005). Panda (3.0 ha) is a steeply dipping pipe and has complex internal geology (Figure 2.5a and 2.5c), comprising numerous discontinuous, highly variable, predominantly coarse-grained olivine-rich RVK and lesser amounts of fine-grained massive mud-rich RVK. Both facies show abundant fresh wood fragments and minor amounts of xenolithic shale and granodiorite that ranges in size from < 2 mm to tens of centimeters. Juvenile-rich coarse to very coarse-grained PK occurs in the deeper portions of the pipe, which has a sharp contact with the VK units and comprises abundant juvenile lapilli and CK autoliths with minor xenolithic shale and granodiorite set in a groundmass dominated by fine-grained serpentine (McElroy et al. 2003; Nowicki et al. 2004). Koala is slightly larger (4.5 ha) than Panda with a slightly lower wall angle (78-80º), occupied by a well-defined, sub-horizontally layered sequence of VK units separated by a distinctive layer of siltstone, showing six phases from top to bottom (Figure 2.5d)

(Nowicki et al. 2004). The Misery Main pipe is an elongated and steep-sided body of only 1.5 ha surface area. The pipe infill is primarily RVK with minor PK, whereas CK occurs in the peripheral dykes (Fedortchouk et al. 2010; Mustafa et al. 2003). Armstrong et al. (2004) recognized two distinct types of kimberlites in the Ekati Mine property: dolomite-bearing and carbonate-bearing. The Misery and Koala kimberlites belong to the calcite-bearing group, suggested to originate from magmas with lower CO_2/H_2O ratios (Armstrong et al. 2004; Crawford et al. 2006; Nowicki et al. 2004; Nowicki et al. 2008).

Table 2.1 Diamond grade and geology of Fox, Panda, Koala and Misery kimberlite pipes

Kimberlite	Fox	Panda	Koala	Misery
Grade (ct/t)	0.3[a]	1[b]	0.8 [a]	4.5 [a]
Age (Ma)	56.2 ± 3.2[c]	53.3 ± 0.6[d]	53.3 ± 0.9[d]	68.9 ± 5.4[c]
Pipe morphology and internal geology[e]	Single pipe, predominantly RVK in upper level and MVK in lower level	Single pipe, RVK with minor PK	Sub-horizontally layered pipe, predominantly RVK and PK, minor CK	Cluster of seven pipes, predominantly RVK, some PK, minor CK
Crystalization T[f] (°C)		967-1086		1053-1138
*f*O2 ΔNNO (Ol-Sp)[g]		-2.8		-2.9
*f*O2 ΔNNO (Prv)[h]		-2.5		5.7
Class[i]	1	3	3	3

a: Diamond grades of Fox, Koala and Misery (Carlson et al. 2015)
b: Diamond grade of Panda (Fedortchouk et al. 2005)
c: U-Pb age of perovskite (Sarkar et al. 2015)
d: Rb-Sr age of phlogopite (Creaser et al. 2004)
e: Pipe morphology and internal geology of kimberlites (Nowicki et al. 2004). PK: pyroclastic kimberlite; RVK: resedimented volcaniclastic kimberlite; MVK: massive volcaniclastic kimberlite; CK: coherent kimberlite.
f: Crystallization temperature of kimberlites (Fedortchouk and Canil 2004; Fedortchouk et al. 2005).
g: fO_2 estimated by olivine (Ol)-spinel (Sp) oxygen barometry at 1 GPa (Fedortchouk et al. 2005). $\Delta NNO = \log fO_2$ sample - $\log fO_2$ NNO at P and T
h: $\log fO_2$ by Fe contents in perovskite (Prv) (Canil and Bellis 2007)
i: Kimberlite classification following Skinner and Marsh (2004).

2.2 Methods and Samples

2.2.1 Choice of Kimberlite Localities

This study used diamonds from Snap Lake and four Ekati kimberlites (Fox, Panda, Koala, Misery), with presumably different fluid and emplacement histories indicated by the different petrography and geology of the kimberlites: The Snap Lake intrusion is a dyke consisting of a single coherent (hypabyssal) kimberlite which can be subdivided into a volumetrically dominant coherent kimberlite (HKM) and a subordinate coherent phlogopite-rich kimberlite (HKP). The four Ekati kimberlites are pipe-like bodies but vary in pipe morphology and internal geology in detail (See Chapter 1.3.4). Panda, Koala, and Misery are small (< 5 ha surface areas) Class 3 pipes filled with predominantly resedimented volcaniclastic kimberlite (RVK) with minor pyroclastic kimberlite (PK) and/or coherent kimberlite (CK), formed by a discrete single pipe intrusion (Panda, Koala) or multiple overlapping intrusions (Misery). Fox is a Class 1 kimberlite and one of the largest pipes in the field (17 ha surface area), containing MVK in the lower portion and RVK in the upper portion of the pipe (Nowicki et al, 2004).

2.2.2 Diamond Samples Used in This Study

2.2.2.1 Diamond samples from Snap Lake Mine

The study used 251 diamonds selected from two parcels from Snap Lake kimberlite (Table 2.2; Appendix A: Table EA1). Parcel 1 consists of 96 diamonds ranging from +300 μm to +1.7 mm, from kimberlite lithologies HK1, HK2, HK4, HK5/HK5-6. Parcel 2 consists of 155 diamonds ranging from +300 μm to +1.18 mm, from kimberlite lithologies: HK1, HK2, HK3, HK4, HK6. For this study, I selected diamonds that are +300 μm and larger, have octahedral or tetrahexahedral (THH) crystal morphology, with more than 50 %

of the diamond surface remaining if broken. I rejected all the cubes, complex cubo-octahedron forms, and fragments with ambiguous morphologies resulting from fracture of the crystals. However, a few fragments were selected for FTIR analysis. The selected diamonds represent all lithofacies at Snap Lake: 77 stones from HK1, 83 stones from HK2, 20 stones from HK3, 27 stones from HK4 and 44 stones from HK5-HK6.

2.2.2.2 Diamond samples from Ekati Mine kimberlites

In total, I selected 13 diamonds (2 diamonds from Fox, 2 diamonds from Koala, 4 diamonds from Misery and 5 diamonds from Panda, Figure 2.6) from four Ekati kimberlites for detailed AFM study. Diamonds from Fox belong to one parcel of 3 carats in total containing micro-diamonds < 1mm, and the diamonds from Koala, Misery and Panda used in this study are from the same parcels used by Fedortchouk et al. (2010), where the parcel weight and diamond sizes were reported. The morphological investigation of these diamond parcels was conducted earlier (Fedortchouk et al. 2010; Gurney et al. 2004). For this study, I selected diamonds with kimberlite-induced resorption (Fedortchouk and Zhang 2011; Zhang and Fedortchouk 2012), with ditrigonal {111} faces and a few shallow trigons on {111} faces. While an attempt was made to select diamonds with only kimberlitic resorption features, several diamonds show trigonal {111} faces and may represent a combination of kimberlite-induced and mantle-derived resorption features, such as P2, P3, P4 and P36 from Panda (Figure 2.6).

Table 2.2 Summary table of two parcels of Snap Lake diamonds. HK5-6 is the highly altered facies that cannot be assigned to HK5 or HK6 with certainty. O = octahedral diamonds, THH = tetrahexahedral diamonds.

Sample	# of book	Total number of diamonds	Number of diamonds selected for study				Kimberlite lithology	Number of diamonds in size groups					
			O	THH	AFM study	FTIR study		+1.7 mm	+1.18 mm	+850 µm	+600 µm	+425 µm	+300 µm
Total (two parcels)		251	78	13	16	82		4	10	19	37	72	109
Parcel 1													
PA099811	1/1	10	6	1	1	7	HK4	2	0	1	0	3	4
PA100511	1/1	7	3	0	1	3	HK1	0	1	0	0	3	3
PA102811	1/1	8	6	0	2	4	HK2	0	1	2	2	2	1
PA104411	1/1	8	1	0	0	1	HK2	0	1	1	1	2	3
PA106111	1/1	10	5	0	2	4	HK5	0	1	2	2	1	4
PA106411	1/1	10	3	0	1	3	HK2	1	0	1	0	4	4
PA110011	1/1	6	2	0	0	2	HK1	0	2	0	0	1	3
PA111311	1/1	9	4	0	1	3	HK1	0	1	0	0	3	5
PA113611	1/1	9	4	0	1	2	HK2	1	0	0	2	4	2
PA113711	1/1	9	3	0	2	3	HK4	0	1	1	3	3	1
PA114411	1/1	10	2	4	0	6	HK5-6	0	1	2	6	1	0
Total (parcel 1)		96	39	5	11	38		4	9	10	16	27	30
Parcel 2													
PA076011	1/1	8	4	0	0	3	HK6	0	0	0	2	3	3
PA076111	1/2	10	5	0	0	3	HK1	0	0	1	4	2	3
PA076111	2/2	6	1	2	0	2	HK1	0	0	0	0	0	6
PA076411	1/2	10	0	0	0	0	HK2	0	0	2	0	3	5
PA076411	2/2	2	0	1	0	1	HK2	0	0	0	0	0	2
PA099311	1/2	10	0	2	0	1	HK3	0	0	2	5	1	2
PA099311	2/2	4	2	0	0	1	HK3	0	0	0	0	0	4
PA100011	1/1	6	1	0	0	1	HK1	0	0	0	0	3	3
PA102711	1/2	10	4	0	1	4	HK2	0	0	0	0	6	4
PA102711	2/2	5	1	0	0	0	HK2	0	0	0	0	0	5
PA103411	1/1	6	0	0	0	0	HK3	0	0	0	1	2	3
PA103811	1/1	8	4	0	3	4	HK6	0	0	0	1	3	4
PA105311	1/1	7	1	0	1	1	HK1	0	0	0	0	1	6
PA106311	1/3	10	2	0	0	2	HK1	0	0	1	1	8	0
PA106311	2/3	10	2	0	0	3	HK1	0	0	0	0	3	7
PA106311	3/3	3	2	0	0	2	HK1	0	0	0	0	0	3
PA107211	1/1	3	0	0	0	2	HK1	0	0	0	0	1	2
PA108411	1/1	8	3	1	0	4	HK6	0	0	1	1	3	3
PA110711	1/1	10	3	0	0	4	HK2	0	1	1	0	2	6
PA109111	1/2	10	2	0	0	2	HK2	0	0	1	4	2	3
PA109111	2/2	1	0	0	0	0	HK2	0	0	0	0	0	1
PA111511	1/1	8	2	2	0	4	HK4	0	0	0	2	2	4
Total (parcel 2)		155	39	8	5	44		0	1	9	21	45	79

2.2.3 Diamond Oxidation Experiments

The morphology of positively oriented trigonal etch pits developed at known conditions was studied using products of diamond oxidation experiments done by my supervisor Yana Fedortchouk. The experiments were conducted at atmospheric pressure (0.1 MPa) in a gas-mixing furnace at ETH Zurich with oxygen fugacity (fO_2) controlled by a mixture of CO_2 and H_2 gases at $\log fO_2$ = -9 to -16 at 900-1050 °C (Table 2.3). The details of sample preparation, data collection and processing for the AFM examination are summarized in Chapter 2.2.6.

Table 2.3 The experimental conditions and the type of resorption features formed in experimental runs GM-1 to GM-10 at 0.1 MPa.

Run	Composition	Resorption features formed	Conditions					
			Diamond	T, ºC	$\log fO_2$	CO_2	H_2	Duration (min)
GM-4		Positive trigons	Exp18	1000	-12	185	15	360
GM-5		Positive trigons	Exp5	900	-14	184	16	150
GM-7		Positive trigons	Exp10	1050	-10	195.5	4.5	180
GM-8		Negative trigons	Exp11	1150	-9	191.6	8.4	35
GM-9	$Na_2Si_2O_5$	Positive trigons + corrosions	AL5	900	-13	194.6	5.4	180
GM-10	$Na_2Si_2O_5$	Positive trigons + corrosions	Exp17	900	-13	194.7	5.4	180

2.2.4 Study of Diamond Morphology

The flowchart in Figure 2.7 summarizes the procedures of diamond examination by optical microscopy, SEM, FTIR and AFM. First, I examined and photographed the diamonds under a stereomicroscope and under reflected light with a petrographic

microscope. The crystals were cleaned in ethanol before examination. Octahedrons and tetrahexahedrons with > 50% of the diamond surface present were examined.

The preliminary morphological groups for the selected Snap Lake diamonds was defined using optical microscopy. The morphology, color and color intensity, and presence of inclusions were recorded under the stereomicroscope, and examined the surface growth and resorption features using the stereomicroscope combined with the petrographic microscope under reflected light. The crystals were devided into octahedral and tetrahexahedral (THH) forms based on the preservation of the original octahedron shape. Tetrahexahedral crystals may preserve up to 10% of the {111} faces but were still classified as THH based on the rounded crystal shape and the large degree of resorption. The morphologies of twinned diamonds and aggregates were classified according to the shapes of the constituent crystals. The octahedral diamonds were then divided based on the shape of {111} faces (trigonal vs. ditrigonal, Figure 1.6) and character of resorption on the {111} faces, such as the presence of step faces, and the presence and type of the etch pits (negative and positive trigons, trigon-hexagons, hexagons) and laminae (shield-shaped, serrate or irregular-shaped, Figure 1.13). Diamonds of the same morphological group were further divided into sub-groups by the character of resorption on edges (THH faces), including the presence and type of cavities (shallow depressions or deep cavities) and hillocks (sharp or smooth), and the presence of striations and circular pits.

After the preliminary morphological groups were defined, representative examples from each group were selected for further Scanning Electron Microscopy (SEM) examination (29 stones from Snap Lake kimberlite). The collected SEM data were used to refine the morphological groupings for each diamond population. SEM was also used to

confirm the presence of positive trigons with a side length less than 1 μm on Snap Lake diamonds. Prior to SEM the diamonds were first cleaned with a boiled HNO_3-H_2SO_4 mixture (3:5 volume proportion) at ~200 °C for at least 30 minutes, and then in distilled water in an ultrasonic bath for 15 minutes. The crystals were mounted on a metal plate with carbon tape after cleaning and were coated with gold prior to the SEM examination.

The SEM work was conducted using a Field Emission Scanning Electron Microscope (FE-SEM) Hitachi S-4700 FEG at the Institute for Research in Materials, Dalhousie University. The examination was performed using an accelerating voltage of 10-15 kV, and beam current of 15 μA. The {111} face of the selected crystals was first photographed at low magnification (< 300x) and then examined the growth and resorption features on the {111} faces and edges (THH faces) at high magnifications (up to 6000x). The SEM data were used to refine the morphological groupings for each diamond population and to confirm the presence of small positive trigons on some Snap Lake diamonds.

After the SEM examination, crystals representative of different morphological groups (82 stones from Snap Lake kimberlite; Appendix A: Table EA4) were selected for examination by Fourier Transform Infrared Spectroscopy (FTIR) to obtain the N content and aggregation state in the diamonds.

2.2.5 Study of Nitrogen Defects (Fourier Transform Infrared Spectroscopy)

Diamonds selected for Fourier Transform Infrared Spectroscopy (FTIR) were cleaned with aqua regia (HNO_3-HCl in 1:3 volume proportion) to remove the gold coating and other possible metal impurities, and then in a HNO_3-H_2SO_4 mixture (3:5 volume

proportion) to remove the carbon from the SEM tapes and other surface contaminants. Both acid mixtures were boiled at ~200 °C for at least 30 minutes. The crystals were cleaned in distilled water in ultrasonic bath for 15 minutes after the acid baths. The crystals were mounted on the edge of a glass slide with the {111} faces facing the IR beam before the FTIR analysis. The measurements were done using a liquid cooled Thermo Nicolet Nexus 470 FTIR spectrometer coupled with a continuum infrared microscope equipped with a KBr beam splitter at the Department of Earth and Atmospheric Sciences at the University of Alberta. Absorption spectra were measured in transmission mode in the range of 4000-650 cm^{-1} with a resolution of 8 cm^{-1}, and were collected for 200 s through a 100 × 100 μm^2 spot. Sample spectra were first baselined using the Macros Basic and the OMNIC 32 software suites. A normalized Type II diamond spectrum used as a standard for background correction was subtracted from the spectra to convert absorbance to absorption coefficient. After the conversion was done, sample spectra were de-convoluted into the A, B and D components (e.g. Boyd et al. 1995) using least squares techniques (Stachel et al. 2006). Nitrogen concentrations (atomic ppm) were calculated from absorption coefficient values at 1282 cm^{-1} using the factors derived by Boyd et al. (1994) for the A center (16.5 ± 1) and Boyd et al. (1995) for the B center (79.4 ± 8). The detection limit for N is about 10 ppm and the analytical precision is 10-20 % of the concentration (Stachel et al. 2006).

2.2.6 AFM Analyses

2.2.6.1 Sample Preparation and Mounting

Atomic Force Microscopy (AFM) was used to obtain quantitative crystallographic information for the individual resorption features on diamond surfaces. For Snap Lake diamonds, representative examples of different morphological groupings and from

lithofacies with different degree of alteration were selected. For Ekati diamonds, crystals with kimberlitic resorption features from four pipes (Fox, Koala, Panda and Misery) were selected, but the kimberlite facies from which the diamonds came from are not known.

All the selected diamond crystals were cleaned with aqua regia (HNO_3-HCl in 1:3 volume proportion) to remove the gold coating and other possible metal impurities, and then in a HNO_3-H_2SO_4 mixture (3:5 volume proportion) to remove the carbon from the SEM tapes and other dirt. Both acid mixtures were boiled at ~200 °C for at least 30 minutes. Later the crystals were cleaned in distilled water in an ultrasonic bath for 15 minutes.

For each selected diamond, the crystal was mounted in the center of a steel mounting disk (Bruker, model SD-101, 12mm diameter) with an adhesive pad (Bruker, model STKYDOT). Attempts were made to orient the examined {111} face parallel to the horizontal plane, crystals with an uneven face opposite to the examined {111} face may still have a tilt. To solve this problem, some glue (taken from the adhesive pad) was put underneath the crystal to orient the examined {111} face horizontally. Prior to the AFM measurements, all the selected diamonds were photographed at 100× and 200× magnification (500× for minute features such as positive trigons) under an optical microscope in reflected light with a partially closed aperture stop allowing to enhance the outline of the resorption features.

2.2.6.2 Data Collection

All the quantitative imaging of the diamond {111} faces was done with a Veeco Multimode 8 atomic force microscope equipped with a J scanner (Bruker, maximum coverage 125 µm × 125 µm × 5 µm in x, y and z dimensions), operating in ScanAsyst Mode with Nanoscope software (v8.10) under ambient conditions at the Department of Earth

Sciences, Dalhousie University. ScanAsyst Air Probes (Bruker, silicon tip on nitride lever, spring constants 0.4-0.8 $N \cdot m^{-1}$, resonant frequency 50-90 kHz, nominal tip radius of curvature 2 nm) were used for the image collection. Scanned areas ranged from 5 × 5 to 80 × 80 μm^2. To obtain the images of minute resorption features such as positive trigons on diamonds from Snap Lake mine, the scanned areas was usually from 5 × 5 to 10 × 10 μm^2. The scan angles were set at 0 degree for all the scans. The scanning frequency was dependent on the size of the scanned areas: I used 0.2-0.4 Hz for areas greater than 30 × 30 μm^2 and 0.5-0.8 Hz for smaller areas to optimize the match between the trace and retrace lines. All the scans were conducted with 512 sample lines.

2.2.6.3 Data Processing

Images were analyzed using NanoScope Analysis (ver. 1.20). All the images were processed using the Plane Fit function to remove the tilt in both X and Y directions (Plane Fit Mode: XY; Plane Fit Order: 1st order). Cross-section profiles of individual etch pits were obtained by "section analyses" where the marker line was drawn across the middle point of one side of the trigon to the opposite vertex, or the middle points of two opposite sides for trigon-hexagons and hexagons. The division between trigons, trigon-hexagons, and hexagons was based on the relative length of short and long sides (Table 2.4, Figure 2.8):

Table 2.4 Classification of etch pits based on the relative length of short and long sides

Type of etch pit	Length of the short pit side
Trigon	Zero (no truncated corner present)
Truncated trigon	< 1/3 the longer side
Trigon-hexagon	≥ 1/3 but < 2/3 of the longer side
Hexagon	≥ 2/3 of the longer side

For each diamond, I routinely measured 5-10 negative trigons (some diamonds show less than 5 negative trigons, or most of the trigons were too large for AFM measurements), 8-20 positive trigons and 1-3 hexagons when present. The measured parameters included: (1) the diameter (the distance between the middle point of one side and the opposite vertex for trigons, or the distance between two opposite sides for trigon-hexagons and hexagons); (2) the depths (distance between the {111} face and bottom of the pit); (3) the angles between the micro-faces formed by the pit walls and the {111} faces (reported as $\alpha_{\{111\}}$) (Figure 2.9a).

Some diamonds had multiple trigons where a complete trigon is enclosed by an incomplete trigon (or "half trigon", Fedortchouk 2015), which is a shallow trigon with only part of the walls developed on two sides (Figure 2.10a). I ignored the incomplete trigon for measurements, and made the measurements only based on the inside complete trigon.

Some etch pits had walls with multiple steps. For such pits, I selected the side with the most steps, recorded the number of steps and measured the heights and widths of each step (Figure 2.10b). If two sides had the same number of steps, I recorded the number of steps on both sides and measured all the steps. Snap Lake diamonds show etch pits with micro-steps (Figure 2.12b and 2.13d) that were too small (~10-200 nm in height and width) for determination of the exact number of steps and measurement.

Although an attempt was made to orient the examined {111} faces parallel to the horizontal plane and to correct the collected raw images with the Plane Fit operation, a small uncertainty in the measurement of dimension and angles could have been introduced due to a minor tilt (usually < 1º after the Plane Fit operation) of the {111} face. Therefore, I routinely took three measurements of all the parameters (diameter, depth and $\alpha_{\{111\}}$) in

three directions and averaged these measurements. The trigons with only one truncated corner had the diameter in one direction slightly shorter than the other two directions (Figure 2.11a and 2.11b, diameter in direction 2 is ~10% shorter compared to the other two directions). In this case, I still averaged the measurements in three directions as the diameter of the trigon. If the trigon had one corner "cut off" by other surface features such as irregular laminae on diamonds (Figure 2.11c and 2.11d, direction3), I obtained the diameter from measurements in the other two directions. If there was uneven resorption of the {111} face (Figure 2.11d, direction2) and the depth measured in one direction was significantly shallower than the other two directions (~20% difference), the measurements in the other two directions were averaged as the depth of the trigons.

In order to classify and compare the variety of the etch pits observed on natural and diamonds etched experimentally in this study, the pits were divided based on the shape of their bottoms and walls (Figure 2.9). Three types of pit bottoms were distinguished: 1) flat bottom, 2) point-bottom and 3) curved bottom. The flat-bottomed (f/b) pits have bottoms that are parallel to the (111) plane, and show a straight line in the cross-section profiles when no other pits are developed on the bottom (Figure 2.10b, 2.13b). For the depths of f/b pits, I usually measured the distance between the center of the bottom and the {111} face (Figure 2.9a, 2.10d). However, smaller trigons (positive or negative) sometimes developed all over the bottom of a negative trigon and make it difficult to measure the accurate depth of the negative trigon (Figure 2.12a, 2.12c and 2.13c). In such case, I selected a point which is close to the center of the bottom of the negative trigon (those relatively deeper positive trigons were avoided) and measured the distance between this point and the {111} face as an approximation of the depth of the negative trigon, since the

small trigons usually have much shallower depths compared to negative trigons (Figure 2.12b, 2.13d). The point-bottomed (p/b) pits show a chevron-shaped cross-section profile with pointy bottoms (Figure 2.9). The curved-bottomed pits (c/b) show more rounded bottoms compared to p/b pits (Figure 2.9f, 2.15d). To measure the depth of a p/b or c/b pit, the distance between the deepest point in the pit and the {111} face was measured as the depth (Figure 2.9b, 2.14b, 2.15d). The flat bottoms are observed in negative and positive trigons (or trigon-hexagons) and hexagons, while the point bottoms and curved bottoms are usually observed in trigons, and rarely in small hexagons. Some trigons have bottoms that seem transitional between a flat bottom and a point bottom (Figure 2.17). I recorded this type of bottom as p/b.

I distinguished three types of pit walls based on the shape of the cross-section profiles (Figure 2.9): (1) the V type wall, which shows a straight line of the wall in the profile, and the whole profile of the pit resembles the letter "V" (Figure 2.10b, 2.14b); (2) the U type wall, which shows a concave profile of the wall showing decreasing $\alpha_{\{111\}}$ from top to bottom, and the whole profile of the pit resembles the letter "U" (Figure 2.12b, 2.12d, 2.15b, 2.15d); 3) the Y type wall, which shows a convex profile of the wall, and the whole profile of the pit resembles the letter "Y" (Figure 2.13b, 2.13d, 2.16b, 2.16d, 2.16f). The U type and Y type walls may show a profile consisting of several straight segments or a curved line. To measure the $\alpha_{\{111\}}$ of V type walls, I measured the angle of the wall between two marker lines on the cross-section profile (Figure 2.14b). To measure the $\alpha_{\{111\}}$ of U type and Y type walls with a profile consisting of two straight segments, I measured the $\alpha_{\{111\}}$ of each segment (Figure 2.13b). The Y (or U) type walls are distinguished from V type walls by the difference between angels of two segments. If $\alpha_1 > \alpha_2$ and the difference

is great than 1º, the wall is determined U type (Figure 2.9c). Similarly, if $\alpha_1 < \alpha_2$ and their difference is great than 1º, then the wall is determined as Y type (Figure 2.9g). When the difference between two angles is less than 1º, the wall is V type.

It is noted that some p/b trigons with U type walls look like f/b trigons when the angles between the lower segments and the {111} faces are very small (Figure 2.15b). If the sum of the angles ($\beta_1 + \beta_2$ in Figure 2.9e) is greater than 1°, the pits were recorded as p/b trigons with U type walls; otherwise, the pits were regarded as f/b trigons with V type walls. Some pits may have wall profiles showing Y shape in the upper part and transition into U shape near the bottom (e.g. Figure 2.13d); the walls would be regarded as U type if the transition part with smaller $\alpha_{\{111\}}$ makes up a prominent proportion of the total wall, otherwise it was determined as Y type. To measure the $\alpha_{\{111\}}$ of U type and Y type walls with curved profiles, I arbitrarily divided the curved profile into several segments and measured the angle as an approximation of the $\alpha_{\{111\}}$ of the segments (Figure 2.13d). If the wall has steps, the $\alpha_{\{111\}}$ of each step was measured. However, if micro-steps were present, I selected several steps arbitrarily and measured the $\alpha_{\{111\}}$ of each step. If a trigon (trigon-hexagon) has truncated corners, I measured the $\alpha_{\{111\}}$ of the walls on the corners as wall.

When large trigons develop smaller trigons on their bottom, they could be described as trigons with stepped walls or trigons containing smaller trigons on the bottom. This can be addressed by comparing the relative size of the inside trigons to the larger outside trigon and illustrated in Figure 2.18d. For example, the trigons in Figures 2.10a, 2.18a have multiple smaller trigons developed on the bottom, and the second largest inside trigon covers an area more than half of the bottom of the largest outside trigon. In this case, the walls of the largest outside trigon were determined as stepped. If the smaller trigon only

covers an area less than 1/4 of the bottom of the larger outside trigon (Figure 2.18a-2.18c), it is more reasonable to regard these smaller trigons as "additional trigons" on the bottom of the outside trigon (the additional trigons in Figure 2.18a-2.18c can be called "corner trigons" in Fedortchouk 2015) and the walls as not stepped. The heights (the distance between the bottom of the additional trigon and the bottom of the largest outside trigon) of the additional trigons were recorded.

Deep holes developed on the bottom of some positive trigons were also observed on diamond Exp10. I measured the diameter of the hole and recorded the depth of the hole as part of the total depth of the trigon (Figure 2.19). The $\alpha_{\{111\}}$ of the walls of the hole was also recorded.

2.2.6.4 Calculation of Uncertainties of Parameters Measured on Diamond Surface

Three major parameters of the etch pits were measured with AFM: diameter, depth and the wall angle $\alpha_{\{111\}}$. Errors in measurement come from three sources (Table 2.5):

Table 2.5 Summary of the sources of uncertainty and total uncertainty for each measured parameter.

Parameter	Source of uncertainty		Total uncertainty
	Systematic Errors	Random Errors	
Diameter	AFM uncertainty after calibration (1.4%); Tilt of the raw image before Plane Fit operation (< 0.2%)	Subjective selection of measurement section (0.6%)	< 2.5%
Depth	AFM uncertainty after calibration (1.4%); the remaining tilt and the compression of the image after the Plane Fit operation (< 4%);	Subjective selection of measurement section (0.3%)	< 6%
$\alpha_{\{111\}}$	AFM uncertainty after calibration (< 2º); Tilt of the raw image and the remaining tilt after the Plane Fit operation (< 1º)	Subjective selection of measurement section (< 1º)	< 4º

(1) AFM uncertainty (1.4% in x, y and z directions) after the calibration.

The distance d between any two points in three-dimensional space is:

$d = ((\Delta x)^2 + (\Delta y)^2 + (\Delta z)^2)^{1/2}$, where Δx, Δy and Δz are the distances between the two points in x, y and z directions. While

$$d' = ((\Delta x)^2(1 \pm 0.014)^2 + (\Delta y)^2(1 \pm 0.014)^2 + (\Delta z)^2(1 \pm 0.014)^2)^{1/2} = (1 \pm 0.014)\, d$$

where d' is the measured value by the AFM probe for the distance between the two points, thus the AFM uncertainty (1.4%) will produce 1.4% uncertainty in the measurement of diameter and depth.

Also, the uncertainty for $\tan\alpha_{\{111\}}$ will be $\pm 2.8\%$ ($\frac{(1 \mp}{(1 \pm 0.014)} \frac{1}{-1} \times 100\%$).

Let $\tan\alpha_{\{111\}} = m$ ($m > 0$), then the uncertainty for $\alpha_{\{111\}}$ is

$$\frac{\arctan m(1 \pm 0.028) - \arctan m}{\arctan m}$$

Let $f(m) = \frac{\arctan m(1 \pm 0.028) - \arctan m}{\arctan m}$, this is an even function and has the limit when $m \to 0$.

According to L'Hôpital's rule:

$$\lim_{m \to 0} f(m) = \frac{(\arctan m(1 \pm 0.028) - \arctan m)'}{(\arctan m)'} = \frac{(1 \pm 0.028)\frac{1}{1+m^2} - \frac{1}{1+m^2}}{\frac{1}{1+m^2}} = 1 \pm 0.028.$$

This will produce less than 2º uncertainty (2.8% × 65º = 1.82º) in this study (the $\alpha_{\{111\}}$ is usually less than 65º).

Thus, the 1.4% AFM uncertainty produces 1.4% uncertainty for both diameter and depth measurements, and less than 2º uncertainty for angle measurement.

(2) Tilt of the {111} diamond face.

This includes the initial tilt (0-3º) of the {111} face relative to the horizontal plane before the Plane Fit operation, and the remaining tilt (0-1º) after the Plane Fit operation, which will also cause compression in the direction of measurement. Assuming the raw image of a p/b trigon has a 3º tilt in the direction of measurement before the Plane Fit operation, the Plane Fit operation rotates the profile 2º in the anticlockwise direction and the tilt remains 1º after the operation (Figure 2.20a and 2.20b). After the Plane Fit operation, the diameter of the trigon in the direction of measurement will be compressed, while the depth of the trigon remains the same as the actual depth d_{real} (Figure 2.20b):

$$D_{fit} = D_{real} \times \frac{\cos(3°)}{\cos(1°)};\ \tan(\alpha_{fit}) = \tan(\alpha_{real}) \times \frac{\cos(1°)}{\cos(3°)};\ \frac{\cos(3°)}{\cos(1°)} \approx 0.9988$$

Where D_{real} and α_{real} are the actual diameter and $\alpha_{\{111\}}$ of the trigon, while D_{fit} and α_{fit} are the changed diameter and $\alpha_{\{111\}}$ due to the Plane Fit operation, and

$$D_{measured} = D_{fit} \times \cos(1°) = D_{real} \times \cos(3°) \approx 0.9986 D_{real}$$

$$\alpha_{measured} = \alpha_{fit} + 1° = \arctan\left[\tan\left(\alpha_{real}\right) \times \frac{\cos(3°)}{\cos(1°)}\right] + 1° < \alpha_{real} + 1°$$

$$d_{measured} = \frac{d_{real}}{\sin(\alpha_{fit})} \times \sin(\alpha_{fit} + 1°) = d_{real} \times \left[\cos(1°) + \tan(\alpha_{fit})\sin(1°)\right]$$

where D_{real}, $\alpha_{measured}$ and $d_{measured}$ are the measured values for diameter, $\alpha_{\{111\}}$ and depth of the trigon. In my measurements, the $\alpha_{\{111\}}$ is usually less than 65º, then $d_{measured} < d_{real} \times [\cos(1º)+\tan(65º)\sin(1º)] \approx 1.0373 d_{real}$

Thus, an initial tilt of 3° will produce < 0.2% error for the diameter measurement; the initial tilt and the tilt after plane fit will produce less than 1º error for the angle measurement; the remaining tilt (1º) and the compression in the direction of measurement will produce < 4% error for the depth measurement;

(3) Subjective selection of the measurement section (the position where the line was drawn across the pits to acquire the section plot; the position where the plot markers were placed on the section plot).

I conducted 10 repeated measurements on one f/b trigon with V type walls on diamond K95-A1-1 from Koala kimberlite (Table 2.6, Figure 2.21). The standard deviations for the measurement of diameter, depth and $\alpha_{\{111\}}$ are approximately 0.03 μm, 0.6 nm and 0.6º, respectively. Thus, the uncertainties introduced by subjective selection of the measurement are 0.6%, 0.3% and < 1º for diameter, depth and $\alpha_{\{111\}}$.

The total uncertainty for diameter measurement is < 2.5% ((1.014 × 1.002 ×1.006-1) × 100% ≈ 2.2%), for depth measurement is < 6% ((1.014 × 1.04 × 1.003-1) ×100% ≈ 5.8%), and for angle measurement is < 4º (2º + 1º +1º = 4º).

Table 2.6 The measurements on diamond K95-A1-1 from Koala kimberlite. d1, d2, d3 refers to direction 1, 2, and 3 in Figure 2.21; Avg = Average

Measurement #	Diameter, μm			Avg	Depth, nm			Avg	Wall angle $\alpha_{\{111\}}$, degree			Avg
	d1	d2	d3		d1	d2	d3		d1	d2	d3	
1	4.451	4.512	4.533	4.50	190.309	188.961	193.102	190.8	19.9	20.3	19.9	20
2	4.467	4.525	4.489	4.49	190.791	187.773	193.487	190.7	21.6	21.9	19.4	21
3	4.519	4.508	4.514	4.51	191.946	189.186	196.055	192.4	19	20.3	20.2	20
4	4.458	4.490	4.377	4.44	190.823	187.452	192.524	190.3	21.4	19.4	20.1	20
5	4.492	4.463	4.498	4.48	191.850	189.924	193.102	191.6	19.6	20.9	18.6	20
6	4.454	4.512	4.501	4.49	191.497	187.099	194.000	190.9	21.1	20.6	22.3	21
7	4.471	4.559	4.544	4.52	191.144	187.067	192.845	190.4	19.9	20.8	19.6	20
8	4.526	4.535	4.585	4.55	191.529	187.164	193.102	190.6	19.1	19.7	20.5	20
9	4.452	4.528	4.545	4.51	191.721	187.292	193.358	190.8	20.4	21.8	21.6	21
10	4.472	4.464	4.486	4.47	191.625	187.452	194.386	191.2	19.2	21.7	20.3	20

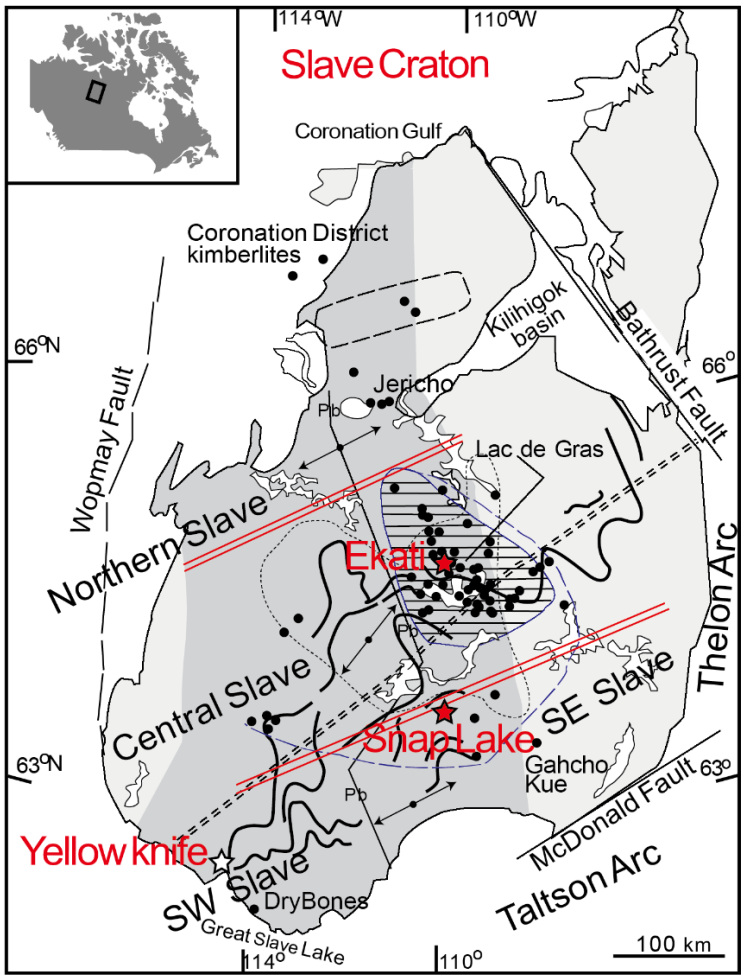

Figure 2.1 Schematic map of the Slave Craton (Northwest Territories, Canada), revised from Kopylova and Caro (2004). Snap Lake and Ekati Mine are marked by red stars, other kimberlite pipes are marked by small black circles. The boundaries between northern, central and southern lithospheric domains marked by double red lines, are distinguished by distinct compositions of garnet in kimberlite concentrates (Grütter et al. 1999). The SW and SE Slave domains are separated by the Pb isotopic boundary (thin continuous line) of Thorpe et al. (1992). The darker area represents the postulated surface and subsurface extent of the Central Slave Basement Complex (proto-craton of Ketchum and Bleeker, 2001). The thick continuous curves mark the orientation of pre-2.63 Ga D1 fold structures (Davis et al. 2003); double dashed line traces the northern boundary of the 2.63-2.62 Ga diorite with the granodiorite plutons of the Defeat Suite (Davis et al. 2003). Orientation of the S-wave polarization (bars with arrows) indicates the directions of mantle anisotropy (Bank et al. 2000a). The location of the conductive mantle anomaly (Jones et al. 2001) is contoured by a thin dashed line. The minimum extent of a shallow ultra-depleted layer (horizontal lined pattern) and deeper Archaean lherzolitic layer (Griffin et al. 1999b) of the Central Slave are shown with dashed outlines.

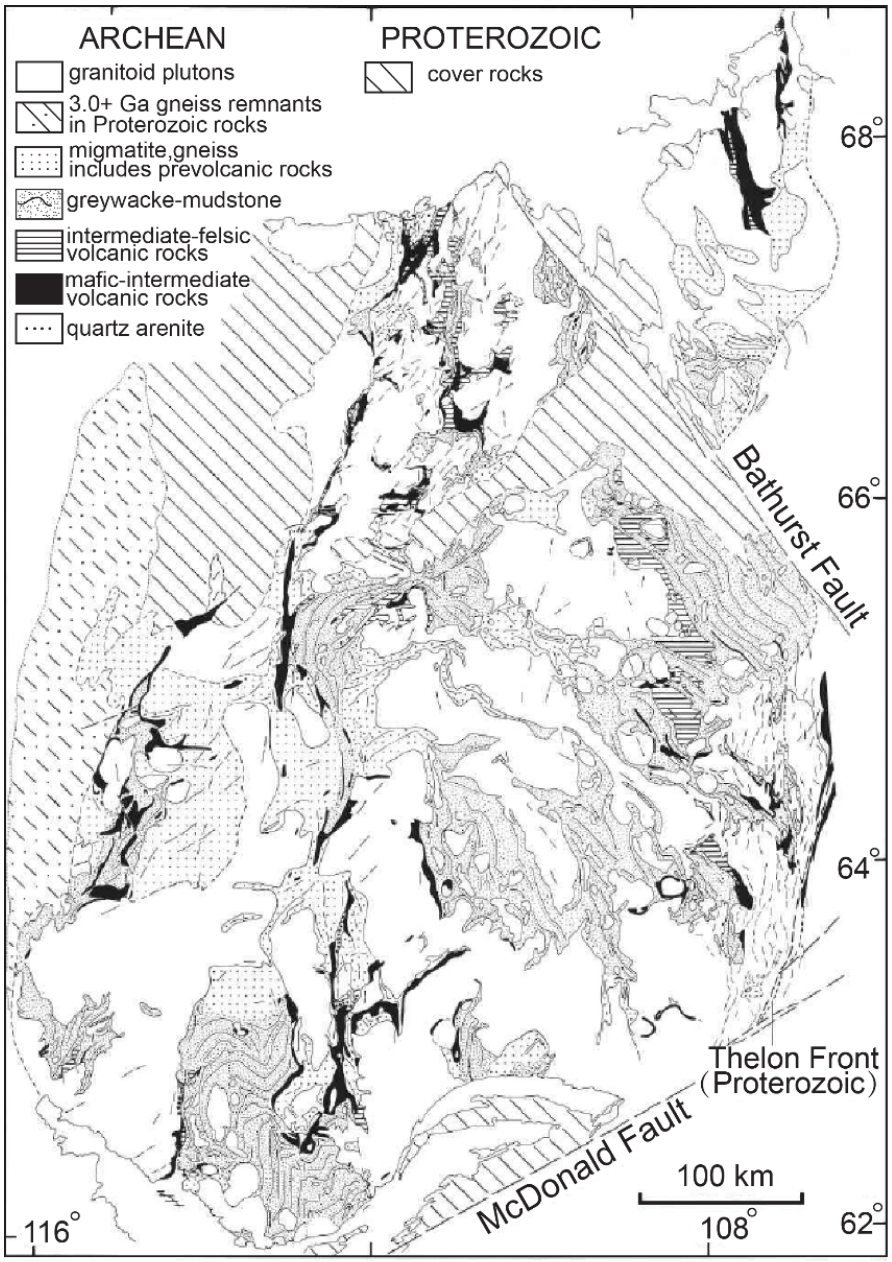

Figure 2.2 Generalized lithological map of the Slave Province. Foliations in granitoid rock and fold trends in supracrustal rocks are shown as thin curving and broken lines. Darker lines offsetting foliations and supracrustal units are (mainly) Proterozoic faults; some (standard symbol) are in part thrusts. Reproduced from Padgham and Fyson (1992).

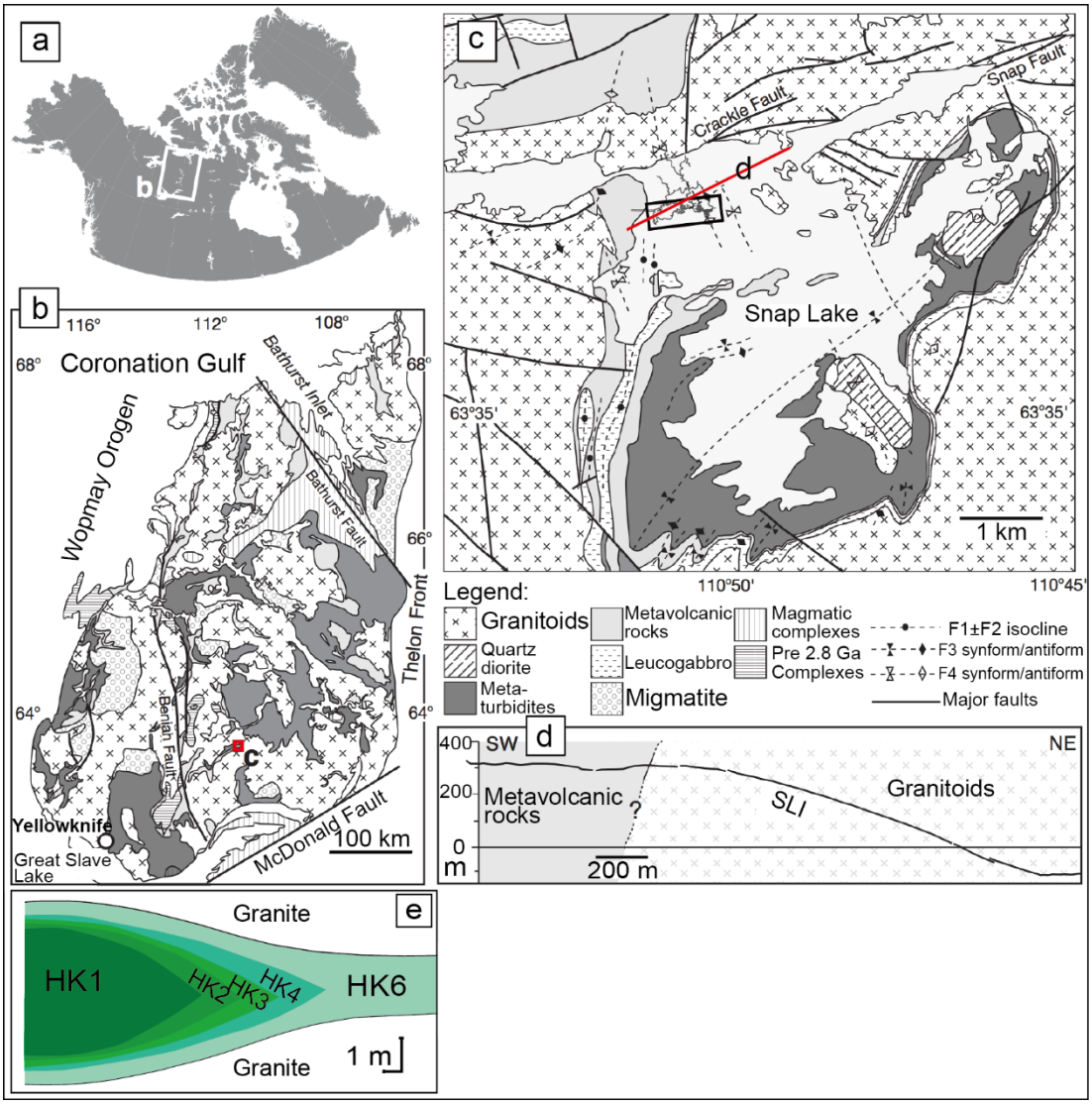

Figure 2.3 (a) Map of Canada showing the location of the Slave Craton, Northwest Territories. (b, c) Summary geological maps of (b) the Slave Craton and (c) the Snap Lake area, showing the location of mine-works. (d) NE–SW-trending profile (see (c)) of the Snap Lake Intrusion produced from vertical intercepts of kimberlite in boreholes. (e) Simplified cross-section profile of the Snap Lake ore body showing the kimberlite facies with various degree of alteration. Images (a)-(d) are reproduced from Gernon et al. (2012). Image (e) is from Alexandrina Fulop (personal communication).

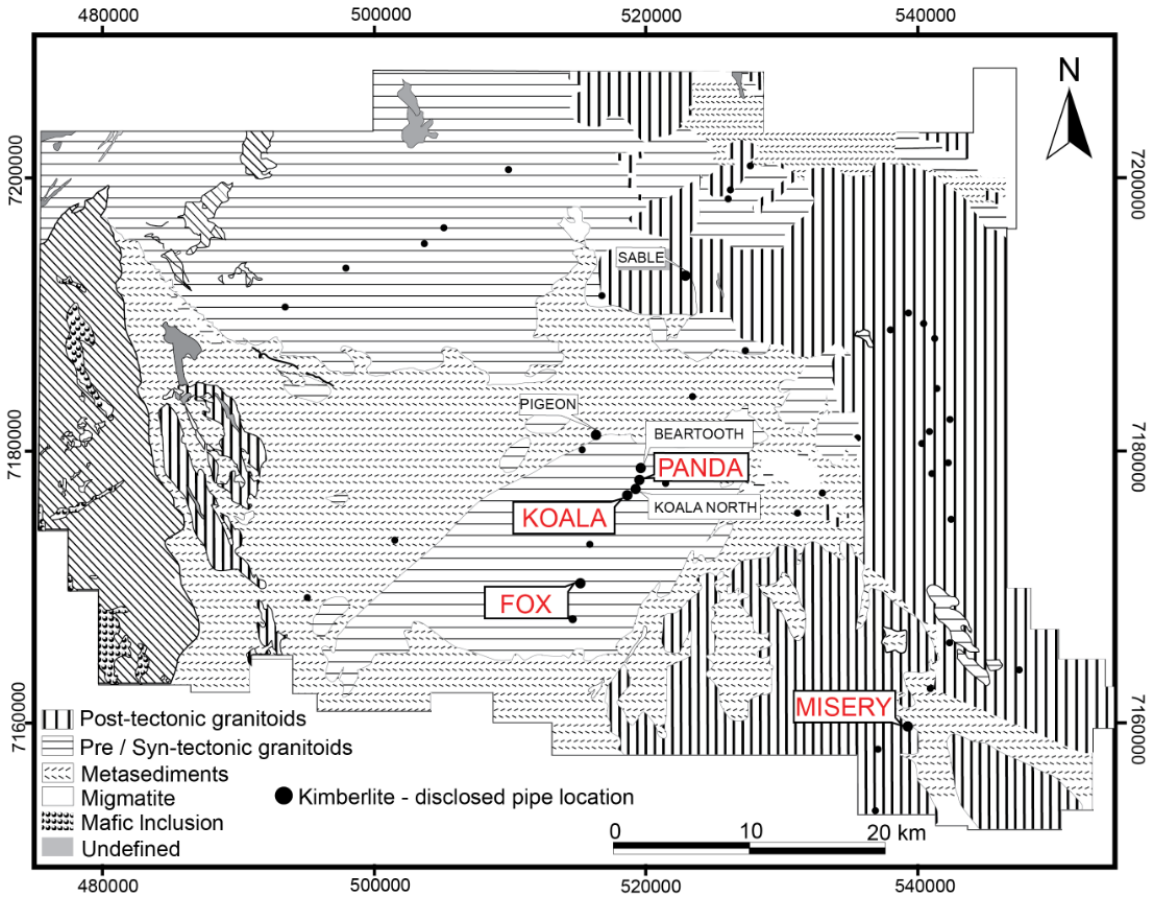

Figure 2.4 Generalized map of the bedrock geology of the Ekati property showing the main rock types present and disclosed kimberlite locations, reproduced from Nowicki et al. (2004).

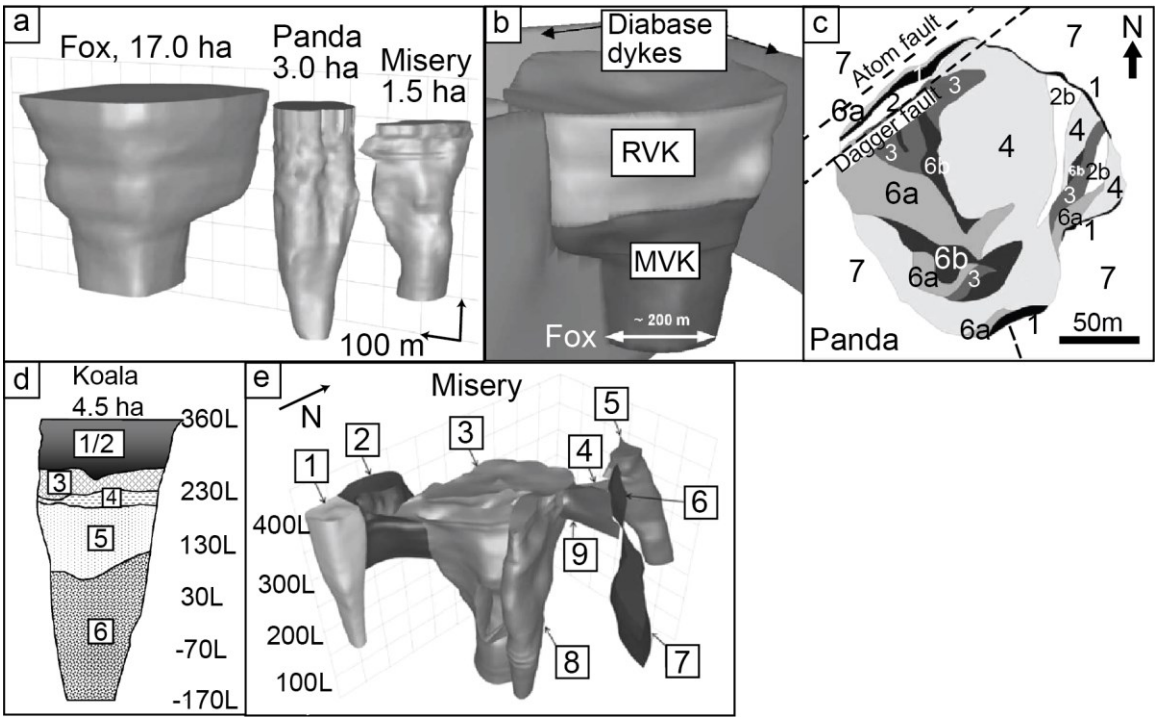

Figure 2.5 (a) Three-dimensional models of Fox, Panda and Misery pipes illustrating variation in pipe size and morphology. (b) Three-dimensional model of the Fox pipe looking south. The upper zone contains RVK with minor olivine rich VK overlying uniform MVK and MVK breccia with granodiorite boulder zones evident within the MVK and at the contact between RVK and MVK. Wall rock diabase dykes are also shown. (c) Plan view of Panda pit illustrating the distribution of different kimberlite and associated rock types. 1— moist, pliable black mud; 2a—quartz-rich sand; 2b—kimberlitic (olivine-rich) sand; 3—massive, pale, olivine-rich VK; 4—bedded, pale, olivine-rich VK; 6a and 6b—dark, fine-grained mud-rich RVK (subdivided for mining purposes). (d) Vertical section through a geological model of the Koala kimberlite. Phase 1 and 2—thick graded sequence ranging from fine-grained well sorted silty to sandy kimberlite, to coarse-grained olivine-rich VK; Phase 3—intermixed mud-rich and olivine-rich RVK comprising multiple graded units; Phase 4—wood-rich uniform siltstone; Phase 5—massive to crudely bedded mud-rich RVK with granite boulder zones in lower levels; Phase 6—uniform PK and minor PK breccia. (e) Three-dimensional model of the Misery kimberlite complex. Misery Main (3), Misery South (1), Misery Southwest Extension (2) and Misery Northeast (5) pipes are occupied by VK, whereas the Misery East pipe (7), East and Northeast extensions (9, 4) and Misery Mid-east dyke (6) are CK. Misery Northeast extension (8) contains both CK and possible MVK. Modified after Nowicki et al. (2004).

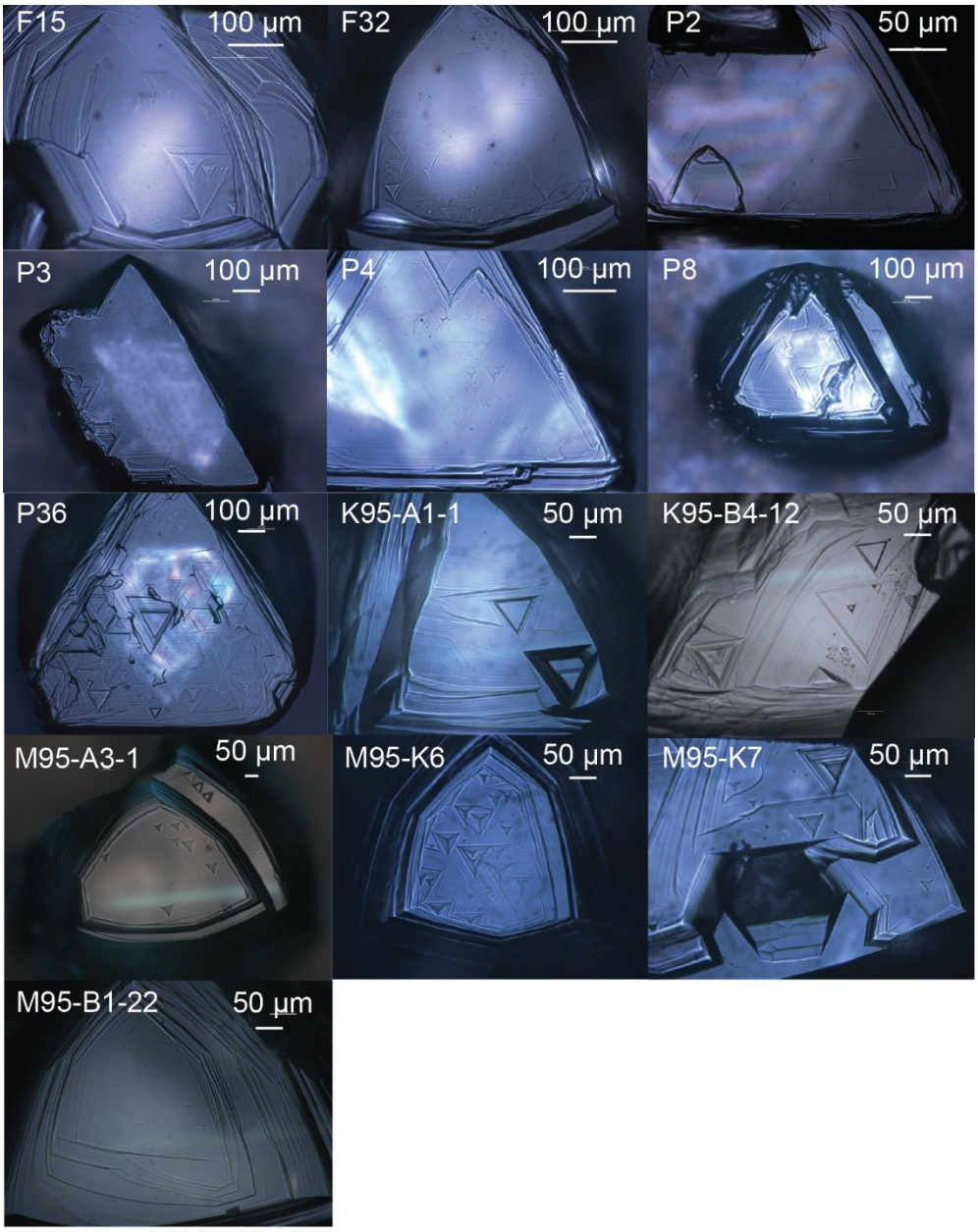

Figure 2.6 Optical images of the selected diamonds from Fox (F15, F32), Panda (P2, P3, P4, P8, P36), Koala (K95-A1-1, K95-B4-12) and Misery (M95-A3-1, M95-K6, M95-K7, M95-B1-22) kimberlite pipes.

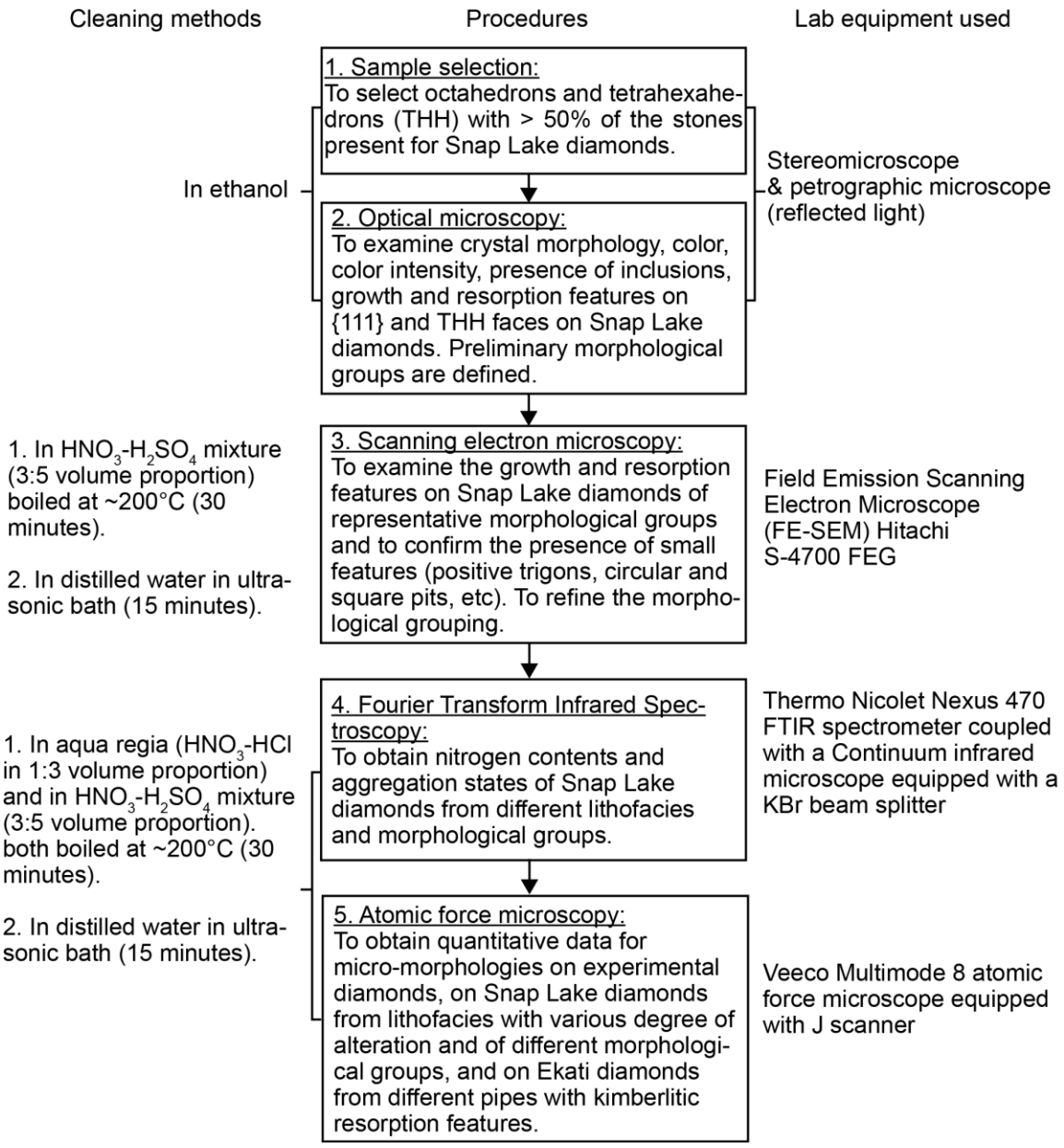

Figure 2.7 Flowchart showing the procedures, cleaning methods and laboratory equipment used for examination of diamonds in this study.

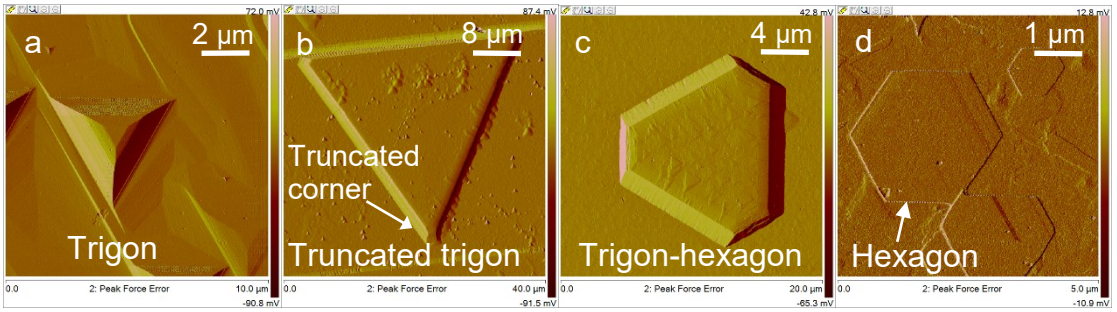

Figure 2.8 Illustration of different types of etch pits. (a) A positive trigon on experimental diamond Exp17, no corner is truncated. (b) A negative trigon on diamond SNP6-1 with truncated corners. (c) A negatively-oriented trigon-hexagon on diamond SNP3-8. (d) A hexagon on experimental diamond Exp17.

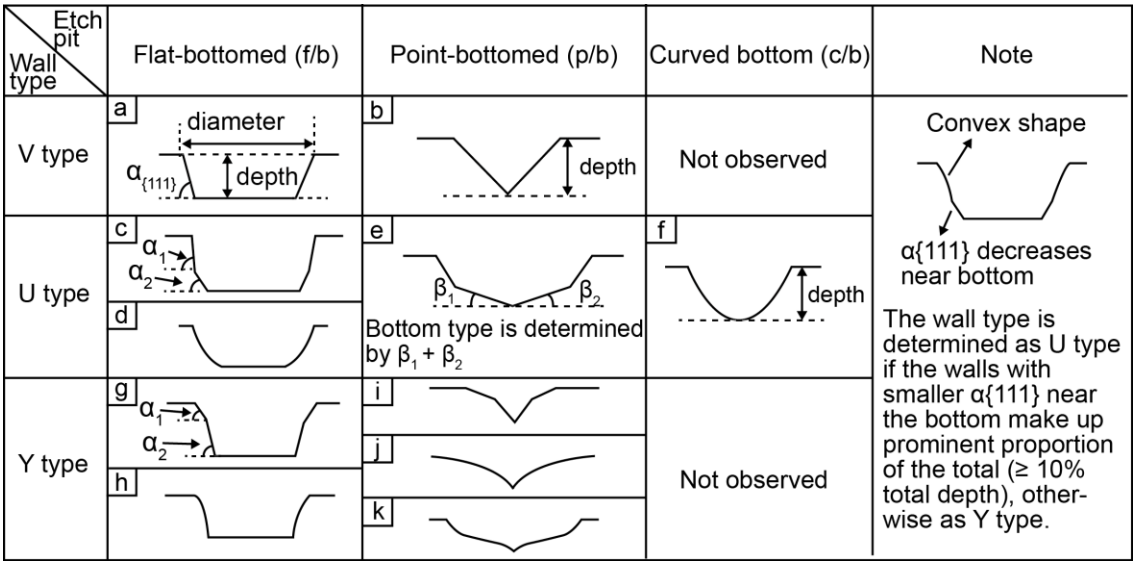

Figure 2.9 Classification of etch pits shown in simplified cross-section profiles with different wall types that have been observed on natural and experimental diamonds. Steps or micro-steps and trigons on the bottoms are not shown in the profiles.

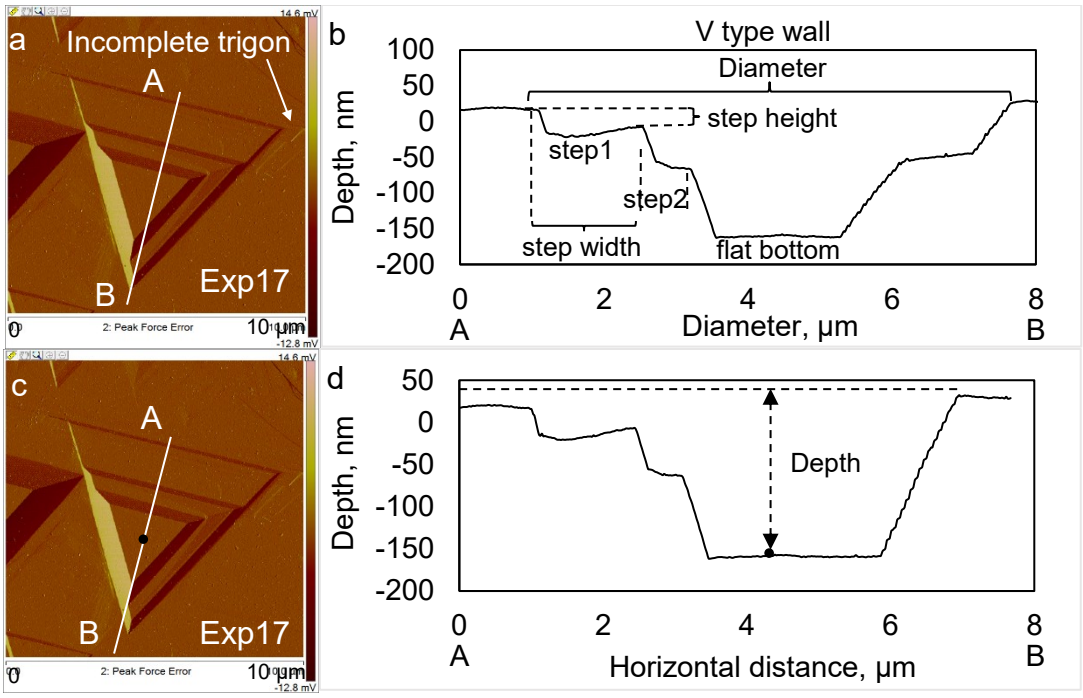

Figure 2.10 Illustration of AFM measurements of pit diameter and depth, width and height of steps. AFM image and cross-section profile of one positive trigon on diamond Exp 17 with stepped walls (V type). The center of the bottom is marked with a black dot in (c) and (d). (b) The cross-section (marked by line AB in (a)) profile showing the diameter of the trigon. Two steps are shown in the profile. The height and width of step1 are marked. The profile of the trigon in (b) corresponds to the simplified profile in Figure 2.9a. (d) The cross-section (marked by line AB in (c)) profile of the trigon showing the depth of the trigon. The depth is the distance between the center point (the black dot in (c), (d)) of the bottom and the {111} face. Note that the distance between the bottom and the {111} face which is to the right of the profile is slightly higher (could be less resorbed) than the {111} face to the left.

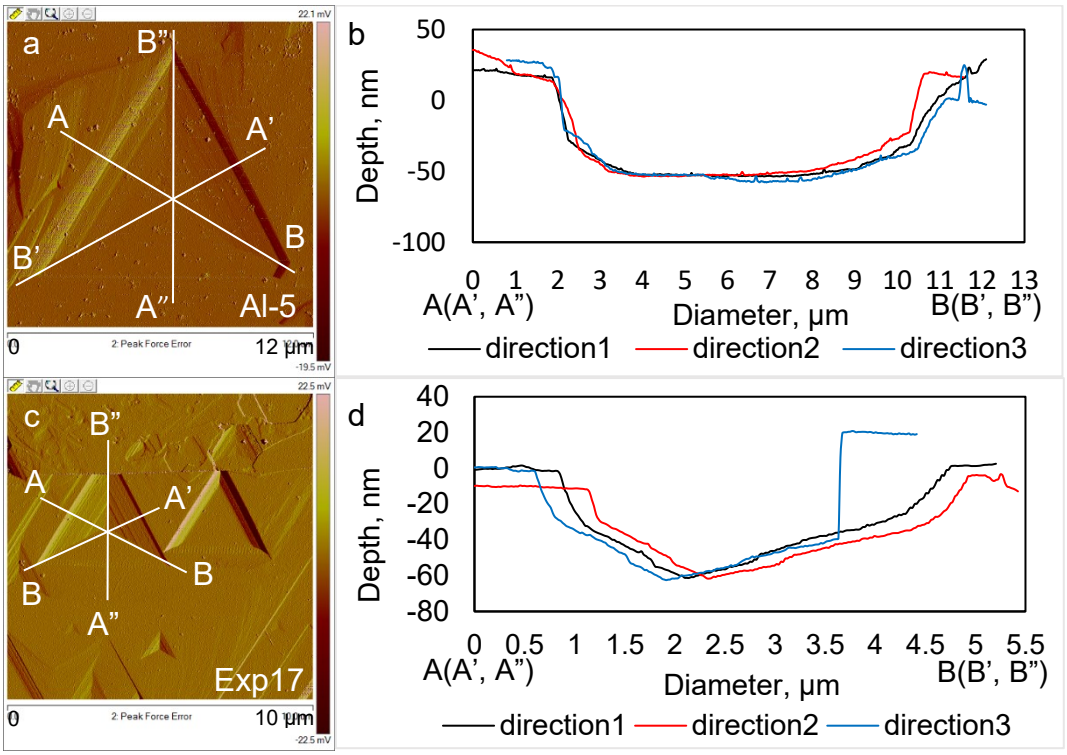

Figure 2.11 Illustration of AFM measurements of pits with unequal diameters in different directions. (a) One positive trigon on diamond AL-5. (b) The profile of the trigon in direction1(AB), 2(A’B’) and 3(A”B”). (c) One positive trigon on diamond Exp17. (d) The profile of the trigon in direction1(AB), 2(A’B’) and 3(A”B”).

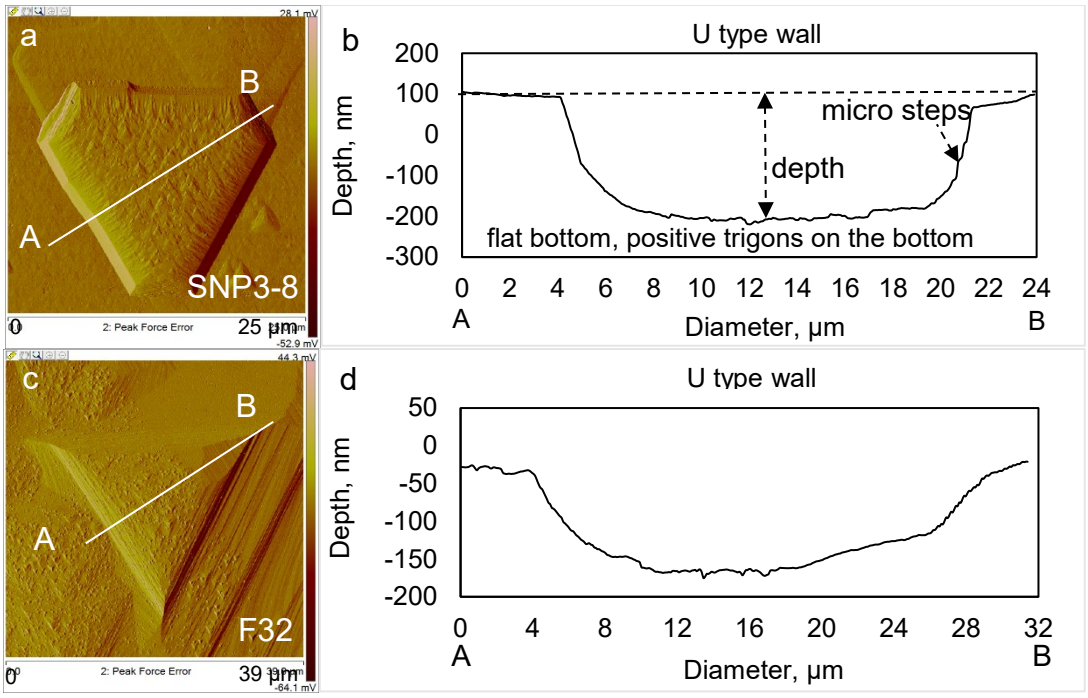

Figure 2.12 AFM images and cross-section profiles for a f/b trigon-hexagon on diamond SNP3-8 from Snap Lake kimberlite with U type walls (a, b). A f/b negative trigon with U type walls on diamond F32 from Fox kimberlite (c, d). The profiles in (b), (d) correspond to the simplified profiles in Figure 2.9c and 2.9d, respectively.

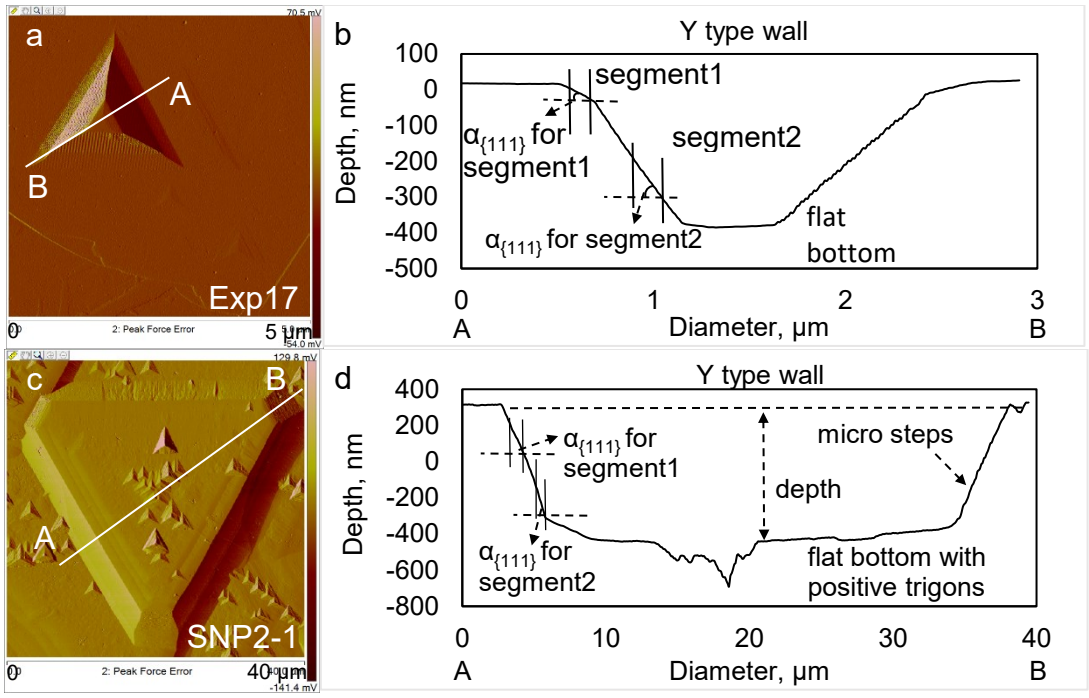

Figure 2.13 AFM images and cross-section profiles for a f/b positive trigon with Y type walls on diamond Exp17 (a, b) and a f/b negative trigon with Y type walls on diamond SNP2-1 (c, d). The profiles in (b), (d) correspond to the simplified profiles in Figure 2.9g and 2.9h, respectively. There are positive trigons developed on the bottoms of the pits in a and g, the distance was measured between a subjectively selected point close to the center of the bottom and the {111} face as the depth of the pits. Two segments are selected in both (b) and (d) by marked lines, and the $\alpha_{\{111\}}$ of each segment is marked.

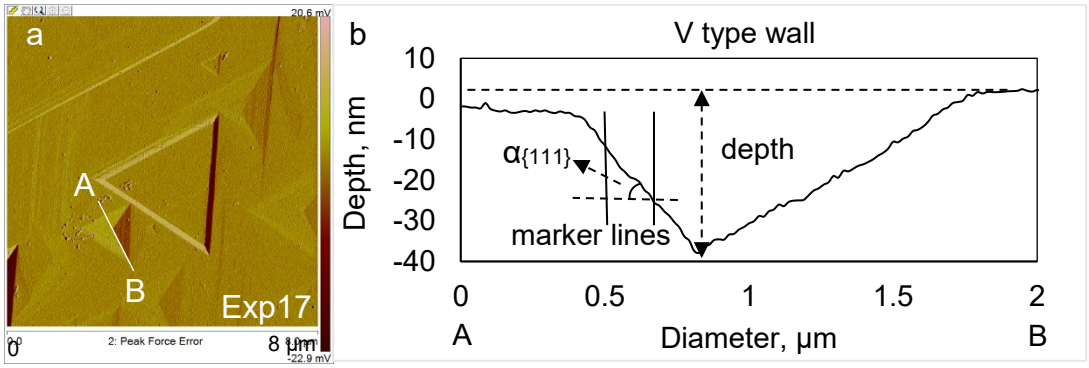

Figure 2.14 AFM image and cross-section profile for a p/b positive trigon with V type walls on diamond Exp17 (a, b). The profile in (b) corresponds to the simplified profiles in Figure 2.9b.

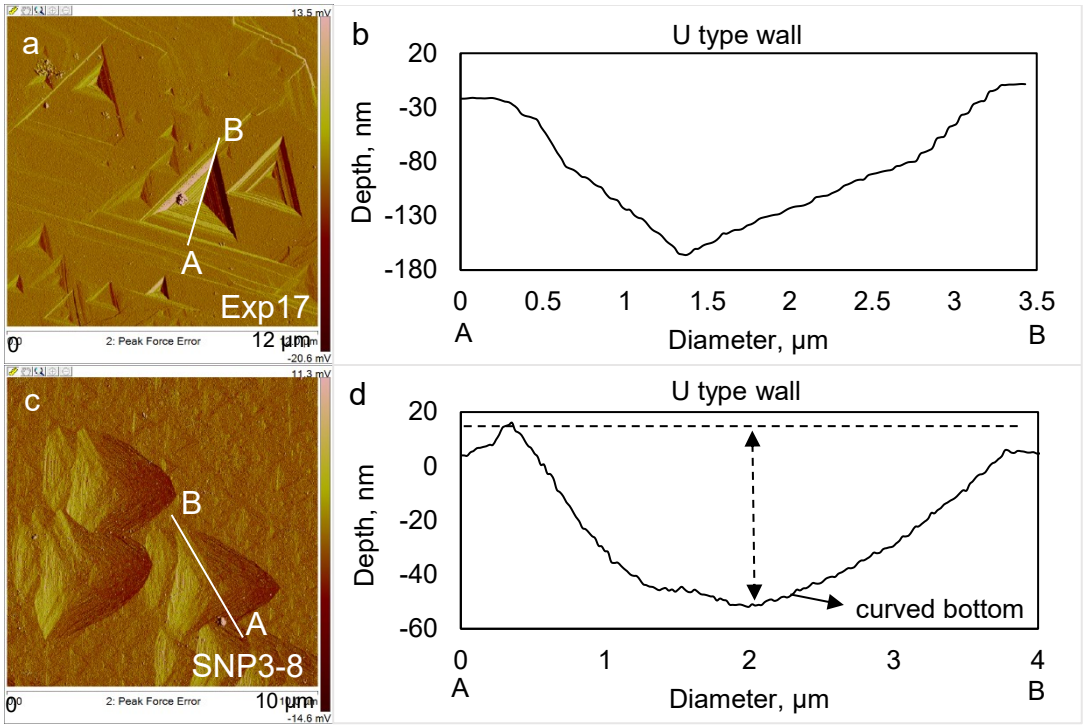

Figure 2.15 AFM images and the cross-section profiles for a p/b positive trigon with U type walls (a, b) on diamond Exp17 and a c/b positive trigon with U type walls on diamond SNP3-8 from Snap Lake kimberlite (c, d). The profiles in (b), (d) correspond to the simplified profiles in Figure 2.9e and 2.9f, respectively.

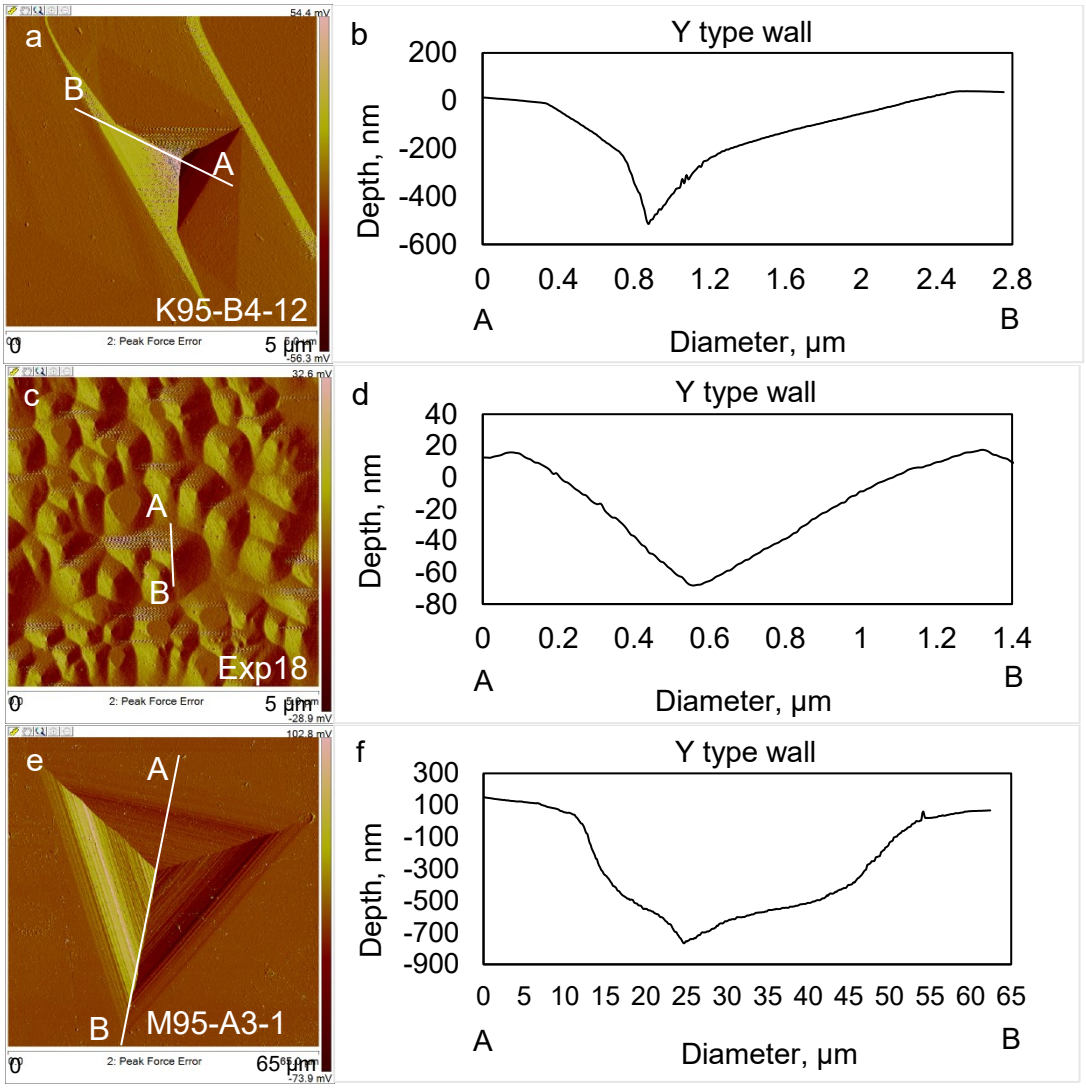

Figure 2.16 AFM images and cross-section profiles for a p/b negative trigon with Y type walls on diamond K95-B4-12 from Koala kimberlite (a, b), a p/b positive trigon with Y type walls on diamond Exp18 (c, d), a p/b negative trigon on diamond M93-A3-1 from Misery kimberlite (e, f). The profiles in (b), (d), (f) correspond to the simplified profiles in Figure 2.9i, 2.9j and 2.9k, respectively.

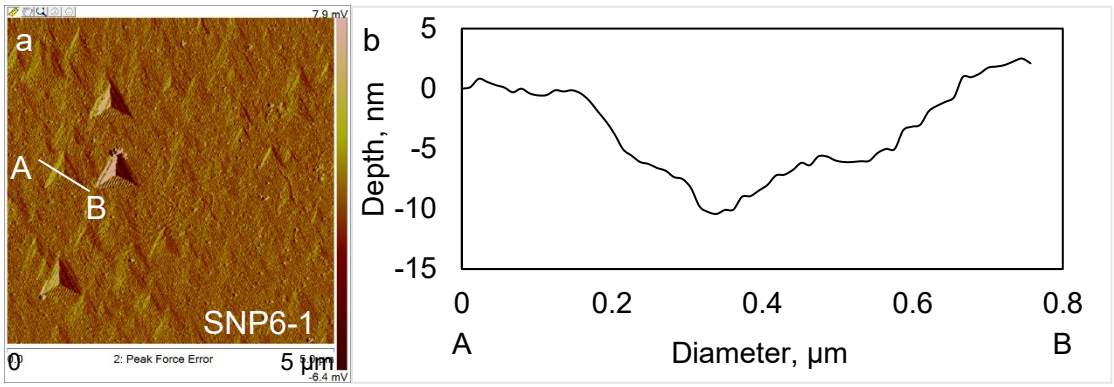

Figure 2.17 (a) AMF image showing one positive trigon on diamond SNP6-1 from Snap Lake kimberlite. (b) Cross-section profile of the trigon showing transition between flat bottom and point bottom.

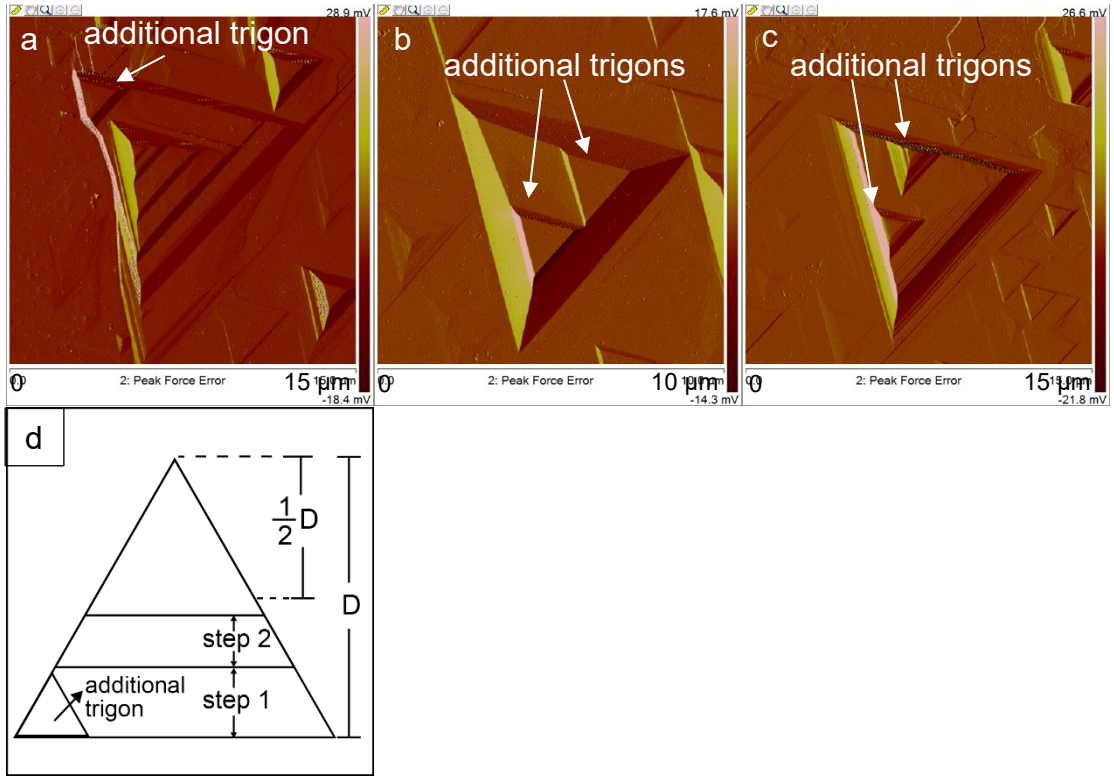

Figure 2.18 (a-c) AFM images of three positive trigons on diamond Exp17 with additional trigons developed inside. (d) Illustration of inside trigons forming steps or additional trigons, D is the diameter of the largest outside trigon.

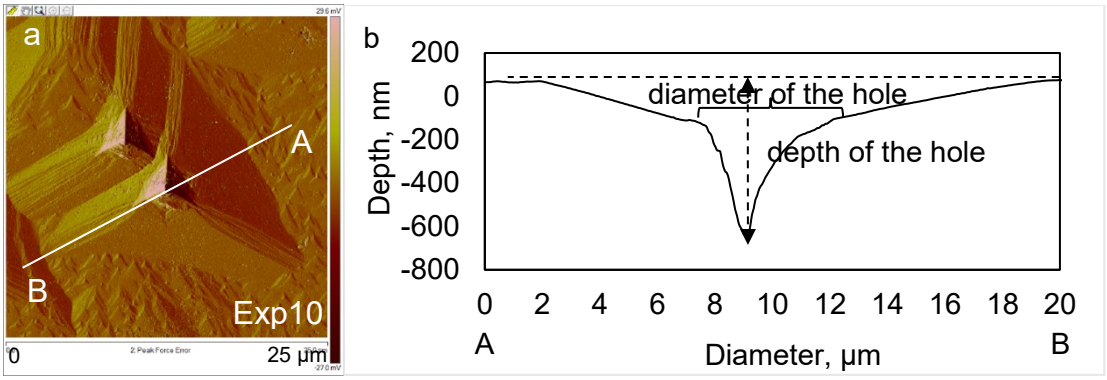

Figure 2.19 AFM image (a) and cross-section profile (b) for a positive trigon on diamond Exp10 with a deep hole on the bottom.

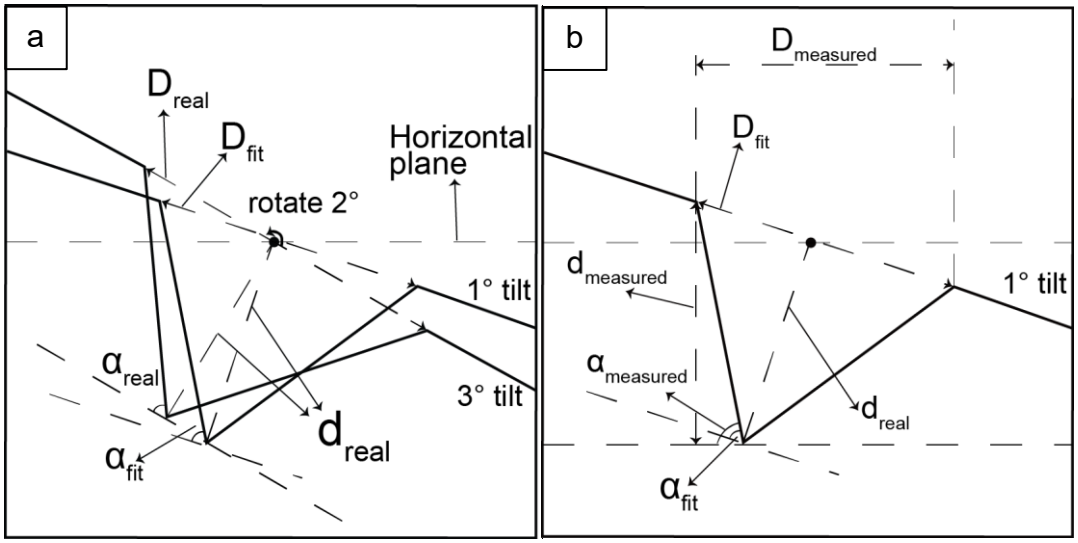

Figure 2.20 Simplified cross-profile for a p/b trigon with V type walls with initial tilt 3º before the Plane Fit operation (a) and the profile with remaining tilt 1º after the Plane Fit operation (b).

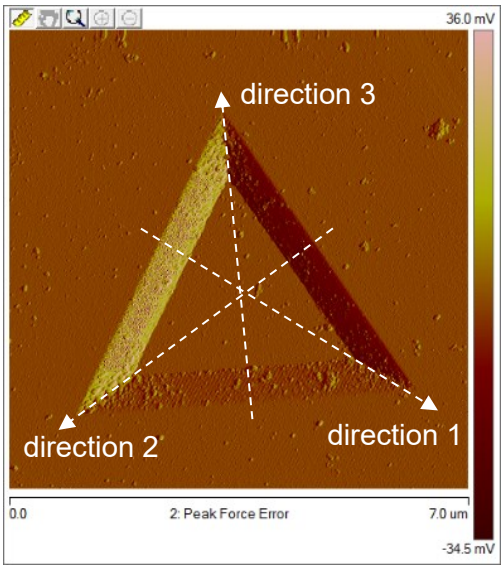

Figure 2.21 AFM image of single f/b trigon on diamond K95-A1-1 from Koala kimberlite. The three directions of the measurements are marked in the image.

CHAPTER 3. POSITIVE TRIGONS FROM SNAP LAKE DIAMONDS AND EXPERIMENTS

3.1 Introduction

Negative trigons are the most common resorption features on diamonds. However, diamonds from Snap Lake diamonds show positive trigons, which is unusual and absent on diamonds from Ekati kimberlites. Experimental data on positive trigons are very limited. In this chapter, I focus on positive trigons specifically and support the study of natural Snap Lake diamonds with data from diamond oxidation experiments at 0.1 MPa. The results present in this chapter are discussed in chapter 5 to understand what is unusual in emplacement conditions of Snap Lake kimberlite that resulted in the widespread development of positive trigons, the mechanism of formation of positive trigons and how it can be used to examine fluid system in kimberlites.

3.2 Diamond Samples

The study used 91 diamonds (including 79 octahedral and 12 THH crystals) selected from 251 diamonds larger than 300 μm in diameter from two diamond parcels provided by De Beers (Table 2.2; Appendix A: Table EA1). This study did not use cubes, complex cubo-octahedron forms, and fragments with undistinguishable morphology due to breakage. Only octahedral diamonds with at least 50% of the initial faces present and tetrahexahedral diamonds were selected for morphological study. The selected diamonds represent all six lithofacies of Snap Lake dyke: HK1 (25 diamonds), HK2 (25 diamonds), HK3 (4 diamonds), HK4 (14 diamonds), and HK5-HK6 (23 diamonds). Sixteen diamonds

from different morphological groups and lithofacies were selected for further AFM examination (Figure 3.16, Table 3.1; Appendix A: Table EA3).

Table 3.1 Snap Lake diamonds measured by AFM and number of etch pits scanned on each stone.

Diamond #	Diamond name	Kimberlite facies	Morphological group	#sides scanned	# of pits scanned		
					Negative trigon/trigon-hexagon	Positive trigon	Hexagon
1	SNP2-1	HK1	SG5	1	3	11	1
2	SNP8-9		?	1	0	11	0
3	SNPO13-2		SG6	1	2	9	0
4	SNP3-6	HK2	SG9	1	0	8	1
5	SNP3-8		SG6	1	2	10	0
6	SNP6-1		SG5	1	8	19	0
7	SNP9-1		SG10	2	0	11	1
8	SNPO9-1		SG1	1	0	8	0
9	SNP1-9	HK4	SG7	1	0	10	0
10	SNP10-6		SG1	1	5	0	1
11	SNP10-9		SG2	1	1	9	2
12	SNP5-2	HK5	SG2	1	3	0	0
13	SNP5-3		SG4	1	11	12	2
14	SNPO12-2	HK6	SG4	1	4	9	0
15	SNPO12-3		SG6	2	2	18	0
16	SNPO12-8		SG2	1	1	9	0

3.3 Experimental and Analytical Methods

During initial examination of diamonds using a stereomicroscope the general morphology, color, color intensity, and presence of inclusions for the selected 91 diamonds were recorded. Further study of growth and resorption features on diamond surfaces for morphological grouping used a stereomicroscope and petrographic microscope under reflected light with a partially closed aperture stop. Resorbed diamonds with more than 50% of {111} faces preserved were classified as octahedrons, and with less than 50% of {111} faces preserved as tetrahexahedrons. Tetrahexahedral crystals (THH) may preserve a small proportion of the {111} faces but were still classified as THH based on the rounded crystal shape and the large degree of resorption. The morphologies of twinned diamonds and aggregates were classified by the shape of constituent crystals. The octahedral diamonds were then divided into 12 morphological groups (Figure 3.14) based on the shape of {111} faces (trigonal vs. ditrigonal) and character of resorption on the {111} faces, such as the presence of step faces, and the presence and type of the etch pits (negative and positive trigons, trigon-hexagons, hexagons) and the laminae (shield-shaped, serrate- or irregular-shaped). These morphological groups were further divided into sub-groups based on the character of resorption along the crystal edges (THH faces), including the presence and type of cavities (shallow depressions vs. deep cavities), hillocks (sharp vs. smooth), and the presence of striations and circular pits.

The preliminary morphological grouping was refined using Scanning Electron microscopy (SEM) examination of representative examples from each group (29 diamonds). SEM study also confirmed the presence of positive trigons on diamonds, where

the small size of the positive trigons (less than 1 μm) precludes their observation by optical microscopy. For details of SEM examination, see Chapter 2.2.4.

The study also used diamond crystals that had been used in oxidation experiments (Table 2.3, Figure 3.1 with T-fO_2 conditions) done by my supervisor Yana Fedortchouk. The experiments were conducted at 0.1 MPa in a vertical gas mixing furnace at ETH Zurich. Oxygen fugacity (fO_2) was controlled by a mixture of CO_2 and H_2 gases at log fO_2 = -9 to -16. The experiments used six colourless octahedral diamonds (< 1mm in size and 0.5-1 mg) from Yakutian kimberlites with minor resorption features and minor or no visible defects (inclusions or fractures). The diamonds were photographed before the experiment, weighed, washed ultrasonically for 5 min in alcohol, placed on the bottom of an open AuPd or MgO capsule (1 cm long with inner diameter 5 mm) located inside an aluminium oxide crucible. The crucible was attached to the sample holder by platinum wire. In two runs (GM9, GM10), a mixture of Na_2CO_3 and SiO_2 reacting at the run conditions to produce $Na_2Si_2O_5$ was added into the capsule. In the beginning of each run the crucible with the diamond was placed at the top of the furnace tube above the hot zone and held at a temperature of about 200 °C until the desired gas mixing ratio was achieved. The sample was then moved into the hot zone and held at the run T and fO_2 for the duration from 3 to 9 hours. Tests showed that no oxidation occurred to the diamond during the first 5 min at the top of the furnace tube. At the end of experiment, the platinum wires holding the crucible were burnt through by an electrical current, causing the sample to fall into a water-filled reservoir at the bottom at the furnace for rapid, almost instantaneous cooling. Afterwards the surface features developed on the diamond as a result of the oxidation were imaged using an optical microscope and SEM.

Detailed morphological study of selected natural and experimental diamonds was conducted on a Veeco Multimode 8 atomic force microscope at Department of Earth Sciences, Dalhousie University. Images were analyzed using NanoScope Analysis (ver. 1.20). All the images were processed using the Plane Fit function to remove the tilt in both x and y directions. The parameters of individual etch pits (diameter, depth, shape, wall angles) were examined on cross-section profiles using section analyses tool. For the details of sample preparation, data collection and processing, see Chapter 2.2.6. The pits were classified based on the bottom and wall morphology (Figure 2.9).

The three sources of uncertainty in AFM measurements are discussed in Chapter 2.2.6.4. These include: (1) AFM uncertainty (1.4% in x, y and z directions) after the calibration. (2) Tilt of the {111} face of the diamond due to uneven placement on the metal plate. (3) Subjective selection of the measurement section (the position where the line was drawn across the pits to get the section plot; the position where the plot markers were placed on the section plot). The total uncertainty is estimated as < 2.5% for diameter measurement, < 6% for depth measurement, and < 4º angle measurement.

3.4 Results

3.4.1 Experiments at Variable Temperature and Oxygen Fugacity

Run GM-8 was conducted at the highest temperature (1150 ºC) and fO_2 of CCO +1.5 (1.5 log units above the CCO buffer), and the diamond (Exp11) developed negative trigons. The negative trigons with curved bottoms and convex shapes coalesce and form a very rough surface on the {111} face (Figure 3.2). The other five diamonds etched in the T range 900-1050 ºC developed only positive trigons on {111} faces (Figure 3.3), with morphology and distribution density varying on different diamonds (Figure 3.4).

Diamond Exp5 (GM-5 run), etched at conditions more reduced than the CCO buffer (900 ºC and CCO -0.3), developed a surface covered by positive trigons with zigzag outlines that are densely attached to each other (Figure 3.5c, 3.8c). There are also flat areas on the diamond with small and shallow trigons (Figure 3.5b, 3.8a) with diameters (up to 4 μm). that positively correlate with their depths (up to 250 nm) (Figure 3.7b). The unique feature of this diamond is the presence of positively-oriented dendritic depressions that differ from positive trigons (Figure 3.6) and resemble graphite growth features reported by Khmelnitsky and Gippius (2014).

Much less dense development of trigons (Figure 3.4b, 3.4c) is observed on two diamonds (Exp17 and AL5), etched at 900 ºC and at more oxidized conditions (CCO +0.7) in the presence of sodium silicate melt. Both diamonds have mainly f/b trigons (Figure 3.5) with similar dimensions to those on diamond Exp5 (Figure 3.7b-3.7d). They also developed sharp corrosive features along the crystal edges (Exp17) and within irregular areas of {111} faces on diamond AL5 (Figure 3.3). These corrosive areas on diamond AL5 show trigons developed inside the cavities that are difficult to measure by AFM, but these trigons are

generally larger compared to trigons outside the cavities. The trigons show a positive correlation between diameter and depth that reaches 570 nm on diamond AL5 (Figure 3.7c) and 800 nm on diamond Exp17 (Figure 3.7d). In addition to simple positive trigons (Figure 3.9a and 3.10q), both diamonds developed trigons with truncated corners (trigon-hexagons) (Figure 3.9c, 3.9e and 3.10e) with depths up to 600 nm. Diamond Exp17 also shows complex trigons with multiple steps and small trigons on the bottom (Figure 3.10c), and small hexagons < 5 μm in diameter and < 50 nm in depth (Appendix A: Table EA2).

Diamond Exp18 was etched at 1000 ºC and CCO +0.3, produced pits smaller than 2 μm in diameter with depths < 100 nm (Figure 3.7e). The pits are attached to each other, rounded, and cover the whole diamond surface (Figure 3.11). For such embryonic pits, I could not reliably distinguish point-bottomed (p/b) from flat-bottomed (f/b) shapes. These trigons resemble positive trigons produced in exotic etchants such as KNO_3 and $NaNO_3$ in other experimental studies, where the p/b and f/b trigons are suggested to be associated with dislocations and surface defects, respectively (de Theije et al. 2001; Khokhryakov and Palyanov 2006).

Diamond Exp10 etched at more oxidized conditions (CCO +1.7) and higher T (1050 ºC) than diamonds Exp5, Exp17, AL-5 and Exp18, shows several distinct types of positive trigons: large individual trigons with or without a 'hole' on the bottom (Figure 3.12c, 3.12e) and small attached trigons (Figure 3.12a). The embryonic trigons (~1 μm or less in diameter and < 10 nm in depth) cover the whole surface of the {111} diamond face, and may be related to point defects (de Theije et al. 2001). The large trigons (diameter ~10-18 μm, Figure 3.7f) include both f/b and p/b and show distinct striations at the joints of the walls (Figure 3.12c, 3.12e). They can be divided into two groups by the presence of deep

"holes" on the bottom (Figure 3.7f). The $\alpha_{\{111\}}$ angles are ~2º, but the angles of the "hole" walls are 6º, 10º, 30-33º, 43º and 48º (Appendix A: Table EA2).

The development of positive trigons during the experiment partially altered the original morphologies of pre-existing naturally-developed negative trigons. The initial negative trigons on {111} faces of diamonds AL5 and Exp18 developed truncated corners after the experiments (Figure 3.13).

3.4.2 General Morphologies and Negative Trigons on Snap Lake Diamonds

The octahedral and tehtrahexahedral Snap Lake diamonds were divided into 12 morphological groups (SG1-SG12) based on the shape of their {111} faces (trigonal vs. ditrigonal) and resorption features such as step faces, laminae, the number and character of negative trigons and hexagons (Figure 3.14). Diamonds from the same group may show different resorption features along their edges (Figure 3.15). For detailed description of morphological grouping and edge resorption, see Chapter 4.3.1. Diamonds from different lithofacies may show various morphological groups but the proportion of diamonds of major morphological groups is similar (Figure 4.5).

In total, measurements were obtained for 42 negative trigons (and trigon-hexagons) on 11 diamonds, and 8 hexagons on 6 diamonds (Table 3.1). Section analysis of the AFM scans shows that all negative trigons and hexagons are predominantly f/b (Figure 4.9-4.12; Appendix A: Table EA3). Only SNP10-6 and SNP5-2 of the 11 diamonds have few p/b trigons (Figure 4.13; Appendix A: Table EA3). The diameter of the negative trigons is up to 45 μm, and the depth is up to ~1 μm. The negative trigons on diamonds form HKM show positive correlation of diameter and depth, whereas no distinct relationship exists

between the diameter and depth of the negative trigons on diamonds from HKP. The unique feature of all negative trigons on Snap Lake diamonds is truncated corners to a degree that makes them transitional into hexagons (Figure 3.17).

3.4.3 Positive Trigons on Snap Lake Diamonds

All 91 selected diamonds from Snap Lake kimberlite have positive trigons. On some diamonds, these trigons are so small (< 1 μm) that they can only be seen under SEM, while on others they can be observed with an optical microscope. Positive trigons mostly develop on {111} faces, but are also often present on the rounded THH edges of resorbed diamonds (Figure 3.18). This is different from the negative trigons occurring only on {111} faces, as described in my study and in the literature. Distribution of the positive trigons on diamond crystals can be uniform (Figure 3.19b) or patchy, with uneven distribution of larger and smaller trigons in different areas of {111} faces (Figure 3.19d), which sometimes show vermicular lines (Figure 3.19f). The diameter of the positive trigons ranges from < 1 μm up to 13 μm (Figure 3.20c) and correlates with the trigon depth (Figure 3.27). Less resorbed diamonds (e.g. SNPO16-2) have only minute-sized (≤ 0.5 μm) positive trigons with depth < 20 nm, which could be detected only on SEM and AFM. The diameter of the positive trigons roughly correlates with kimberlite lithology and decreases from fresh facies (HK1 and HK3) and slightly altered facies (HK2 and HK4) towards highly altered facies (HK5 and HK6) (Figure 3.20b, 3.20c). No correlation between the size of the positive trigons and general diamond morphology was found.

The geometry of the positive trigons was examined using AFM for 154 positive trigons on 14 diamonds (Table 3.1; Appendix A: Table EA3), and the types of positive trigons (Figure 3.21) present on each diamond are summarized in Table 3.2. Positive

trigons on diamonds from HKP show a clustering of diameters at < 2.5 μm and depths at < 350 nm, while positive trigons on diamonds form HKM have wider range of diameters at < 7 μm, and a few at 10-12 μm, with depths up to ~600 nm (Figure 3.26a). Only two diamonds (SNP8-9 and SNP9-1) have trigons larger than 4 μm. Another four diamonds have trigons up to 4 μm in diameter, and the remaining eight diamonds have only trigons up to ~2 μm (Figure 3.27). Trigons larger than 3 μm were only observed on diamonds from HK1 and HK2 facies.

The trigons can be divided into three groups (Figure 3.27): (1) p/b and f/b trigons with straight sides and multiple steps; (2) curved-sided trigons with fine poorly-defined steps and rounded bottoms; (3) small trigons (diameter < 1 μm), for which the morphology cannot be reliably distinguished. The first group of stepped trigons with diameters up to 8 μm is present on most of the studied diamonds (except SNP3-8). These trigons show a clear positive correlation between diameter and depth (Figure 3.27), and have similar slopes for most diamonds (e.g. SNP2-1, SNP3-6, SNP10-9 in Figure 3.27) but a gentler slope for SNP8-9 (Figure. 3.27). The trigons are mostly V-shaped, but can be U- or Y-shaped (Figure 3.22; Appendix A: Table EA3). When these trigons are small they develop asymmetric steps distributed around the edges of the trigon such as on diamond SNPO9-1 (Figure 3.23). Some trigons in this group show truncated corners which transition into hexagonal shapes (Figure 3.25a, 3.25c). The second group of trigons has curved sides, for which the steps become finer and the bottom can be flat or curved (Figure 3.24), some trigons in this group also show truncated corners (curved f/b II in Figure 3.21; Figure 3.24c). These trigons are absent on the two diamonds from HK4. They occur on one diamond from HK1, three out of five diamonds from HK2, and two diamonds from HK5 and -6 (Table

3.2). The non-truncated trigons (curved f/b I, c/b) in this group follow a gentler diameter vs. depth trend compared to the larger truncated trigons (curved f/b II) (Figure 3.27). The last group is composed of trigons smaller than 1 μm in diameter and few tens of nm in depth. These represent embryonic stages of trigon development and are present on all the studied diamonds.

Table 3.2 Summary of positive trigon types present on each Snap Lake diamond studied by AFM. 1 = present

Diamond	Kimberlite facies	Morphology group	Straight f/b	Straight p/b	Asymmetric f/b	Asymmetric p/b	Curved f/b I	Curved f/b II	Curved c/b	Truncated f/b
SNP2-1		SG5		1						
SNP8-9	HK1	?		1					1	
SNPO13-2		SG6			1	1				
SNP3-6		SG9		1						
SNP3-8		SG6	1						1	
SNP6-1	HK2	SG5	1	1					1	
SNP9-1		SG10		1			1	1		
SNPO9-1		SG1			1	1				
SNP1-9	HK4	SG7	1	1						
SNP10-9		SG2	1	1						
SNP5-3	HK5	SG4		1	1					1
SNPO12-2		SG4	1	1						1
SNPO12-3	HK6	SG6	1	1					1	
SNPO12-8		SG2	1	1					1	

3.5 Summary

(1) Negative trigons form at higher temperature (1150 ºC) and fO_2 ($\log fO_2$ = -9) at atmospheric pressure. Positive trigons form when T ≤ 1050 ºC and $\log fO_2 \leq -10$.

(2) The size of positive trigons increases as the difference between fO_2 and CCO buffer increases (when fO_2 > CCO).

(3) The morphologies of positive trigons are various when size is small (< 5 μm), and become similar when size reaches > 10 μm.

(4) All the Snap Lake diamonds show positive trigons. The development of positive trigons overprints the pre-existing negative trigons.

(5) Positive trigons are generally smaller on diamonds from HKP than those on diamonds form HKM. The size of positive trigons decreases from fresh facies to altered facies.

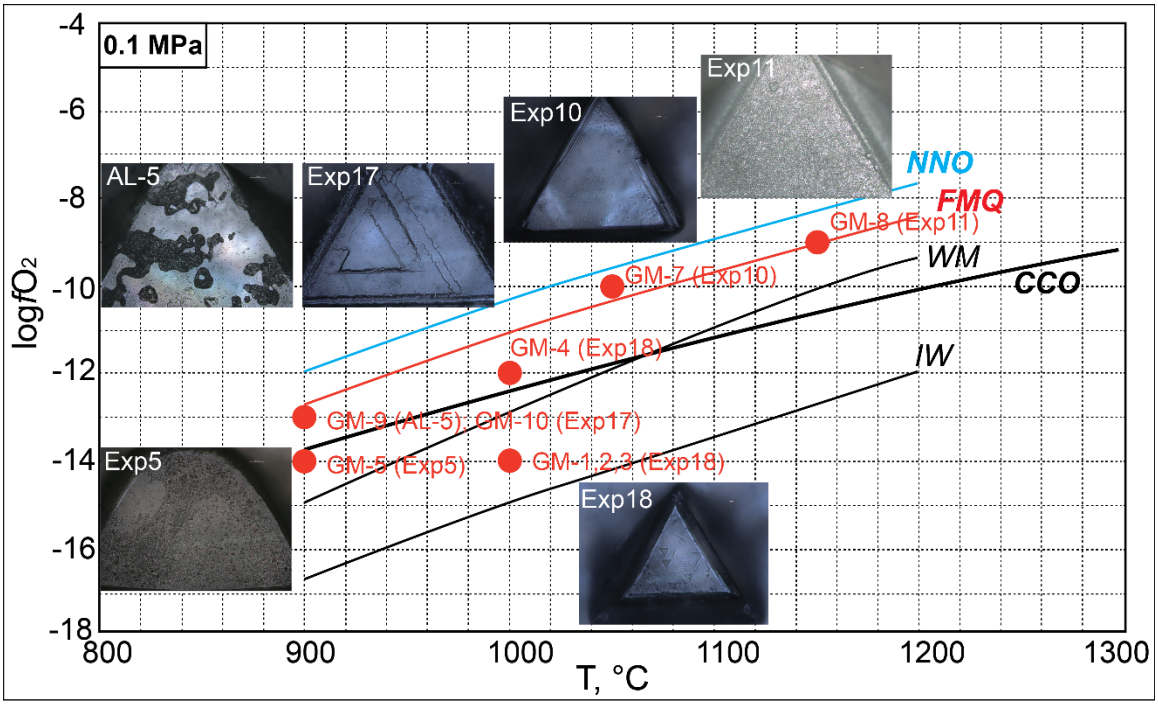

Figure 3.1 Plot showing the fO_2 and temperature applied to each diamond in oxidiation experiments done by Yana Fedortchouk, compared to NNO, FMQ, WM and IW buffers by Frost (1991) and CCO buffer by Frost and Wood (1997). Run GM-1, 2, 3 on Exp18 did not produce significant resorption.

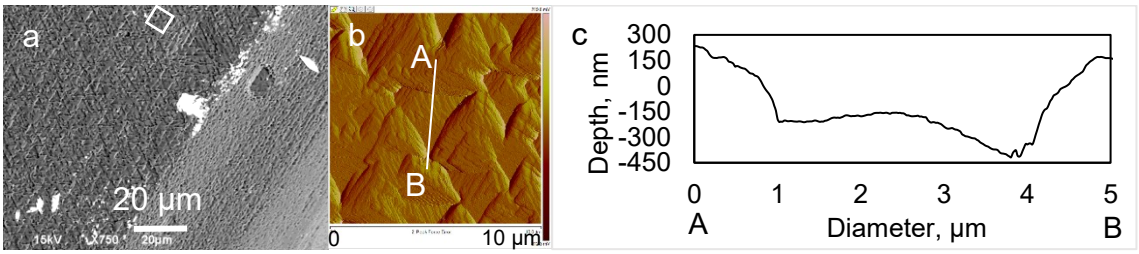

Figure 3.2 (a) SEM image of diamond Exp11. (b) AFM image of the area marked in (a). (c) The profile of the negative trigon marked in (b) along line A-B.

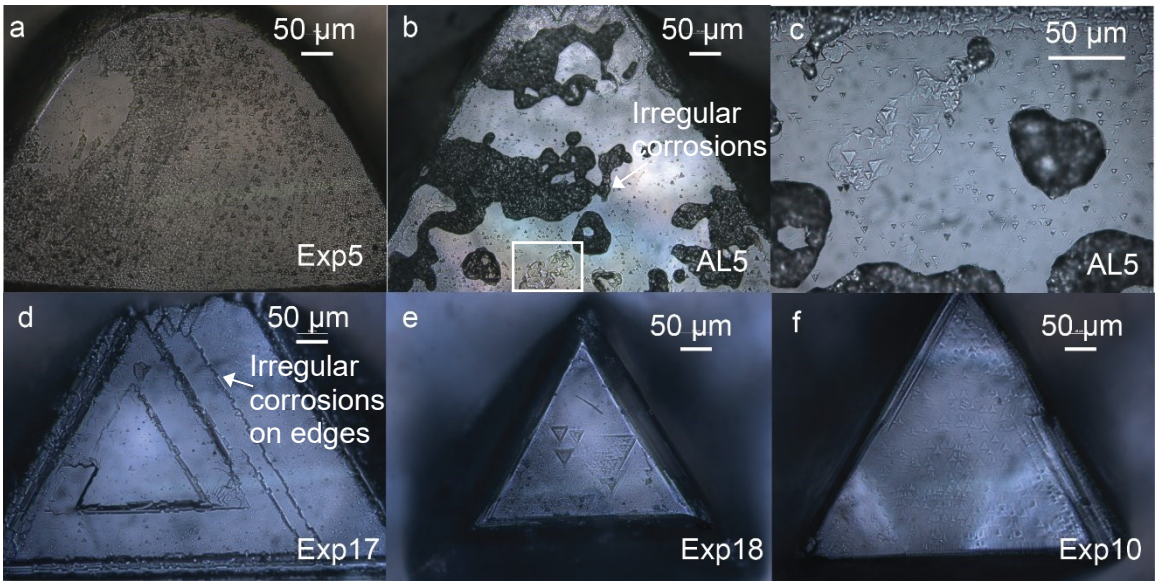

Figure 3.3 Optical images of the experimental diamonds Exp5 and Exp17 after experiments. Image (c) is the magnification of corrosion features marked in (b) in the rectangle.

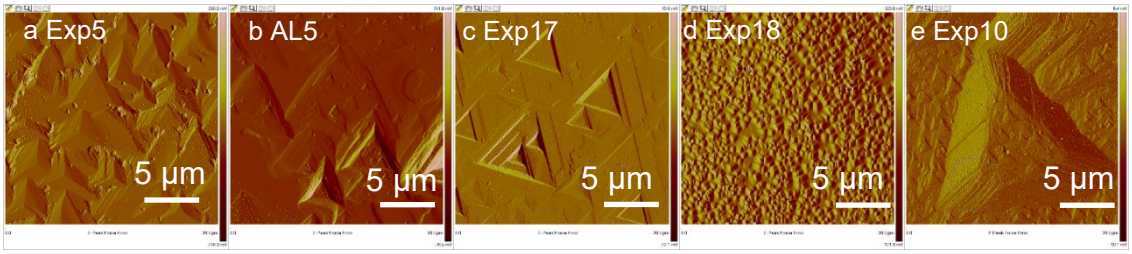

Figure 3.4 AFM images showing variation in density of positive trigon distribution on diamonds Exp5, Exp10, Exp18, Exp17 and AL5. All the images are captured from areas of 20×20 μm^2 in size. Note that positive trigons more densely distributed on diamonds Exp5, Exp10 and Exp18, compared to Exp17 and AL5.

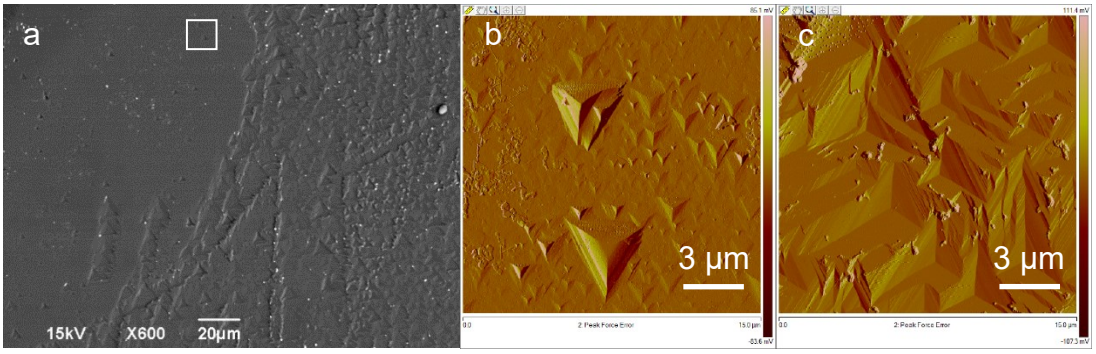

Figure 3.5 (a) SEM image of diamond Exp5. (b, c) AFM images captured from different areas (15 × 15 μm^2 in size) on diamond Exp5 showing trigon with different morphologies. The area where image (b) was captured is marked in (a) and shows small trigons of simple forms and several large trigons with zig-zag outlines. Image (c) was captured in the area where the trigons are densely attached to each other and shows trigons with zig-zag outlines only.

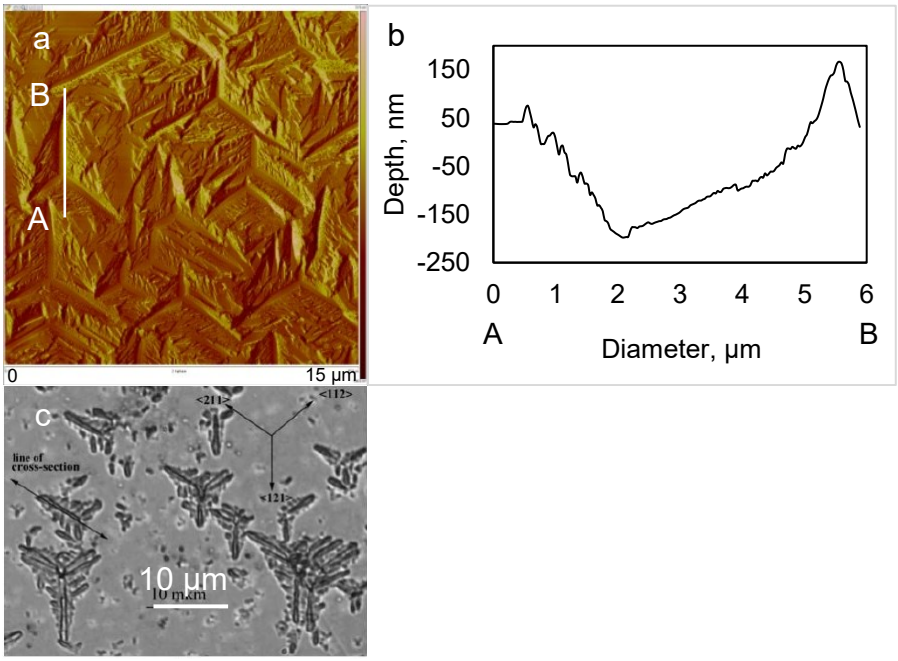

Figure 3.6 (a) Dendritic depressions on diamond Exp5. (b) Cross-section profile of the depression along line A-B marked in (a). (c) Graphitization after annealing diamond at 1680 ºC by Khmelnitsky and Gippius (2014).

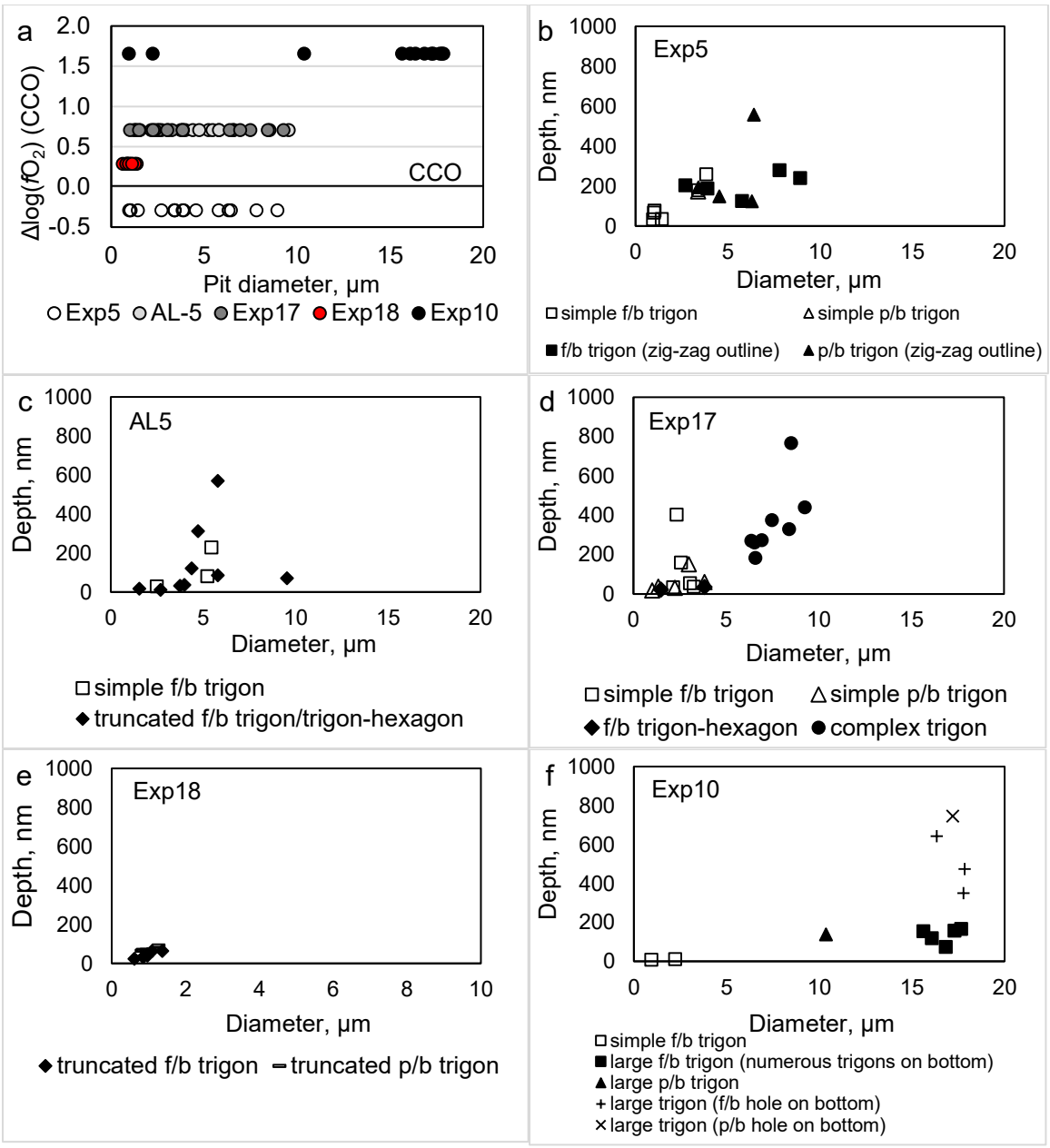

Figure 3.7 (a) The diameter of measured positive trigons on each diamond vs. $\Delta\log(fO_2)$ compared to the CCO buffer calculated using the equation of Frost and Wood (1997). Images (b-f) show the relationship between diameter and depth of the measured trigons on each diamond.

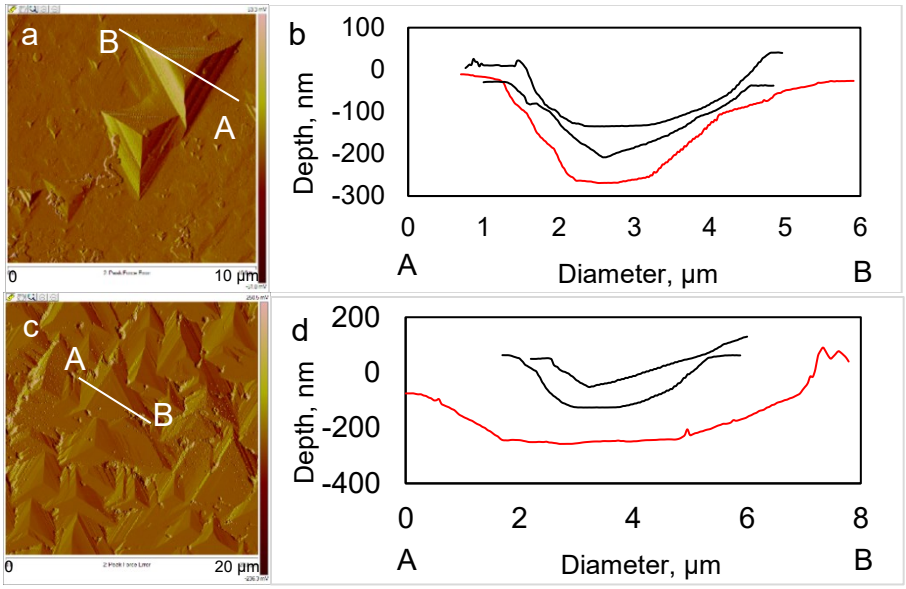

Figure 3.8 (a) One simple trigon (U type wall) on diamond Exp5 and its cross-section profile in (b) (red line). Profiles (black lines) of one simple p/b (U type wall), one simple f/b trigon (U type wall) are also illustrated in (b). (c) One trigon with zig-zag outline (Y type wall) on diamond Exp5 and its cross-section profile in (d) (red line). Profiles (black lines) of other p/b (U type wall) and f/b trigons (U type wall) with zig-zag outlines and different wall types are also illustrated in (d).

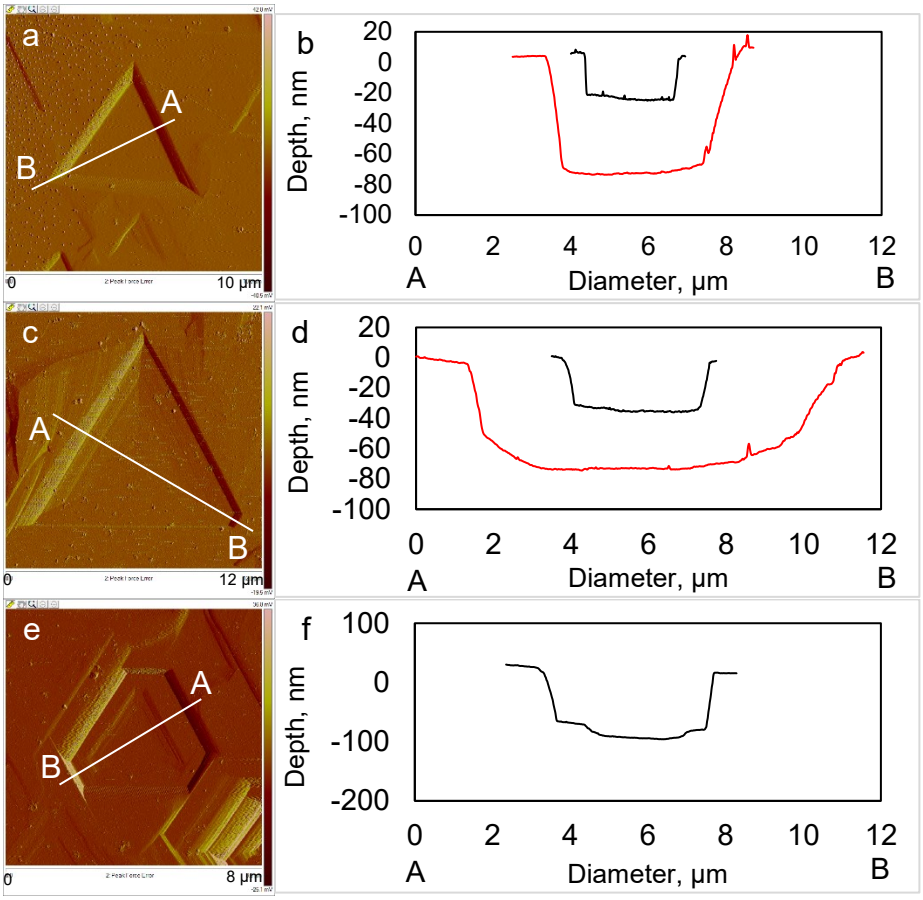

Figure 3.9 (a) One simple trigon (Y type wall) on diamond AL5 and its cross-section profile in (b) (red line). Profile (black lines) of a simple f/b trigon is also illustrated in (b) (black line). (c) One truncated trigon (U type wall) on diamond AL5 and its cross-section profile in (d) (red line). Profiles (black lines) of one smaller f/b truncated trigon (Y type wall) are also shown in (d). (e) One trigon-hexagon (Y type wall) on diamond AL5 and its profile in (f).

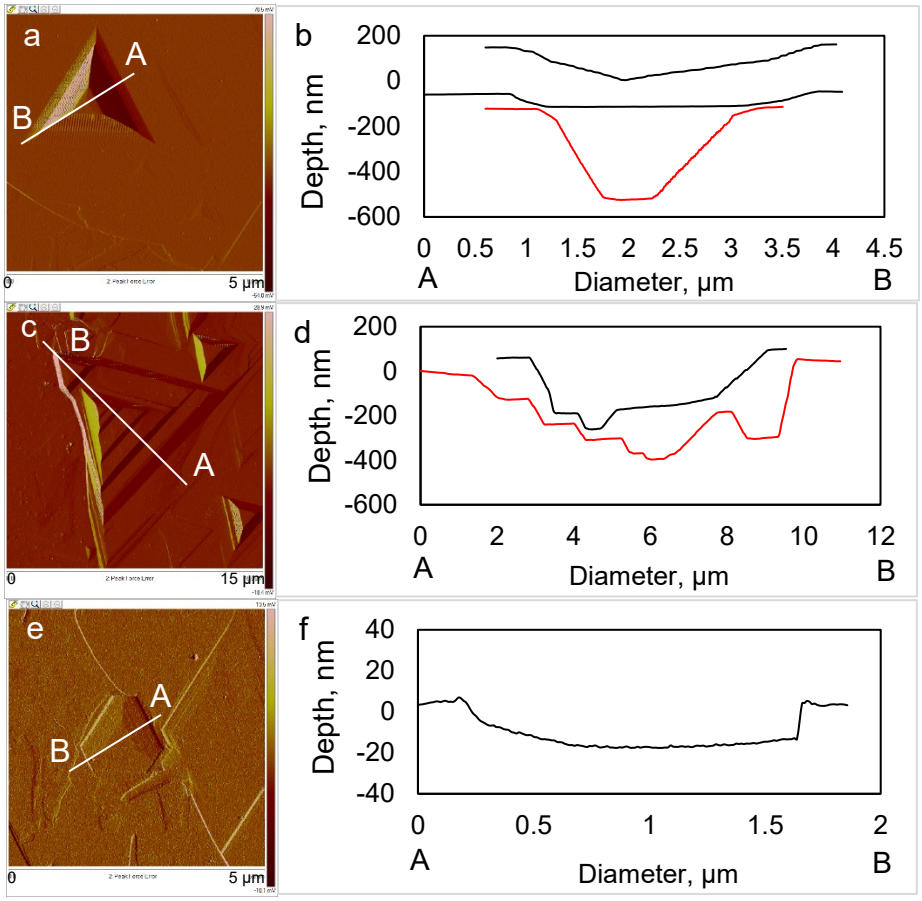

Figure 3.10 (a) One simple f/b trigon (Y type wall) on diamond Exp17 and its cross-section profile in (b) (red line). Profiles (black lines) of other simple p/b (U type wall) and f/b (U type wall) trigons with different wall types are also illustrated in (b). (c) One complex trigon (V type wall) on diamond Exp17 and its cross-section profile in (d) (red line). Profile of another complex trigon (Y type wall) is also shown in d (black line). (e) One trigon-hexagon (U type wall) on diamond Exp17 and its cross-section profile in (f).

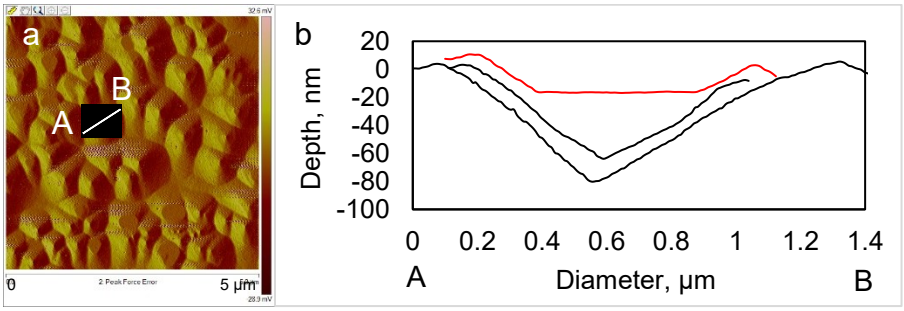

Figure 3.11 One f/b truncated trigon on diamond Exp18 (a) and its cross-section profile in (b) (red line). Profiles (black lines) of two p/b truncated trigons are also illustrated in (b).

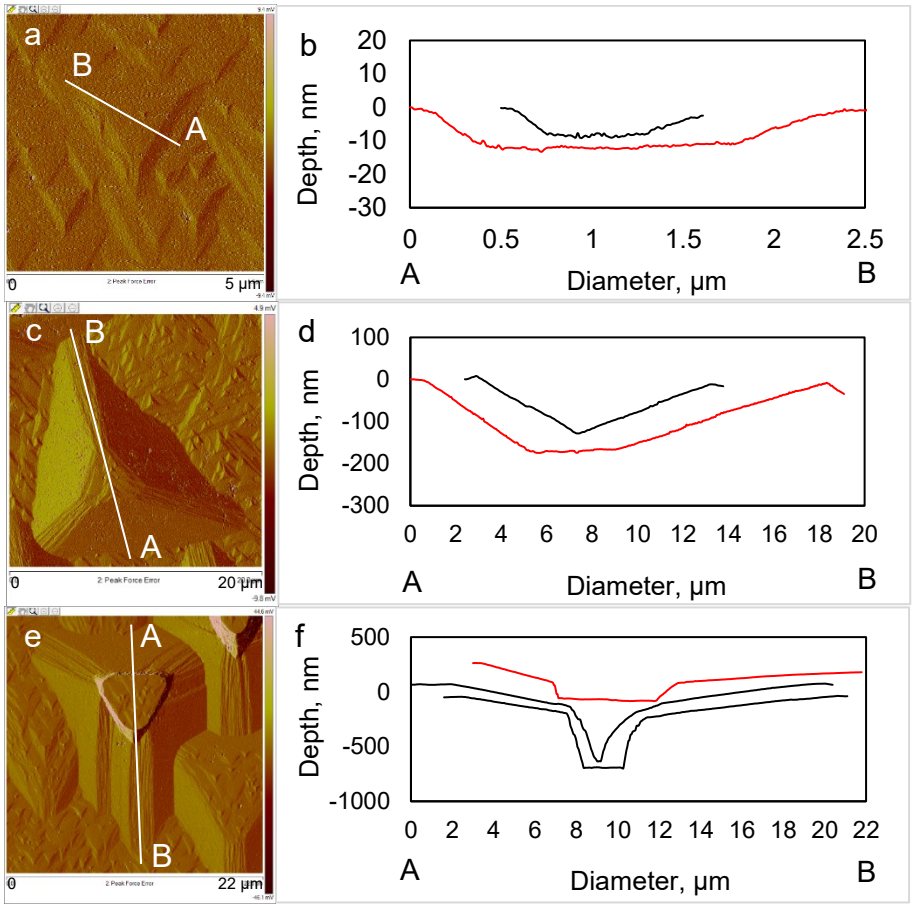

Figure 3.12 (a) One simple trigon (V type wall) on diamond Exp10 and its cross-section profile in (b) (red line). Profile of a smaller simple f/b trigon (V type wall) is also illustrated in (b). (c) One large f/b trigon (V type wall) on diamond Exp10 and its cross-section profile in (d) (red line). Profile of a large p/b trigon (V type wall) is also shown in (d) (black line). (e) One large f/b trigon (Y type wall) with a hole on diamond Exp10 and its profile in (f) (red line), profiles of large f/b and p/b trigons (Y type wall) of similar size are also shown in (f) (black line).

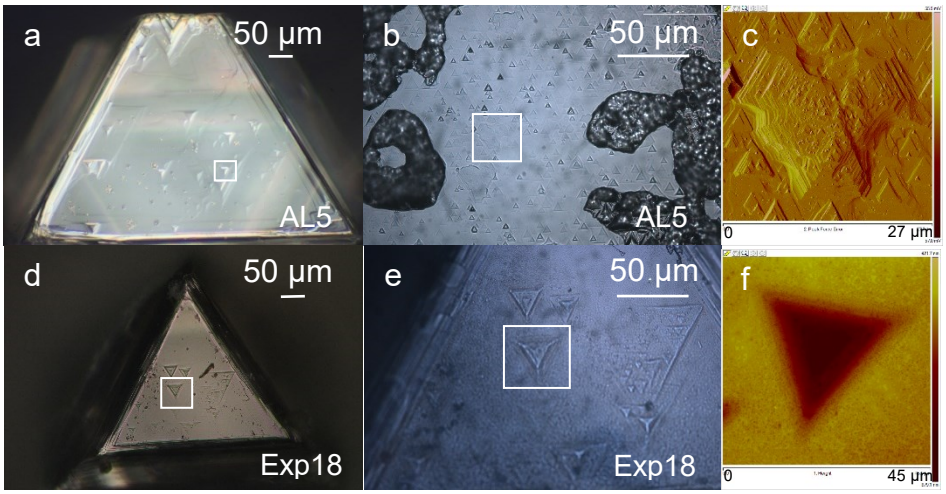

Figure 3.13 Optical images of diamonds AL5 and Exp18 before experiments (a and d) and after experiments (b and e). The negative trigons (marked by squares in a and d) developed truncated corners (marked by squares in b and e) and are shown in the AFM images (c and f).

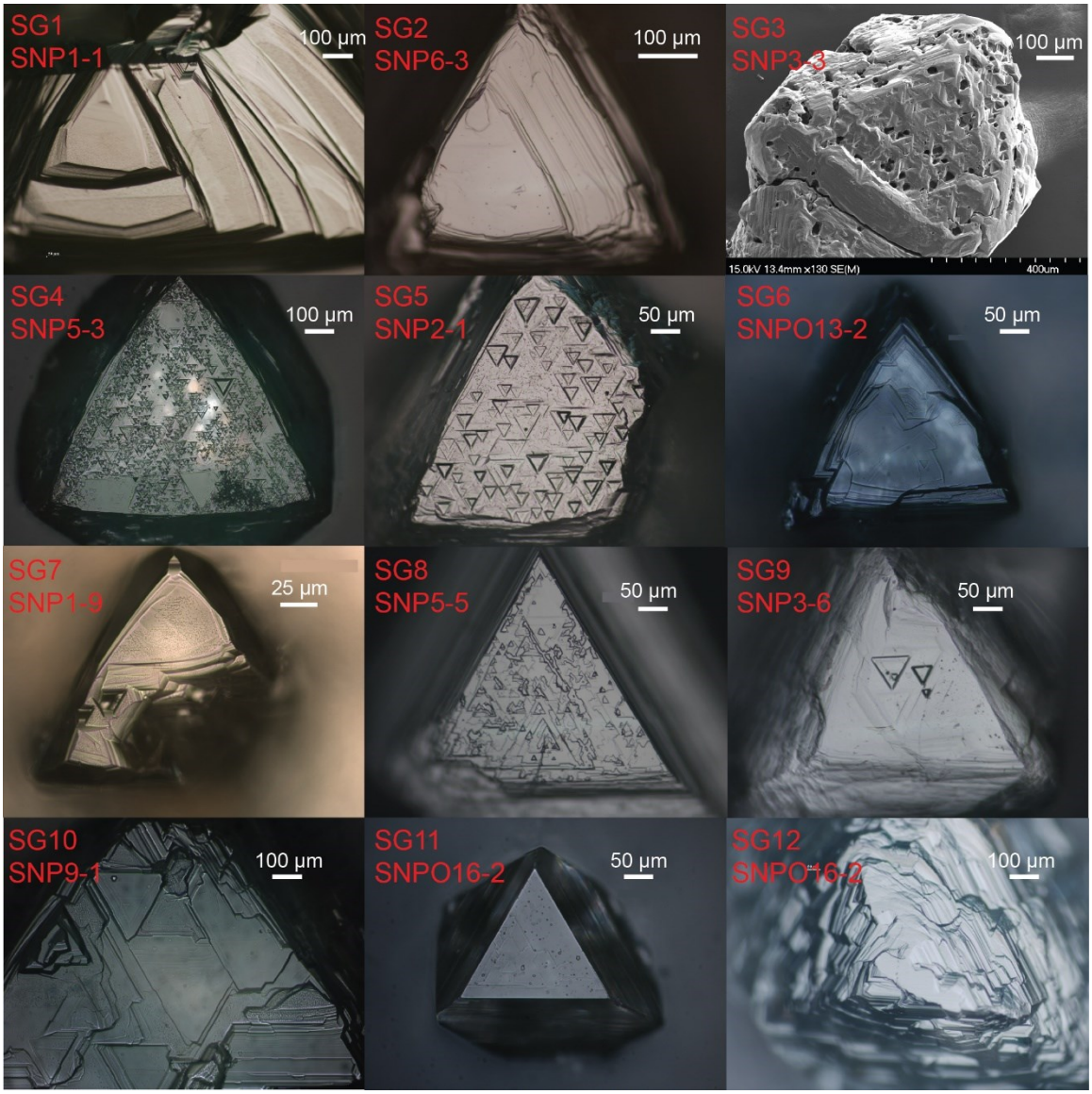

Figure 3.14 Illustration of {111} faces of Snap Lake diamonds assigned to morphological groups SG1-SG12 with ditrigonal or trigonal {111} faces and various features on {111}. See Chapter 4.3.1 for the detailed description of each group.

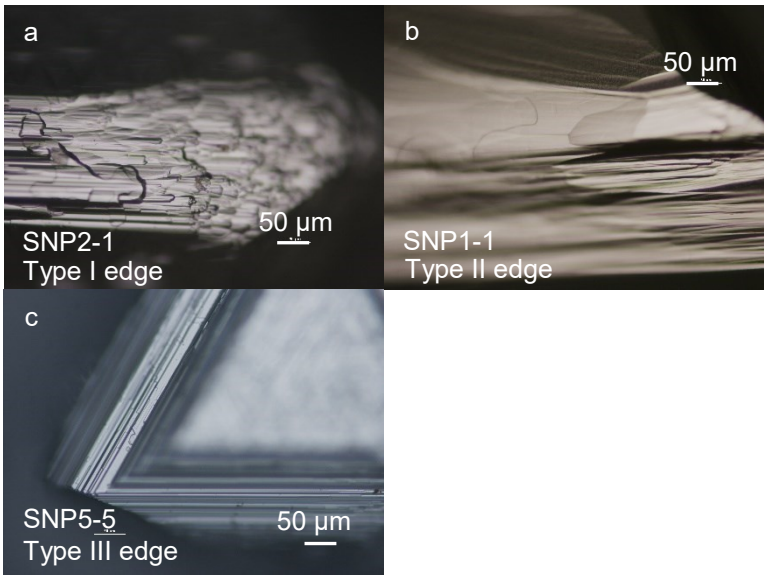

Figure 3.15 Illustration of Type I-III edges on Snap Lake diamonds. (a) Type I edge with deep cavities and sharp corners. (b) Smooth Type II edge with shallow depressions. (c) Type III edge with parallel striations.

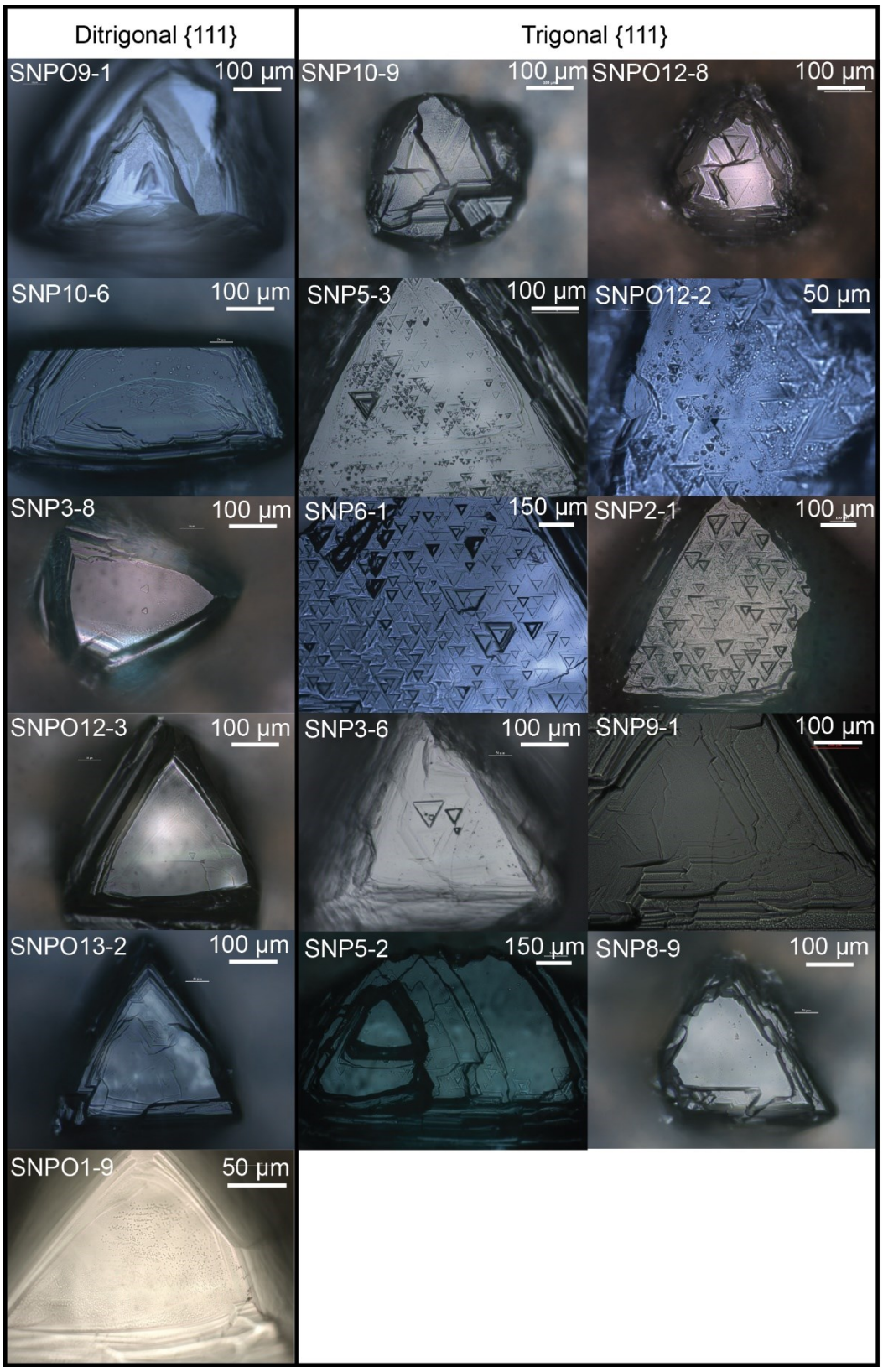

Figure 3.16 Optical images of the 16 Snap Lake diamonds selected for AFM study.

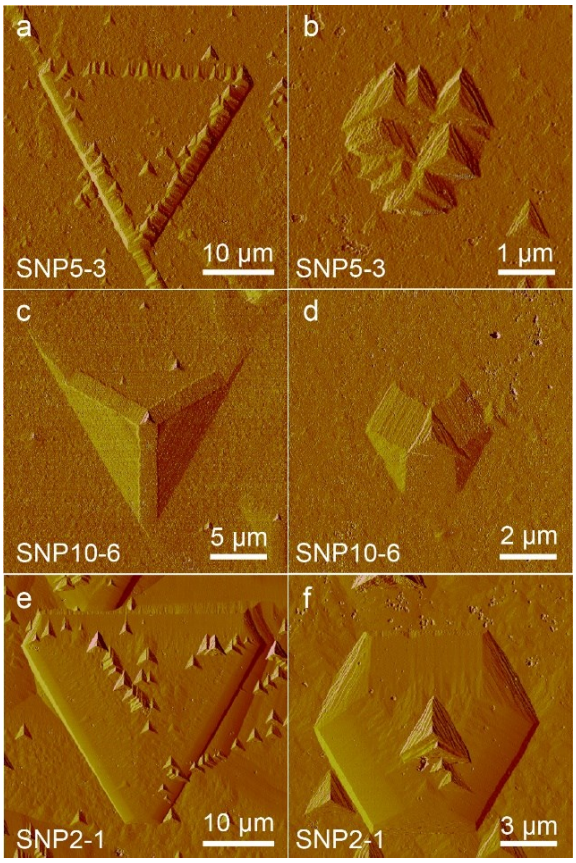

Figure 3.17 Development of truncated corners on negative trigons on Snap Lake diamonds (a, c, e), some pits become trigon-hexagons (b) or hexagons (d, f).

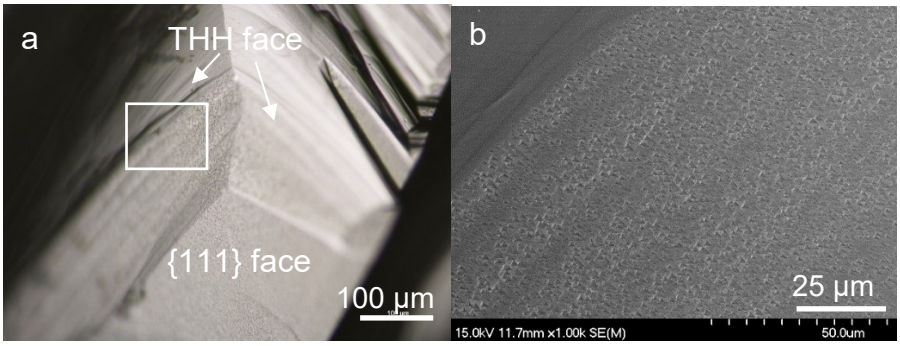

Figure 3.18 Illustration of positive trigons developed on {111} faces and on edges (THH faces) on Snap Lake diamond SNP1-1. Image (b) is the SEM picture of the area highlighted in (a).

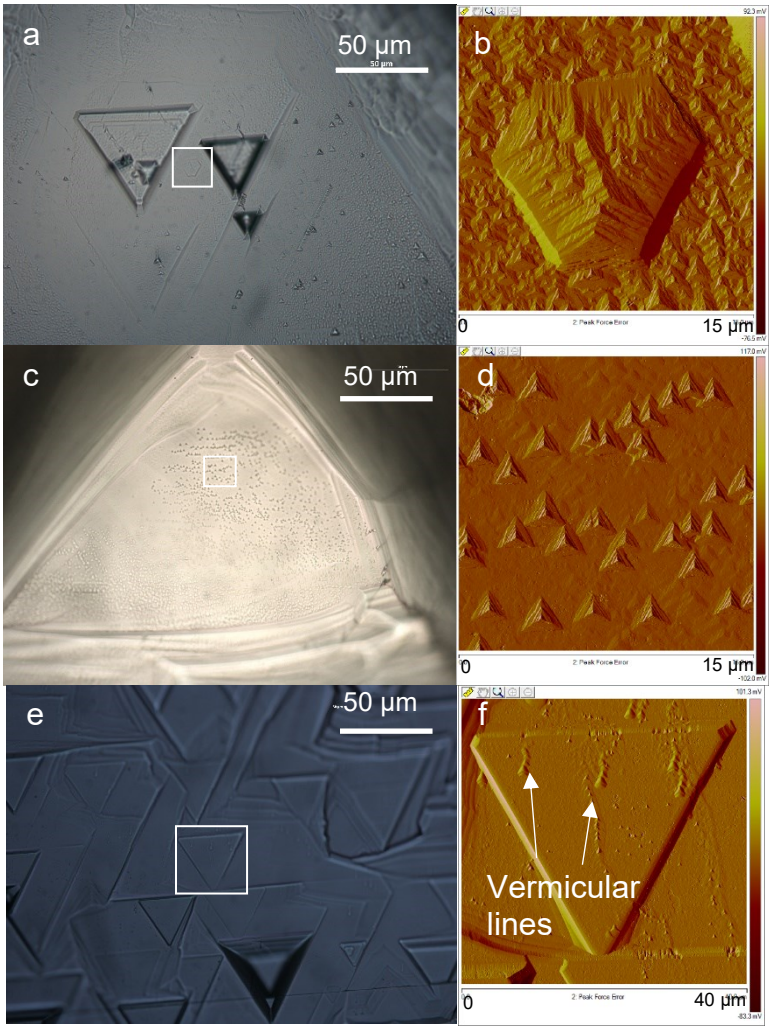

Figure 3.19 Positive trigons showing uniform distribution (a) and patchy distribution with sub-parallel linear features (c) and vermicular lines (f). Images (b) (d) and (f) show the areas highlited in (a) (c) and (e), respectively. Note that the trigons forming the linear features in (d) and (f) are surrounded by smaller and shallower trigons.

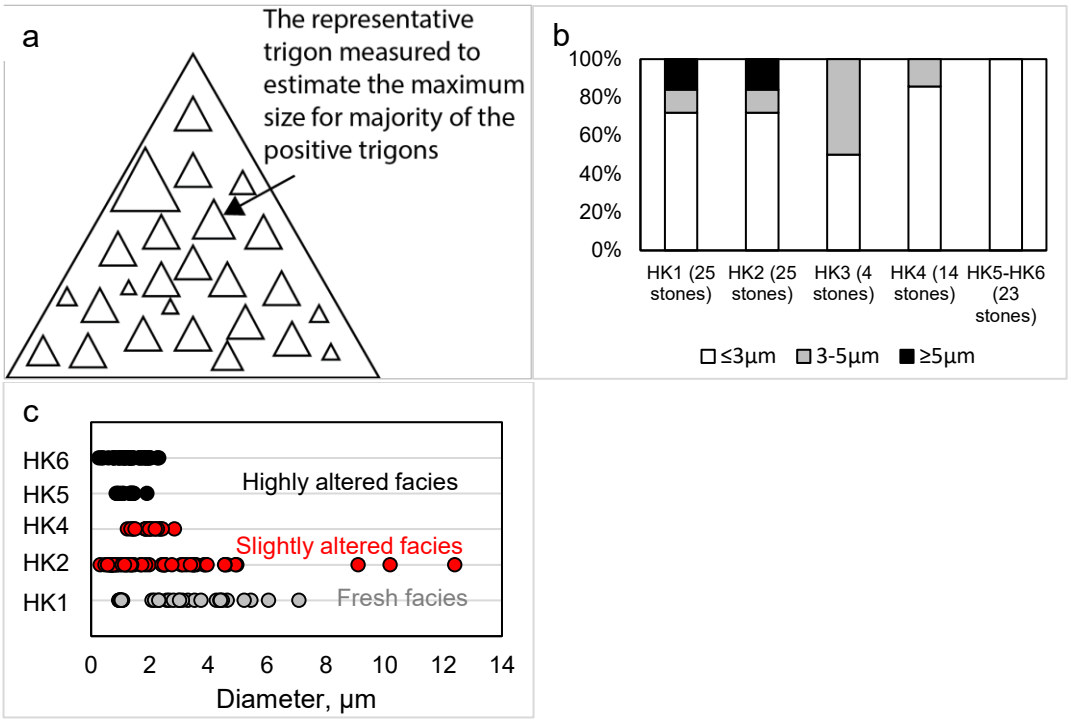

Figure 3.20 (a) Representative trigon measured on a hypothetical {111} face to estimate the maximum size for majority of the positive trigons. (b) Percentage of diamonds with maximum positive trigon size of ≤ 3 µm, 3-5 µm, ≥ 5 µm in each facies. (c) The diameter range of positive trigons measured by AFM on Snap Lake diamonds from each facies.

.

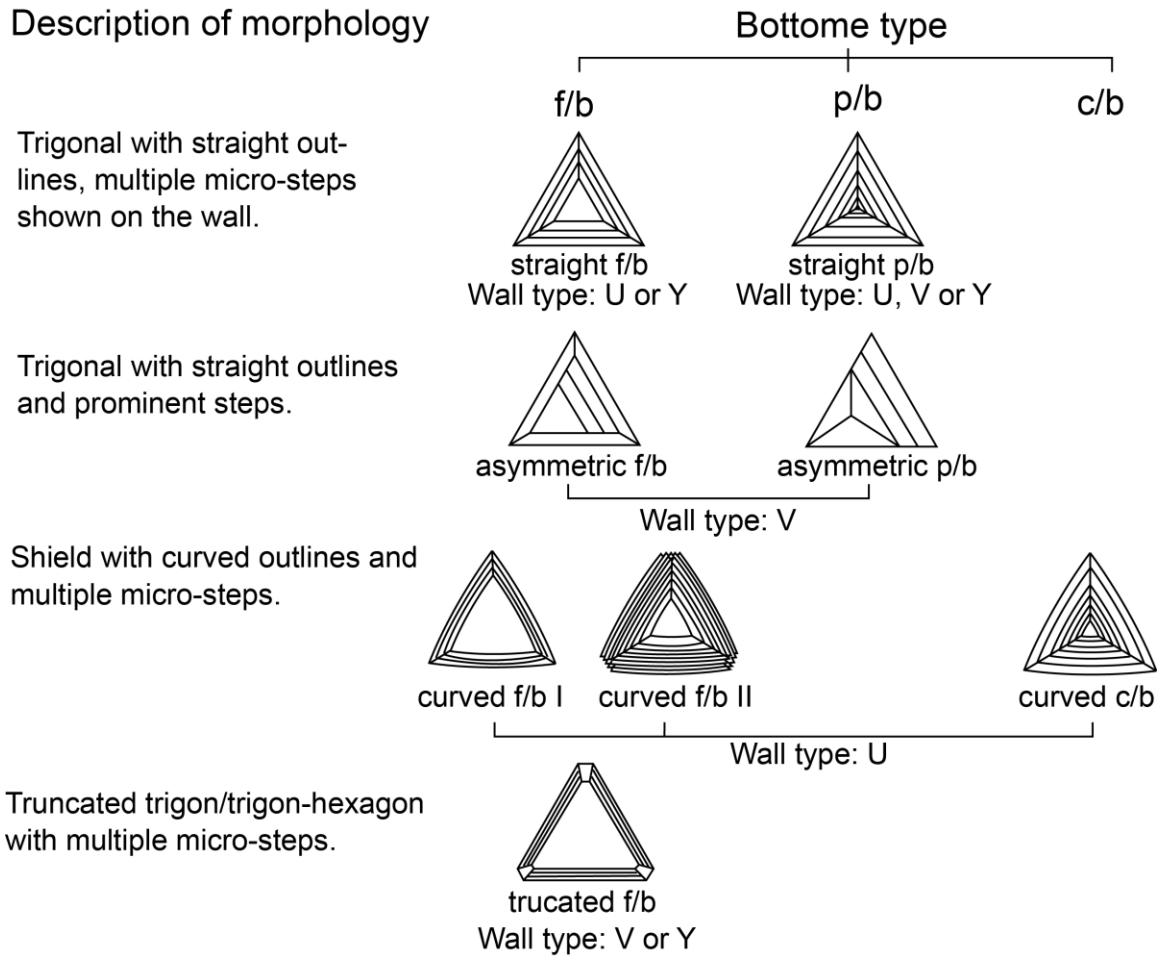

Figure 3.21 Sketch of different types of positive trigons on Snap Lake diamonds.

.

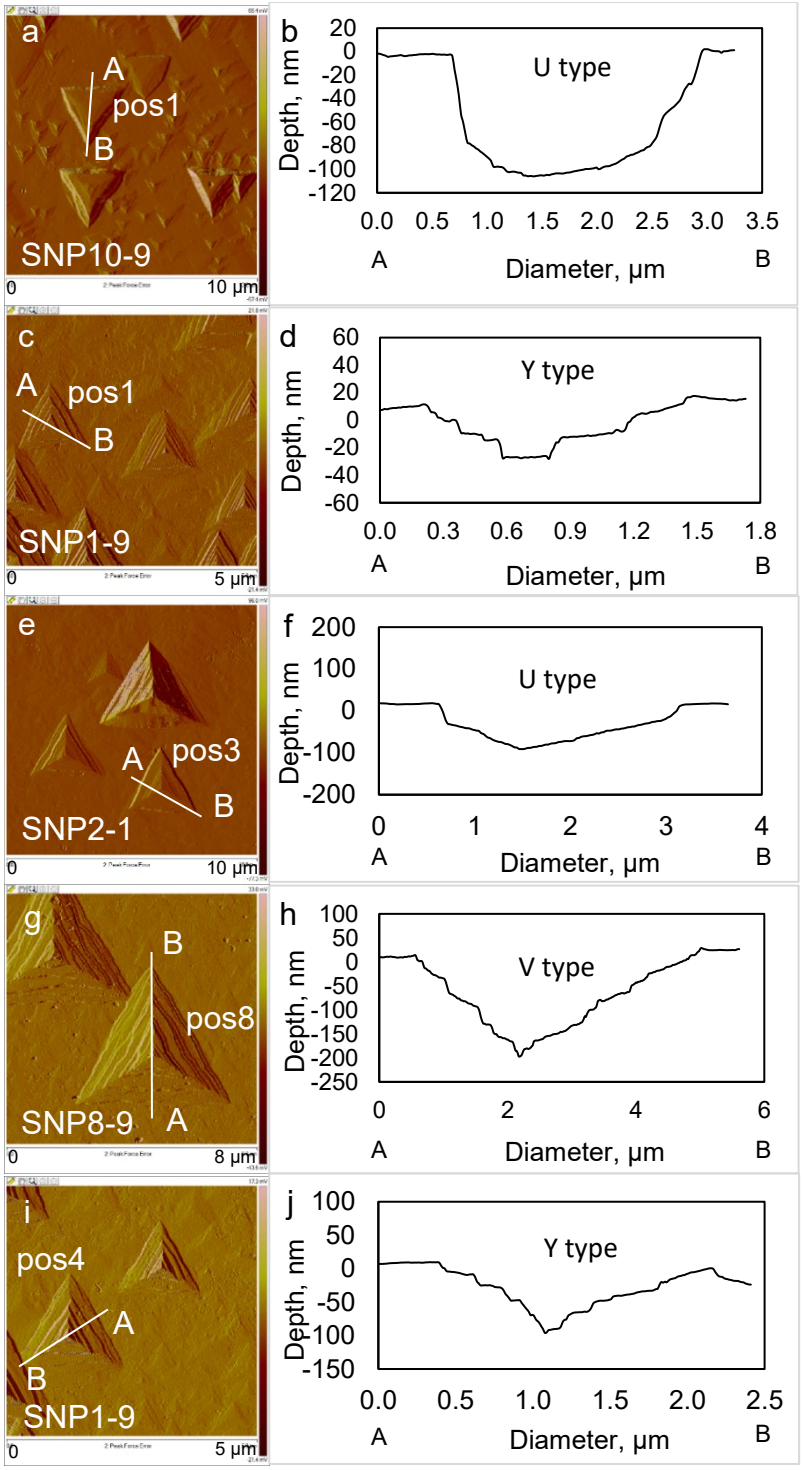

Figure 3.22 AFM images and cross-section profiles showing straight f/b trigons with U type wall (pos1 on SNP10-9) (a, b), Y type wall (pos1 on SNP1-9) (c, d), straight p/b trigons with U type wall (pos3 on SNP2-1) (e, f), V type wall (pos8 on SNP8-9) (g, h), and Y type wall (pos4 on SNP1-9) (i, j).

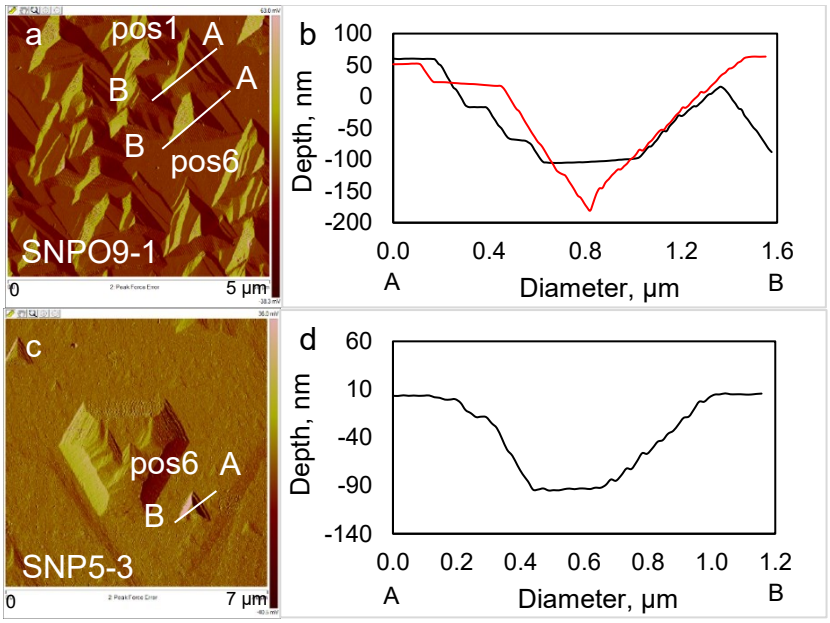

Figure 3.23 AFM images and cross-section profiles showing one asymmetric f/b trigon (pos1 on SNPO9-1 in (a), profile is shown with black line in (b)), one asymmetric p/b trigon (pos6 on SNPO9-1 in (a), profile is shown with red line in (b)), one asymmetric f/b trigon (pos6 on SNP5-3 in (c) and its profile in (d)). All the three trigons have V type walls.

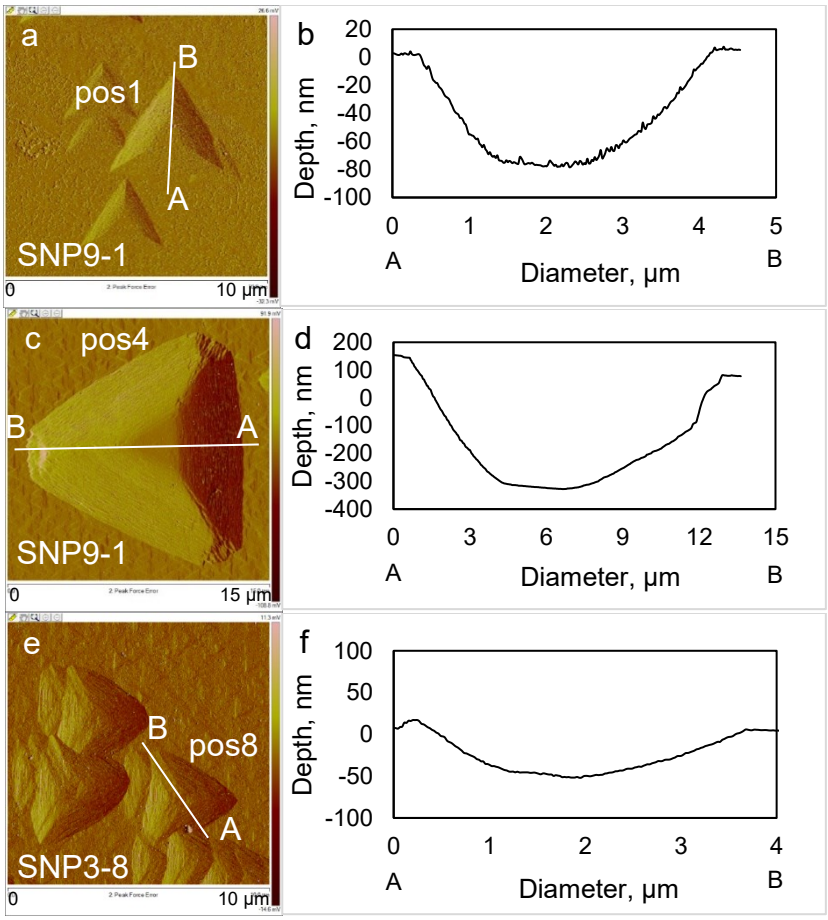

Figure 3.24 AFM images and cross-section profiles showing one trigon of curved f/b I type (pos1 on SNP9-1) (a, b), one trigon of curved f/b II type (pos4 on SNP9-1) (c, d) and curved sided c/b type (pos8 on SNP3-8) (e, f). All the three trigons have U type walls.

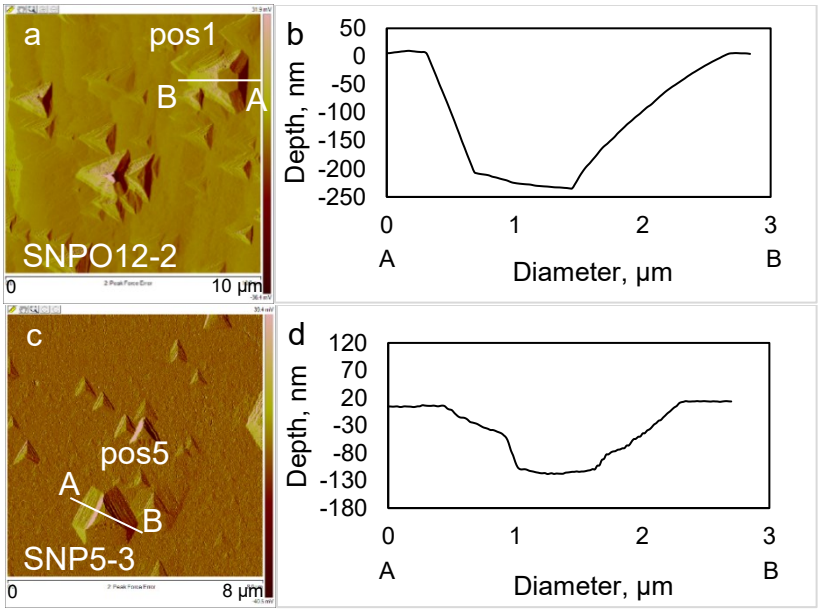

Figure 3.25 AFM images and cross-section profiles showing one truncated trigon with V type wall (pos1 on SNPO12-2) (a, b) and one trigon-hexagon with Y type wall (pos5 on SNP5-3) (c, d).

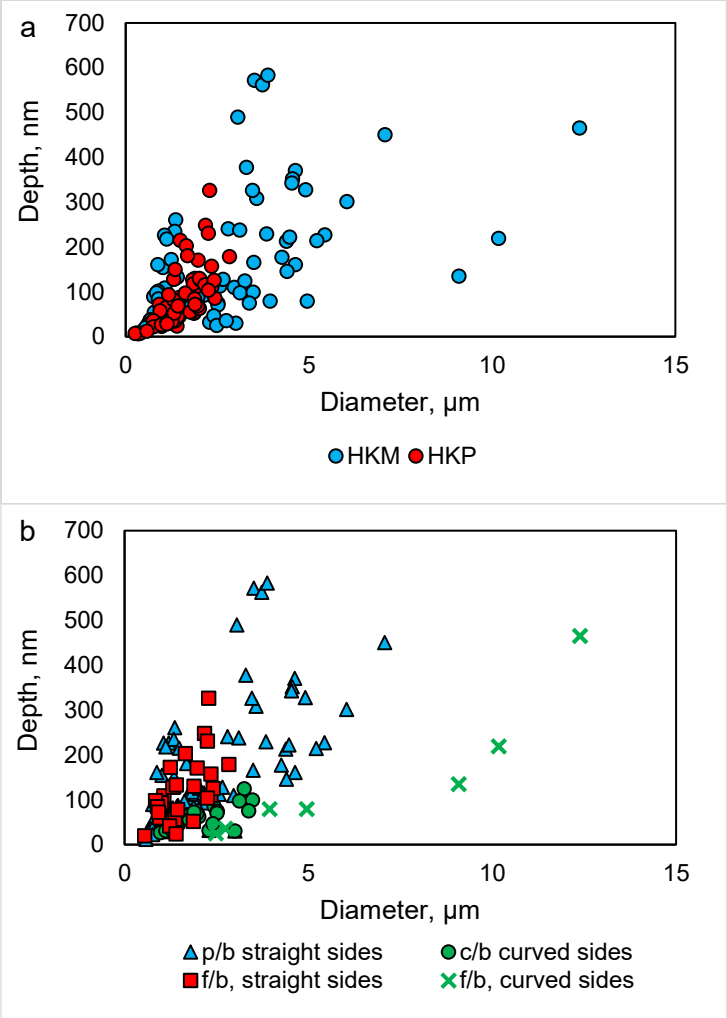

Figure 3.26 (a) Diameter vs. depth relationship of all measured positive trigons on diamonds from lithofacies HKM and HKP. (b) Bottom type and shape of side of trigons shown in (a).

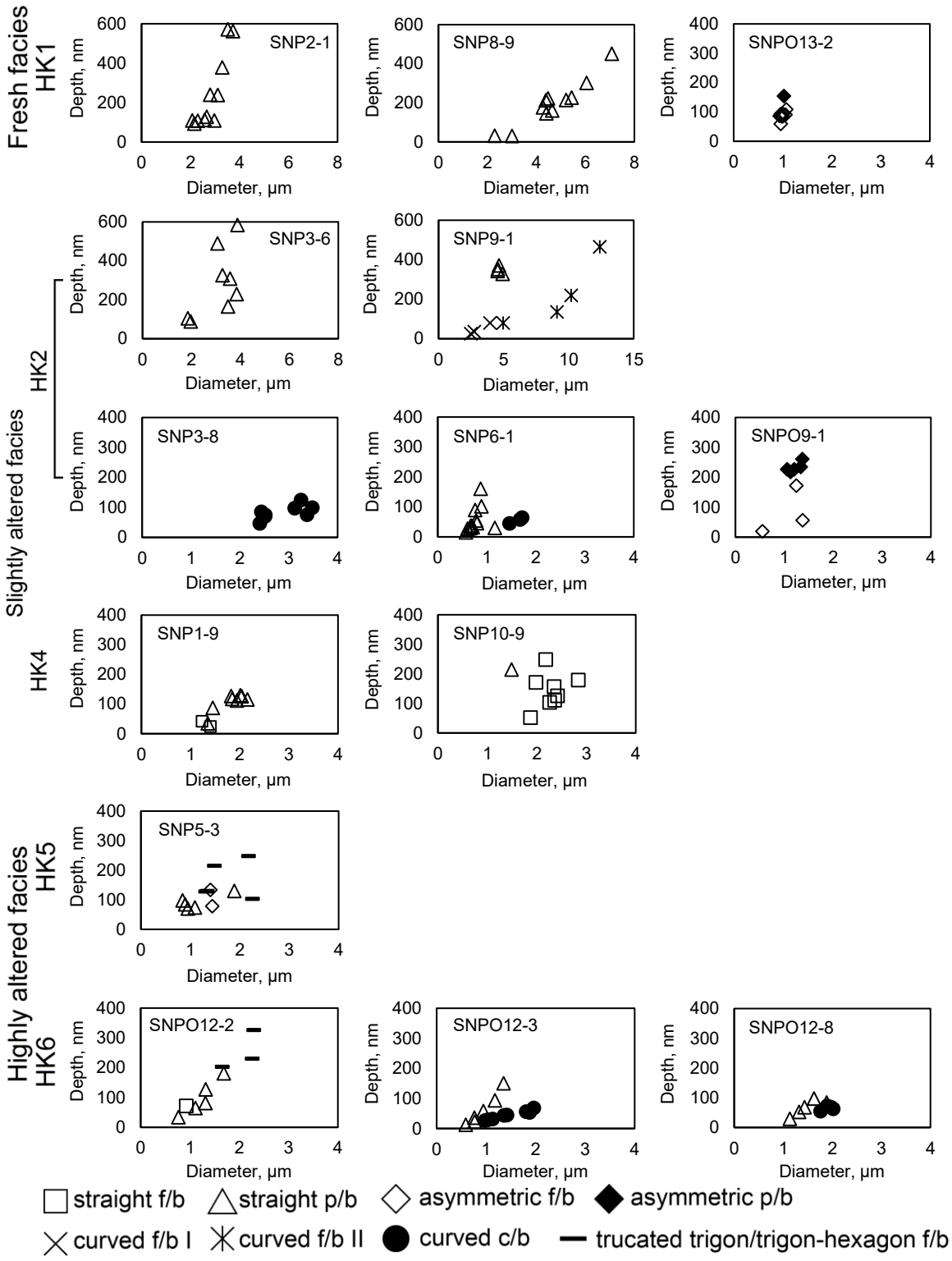

Figure 3.27 Diameter vs. depth relationship of positive trigons on each Snap Lake diamond studied by AFM.

CHAPTER 4. NEGATIVE TRIGONS ON DIAMONDS FROM SNAP LAKE AND EKATI KIMBERLITES

4.1 Introduction

The diameter vs. depth relationship for negative trigons is characteristic of the composition of kimberlitic fluid (Fedortchouk 2015). In this chapter, I present detailed AFM data of negative trigons on Snap Lake diamonds showing the diameter vs. depth relationship, and compare them to diamonds from four Ekati kimberlite pipes (Fox, Panda, Koala and Misery) with presumably different emplacement conditions from the Snap Lake dyke, suggested by their geological features. How the fluid composition and behavior derived from study of negative trigons affected kimberlite geology is discussed in Chapter 5.

4.2 Diamond Samples

Diamonds from Snap Lake mine were examined by an optical microscope and SEM to define the morphological groups based on resorption features on {111} faces and edges, and were examined by FTIR for N content and aggregation state. For the description of Snap Lake diamonds, see Chapter 2.2.2, and for details of examination by optical microscope, SEM, and FTIR, see Chapter 2.2.4-2.2.5. I selected 13 Snap Lake diamonds of 7 different morphological groups for measurements of negative trigons and a few hexagons by AFM (Table 3.1). For details of AFM measurements, see Chapter 2.2.6.

The diamond morphology of the Ekati parcels was studied previously (Fedortchouk et al., 2010; Zhang and Fedortchouk, 2012). Zhang and Fedortchouk (2012) identified

diamonds with kimberlite-induced and mantle-derived resorption features. For AFM measurements in this study, I selected diamonds with kimberlite-induced resorption features based on the criteria developed in Zhang and Fedortchouk (2012), which include ditrigonal {111} faces and a few shallow trigons on {111} faces (Figure 2.6). Several diamonds (P2, P3, P4 and P36 from Panda) with trigonal {111} faces were also selected, which likely represent a combination of kimberlite-induced and mantle-derived resorption. In total, 13 diamonds from four Ekati kimberlites (2 diamonds from Fox, 5 diamonds from Panda, 2 diamonds from Koala, and 4 diamonds from Misery) were measured with AFM (Appendix A: Table EA6).

4.3 Results

4.3.1 General Description and Morphological Groups of Snap Lake Diamonds

The abundance of octahedral diamonds varies from ~20-50% in the six lithofacies (HK1-HK6) of the Snap Lake kimberlite (Table 4.1, Figure 4.1a). Cubes are less common than octahedrons, composing ~20-30% of the diamonds from most facies except for HK6 (8.3%) and HK5-6 (no cubes). THH crystals comprise only a small proportion (~0-10%) of the diamonds from most facies except HK5-6 (40%). Diamonds from the phlogopite-rich facies (HKP) are more resorbed (O/THH = 1, 3.7 and 11 in HK3, HK4 and HK6 respectively) compared with the main phlogopite-poor coherent facies (HKM) (O/THH =11.5 and 24 in HK1 and HK2, no THH in HK5). Fragments comprise about 20-50% of the diamonds in each subfacies.

Most diamonds are colorless (white) (~50-70% in all facies), with ~0-30% yellow diamonds, ~0-15% brown diamonds, ~0-10% grey diamonds (except for HK5 with 20%

grey diamonds), and ~0-4% black diamonds (except for HK3 with 20% black diamonds) (Table 4.1, Figure 4.1b).

The various types of surface dissolution features on octahedral and THH diamonds from Snap Lake kimberlite are given in Table 3.2. The main resorption forms are etch pits (negative and positive trigons, hexagons) and cavities. They show similar distribution patterns on diamonds from all lithofacies and positive trigons are present on all studied diamonds (See Chapter 3). Step faces, shield-shaped, and serrate laminae are also common on octahedrons from HK1-HK6. Elongated hillocks are more common than pyramidal hillocks on diamonds from all the facies. Striations are present on all diamonds. Frosting and square pits are more prevalent on diamonds from HKP (HK3, HK4 and HK6) than those from HKM (HK1, HK2, HK5), while circular pits show similar distribution patterns on diamonds from HKP (HK3, HK4 and HK6) and HKM (HK1, HK2, HK5).

Table 4.1 Summary of diamond morphology and color from Snap Lake kimberlite

	# of stones						
	Fresh facies		**Slightly altered facies**		**Highly altered facies**		
Morphology	HK1 (77 stones)	HK3 (20 stones)	HK2 (83 stones)	HK4 (27 stones)	HK5 (10 stones)	HK6 (24 stones)	HK5-6 (10 stones)
Octahedron	23 (29.9%)	2 (10.0%)	24 (28.9%)	11 (40.7%)	5 (50.0%)	11 (45.8%)	2 (20.0%)
THH	2 (2.6%)	2 (10.0%)	1 (1.2%)	3 (11.1%)	0	1 (4.2%)	4 (40.0%)
Cubes	14 (18.2%)	5 (25.0%)	16 (19.3%)	8 (29.6%)	2 (20.0%)	2 (8.3%)	0
Fragments	38 (49.4%)	11 (55.0%)	42 (50.6%)	5 (18.5%)	3 (30%)	10 (41.7%)	4 (40.0%)
O/THH	11.5	1	24	3.7	-	11	0.5
Colour							
White	38 (49.4%)	12 (60.0%)	47 (56.6%)	15 (55.6%)	7 (70.0%)	16 (66.7%)	9 (90.0%)
Yellow	25 (32.5%)	2 (10.0%)	21 (25.3%)	9 (33.3%)	0	6 (25.0%)	0
Brown	12 (15.6%)	0	13 (15.7%)	1 (3.7%)	1 (10.0%)	2 (8.3%)	1 (10.0%)
Grey	2 (2.6%)	2 (10.0%)	2 (2.4%)	1 (3.7%)	2 (20.0%)	0	0
Black	0	4 (20.0%)	0	1 (3.7%)	0	0	0

Table 4.2 Summary of surface features on Snap Lake diamonds. HK5-6 is the highly altered facies which cannot be assigned to HK5 or HK6 with certainty.

	Octahedron									THH								
Lithofacies	HK1	HK2	HK5	Total	HK3	HK4	HK6	Total	HK5-6	HK1	HK2	HK5	Total	HK3	HK4	HK6	Total	HK5-6
Surface features																		
Negative trigons	19	19	2	40	2	8	9	19	1	0	1	-	1	1	1	0	2	2
	83%	79%	40%	77%	100%	73%	82%	79%	33%	0%	100%	-	33%	50%	33%	0%	33%	67%
Hexagons/trigon-hexagons	13	18	1	32	1	8	7	16	1	0	0	-	0	1	2	0	3	3
	57%	75%	20%	62%	50%	73%	64%	67%	33%	0%	0%	-	0%	50%	67%	0%	50%	100%
Positive trigons	23	24	5	52	2	11	11	24	3	2	1	-	3	2	3	1	6	3
	100%	100%	100%	100%	100%	100%	100%	100%	100%	100%	100%	-	100%	100%	100%	100%	100%	100%
Step faces	8	7	0	16	1	3	3	7	2	0	0	-	0	0	0	0	0	0
	35%	29.2%	0%	31%	50%	27%	27%	29%	67%	0%	0%	-	0%	0%	0%	0%	0%	0%
Shield-shaped laminae	7	11	2	20	1	8	7	16	0	0	0	-	0	0	0	0	0	0
	30%	46%	40%	39%	50%	73%	64%	67%	0%	0%	0%	-	0%	0%	0%	0%	0%	0%
Serrate laminae	0	0	3	3	0	0	0	0	0	0	0	-	0	0	0	0	0	0
	0%	0%	60%	6%	0%	0%	0%	0%	0%	0%	0%	-	0%	0%	0%	0%	0%	0%
Cavities	8	15	1	24	0	6	6	12	3	1	1	-	2	1	2	0	3	3
	35%	63%	20%	46%	0%	55%	55%	50%	100%	50%	100%	-	67%	50%	67%	0%	50%	100%
Pyramidal hillocks	5	1	0	6	0	2	4	6	1	1	0	-	1	1	1	0	2	3
	22%	4%	0%	12%	0%	18%	36%	25%	33%	50%	0%	-	33%	50%	33%	0%	33%	100%
Elongated hillocks	12	15	1	28	0	9	7	16	3	0	1	-	1	1	2	0	3	3
	52%	63%	20%	54%	0%	82%	64%	67%	100%	0%	100%	-	33%	50%	67%	0%	50%	100%
Striations	23	24	5	52	2	11	11	24	3	2	1	-	3	2	3	1	6	3
	100%	100%	100%	100%	100%	100%	100%	100%	100%	100%	100%	-	100%	100%	100%	100%	100%	100%
Ruts	1	3	0	4	0	1	0	1	0	0	0	-	0	1	0	0	1	0
	4%	13%	0%	8%	0%	9%	0%	4%	0%	0%	0%	-	0%	50%	0%	0%	17%	0%
Frosting	3	2	0	5	1	3	4	8	3	1	0	-	1	2	2	0	4	0
	13%	8%	0%	10%	50%	27%	36%	33%	100%	50%	0%	-	33%	100%	67%	0%	67%	0%
Circular pits	4	4	0	8	0	2	2	4	0	0	1	-	1	1	0	0	1	2
	17%	17%	0%	15%	0%	18%	18%	17%	0%	0%	100%	-	33%	50%	0%	0%	17%	67%
Square pits	4	5	0	9	0	4	3	7	0	0	1	-	1	2	0	0	2	3
	17%	21%	0%	17%	0%	36%	27%	29%	0%	0%	100%	-	33%	100%	0%	0%	33%	100%
Total	23	24	5	52	2	11	11	24	3	2	1	0	3	2	3	1	6	3

The Snap Lake diamonds were classified into 12 morphological groups (SG1-SG12, Figure 4.2, Table 4.3) based on the resorption features on {111} faces (Figure 4.3), with the related sub-groups based on the resorption characters of the edges, as summarized in Figure 4.4.

Three types of edges were identified on Snap Lake diamonds. Type I edges have striations with sharp hillocks or stepped corners (Figure 4.4a), and deep cavities with irregular outlines and striated bottoms (Figure 4.4b). Type II edges are generally smooth compared to Type I edges, occasionally with shallow depressions and circular pits (Figure 4.4c), and rounded hillocks. Type III edges show fine parallel striations (Figure 4.4d). Cavities are rare on this type of edge.

Diamonds of SG1, SG2, SG4, SG6, and SG7 show both Type I and Type II edges, subdivided into SG1a, 2a, 4a, 6a, 7a and SG1b, 2b, 4b, 6b, 7b respectively (Table 4.3). Diamonds of SG3, SG5, SG9 and SG10 show Type I edges only. Tetrahexahedral diamonds covered by Type I edges are classified as SG12. Type III edges are present on SG8 diamonds and the nearly unresorbed SG11 diamonds, and are probably the result of growth instead of resorption.

The main morphological groups (SG1, SG2, and SG6) are similar for diamonds from HK1, HK2, HK4 and HK6 (Figure 4.5). Diamonds of SG3, SG9, SG10 and SG11 groups are not present in HK4 and HK6. All the SG12 diamonds occur in the most altered facies HK5-6, but THH crystals from other facies with undefined edge types (due to fragmentation) may also belong to this group. HKM has diamonds of SG3, SG9, SG10 and SG11, which are absent from HKP. Diamonds from these groups may represent mantle induced-resorption (SG3) or growth forms (SG11), or a combination of kimberlite induced

and mantle-derived resorption (SG9, SG10). The degree of alteration does not have notable effect on the major resorption types on {111} faces. The numbers of stones with different edge types are summarized in Figure 4.6. The proportion of stones that have edges with sharp features (Type I) is generally higher in HKM (HK-1, 2) than in HKP (HK-4, 6) (Figure 4.6), while a higher proportion of stones with smooth features on edges is present in HKP. Type III edges are only found on SG8 and SG11 diamonds and on stones from HK1 and HK5. More diamonds from HK3 and HK5 need to be examined to confirm the different distribution pattern of diamonds with different morphological groups and edge types in these lithofacies.

Table 4.3 Diamond types in parcels from Snap Lake kimberlite. HK5-6 is the highly altered facies which cannot be assigned to either HK5 or HK6 with certainty.

	Type of diamond dissolution	Kimberlite facies						
		HK1	HK2	HK3	HK4	HK5	HK6	HK5-6
SG1	Octahedrons with step faces, a few or no negative trigons occur on ditrigonal {111} faces.							
a	with Type I edges	2	2	0	0	0	1	0
b	with Type II edges	1	2	0	3	0	1	0
SG2	Octahedrons with trigonal {111} faces; a few small negative trigons, hexagons and/or trigon-hexagons occur.							
a	with Type I edges	1	2	0	0	1	2	0
b	with Type II edges	2	2	0	1	0	2	0
SG3	Octahedrons with trigonal {111} faces; Many negative trigons, hexagons and trigon-hexagons occur. Edges belong to Type I.	0	1	0	0	0	0	0
SG4	Octahedrons with ditrigonal {111} faces; highly dense negative trigons, hexagons and trigon-hexagons. Shield-shaped laminae sometimes occur.							
a	with Type I edges	0	0	0	0	1	0	0
b	with Type II edges	0	0	0	0	0	1	0
SG5	Octahedrons with trigonal {111} faces; many negative trigons with a few small hexagons. Shield shaped laminae sometimes occur. Type I Edges.	2	1	0	1	0	0	0
SG6	Octahedrons with ditrigonal {111} faces. A few negative trigons or small hexagons (trigon-hexagons) are present.							
a	with Type I edges	0	0	0	2	0	0	0
b	with Type II edges	3	1	0	0	0	1	0
SG7	Octahedrons with trigonal {111} faces; a few negative trigons, hexagons and shield-shaped laminae occur.							
a	with Type I edges	0	0	1	0	0	0	0
b	with Type II edges	0	1	0	1	0	0	0
SG8	Octahedrons with trigonal {111} faces with serrate laminae. Type III edges.	0	0	0	0	3	0	0
SG9	Octahedrons with trigonal {111} faces; a few negative trigons and hexagons occur. Type I edges.	0	1	0	0	0	0	0
SG10	Octahedrons with trigonal {111} faces and irregular laminae. A few large, deep negative trigons, hexagons and/or trigon-hexagons occur; Type I edges	2	1	0	0	0	0	0
SG11	Nearly unresorbed octahedrons with trigonal {111} faces (Only positive trigons and serrate laminae are observed). Type III edges	1	0	0	0	0	0	0
SG12	Tetrahexahedrons with edge Type II covering large proportion of the surface area.	0	0	0	0	0	0	3
Total # of stone assigned to the types		14	14	1	8	5	9	3
Stones not assigned to a resorption type		11	11	3	6	0	3	3
Total stones		25	25	4	14	5	12	6

4.3.2 Nitrogen Defects of Snap Lake Diamonds

Both internal properties of diamonds and external conditions may affect the diamond resorption morphology. N is the most abundant impurities in diamonds. Previous studies suggested nitrogen content could influence diamond resorption (Mendelssohn and Milledge 1995). In this study, I obtained N content and aggregation in Snap Lake diamonds to examine if there is any correlation between N and diamond resorption morphology.

The amount of N aggregation for a given concentration of N depends on temperature and residence time of diamonds in the mantle, one can calculate the temperature at which diamonds resided in the mantle if the diamond age is assumed (Taylor et al. 1990). Diamonds came from the same mantle lithology experienced the same thermal history, and would show similar mantle resorption features. Thus, if diamonds of certain resorption type follow the same isotherm, this resorption type is likely to be mantle-derived (Zhang and Fedortchouk, 2012).

The total infrared active N content in the 82 selected diamonds ranges from 17 to 2000 ppm. All diamonds are of IaAB with 0-100 % of the N in B defects (Figure 4.7; Appendix A: Table EA4). The N data from most diamonds form two groups (Figure 4.7a). The first group with high N concentrations (500-2800 ppm) and relatively low aggregation states (< 40%), and the second group has N concentrations mostly below 500 ppm and relatively high aggregation states (40-95%). The isotherms calculated using equation from Taylor et al. (1990) and assumed diamond age of 3 Ga (from diamond age of 3.5 ± 0.17 Ga of Panda kimberlite in Ekati Mine, Westerlund et al. 2006) range from 1020-1090 °C for the first group and 1100-1200 °C for the second group. The N systematics of the studied diamonds from Snap Lake overlap with the diamond systematics for both peridotitic and

eclogitic diamonds from other kimberlites (Aulbach et al. 2009; Aulbach et al. 2011; Creighton et al. 2007; De Stefano et al. 2008; Smart et al. 2011; Stepanov 2007; Viljoen et al. 2004).

There is no apparent correlation between the N content or aggregation state and resorption morphology groups (Figure 4.7a) or edge resorption types (Figure 4.7b). The SG4, SG8, SG11, SG12 diamonds plot near the 1165 °C isotherm. The diamonds of SG8 may represent mantle-derived resorption features. Diamonds of SG4 probably show a combination of kimberlite-induced and mantle-derived resorption, evident from the presence of Type I or Type II edges which are shown on the majority of the studied diamonds. The three SG12 diamonds could reflect kimberlite-induced resorption, as they are covered by Type I edges (Figure 4.3). Other groups with possible combination of kimberlite-induced and mantle-derived resorption are SG5, SG9 and SG10, based on the criteria by Zhang and Fedortchouk (2012) and the presence of Type I edges on these diamonds. Diamonds of SG5 and SG10 plot in the T range of 1020-1090 °C and 1090-1120 °C respectively, and the one diamond of SG9 plots near the 1165 °C isotherm.

Some relationship with N defects can be observed for diamonds with different edge type. Diamonds with Type I edges all have < 1000 ppm of N and various aggregation states. Diamonds with Type II edges also show a wide range of N contents, but cluster at the low aggregation part of the diagram. The three diamonds with Type III edges plot near the 1165 °C isotherm.

There is no apparent correlation between the N content or aggregation state and the two kimberlite lithologies (phlogopite-poor HKM and phlogopite-rich HKP) or degree of alteration (Figure 4.8).

4.3.3 Negative Trigons and Hexagons on Snap Lake Diamonds

In total, 42 negative trigons (and trigon-hexagons) on 11 diamonds and 8 hexagons on 6 diamonds from Snap Lake kimberlite were measured with AFM (Table 3.1; Appendix A: Table EA5).

Figure 4.14a shows that negative trigons, trigon-hexagons, and hexagons from HKP and HKM show different trends in terms of the diameter and depth. Pit diameters on diamonds from HKP cluster at < 10 μm, 15-20 μm, and one at 35 μm, while the depth of pits with the same diameters can vary greatly. This is similar to what was described for Grizzly and Koala diamonds and from experiments in H_2O-rich fluid (Fedortchouk 2015). The pits on diamonds from HKM show positive correlation of diameter and depth, and their trend coincides with the trend shown by trigons on Misery diamonds. This positive correlation for Misery diamonds was interpreted to result from more CO_2-rich fluid (Fedortchouk 2015). However, the original dimensions of the negative trigons have been modified, as the truncation of negative trigons may change the initial diameter, and development of positive trigons may lower the surrounding {111} areas and make the negative trigons shallower (Forbes 2017; Keltie 2016). Thus, the observed trend of trigons should be regarded as an estimate of the true relationship between diameter and depth of positive trigons. More experimental data are needed to confirm the veracity of my interpretation.

On Snap Lake diamonds, the negative trigons are predominately flat-bottomed with only a few p/b trigons, while all the trigon-hexagons and hexagons are flat-bottomed. Positive trigons are always present all over the bottoms of the negative f/b pits. The pits measured by AFM range in size from 2.6-46.4 μm in diameter and 10.5-990.5 nm in depth

(Figure 4.14b). Pits with similar diameter can range in depth from 100 nm to 1 μm. They form two types based on the shape of the walls W_{111} walls. Type I pits (Figure 4.9, 4.10) have walls classified as Y type (a small proportion of micro-faces may have decreasing $\alpha_{\{111\}}$ near bottom, but the walls show Y shape in general), while in Type II pits (Figure 4.11, 4.12) the walls have prominent larger $\alpha_{\{111\}}$ at the top and smaller $\alpha_{\{111\}}$ near the bottom, and are classified as U type. Type II pits are limited to the depth range < 400 nm, and are mostly smaller than 20 μm in diameter (Figure 4.14b). All p/b trigons are small, < 20 μm in diameter and < 150 nm in depth. They either form trigons with walls classified as U type (Type III, Figure 4.13), or very shallow simple p/b trigons with one deep positive trigon in the middle and walls classified as V type (Type IV, Figure 4.13).

The morphologies of the negative trigons, trigon-hexagons, and hexagons show no apparent relationship with kimberlite lithology but are linked to the diamond resorption morphology. Diamonds with SG6 morphology with ditrigonal {111} faces and few trigons or trigon-hexagons represent a product of kimberlite-induced resorption according to the criteria from Zhang and Fedortchouk (2012). All negative trigons and trigon-hexagons measured with AFM on these diamonds show only Type II pits with no trigons deeper than 400 nm (Figure 4.11; Appendix A: Table EA5). Examination by optical microscope revealed no deep pits on the sides not measured by AFM. Type II pits are also present on diamonds from SG2, SG9 and SG10 groups (Figure 4.12) which have trigonal {111} faces. The SG9 (a few stepped negative trigons and small deep hexagons on {111} faces) and SG10 (irregular layers, deep stepped negative trigons) groups may represent a combination of kimberlite-induced and mantle-derived resorption (see Zhang and Fedortchouk 2012). However, pits with diameter > 50 μm were not measured with AFM on these diamonds

and may belong to Type I. Other groups showing possible combination of kimberlite-induced and mantle-derived resorption morphology are SG4 and SG5 (trigonal {111} faces and densely distributed trigons), with mostly Type I pits with two diamonds SNP5-3 (SG4) and SNP2-1 (SG5) also showing Type II pits. Types III and IV pits are present only on two diamonds. Diamond SNP5-2 (not assigned to any morphological group) shows Type I and Type III pits. Diamond SNP10-6 (SG1 group) exhibits Type IV pits and some f/b pits not measured with AFM due to an inclination of the {111} face.

4.3.4 Negative Trigons on Ekati Diamonds

In total, 165 negative trigons on 13 diamonds from four Ekati kimberlites (2 diamonds from Fox, 5 diamonds from Panda, 2 diamonds from Koala and 4 diamonds from Misery) were measured with AFM (Appendix A: Table EA6). The diameters of the trigons range from < 1 μm (observed by AFM) up to > 150 μm (observed by optical microscopy) (Figure 4.15), and the depths range from several nanometers to > 2 μm (observed by AFM). Cross-section profiles of the trigons show that both f/b and p/b pits are present on the diamonds from each kimberlite; both f/b and p/b pits have walls of V type, U type and Y type.

Only trigons on the four studied Misery diamonds show distinct positive correlation between the diameter and the depth of the pits (Figure 4.15). Trigons on the five Panda diamonds cover a similar size range to the studied Misery diamonds (~1-45 μm in diameter, and up to 1.2 μm in depth), yet show no correlation between the two dimensions (Figure 4.16c). Both f/b and p/b trigons on Panda diamonds can be divided into three groups based on their diameter: (1) < 15 μm, (2) ~20 μm and (3) ~40 μm, with depths ranging from a few nanometers to ~1.2 μm for trigons of similar diameters. In Koala, one diamond has

only f/b trigons, while the other has both f/b and p/b trigons (Figure 4.16f). The latter diamond has trigons with similar clustering of diameters as in Panda (diameters < 10 μm and ~20 μm), but the small pits with < 10 μm in diameter are much deeper than on Panda diamonds and can reach depths up to 800 nm (Figure 4.16d, 4.16f). On the two diamonds from Fox kimberlite most of the measured f/b and p/b trigons are < 20 μm in diameter and < 200 nm in depth (Figure 4.16b).

Trigons larger than 50 μm in diameter not measured by AFM were observed by optical microscope. The studied Panda diamonds have trigons > 100 μm in diameter, Misery diamonds show trigons > 50 μm in diameter on diamonds M95-A3-1, M95-K6 and M95-K7, and the two Fox diamonds have trigons with diameter ~50-100 μm but with shallow depth as estimated by optical microscopy.

No apparent size or distribution differences were found between f/b and p/b trigons in all studied Ekati diamonds (Figure 4.16). Cross-section profiles for trigons of typical morphology observed on each studied diamond are shown in Figures 4.17-4.35. Both f/b and p/b diamonds have trigons with V, Y, and U wall types. For example, diamond F32 from Fox has p/b and f/b trigons with U type, V type and Y type walls (Figure 4.18, 4.19). P36 diamond from Panda has p/b trigons with U type and Y type walls (Figure 4.24) and f/b trigons with U type, V type and Y type walls (Figure 4.25). Both Koala diamonds show f/b trigons with U type and Y type walls (Figure 4.26, 4.28), and diamond K95-A1-1 has p/b trigons with U type and Y type walls (Figure 4.27). On Misery diamonds p/b trigons have U, V, and Y wall types, and f/b trigons mostly have U type walls. Trigons with truncated corners are observed on diamond F32 from Fox (Figure 4.19d), on diamonds

M95-A3-1, M95-K6 and M95-K7 from Misery (Figure 4.35a-4.35d), on diamond K95-B4-12 from Koala (Figure 4.35e), and on diamond P36 from Panda (Figure 4.35f).

4.4 Summary

(1) Diamonds from HKM and HKP show similar major morphological groups. But the proportion of diamonds with different edges resorption types is different in HKM and HKP.

(2) The kimberlite-induced diamond resorption morphology and edge resorption types are not related to N content and aggregation state.

(3) Negative trigons on diamonds from HKP show positive relationship between diameter and depth, which is absent from negative trigons on diamonds from HKM.

(4) Only diamonds from Misery kimberlite show positive relationship between diameter and depth of negative trigons, which is not observed on diamonds from Fox, Panda and Koala kimberlites.

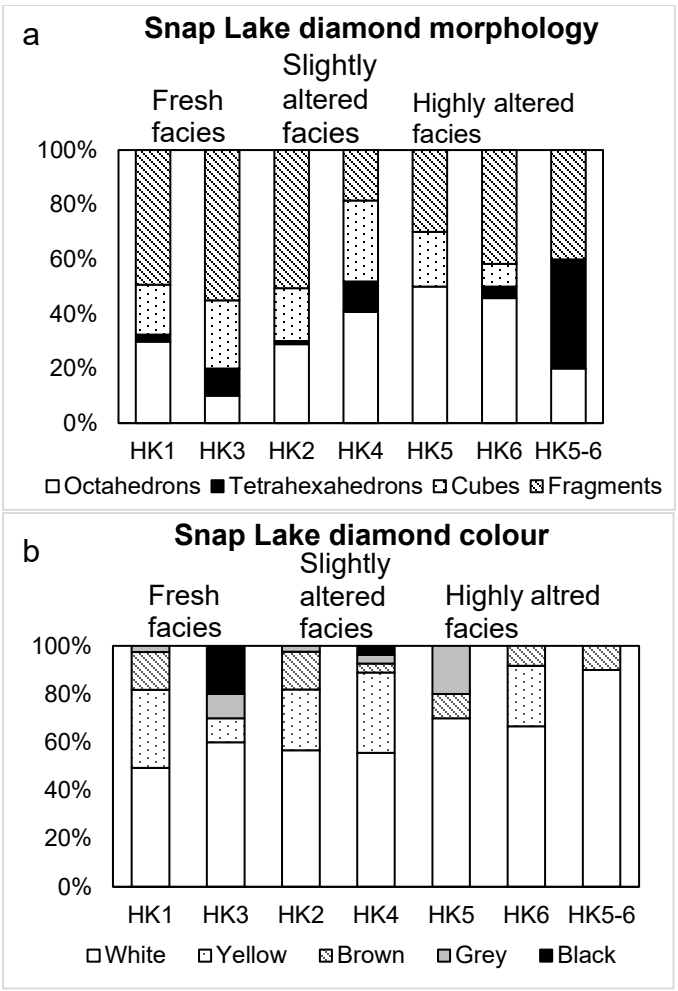

Figure 4.1 Distribution of major morphological forms (a) and colour (b) in diamonds from HK1-6 lithologies of Snap Lake.

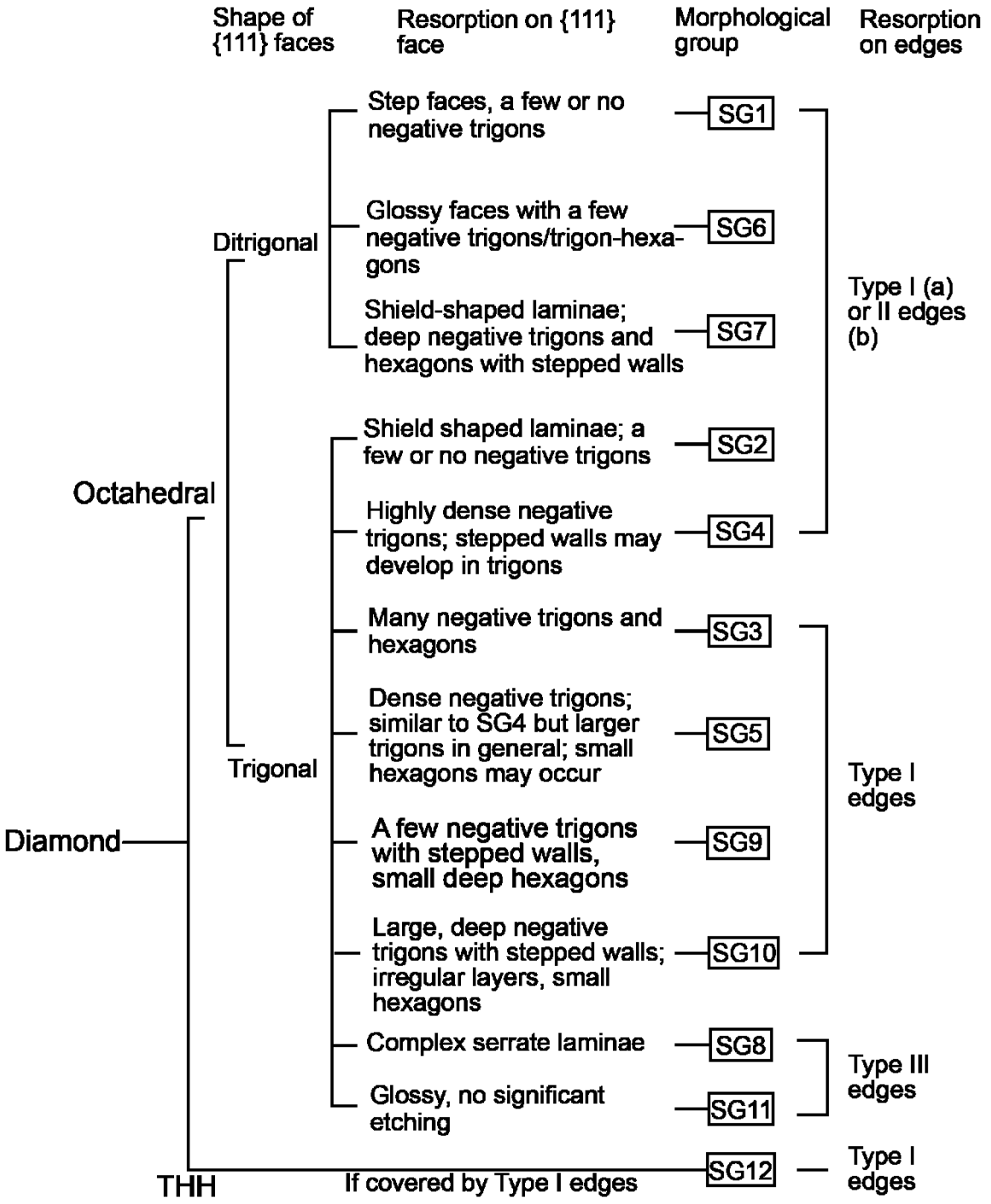

Figure 4.2 Classification tree for the different resorption types in the studied diamonds from Snap Lake kimberlite. SG1-SG12 are different morphological groups.

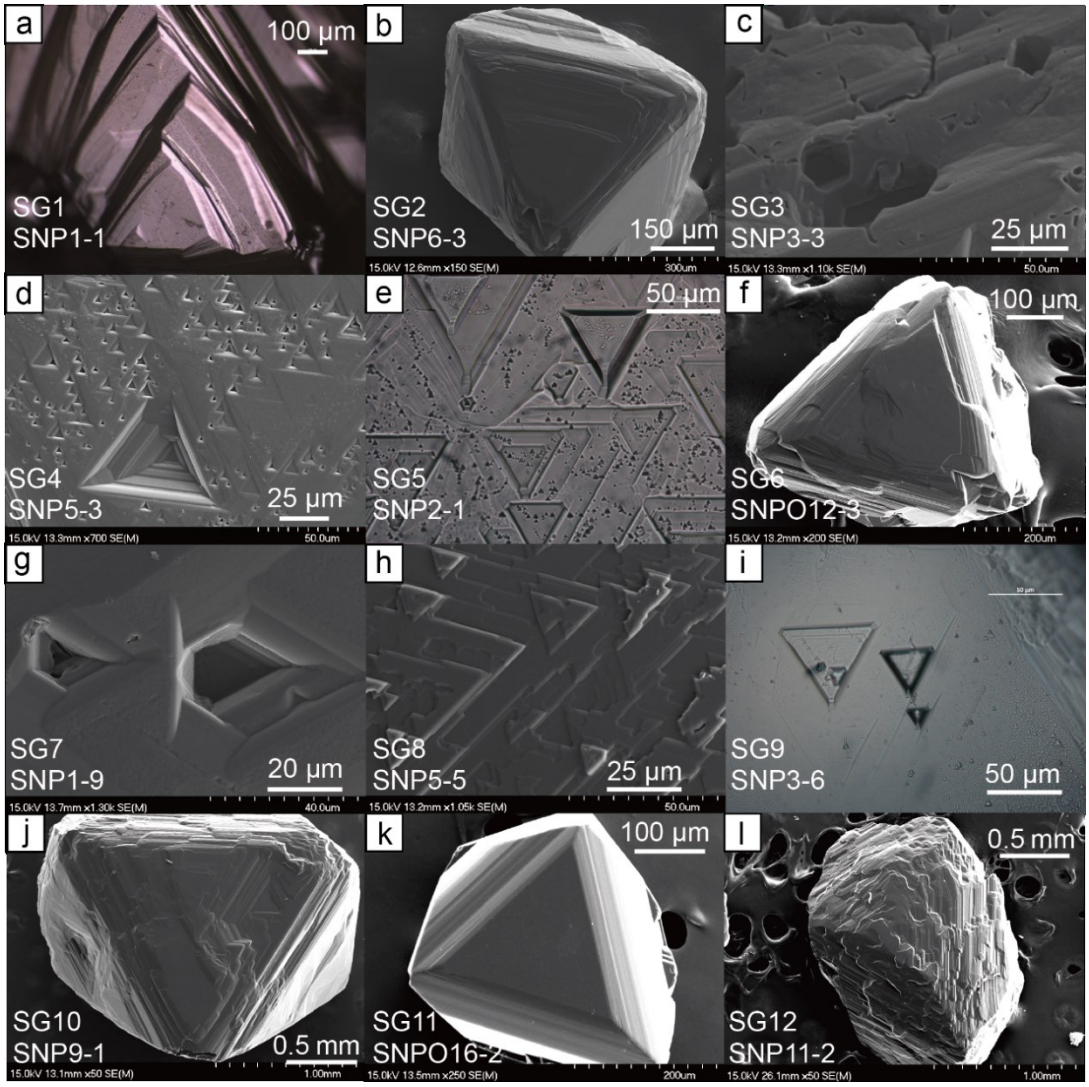

Figure 4.3 Optical and SEM images showing detailed characteristic features of diamonds from morphological groups SG1-SG12. (a) Diamond SNP1-1 of SG1, showing ditrigonal shaped step faces. (b) Diamond SNP6-3 of SG2, showing trigonal {111} face with shield-shaped laminae. (c) Hexagons on diamond SNP3-3 of SG3. (d) Densely distributed negative trigons on diamond SNP5-3 of SG4, note that some trigons have stepped walls. (e) Diamond SNP2-1 of SG5, with many negative trigons and a small hexagon. The trigons are generally larger than those on diamonds of SG4. (f) Diamond SNPO12-3 of SG6, showing ditrigonal {111} face with only a few negative trigons. (g) Deep hexagons on diamond SNP1-9 of SG7. (h) Serrate laminae on diamond SNP5-5 of SG8. (i) Diamond SNP3-6 of SG9, showing a few negative trigons with stepped walls and deep hexagons. (j) Diamond SNP9-1 of SG10, showing trigonal {111} face, irregular shaped layers and one large, deep negative trigon. (k) Diamond SNPO16-2 of SG11, showing glossy, trigonal {111} face. (l) Diamond SNPO11-2 of SG12, a highly resorbed THH diamond crystal covered by Type I edge features.

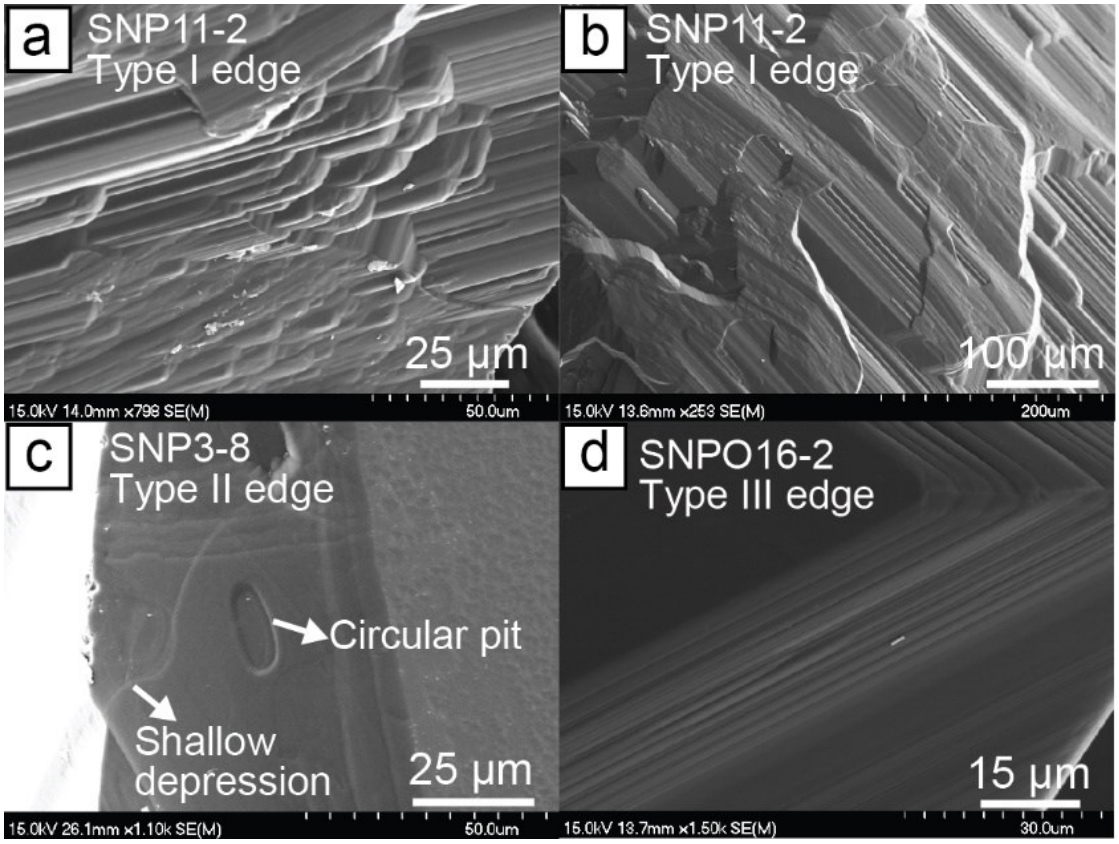

Figure 4.4 SEM images showing detailed features of Type I -III edges. (a) Sharp corners on Type I edge. (b) Deep cavities on Type I edge. (c) Smooth Type II edge with shallow depressions and one circular pit. (d) Type III edges with sharp parallel striations.

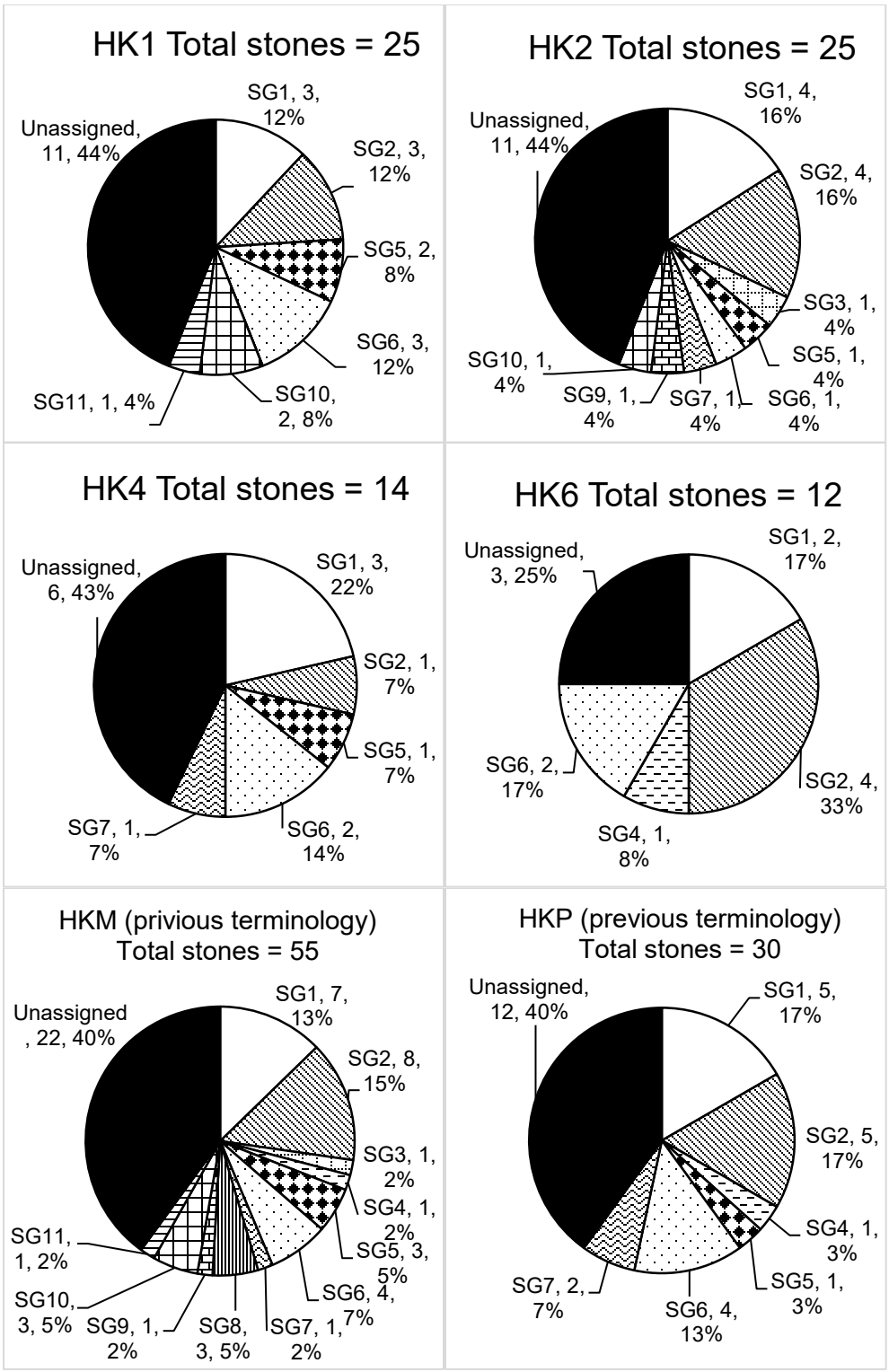

Figure 4.5 Number and proportion of stones of different morphological groups in HK1, HK2, HK4, HK6, HKM and HKP.

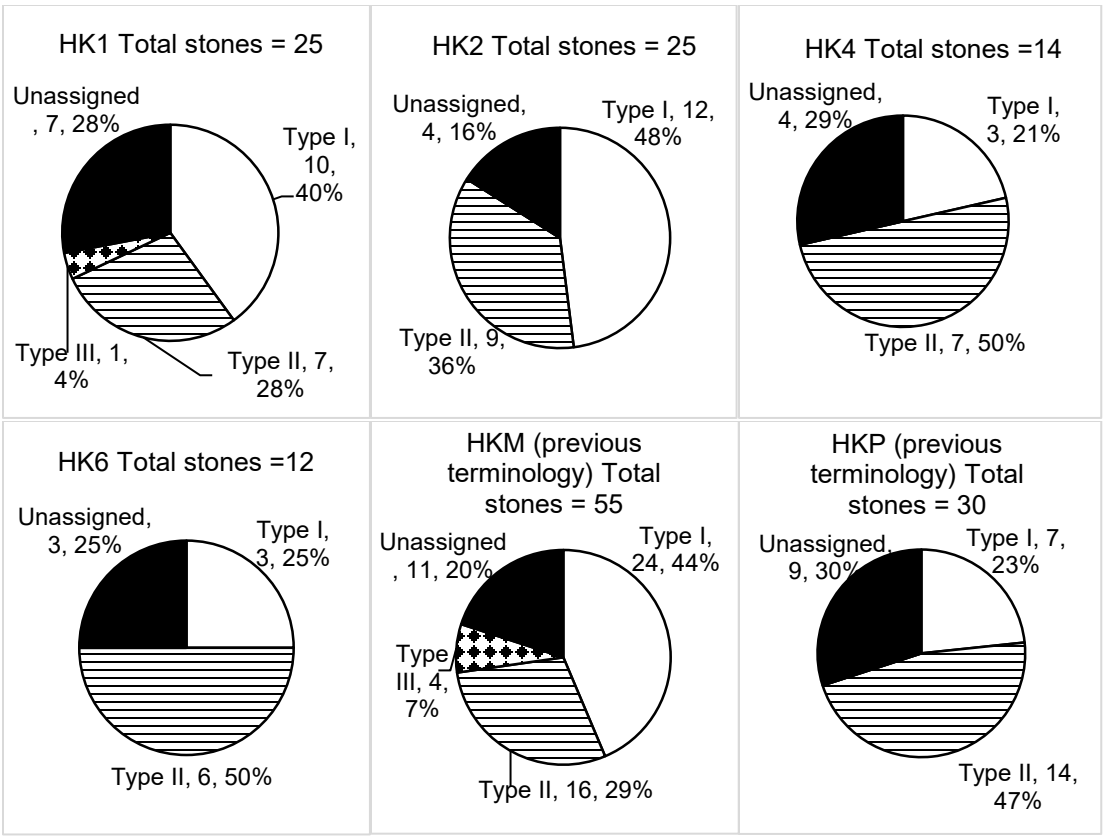

Figure 4.6 Number and proportion of stones of different edge resorption types in HK1, HK2, HK4, HK6, HKM and HKP.

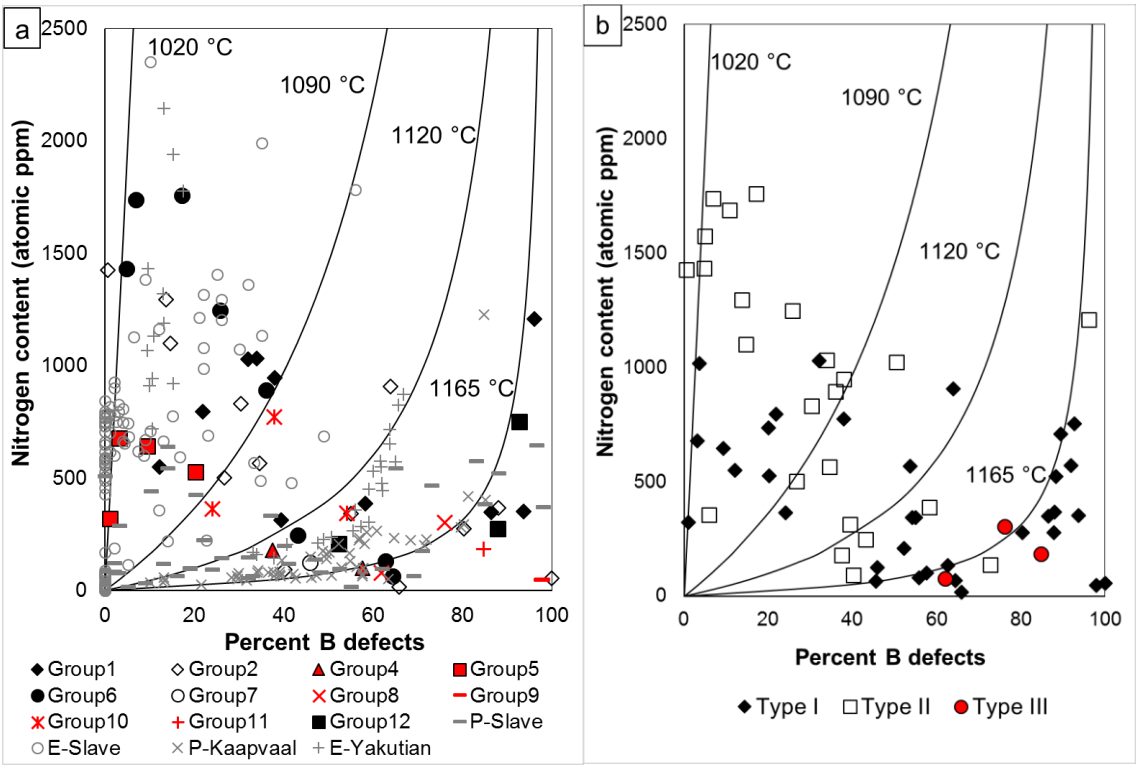

Figure 4.7 Total N content vs. degree of N aggregation of the studied diamonds from different morphological groups SG1-SG12 (a) with different edge resorption types (b). The morphological groups with possible mantle-derived features (SG8), combination of kimberlite-induced and mantle derived features (SG4, SG5, SG9, SG10) and one nearly unresorbed diamond (SNPO16-2, SG11) are plotted in red. The isotherms were calculated using the equation from Taylor et al. (1990) for 3 Ga diamond age estimated from diamond age of 3.5 ± 0.17 of Panda kimberlite in Ekati Mine (Westerlund et al. 2006). The small dashes and open symbols represent diamonds from peridotitic (P) and eclogitic (E) xenoliths in the Slave Craton (Creighton et al. 2007; De Stefano et al. 2008; Aulbach et al. 2009; Aulbach et al. 2011; Smart et al. 2011), respectively. The small crosses represent the N data of diamonds from an eclogitic xenolith in the Yakutian Craton (Stepanov et al., 2007), and inclined crosses represent N data of peridotitic diamonds from a lherzolite from the Kaapvaal Craton (Viljoen et al., 2004).

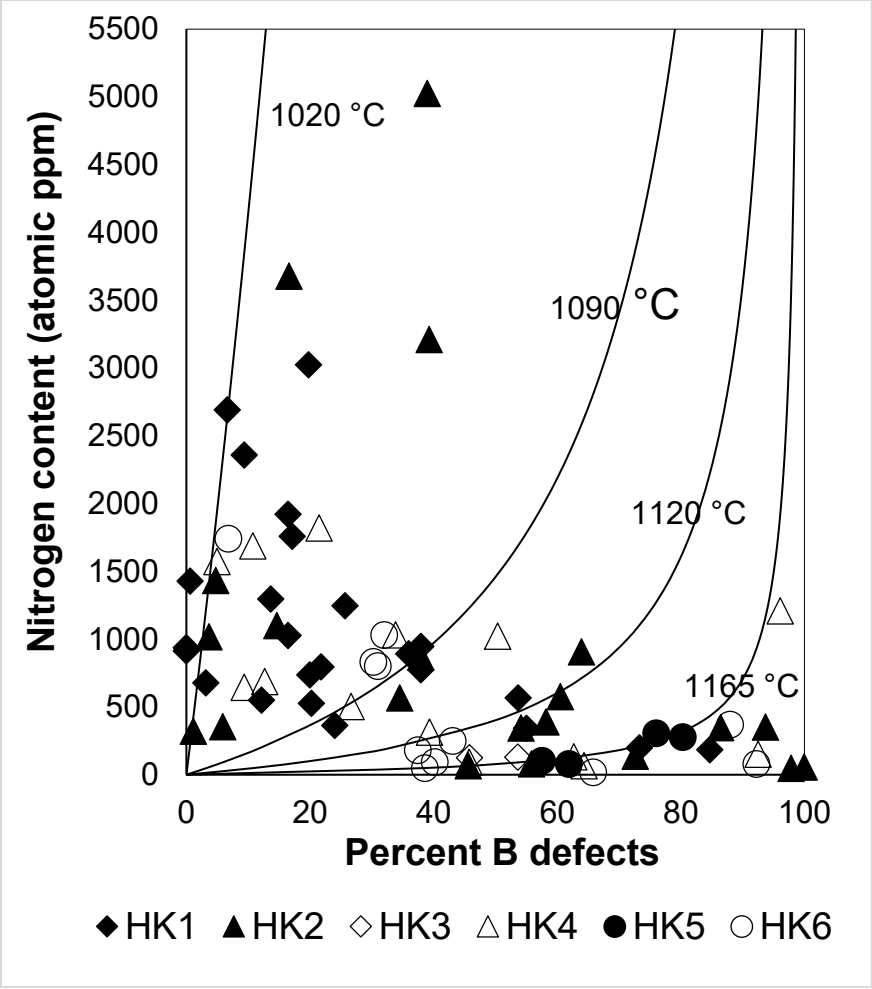

Figure 4.8 Total N content vs. degree of aggregation for the studied diamonds from different lithologies. The isotherms are the same as those in Figure 4.7.

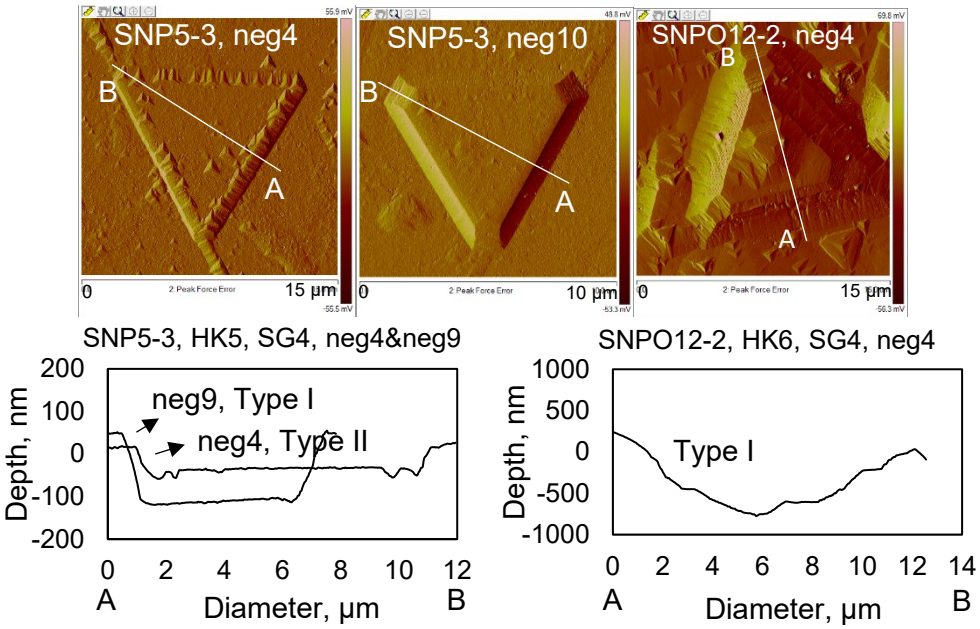

Figure 4.9 AFM images and cross-section profiles of Type I and II pits on diamonds SNP5-3 and SNPO12-2 of SG4.

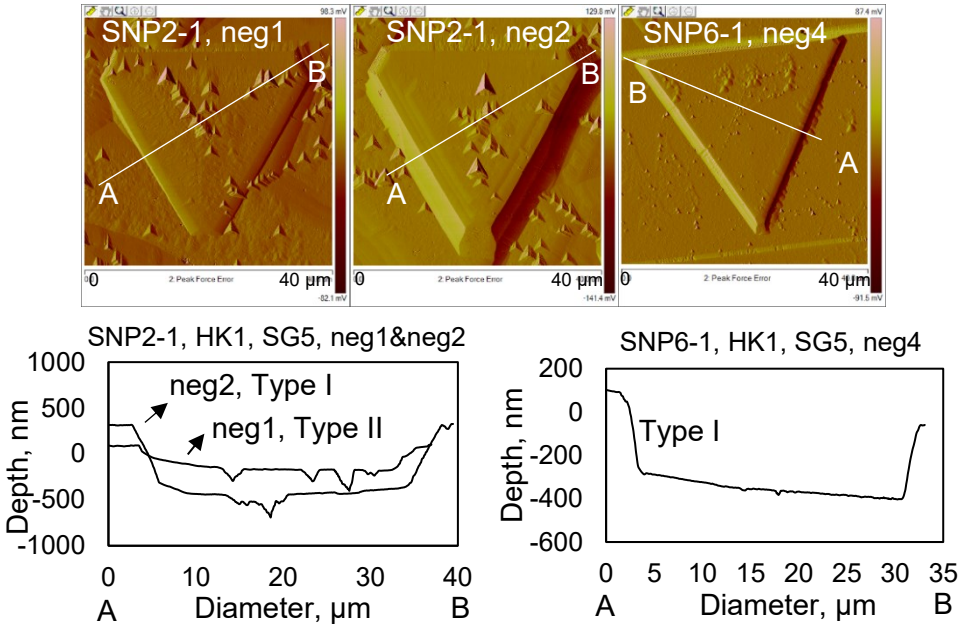

Figure 4.10 AFM images and cross-section profiles of Type I and II pits on diamonds SNP2-1 and SNP6-1 of SG5.

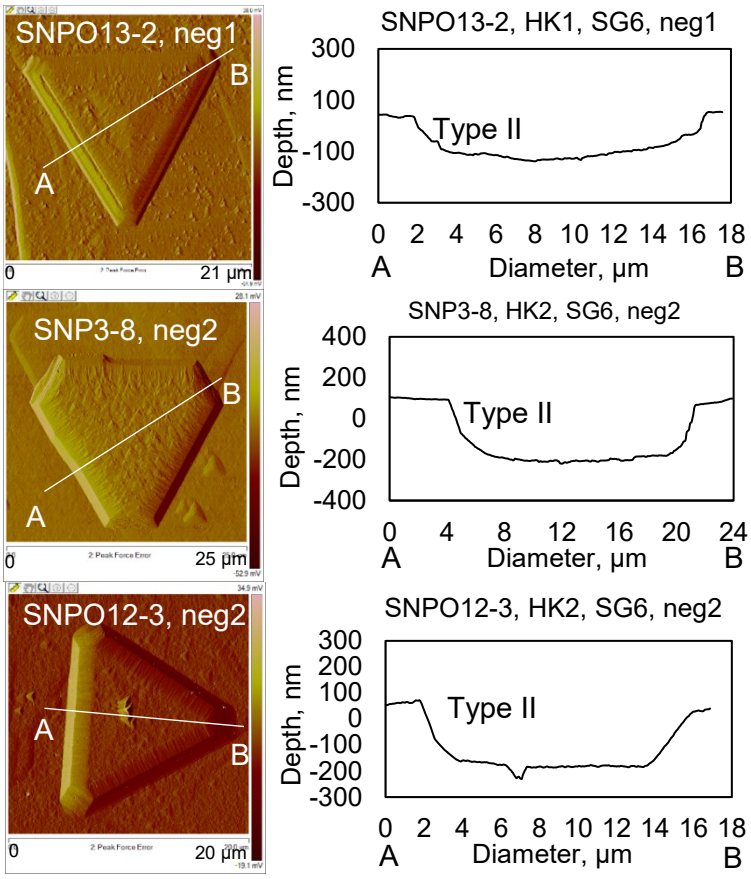

Figure 4.11 AFM images and cross-section profiles of Type II pits on diamonds SNPO13-2, SNP3-8 and SNPO12-3 of SG6.

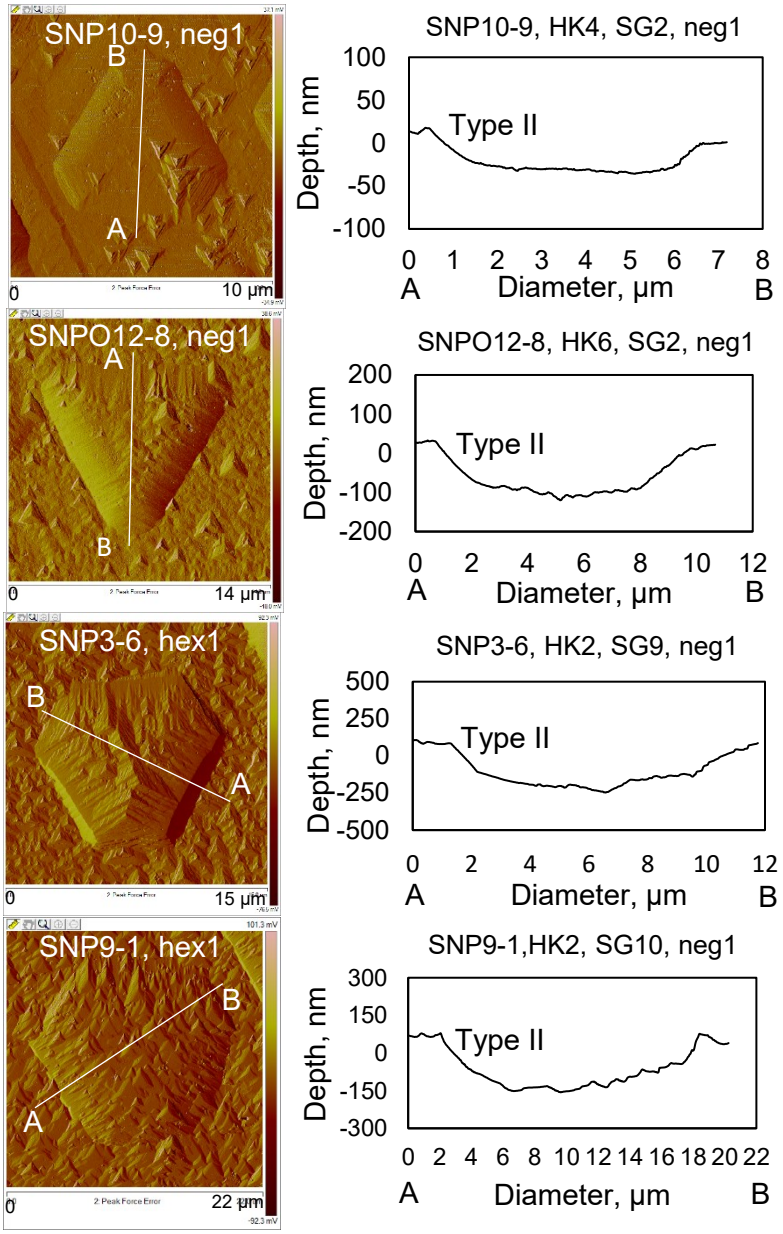

Figure 4.12 AFM images and cross-section profiles of Type II pits on diamonds SNP10-9 of SG2, SNPO12-8 of SG9, and diamonds SNP3-6, SNP9-1 of SG10.

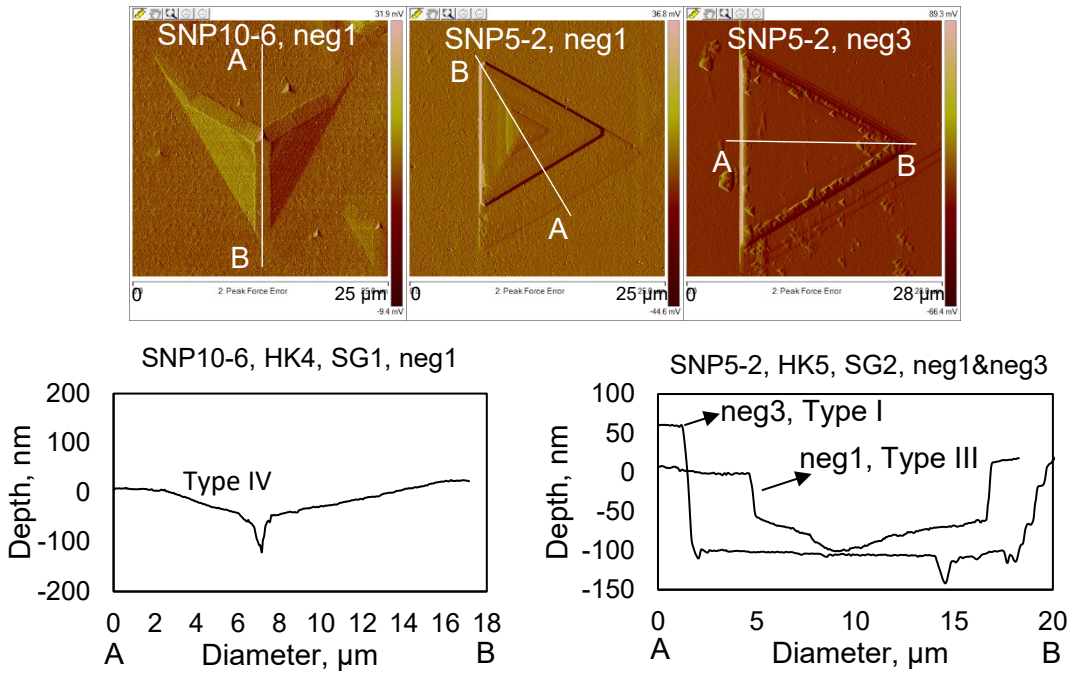

Figure 4.13 AFM images and cross-section profiles of Type IV pits on diamond SNP10-6 of SG1, and Type I and III pits on diamond SNP5-2 of SG2.

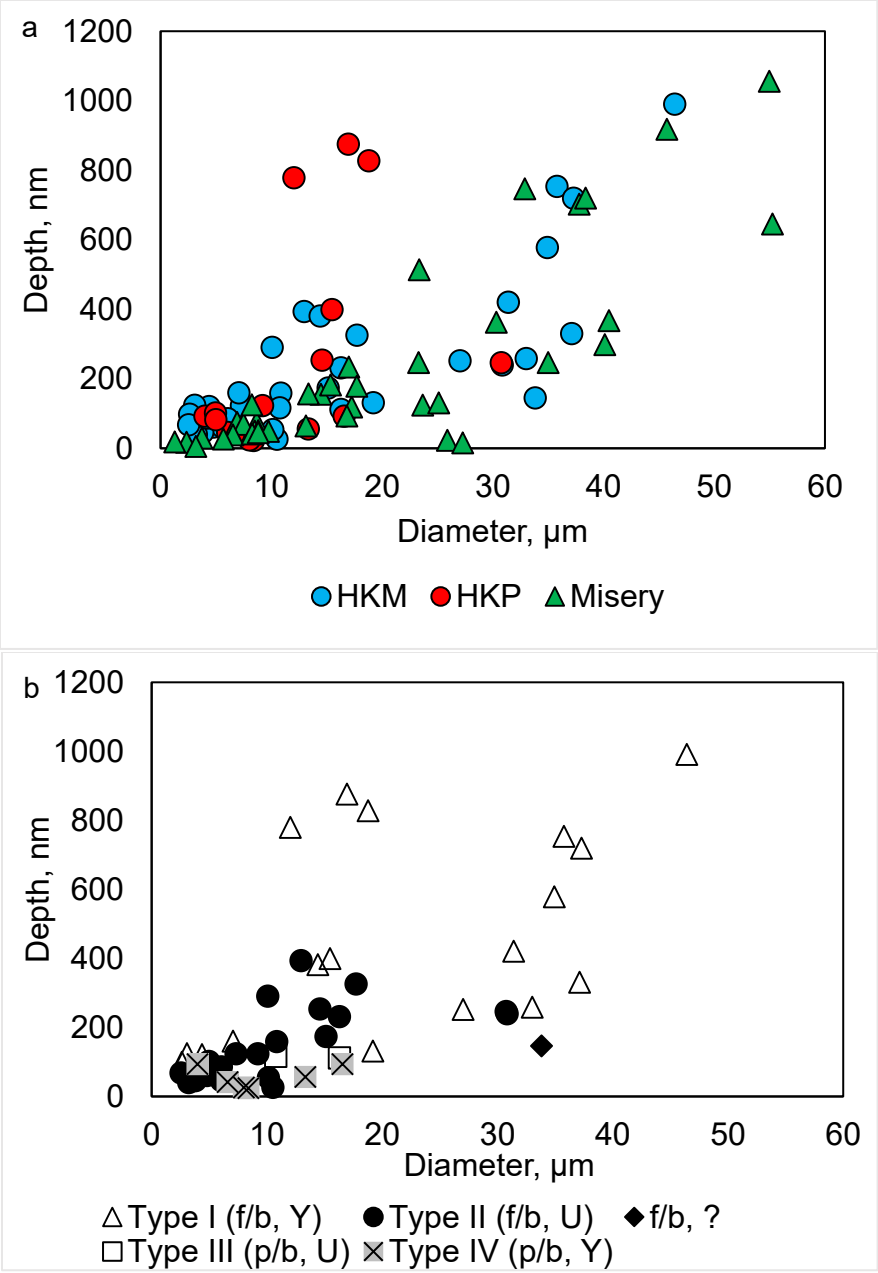

Figure 4.14 The diameter vs. depth relationship of negative trigons, trigon-hexagons and hexagons measured by AFM on Snap Lake diamonds from HKM and HKP in (a), with trigon type marked in (b). Negative trigons measured on diamonds form Misery pipe in Ekati Mine are also plotted in (a).

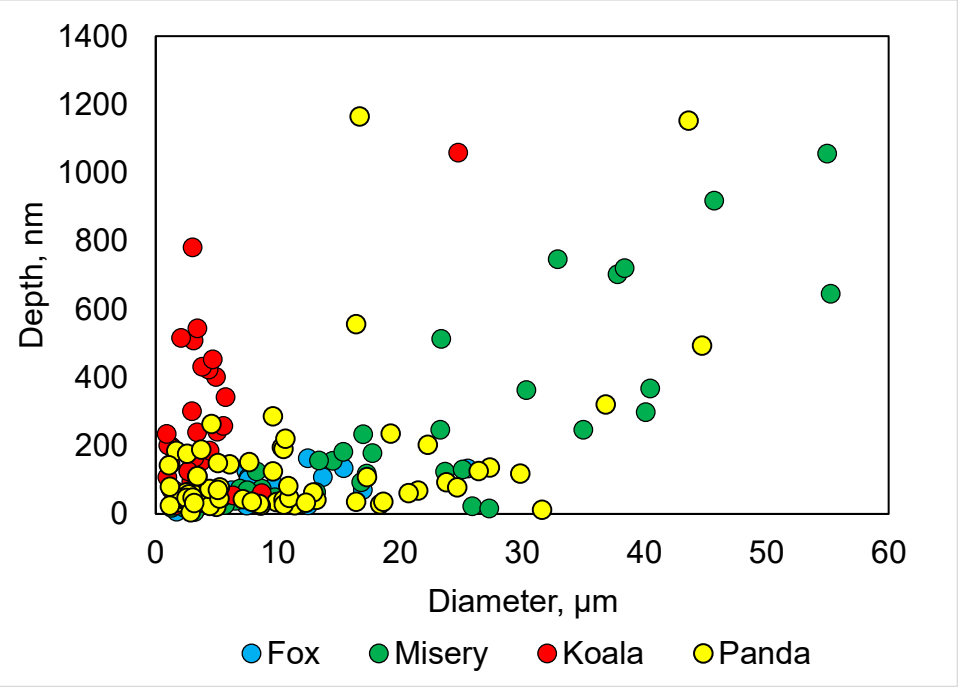

Figure 4.15 The diameter vs. depth relationship of negative trigons on Ekati diamonds distinguished by pipes.

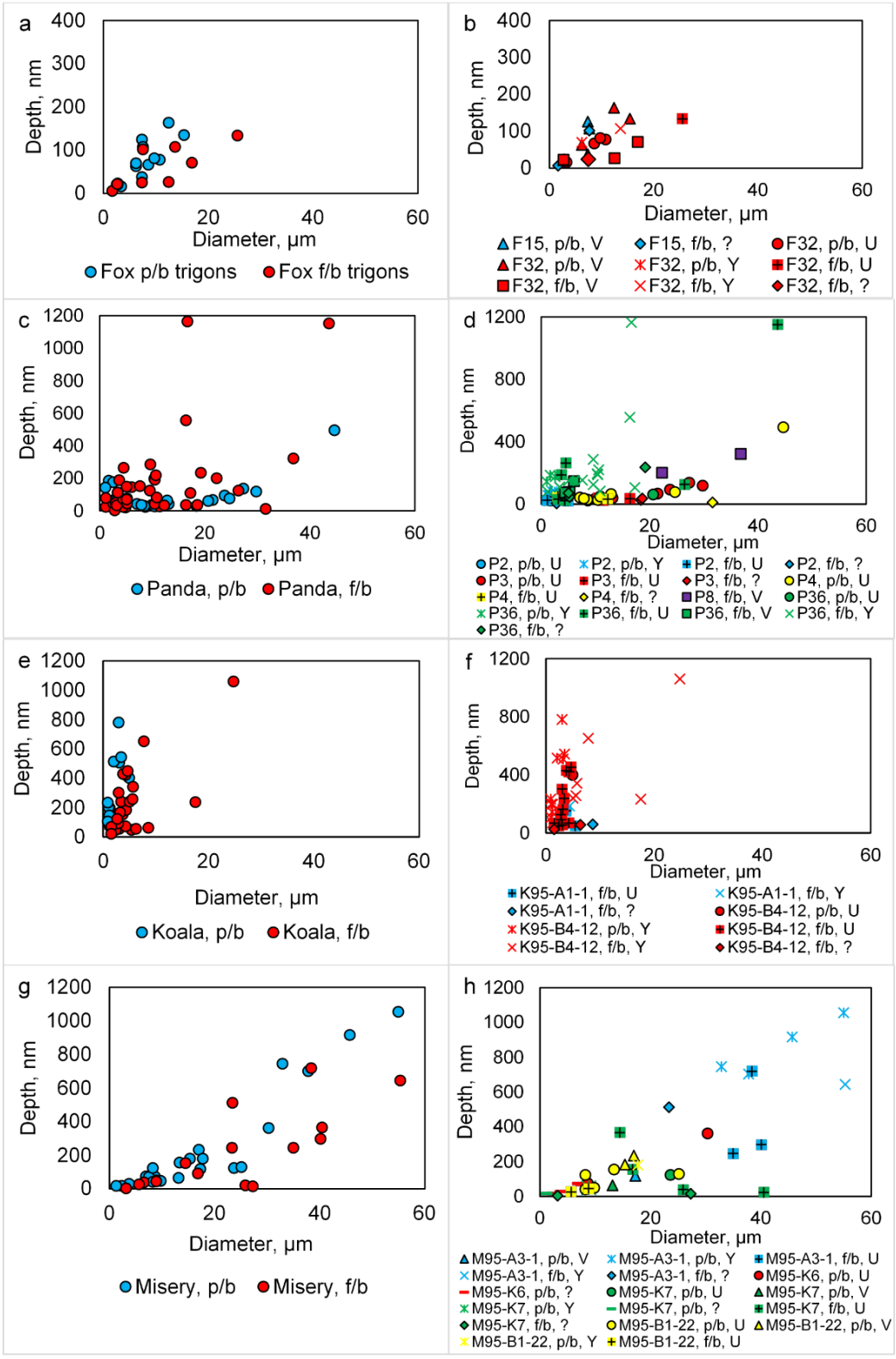

Figure 4.16 The diameter vs. depth relationship of negative trigons on diamonds from Fox (a, b), Panda (c, d), Koala (e, f) and Misery (g, h) kimberlites with bottom type and wall type distinguished.

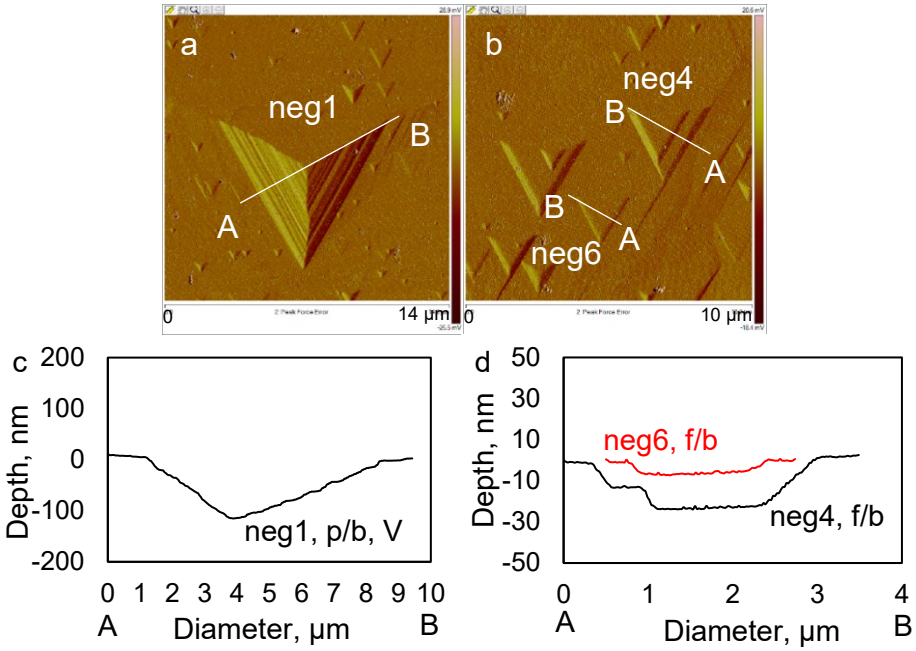

Figure 4.17 AFM images (a, b) and cross-section profiles (c, d) showing morphology of negative trigons on diamond F15 from Fox kimberlite. Information of the trigon (trigon #, bottom type and wall type (if determined)) is marked near its cross-section profile in the same color (same below).

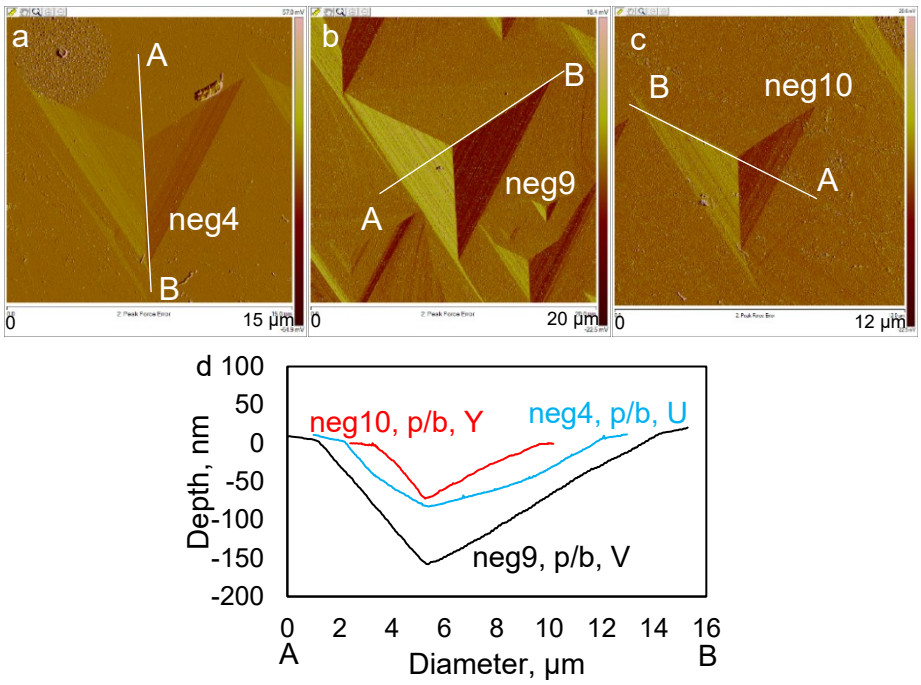

Figure 4.18 AFM images (a-c) and cross-section profiles (d) showing morphology of p/b negative trigons on diamond F32 from Fox kimberlite.

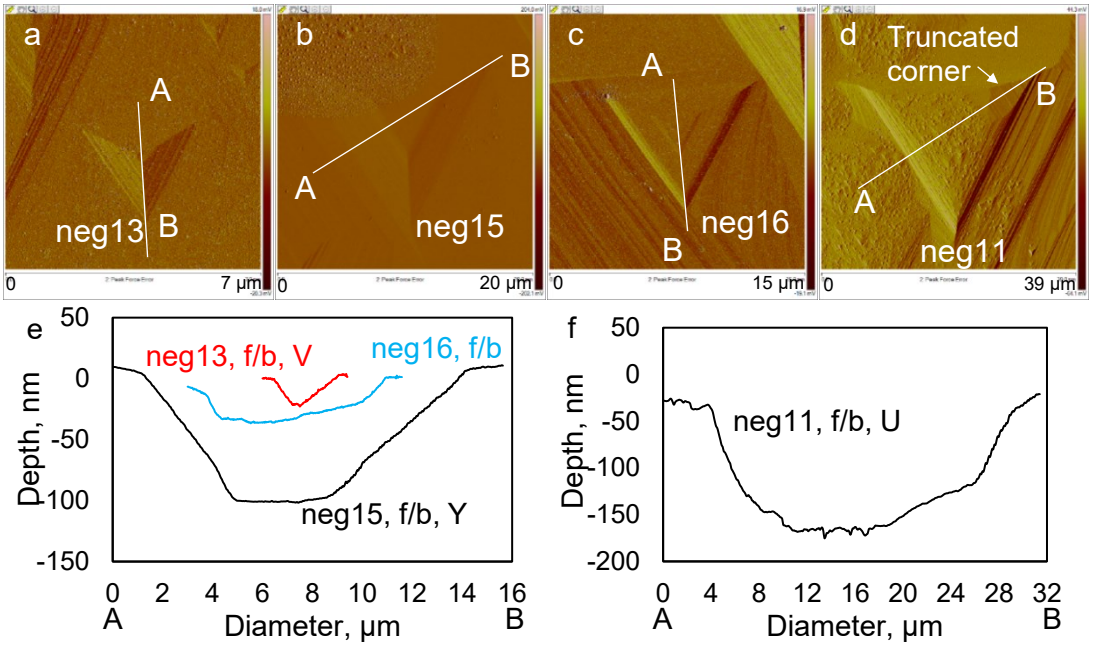

Figure 4.19 AFM images (a-d) and cross-section profiles (e-f) showing morphology of f/b negative trigons on diamond F32 from Fox kimberlite. Image (d) shows a truncated trigon.

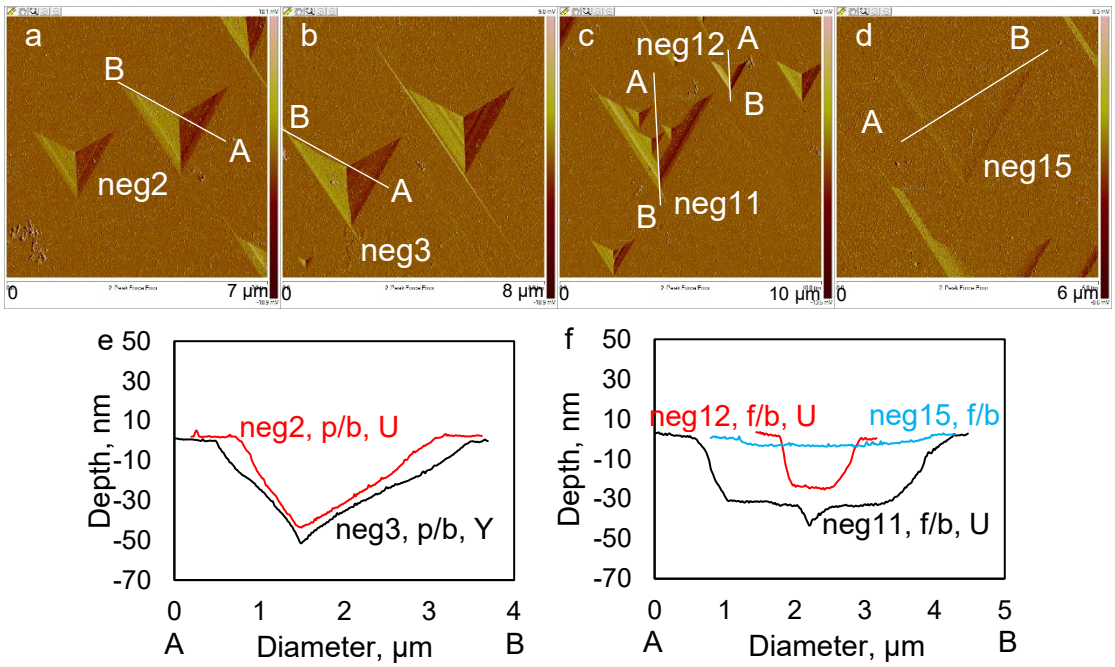

Figure 4.20 AFM images (a-d) and cross-section profiles (e, f) showing morphology of negative trigons on diamond P2 from Panda kimberlite.

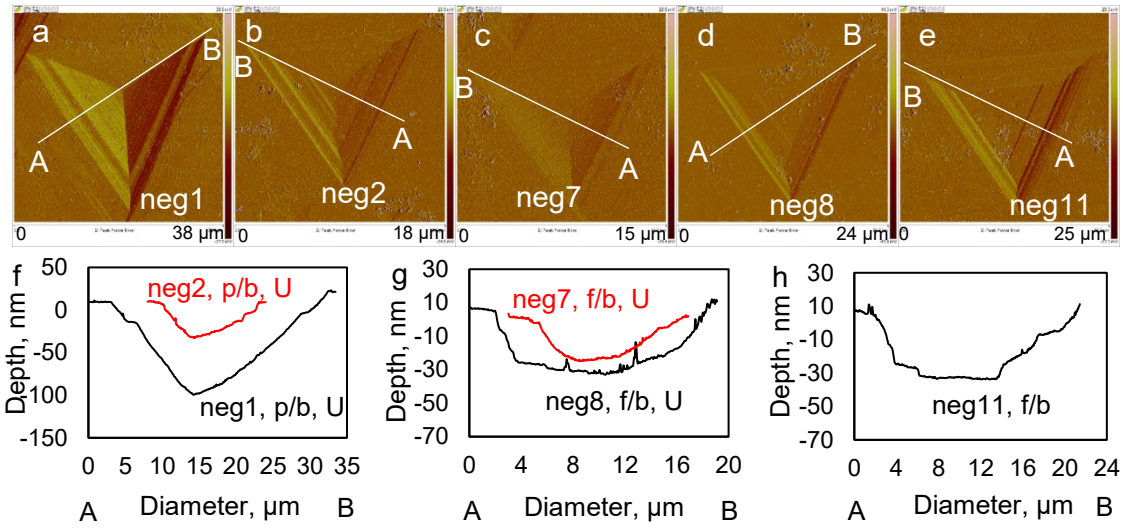

Figure 4.21 AFM images (a-e) and cross-section profiles (f-h) showing morphology of negative trigons on diamond P3 from Panda kimberlite.

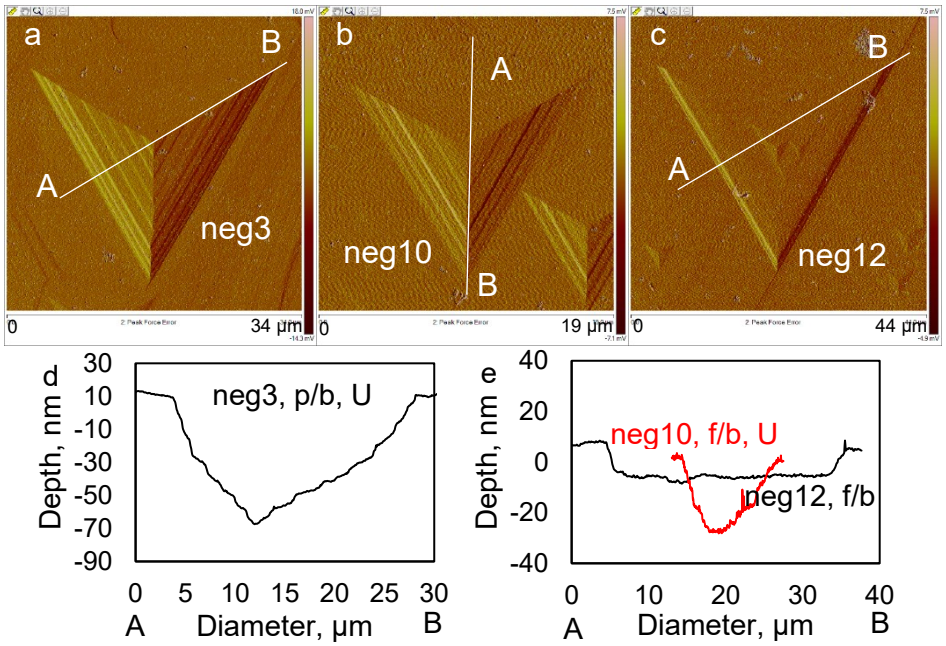

Figure 4.22 AFM images (a-c) and cross-section profiles (d, e) showing morphology of negative trigons on diamond P4 from Panda kimberlite.

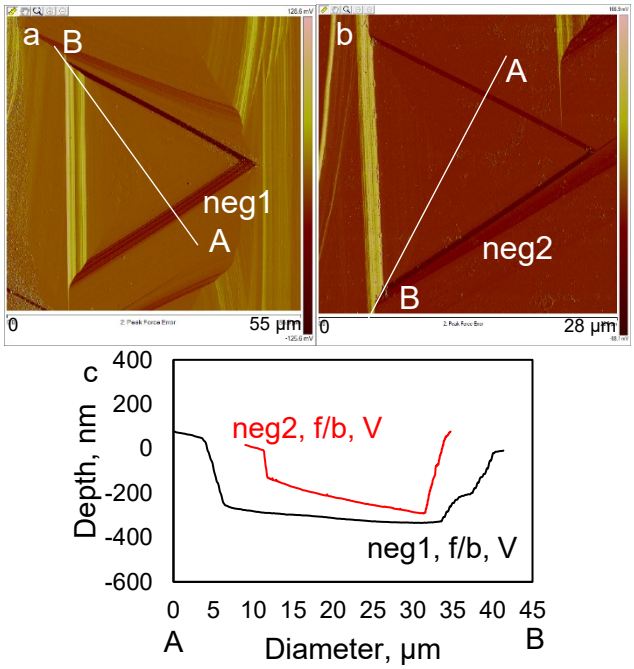

Figure 4.23 AFM images (a, b) and cross-section profiles (c) showing morphology of f/b negative trigons on diamond P8 from Panda kimberlite.

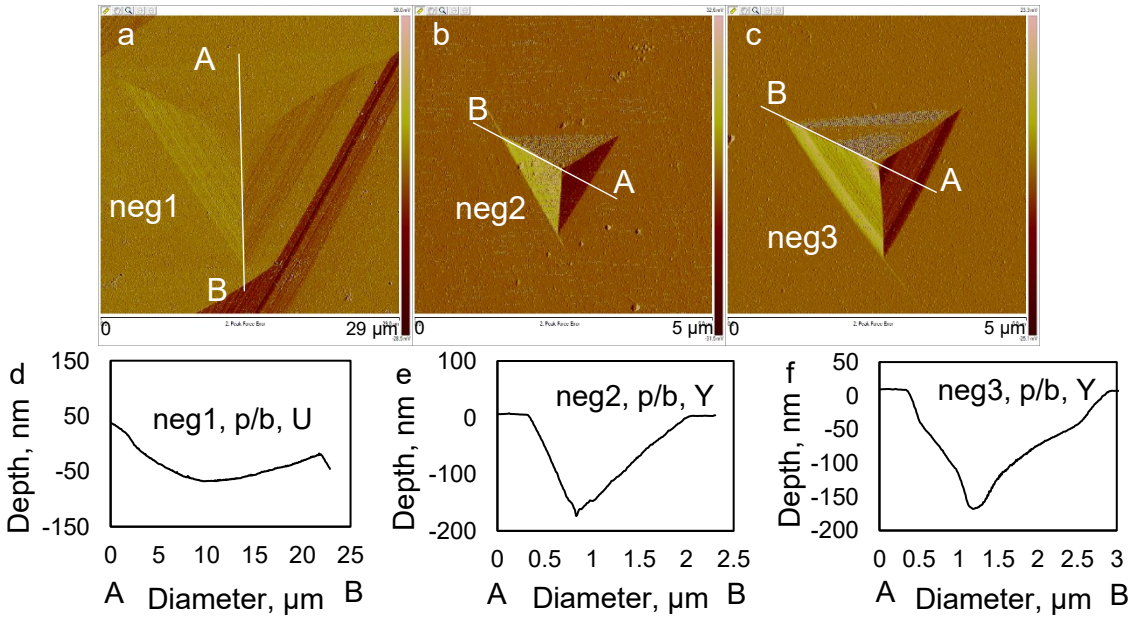

Figure 4.24 AFM images (a-c) and cross-section profiles (d-f) showing morphology of p/b negative trigons on diamond P36 from Panda kimberlite.

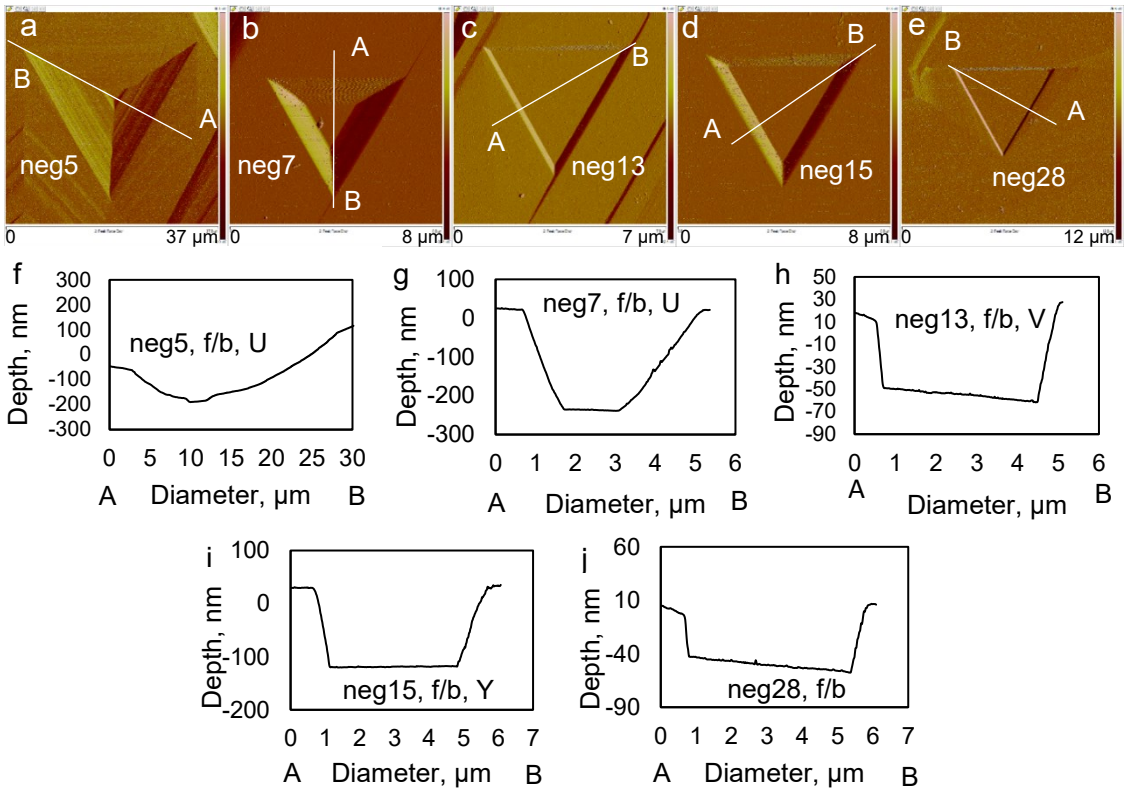

Figure 4.25 AFM images (a-e) and cross-section profiles (f-j) showing morphology of f/b negative trigons on diamond P36 from Panda kimberlite.

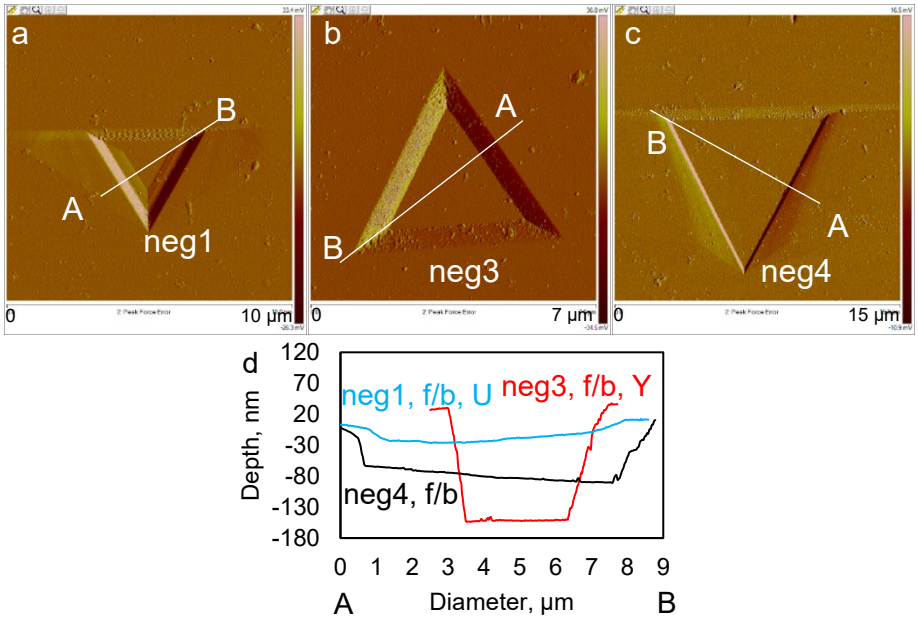

Figure 4.26 AFM images (a-c) and cross-section profiles (d) showing morphology of f/b negative trigons on diamond K95-A1-1 from Koala kimberlite.

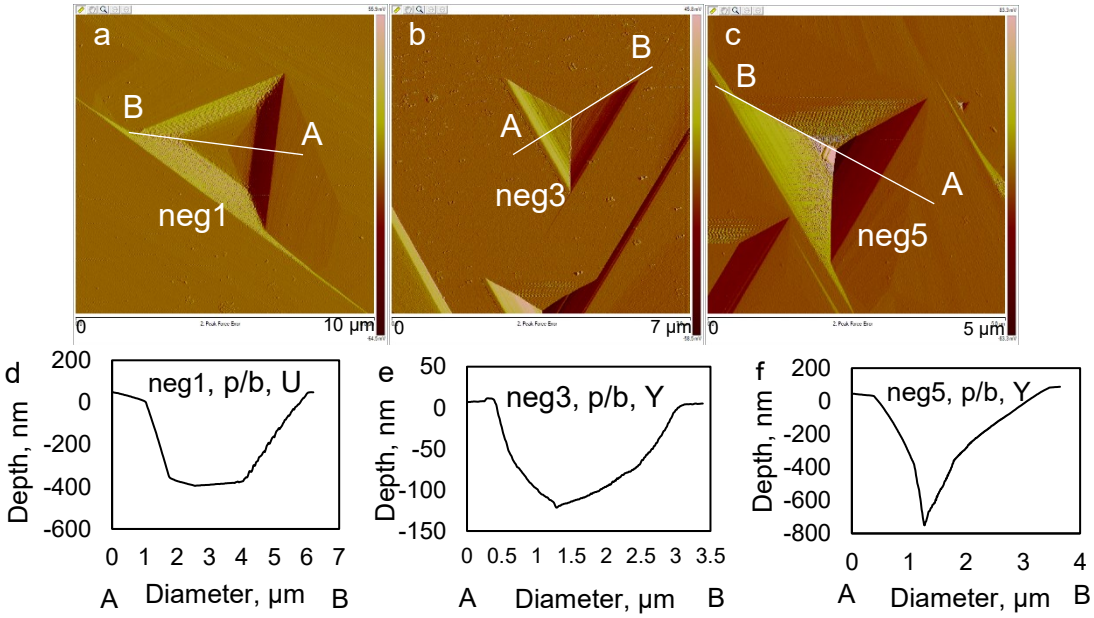

Figure 4.27 AFM images (a-c) and cross-section profiles (d-f) showing morphology of p/b negative trigons on diamond K95-B4-12 from Koala kimberlite.

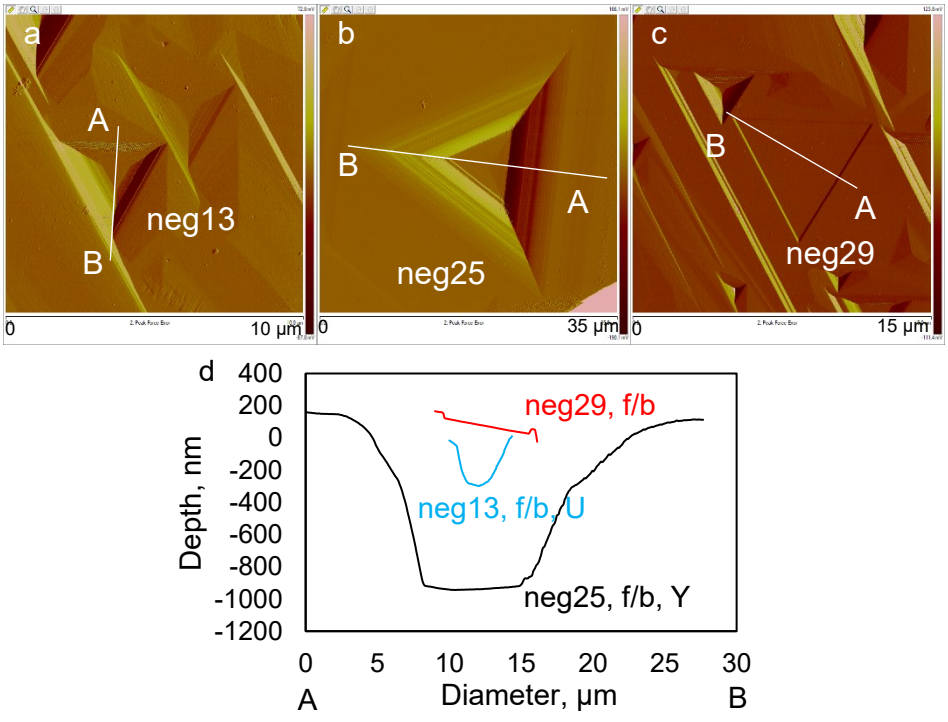

Figure 4.28 AFM images (a-c) and cross-section profiles (d) showing morphology of f/b negative trigons on diamond K95-B4-12 from Koala kimberlite.

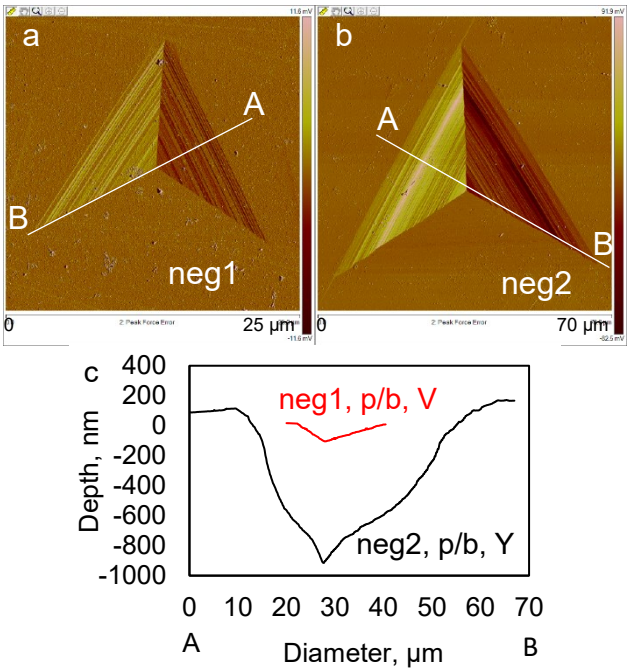

Figure 4.29 AFM images (a, b) and cross-section profiles (c) showing morphology of p/b negative trigons on diamond M95-A3-1 from Misery kimberlite.

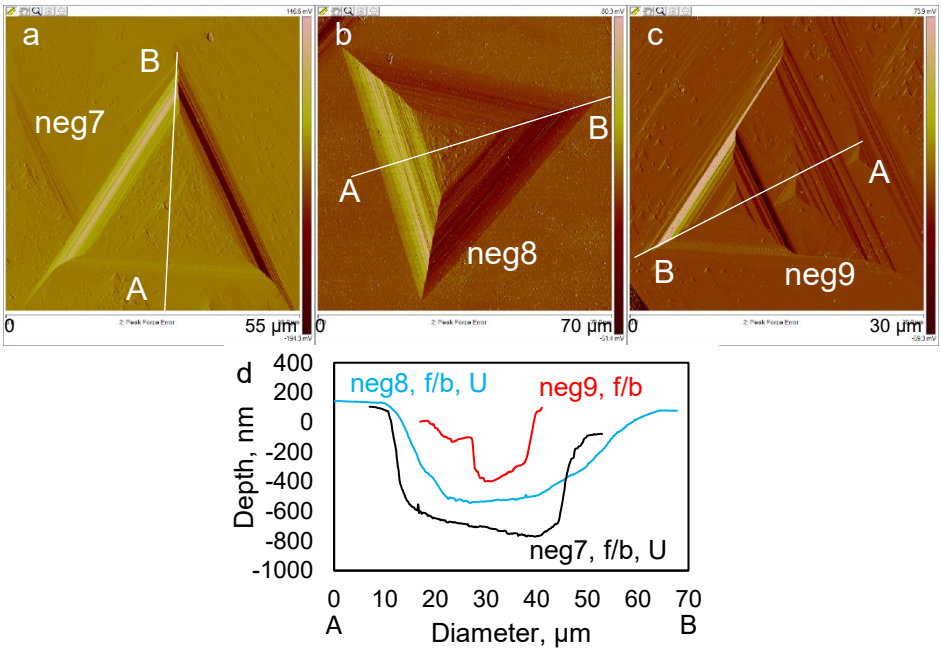

Figure 4.30 AFM images (a-c) and cross-section profiles (d) showing morphology of f/b negative trigons on diamond M95-A3-1 from Misery kimberlite.

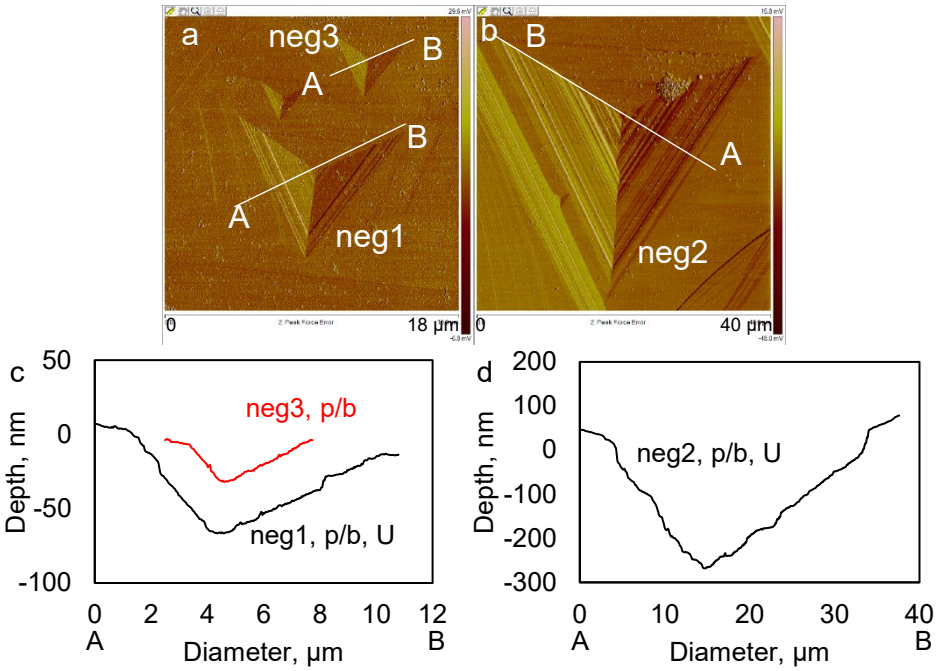

Figure 4.31 AFM images (a, b) and cross-section profiles (c, d) showing morphology of p/b negative trigons on diamond M95-K6 from Misery kimberlite.

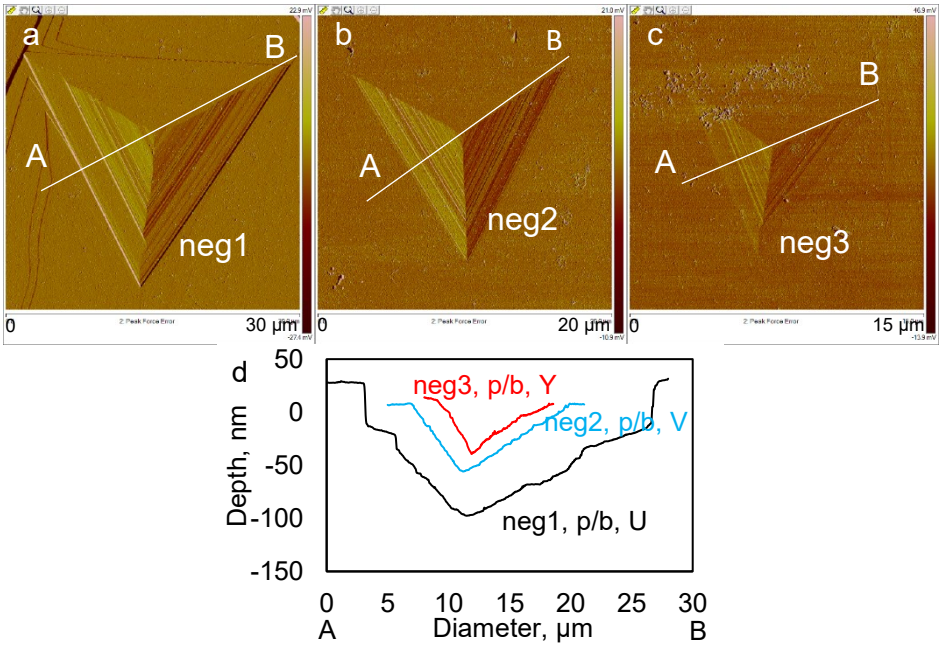

Figure 4.32 AFM images (a-c) and cross-section profiles (d) showing morphology of f/b negative trigons on diamond M95-K7 from Misery kimberlite.

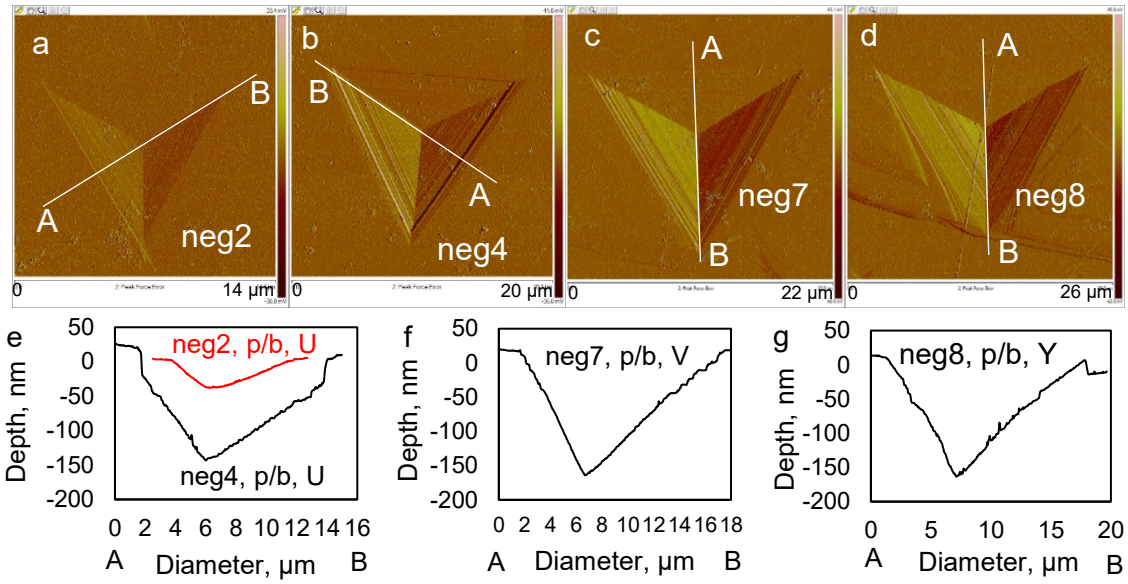

Figure 4.33 AFM images (a-e) and cross-section profiles (f-j) showing morphology of f/b negative trigons on diamond M95-B1-22 from Misery kimberlite.

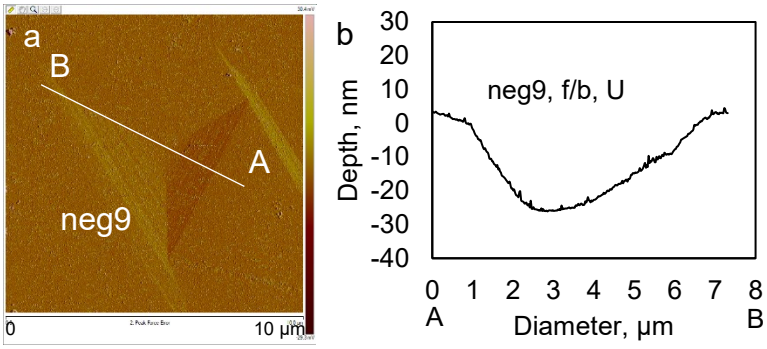

Figure 4.34 AFM image (a) and cross-section profile (b) of one f/b negative trigon on diamond M95-B1-22 from Misery kimberlite.

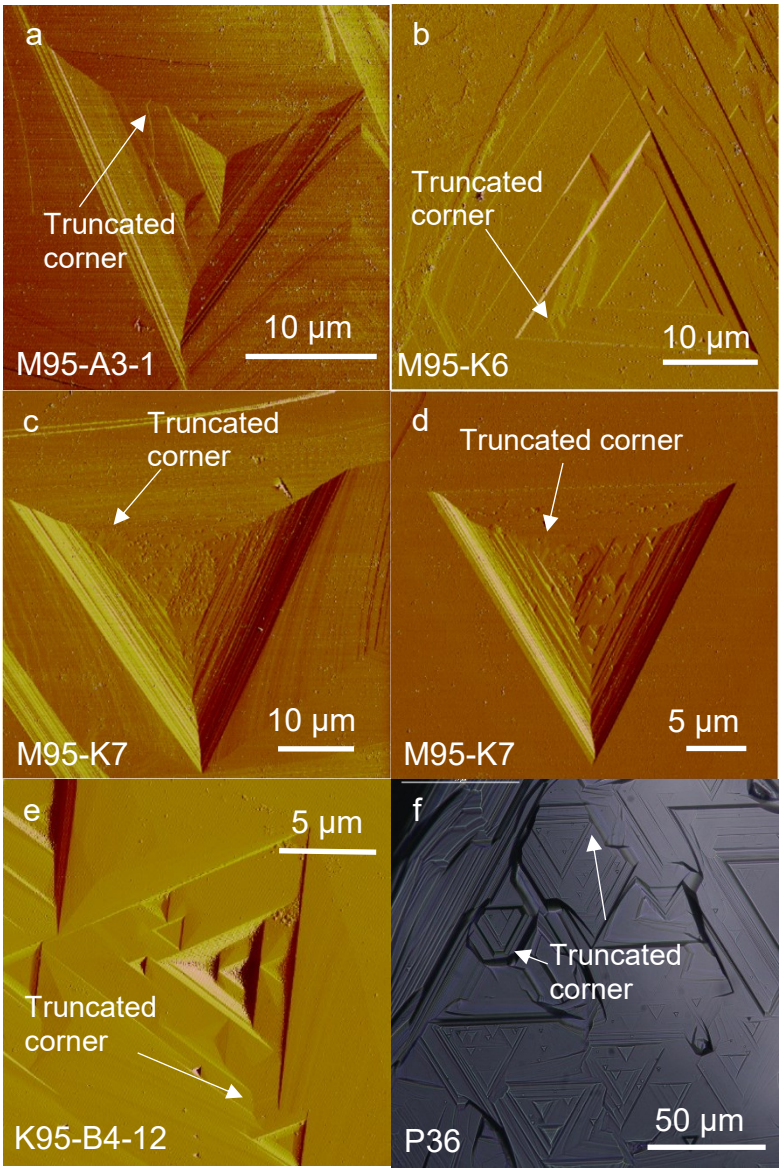

Figure 4.35 AFM images showing truncated negative trigons on diamonds M95-A3-1, M95-K6, M95-K7 from Misery kimberlite (a-d) and diamond K95-B4-12 from Koala kimberlite (e). (f) Optical image showing truncated negative trigons on P36 from Panda.

CHAPTER 5. DISCUSSION

5.1 Origin of Positive Trigons on Snap Lake Diamonds

5.1.1 Where Do Positive Trigons Form?

Positive trigons are very rare on natural diamonds compared to negative trigons (Robinson 1979). Hence, the origin of positive trigons is not very well understood. Robinson (1979) suggested that positive trigons are relatively young features that are formed by low-temperature etching under near-surface conditions, as diamond etching experiments showed that positive trigons can be produced in a strongly oxidizing environment under low (atmospheric or less) to moderate (≥ 0.1 GPa) pressure at temperatures ~650-1000 ℃. However, Yamaoka et al. (1980) showed that positive trigons could develop under high pressure (1.5-4 GPa) and temperatures of 800-1400 ℃ and proposed that the etch pit orientation is controlled by temperature and fO_2, as it was found that positive trigons transformed into negative trigons at elevated temperature, while higher fO_2 required higher reversal temperatures. This can be explained by the relative rate of atom removal on Step 1 (steps of negative directions) and 2 (steps of positive directions) as shown in Figure 5.1 (Evans 1976; Frank et al. 1958; Yamaoka et al. 1980). Positive trigons will form when carbon atoms on Step 1 are removed at a higher rate compared to atoms on Step 2. when the reverse is the case, negative trigons form. The relative atom removal rate is essentially determined by the stability of the different oxygen-carbon complexes formed on the steps. The edges of Step 1 consist of 3-bonded carbon atoms whereas the edges of Step 2 have 2-bonded atoms (Figure 5.5b). At lower temperature, the atoms on Step 2 are stabilized by oxygen atoms forming bridges between carbon atoms so that positive trigons will develop. Increase of temperature reduces the stability of the bridge

formation so that the life time of the oxygen-carbon complex on Step 2 is less than the different complex on Step 1, resulting in reversal of the trigon orientation. Elevated fO_2 causes higher oxygen concentration around the diamond surface so that the dissociation temperature of carbon-oxygen complexes on Step 2 can be increased, thus the higher reversal temperature. The formation of positive trigons under high P and T is also favored by Khokhryakov and Pal'yanov (2010) who produced positive trigons by etching diamond under pressures of 5.7-7.0 GPa and temperatures of 1400-1750 °C.

My study demonstrated that positive trigons on Snap Lake diamonds overprinted all the pre-existing negative trigons. They are present on the bottoms, along the sides or in the center of negative trigons, and add truncated corners to all the negative trigons. The truncated negative trigons, trigon-hexagons, and hexagons (Figure 5.6d) on Snap Lake diamonds show micro-steps only on the sides of positive directions, which is morphologically different to those produced in dissolution experiments by Zhang (2016) (Figure 5.6a, 5.6b) and those on some Ekati diamonds (Figure 5.6c) with micro-steps on all the sides and corners. In addition, most positive trigons on Snap Lake diamonds are small (diameter < 4 μm, Figure 5.2f), resembling the positive trigons present on diamonds AL-5, Exp5 and Exp17 (Figure 5.2c, 5.2e) from our oxidation experiments under atmospheric pressure and 900-1000 °C. In contrast, the positive trigons produced under high T and P are very large in size even when the duration of etching is shorter (Figure 5.2a, 5.2b). All these features imply the resorption event that produced positive trigons on Snap Lake diamond happened at late stage of the dyke emplacement, while the temperature of the kimberlite intrusion was still high enough for diamond oxidation (> 800 °C according to Forbes, 2017). The kimberlite dykes can retain the fluid when the high-temperature

magma was cooling down during emplacement to the surface, while kimberlite pipes lost the fluid during eruption so that no resorption happened at this stage.

In conclusion, my data indicate that although positive trigons can be produced under different experimental conditions, the formation of positive trigons on natural diamonds is related to low-pressure, late-stage resorption events that can be unique to some kimberlites (dykes) but absent in most kimberlites.

5.1.2 Controls on the Development of Positive Trigons

The crystal lattice of the {111} face of an octahedral diamond consists of alternating rows of carbon atoms bound to three neighboring atoms and having one dangling bond (denoted by O in Figure 5.5), in addition to atoms bound to three neighboring atoms as well as one atom from the {111} layer below (denoted by X in Figure 5.5). Angus and Dyble (1975) proposed that trigon formation is initiated at defect sites and enlarged via kink propagation by sequential removal of 2-/3-bonded carbon atoms, assuming negligible surface diffusion. For the enlargement of a negative trigon around a central initiating defect, first removal of one 3-bonded atom (single-kink mechanism) or multiple 3-bonded atoms (multiple-kink mechanism) are needed so that 2-bonded atoms can be removed, which eventually enlarges the trigon by one row in the $<\bar{1}\bar{1}2>$ direction. As shown in Figure 5.1, formation of negative trigons requires that step 2 moves faster than step 1 (Yamaoka et al. 1980), i.e. $k_2 > k_{3e}$, where k_2 and k_{3e} are the specific removal rates of two-bonded atoms and three-bonded atoms on the edge of the pit. In most cases, this is energetically favorable, and agrees with the fact that negative trigons are far more common than positive trigons on natural diamonds.

Positive trigons will form only when $k_2 < k_{3e}$. Some studies suggested this can be reached by forming certain complexes such as a bridge formation of oxygen between 2-bonded carbon atoms on step 2 (Frank and Puttick 1958; Yamaoka et al. 1980). In addition to the effect of complexes, I propose that in Snap Lake dyke, positive trigons formed due to diamonds undergoing resorption close to the surface at low pressure. The diamond crystal lattice was unstable at low pressure, and the energy required to remove 2- and 3-bonded atoms became similar. The resorption event that produced positive trigons on Snap Lake diamonds did not happen in the other Canadian kimberlite pipes, where the kimberlites erupted to the surface.

Our oxidation experiments showed that trigon orientation is affected by fO_2 relative to the CCO buffer and temperature. Negative trigons were produced at one run conducted at 1150 ºC and an fO_2 of CCO +1.5 (1.5 log units above the CCO buffer), while runs with lower temperature and fO_2 produced only positive trigons. The size of positive trigon is related to fO_2 as well (Figure 3.7a). When fO_2 is above CCO, the size of trigons generally increases when fO_2 is further away from CCO, whereas if fO_2 is slightly below CCO, trigons can be relatively large compared to those produced in more oxidizing conditions. The presence of melts may enhance the resorption and development of positive trigons, which is indicated by the deep corrosion features present on diamonds Exp17 and AL5, and the generally larger diameter of the trigons inside the cavities compared to the trigons developed on the relatively smooth surfaces (Figure 3.3c).

5.1.3 Application to Snap Lake Kimberlite System

The formation of positive trigons on Snap Lake diamonds is related to late stage resorption events that did not happen in Ekati kimberlites. This is supported by the absence

of positive trigons on Ekati diamonds and overprinting of positive trigons on all the pre-existing negative trigons on Snap Lake diamonds. The experimentally produced positive trigons under high pressure from 1.5-7.5 GPa at 700-1700 °C (Arima and Kozai 2008; Khokhryakov and Pal'yanov 2010; Khokhryakov and Palyanov 2006; Yamaoka et al. 1980) usually have larger sizes with ~20-100 μm diameters even if the duration of etching is short (0.5 to a few hours), which is very different form the small positive trigons with < 14 μm diameters on Snap Lake diamonds. Etching experiments carried out at atmospheric pressure and 700-950 °C (de Theije et al. 2001; Forbes 2017; Keltie 2016) also produced positive trigons, which are morphologically similar to the ones on Snap Lake diamonds but can still have much larger diameters (up to 30-40 μm). The experimentally produced trigons that show diameters closest to natural positive trigons were produced in air at 700-800 °C or CO_2 at 800 °C, but no etch pits developed when diamonds were etched in CO_2 at 700 °C under atmospheric pressure (Forbes 2017). Meanwhile, the morphologies of positive trigons on Snap Lake diamonds are more like those produced in our experiments under fO_2 of CCO +0.7 and below ~1000 °C on diamonds Exp17, AL5. Thus, I propose that the positive trigons on Snap Lake diamonds were formed under low pressure and fO_2 slightly above the CCO buffer, probably after the emplacement of the magma, in fluid with a relatively high temperature, ranging from > 700 °C to ~1000 °C. The reacting fluid is not related to serpentinization which occurs at low temperatures around 130-400 °C (Afanasyev et al. 2014) and creates strongly reducing conditions (McCollom and Seewald 2013). By comparing the morphology (size, cross-section profiles) of experimentally produced positive trigons (de Theije et al. 2001; Forbes 2017; Keltie 2016; this study) to the natural ones on Snap Lake diamonds, I infer that the origin of this high-temperature

fluid is likely to be magmatic, of which the major components are CO_2 and H_2O. while Kopylova et al. (2010) proposed that external carbonatitic fluid, derived from adjacent carbonate in contact with Snap Lake kimberlite, flushed through the dyke and formed the carbonate veins during early crystallization when the melt was still at high temperature. This external fluid may also result in development of positive trigons on Snap Lake diamonds. Thus, further investigation is needed to clarify the origin of the late high-temperature fluid.

The size of positive trigons is generally larger on diamonds from HKM (Figure 3.26a), and roughly correlates with the degree of alteration (Figure 3.20b, 3.20c). It has been found that higher temperature produces larger pits (Fedortchouk 2015; Forbes 2017), and my study shows that positive fO_2 relative to CCO may also affect the trigon size. Therefore, I propose that during formation of positive trigons, the temperature is higher in most fresh sub-lithologies of HKM (HK1 and HK2) than in HKP, and possibly decreases from ~1000 °C in HK1 to < 900 °C in HK6. Oxygen fugacity may also decrease from HK1 around CCO +0.5, to slightly above CCO in HK6.

5.2 Composition of Fluid and Emplacement Conditions of Ekati and Snap Lake Kimberlites

5.2.1 Review of Experimental Data on the Relationship between CO_2/H_2O Ratio in the Fluid and the Parameters of Trigons

The active etchants of diamonds by oxidation at 1 GPa are suggested to be C-O-H fluids rather than silicate or carbonate melts, while the composition of the etching fluids significantly affects diamond morphology and resorption features (Fedortchouk et al., 2007). Fedortchouk et al. (2007) demonstrated that at 1 GPa and 1150-1500 °C, diamonds

oxidized in H_2O fluid show transformation of octahedral morphology into hexoctahedral morphology with six-sided "ditrigonal" {111} faces with only a few flat-bottomed negative trigons and characteristic circular pits. In contrast, diamonds oxidized in CO_2 fluid preserve the primary octahedral shape with trigonal {111} faces covered by numerous point-bottomed negative trigons and a few hexagons; no circular pits are developed. Further AFM examination of negative trigons (Fedortchouk 2015) demonstrated that cross-section profiles of the trigons are regularly flat-bottomed in H_2O fluid, and round- or pointed-bottomed in CO_2 fluid. The relationship between the diameter and the depth of the trigonal pits is found to be another important indicator of the fluid composition (Fedortchouk 2015). Dissolution in H_2O fluid develops trigons with constant diameter and variable depth, while trigons produced in CO_2 fluid have a large range of diameters showing a strong positive correlation with the depth.

The morphological differences experimentally defined at 1 GPa by Fedortchouk et al. (2007) can apply to a wide range of P up to 7 GPa. High-pressure etching experiments conducted at 5.7-7.0 GPa and 1400-1750 °C by Khokhryakov and Pal'yanov (2010) revealed that in the absence of fluids, the secondary morphology and surface features of diamonds are greatly influenced by the CO_2 and H_2O content in the dissolution medium. Diamond dissolution in dry or CO_2-bearing carbonate melt develops positive trigons, and the dissolution morphology changes from trigon-trioctahedron to dodecahedron. In contrast, with the addition of H_2O, diamonds develop ditrigonal {111} faces with negative trigons and evolve into rounded tetrahexahedrons. Hexagons are present only when $CO_2/(CO_2+H_2O)$ is in the range of 0.81-0.87 by weight (Khokhryakov and Pal'yanov 2010).

The mutual solubility of CO_2 and H_2O is limited due to substantial dissimilarity in polarity of covalent bonds. Carbon dioxide molecule has two polar C=O bonds, but the two bond dipole moments cancel out each other due to the linear geometry of CO_2, and the molecule is non-polar. Water molecule has two polar O−H bonds in a bent geometry, resulting in a net dipole so that the molecule is polar. The mutual solubility of CO_2 and H_2O also depends on P, T and X_{CO2} (Diamond 2003). Zhang (2016) showed that at 1-3 GPa and 1250 °C, a miscibility gap occurs in the binary CO_2-H_2O system and two fluid phases (aqueous and carbonic) coexist over a wide range of P–X conditions. According to Zhang (2016), at 1 GPa and 1250 °C, the bulk molar X_{CO2} (CO_2/(CO_2+H_2O) controls the relative volume proportion of aqueous and carbonic fluids, which determines the resorption morphology of diamonds. Four diamond resorption morphologies are defined by Zhang (2016): (1) pure H_2O resorption morphology (ditrigonal {111} faces, negative trigons, striations, circular pits, and hillocks) when $X_{CO2} = 0$. (2) aqueous resorption morphology (similar to pure H_2O resorption but circular pits are absent) when $X_{CO2} \leq 0.5$. (3) carbonic resorption morphology (trigonal {111} faces and truncated negative trigons) when X_{CO2} = 0.5-0.9. (4) pure CO_2 resorption morphology (trigonal {111} faces, hexagons, truncated/non-truncated positive trigons) when X_{CO2} = 0.9-1. An important indicator of $X_{CO2} > 0.5$ is the truncation of negative trigons, measured as $L_{100}/(L_{100}+L_{111})$ that shows the degree of conversion from negative trigons into hexagons and eventually positive trigons.

5.2.2 Composition of Fluid in Ekati Kimberlites

Fedortchouk (2015) examined diamonds from Ekati kimberlites and compared the diamond resorption morphologies, particularly the shape of cross-section profiles and

diameter vs. depth relationships of the trigons, to the results of dissolution experiments conducted at 1 GPa and 1150-1350 °C in the presence of H_2O or CO_2 fluid. It was suggested by Fedortchouk (2015) that Koala and Grizzly pipes had H_2O-rich kimberlitic fluids, with fluids in Koala showing a lower temperature compared to those in Grizzly, as the f/b trigons on Koala and Grizzly diamonds morphologically resemble the ones produced in H_2O fluid at 1150 and 1350 °C, respectively. The fluids in the Misery pipe were relatively more CO_2-rich and separated at depth, evidenced by the common presence of p/b trigons with a strong positive relationship between diameter and depth, and the high diamond grade accompanied by high proportion of rounded stones, which was interpreted as the result of fast-rounding of diamonds without notable weight loss due to dissolution at high pressure (Zhang et al. 2015). Zhang (2016) concluded that Fox, Koala, Misery and Grizzly kimberlites were once all H_2O-rich, supported by the occurrence of diamonds with pure-H_2O (circular pits on THH faces) or aqueous resorption morphologies in these pipes. Both authors pointed out that the fluids in Grizzly were lost during emplacement, because diamonds from Grizzly show irregular sharp features that are similar to the products of fluid-loss runs at 1 GPa by Fedortchouk et al. (2007).

In my study, examination of the geometry of negative trigons on Ekati diamonds detected notable variation in the diameter-depth relationships of trigons that can be ascribed to differences in CO_2/H_2O ratios in kimberlitic fluids between pipes, similar to the results of Fedortchouk (2015). The trigons on Panda and Koala diamonds show constant diameter with variable depth (Figure 4.16c, 4.17e) and the ubiquitous f/b trigons have simple forms (e.g. Figure 4.23, 4.26, 4.28) resembling the trigons produced in H_2O fluid at 1150 °C by Fedortchouk (2015). This suggests a low CO_2/H_2O ratio of the fluid

compositions in Panda and Koala. All four selected Misery diamonds have ditrigonal {111} faces with well-defined striations along the resorbed edges (Figure 2.6) indicating the kimberlitic fluid was H_2O-rich, whereas the strong positive correlation between diameter and depth of trigons (Figure 4.16g) on Misery diamonds, and the prevalence of p/b trigons implies a higher CO_2/H_2O ratio of the fluid compared to Panda and Koala. Moreover, the morphologies of f/b (some of which show complex stepped walls, Figure 4.30c) and p/b trigons on Misery diamonds are most similar to the trigons produced in CO_2 fluid at 1150 and 1250 °C by Fedortchouk (2015), respectively.

As for Fox, the two selected diamonds both have ditrigonal {111} faces with fine striations along the edges that are typical H_2O-rich resorption features, while f/b and p/b negative trigons are both present. Fedortchouk (2015) reported that the depth range of the AFM scans of diamond surfaces from H_2O fluid runs is two-to-three times shallower than from CO_2 runs. Although I did not scan the entire {111} face of the studied diamonds, my limited AFM data and estimates from optical microscopy show that the depths of the negative trigons on Fox diamonds are generally shallower than those on diamonds from Koala, Panda and Misery. The trigons on Fox diamonds resemble those produced in H_2O fluid at 1250 and 1350 °C by Fedortchouk (2015). Thus, I infer that Fox may have had kimberlitic fluid with the lowest CO_2/H_2O ratio compared to the other three pipes.

Additionally, there are some diamonds from each pipe showing truncated negative trigons, which is an indicator of bulk $X_{CO2} > 0.5$ (Zhang, 2016). It is not clear whether these truncated trigons resulted from resorption in mantle fluids with CO_2-rich composition, or in the CO_2-rich fluid phase separated from the binary CO_2-H_2O system due to immiscibility as suggested by Zhang (2016).

Skinner and Marsh (2004) suggested that the different CO_2/H_2O ratios in kimberlitic fluids control the pipe morphology and internal geology of kimberlites. According to Skinner and Marsh (2004), Class 1 and 3 kimberlites both contain H_2O-rich fluids and tend to crystallize at depth compared to Class 2 kimberlite, which has CO_2-rich fluids and can rise to very shallow levels and interact with groundwater, resulting in phreatomagmatic eruption. Class 3 kimberlites differ from Class 1 kimberlites compositionally and may have crystallized earlier (i.e. deeper), forming a lithological barrier and gas trap for later upwelling volatile-rich magma, which led to explosive eruption due to accumulation of gas. This model assumes that the influence of the CO_2/H_2O ratio in the fluid phase on the kimberlite solidus is similar to that for peridotite (Wyllie 1987), that H_2O-rich magma has a more depressed solidus than the CO_2-rich magma (Figure 1.1). Similarly, Moussallam et al. (2016) proposed H_2O-rich magmas for Class 1 and 3 kimberlites and CO_2-rich magmas for Class 2 kimberlites, but explained the variety of kimberlite types by variation of CO_2 and H_2O solubility in kimberlite magmas with different original volatile composition. H_2O-rich kimberlite tends to initiate pipe formation by degassing at greater depth than CO_2-rich kimberlite since an increase in the H_2O content lowers the CO_2 activity and forces the CO_2 to exsolve, while CO_2-rich magma preserves most of the volatiles to shallower depth where phreatomagmatic eruption occurs. My results support the conclusions of these authors that Class 1 and 3 kimberlites are H_2O-rich. The inferred CO_2/H_2O ratios for the four Ekati kimberlites also give estimate for the relative depth of volatile exsolution, as shown in Figure 5.4. Fox and Misery kimberlites had the greatest and shallowest depths of volatile exsolution, respectively. Panda and Koala had similar intermediate depth of volatile exsolution.

The reconstruction of fluid composition from my study of trigons also agrees with the existing mineralogical and petrographic data. Armstrong et al. (2004) recognized two distinct types of kimberlites in the Ekati Mine property: dolomite-bearing and carbonate-bearing kimberlites. The Misery and Koala kimberlites belong to the calcite-bearing group that was suggested to originate from magmas with lower CO_2/H_2O ratios (Armstrong et al. 2004; Crawford et al. 2006; Nowicki et al. 2004; Nowicki et al. 2008). However, there are mineralogical differences between these two pipes. According to Armstrong et al. (2004), phenocryst and groundmass phlogopite is a major phase in Koala and less abundant in Misery, whereas Koala lacks carbonate phenocrysts and micro-phenocrysts, which are present in Misery. This agrees with my conclusions from the diamond resorption morphology that the kimberlitic fluid in Koala kimberlite had a low CO_2/H_2O ratio, while Misery kimberlite contained more CO_2-rich fluid. Additionally, both Koala and Misery contain abundant Sr–Ba calcite segregations that were presumably formed at temperatures above 600 °C (Armstrong et al. 2004), only the calcite segregations and phenocrysts of calcite in Misery are mantled by narrow rims of calcite-dolomite solid solution, which was suggested to form by precipitation of magmatic fluids (Armstrong et al. 2004). If the fluid had high temperatures > 600 °C, it may have induced resorption of diamonds (Fedortchouk and Canil 2009), which could explain the negative trigons on Misery diamonds showing features (common p/b trigons, positive correlation of diameter and depth) that are thought to be produced by CO_2-rich fluids.

5.2.3 High-temperature Fluids in Different Lithofacies of Snap Lake Kimberlite Dyke

Diamonds from the phlogopite-rich facies (HKP) show a higher degree of resorption compared to the main phlogopite-poor coherent facies (HKM), which is evident from the much lower O/THH ratio of diamonds from HKP (Table 4.1). The main morphological groups (SG1, SG2, and SG6) are similar for diamonds from HKM (HK-1, 2), and HKP (HK-4, 6) (Figure 4.5). The SG2 and SG6 morphological groups represent aqueous resorption based on the criteria of Fedortchouk et al. (2007), suggesting that the fluids in Snap Lake kimberlite were H_2O-rich. However, diamonds showing edges with sharp features (Type I) generally compose a higher proportion of total stones in HKM (HK-1, 2) than in HKP (HK-4, 6), while a higher proportion of stones with smooth features on edges (Type II) is present in HKP (Figure 4.6). The Type III edges are only found on SG8 and SG11 diamonds and present on stones from HK1 and HK5. The lower O/THH ratio and the more common Type II edges of diamonds from HKP indicate the magmatic fluid may have been more H_2O-rich in HKP than HKM. Fedortchouk et al. (2007) suggested that H_2O fluid facilitates diamond rounding and produces relatively smooth surfaces compared to CO_2 fluid. The lower O/THH ratio of diamonds in HKP may also be related to earlier volatile exsolution (Zhang et al., 2015). These preliminary interpretations are further supported by the geometry of etch pits on diamonds. The negative trigons, trigon-hexagons, and hexagons from HKP and HKM are predominantly flat-bottomed, indicating aqueous resorption, but the pits show different diameter vs. depth trends (Figure 4.14a). The pits on diamonds from HKP show clustering of diameters at < 10 μm, 15-20 μm, and one at 35 μm, but the depth of pits with similar diameters can be variable. This is similar to observations of Grizzly and Koala diamonds and products of experiments in H_2O-rich

fluid (Fedortchouk 2015). The pits on diamonds from HKM show a positive correlation of diameter and depth, and their trend coincides with the trend shown by trigons on Misery diamonds. This positive correlation for Misery diamonds was interpreted to result from more CO_2-rich fluid (Fedortchouk 2015). In conclusion, I propose a H_2O-rich C-O-H magmatic fluid in both HKM and HKP with a higher CO_2/H_2O ratio in HKM than in HKP. This may also explain the abundant phlogopite crystallization in HKP lithology, since a higher H_2O activity would favor crystallization of phlogopite (Edgar and Arima 1983).

Unlike trigons on Ekati diamonds, all the negative trigons on Snap Lake diamonds developed truncated corners. Zhang (2016) suggested the truncated corners were produced by resorption in fluids with bulk $X_{CO2} > 0.5$. Instead, I propose that the truncated corners of negative trigons can also be formed by overprint of positive trigons. The degree of negative trigon converted into hexagon can be expressed as $L_{100}/(L_{100}+L_{111})$, calculated as the total length of sides of positive directions divided by the perimeter of the pit (Figure 5.3a). The following nomenclature was proposed by Zhang (2016): sides in the positive direction show tetragons on walls, indicating a {100} face, the walls of these sides are denoted as W_{100}, and the length as L_{100}; and sides in the negative direction show trigons on walls, indicating a {111} face, the walls of these sides and their length are denoted as W_{111} and L_{111}, respectively. Figure 5.3b shows that when the diameter of the pits decreases, the degree of negative trigons converted into hexagons increases. Figure 5.3c shows the absolute value of L_{100} lengths for negative trigons on diamonds from the five kimberlite lithologies, which cluster in a small length range on each diamond. Also, the negative trigons on Snap Lake diamonds show micro-steps only on truncated corners, and the micro-steps are identical to those present in positive trigons. The truncated trigons produced in

dissolution experiments by Zhang (2016) (Figure 5.6a, 5.6b) and those on Ekati diamonds (Figure 5.6c) have micro-steps on all the sides and corners. All these features imply the truncated corners are formed by positive trigons overprinting the pre-existing negative trigons. The results of our oxidation experiments and other studies (Forbes 2017; Keltie 2016) suggest the development of positive trigons is due to a late-stage resorption event close to the surface by fluids with relatively high temperatures at 700-1000 °C.

The CO_2/H_2O ratio of fluids in Snap Lake kimberlite may have been lower than any of the four studied Ekati kimberlites, indicated by the dominance of f/b negative trigons on diamonds in the two Snap Lake parcels (I only observed p/b trigons on one diamond SNP10-6). This could have resulted from greater depth of volatile exsolution and the crystallization of Snap Lake kimberlite to form the dyke, whereas the Ekati kimberlites, containing fluids with relatively higher CO_2/H_2O ratios, tended to reach shallower depth and form pipes (Figure 5.4). Indeed, the recent experimental study by Moussallam et al. (2016) demonstrated that for kimberlite-like melts, H_2O reaches its solubility limit at depths greater than CO_2. Thus, the more H_2O–rich Snap Lake kimberlite magma could have solidified at greater depths via earlier exsolution of fluid.

5.3 Mechanism of Diamond Resorption

5.3.1 Role of Defects vs. Dissolution Conditions

Diamond resorption can be affected by the internal properties of diamond (e.g. crystal forms, defects) (Harrison and Tolansky 1964; Mendelssohn and Milledge 1995; Sunagawa 1984), and dissolution conditions (P-T-fO_2-X (composition of the etchants)) (Arima and Kozai 2008; Fedortchouk et al. 2007; Khokhryakov and Pal'yanov 2007a; Kozai and Arima 2005; Yamaoka et al. 1980; Zhang et al. 2015). Defects (e.g. cracks,

dislocations, growth imperfections) on diamond surfaces may result in faster etch rates than the nearby perfect regions (Harrison and Tolansky, 1964), while N content and aggregation state in the diamond lattice may affect the size and density of etch pits (Mendelssohn and Milledge 1995). Furthermore, Khokhryakov and Palyanov (2006, 2007b) proposed that etch pits showing distinct wall angles, shapes, or distribution are correlated with certain types of internal defects. In addition, studies on albite dissolution showed that deep p/b etch pits can be formed only when ΔG (difference of Gibbs free energy between the bulk crystal and its dissolved molecules) is large enough to open hollow cores around the screw dislocation centers, otherwise dissolution of the crystal produces no etch pits, or just shallow f/b pits at edge dislocations or point defects (Lüttge 2006).

However, some studies argued that in natural diamond dissolution in kimberlite magma the effect of defects is very limited on diamond resorption morphology and geometry of etch pits compared to external dissolution conditions. (Fedortchouk et al. 2007; Zhang 2016; Zhang and Fedortchouk 2012). Similar resorption morphologies are found between diamonds with different external forms (octahedral vs. step-faced octahedral diamonds) under the same dissolution conditions (Arima and Kozai 2008; Fedortchouk et al. 2007; Khokhryakov and Pal'yanov 2007a; Kozai and Arima 2005; Yamaoka et al. 1980; Zhang et al. 2015). The effect of N content and aggregation state on diamond resorption morphologies suggested by Mendelssohn and Milledge (1995) is not supported by my study of Snap Lake diamonds (see Chapter 4.4.2). The lack of correlation between N defects and resorption morphologies is also supported by other studies (Fedortchouk et al. 2007; Zhang et al. 2015), where similar resorption morphologies were found on diamonds

from various sources, with potentially different N contents and aggregation states, under similar dissolution conditions.

Zhang et al. (2015) proposed three stages for the formation of etch pits: the first stage is "defect-controlled" where etch pits initiate at defect sites; the second stage is the "competition" stage, where the degree of distortion caused by defects at the outer rims of the etch pits decreases during the enlargement, and in turn the effect of dissolution conditions progressively increases. In the last "condition-controlled" stage, dissolution conditions overcome the effect of defects on etch pit growth and completely control the removal rate of 2-bonded and 3-bonded carbon atoms, which determines the final morphology of etch pits.

My measurements of trigons on experimental and natural diamonds support the model proposed by Zhang et al. (2015) and suggest that defects play an important role for growth of pits with diameter < 5 μm. The small positive trigons (mostly diameter < 5 μm) show various shapes of cross-section profiles and pit outlines (straight, curved) on diamonds oxidized under same conditions (AL-5 and Exp17), and on Snap Lake diamonds from the same lithofacies with presumably the same dissolution conditions, indicating these trigons are still in the "defect controlled" or "competition" stage. Later the growth of positive trigons can be controlled by dissolution conditions when their size increases, as the large positive trigons (diameter > 15 μm) developed on diamond Exp10 show similar morphologies with constant wall angles ~2º, suggesting these trigons are in the "condition-controlled" stage. The "holes" on the bottom of these trigons with various wall angles can be associated with downward development of pits around newly outcropped defects. In addition, Keltie (2016) showed that the experimentally produced positive trigons (diameter >

10 μm) retained the same cross-section profile as their diameter increased during repeated etching. The negative trigons (mostly > 5 μm in diameter, except for the trigons on Koala diamonds) measured by AFM on diamonds from the same kimberlite have similar morphology, such as the dominantly f/b trigons on Snap Lake diamonds, or resemble trigons experimentally produced in certain P-T-X conditions (see Chapter 5.2.2), such as the negative trigons on Ekati diamonds. These features indicate the growth of negative trigons is already in the "condition-controlled" stage.

5.3.2 Evolution of Trigonal Pits during Their Growth

Based on observation of experimentally produced and natural positive trigons, my inferred evolution of positive trigons is summarized below.

(1) Point-bottomed or flat-bottomed embryonic pits (diameter < 1 μm) are first formed (Figure 3.11, 3.12a). The pits initiated at dislocations will be point-bottomed, and those initiated at surface defects or foreign particles will be flat-bottomed; pits initiated at point defects will have tiny size (diameter < 0.2 μm) (de Theije et al. 2001). However, the resolution of the AFM scanner used does not allow reliable determination of the type of bottom and wall for these embryonic pits.

(2) As the size increases (1-5 μm in diameter), the trigons may form three groups: p/b and f/b trigons show a roughly positive relationship between diameter and depth, and c/b trigons cluster in a small range of diameter and depth (Figure 3.26b). The p/b and f/b trigons can have U, V, Y type walls (Figure 3.22, 3.23), and may show asymmetric shapes (Figure 3.23a), while c/b trigons have U type walls and curved sides (Figure 3.24e, 3.24f). During continuous growth (5-10 μm in diameter), the f/b trigons may develop multiple

steps (Figure 3.10c), and the c/b trigons may evolve into f/b trigons with curved sides (Figure 3.24c, 3.24d), whereas p/b trigons retain their original shape.

(3) After the diameter is larger than 10 μm, the p/b trigons may evolve into f/b trigons (Figure 3.12d), or develop a deep hole on the bottom (Figure 3.12f). The f/b trigons with curved sides may develop truncated (or multiple) corners (Figure 3.24c, 3.24d).

Based on observation of negative trigons on Snap Lake and Ekati diamonds, my inferred evolution of negative trigons is summarized as follows.

(1) Similar to positive trigons, embryonic pits (diameter < 1 μm) are formed first (Figure 4.30). They can develop on bottoms of the larger negative trigons.

(2) The pits may show positive correlation of diameter and depth (Figure 4.16g) or constant diameter with variable depth (Figure 4.16c, 4.16e) when the size increases. The p/b trigons will probably develop into f/b trigons, as the p/b trigons on Snap Lake diamonds are all smaller and shallower than most of the negative trigons (Figure 4.14b). Based on my empirical observation, with the increase of diameter and depth the p/b trigons develop Y type walls (Figure 4.20e, 4.29c), while f/b trigons show U (Figure 4.30d) or Y type (Figure 4.19e, Figure 4.28d) walls instead. However, the exact evolution process is not clear.

5.3.3 Testing of Etching Model for a {111} Diamond Surface

Angus and Dyble (1975) developed a mathematical model for the formation of negative trigons, which includes two limiting etching regimes (single-kink and multiple-kink mechanisms) that are both based on kink propagation by sequential removal of 2-/3-bonded C atoms along <$\bar{1}$10> steps around a central initiating defect (Figure 5.5a, left). For

the enlargement of a negative trigon, first removal of one 3-bonded atom (single kink mechanism) or multiple 3-bonded atoms (multiple kink mechanism) is needed so that 2-bonded atoms can be removed in reverse direction from one kink site or multiple kink sites, which eventually enlarges the trigon by one row in a <112> direction (Figure 5.5b, left). Formation of negative trigons requires that the 2-bonded atoms are more vulnerable to removal than 3-bonded atoms, i.e. $k_2 > k_{3e}$, where k_2 and k_{3e} are specific removal rates of 2-bonded and 3-bonded atoms on edges. This is energetically favorable in most cases, and agrees with the fact that negative trigons are far more common than positive trigons on natural diamonds. Positive trigons will form only when $k_2 < k_{3e}$, which can be reached by forming certain complexes such as a bridge formation of oxygen on the steps of positive directions (Frank and Puttick 1958; Yamaoka et al. 1980).

According to Angus and Dyble (1975), when $k_2/k_{3e} \gg N^2$, negative trigons are developed by single-kink mechanism with slope:

$$m = \frac{k_d}{6k_{3e}r}$$

where N is number of atoms on the edge of an initial central defect; m is atomic unit defined by Angus and Dyble (1975), $m = 1$ stands for one $<\bar{1}10>$ row of X-O-X-O that has been removed horizontally and vertically. The relationship between m and $\alpha_{\{111\}}$ is $\alpha_{\{111\}} = 0.9428m$; k_d is the rate constant of step nucleation in the vertical direction; r is the number $<\bar{1}10>$ rows between trigon center and edge (Figure 5.5c). Thus, the $\alpha_{\{111\}}$ of etch pit walls decreases when the distance from the trigon center increases, showing Y type shape (Figure 5.7a).

If the initial central defect is large enough so that $k_2/k_{3e} \ll N^2$, negative trigons are developed by solely multiple kink mechanism with slope:

$$m = \frac{k_d}{(2k_2k_{3e})^{\frac{1}{2}}}$$

In this case, the $\alpha_{\{111\}}$ of etch pit walls remains constant, showing V type shape (Figure 5.7b). A small trigon ($k_2/k_{3e} \ll N^2$) will grow first by single kink mechanism and then by multiple kink mechanism, the switch occurs when the pit reaches a size when $k_2/k_{3e} \approx N^2$, which gives

$$\mathrm{r} \approx \frac{1}{6}\left(\frac{k_2}{k_{3e}}\right)^{\frac{1}{2}}$$

The cross-section profile of the pit developed by this mixed single-multiple mechanism will also have Y type shape (Figure 5.7c). In addition, Angus and Dyble (1975) suggested that p/b and f/b trigons are formed by etching at dislocation outcrops and large shallow defects (dislocation loop, ring crack, inclusion), respectively.

The model by Angus and Dyble (1975) and predict Y type walls for smaller pits, and V or Y type wall for larger pits, which is presumably to be applicable for both negative and positive trigons. My measurements of trigonal pits on natural and experimental diamonds agree with the prediction of the model proposed by Angus and Dyble (1975), showing that V type walls occur in generally larger pits (Figure 5.8), while Y type walls can occur in small pits (Figure 5.8b) as well as in large pits (Figure 5.8a, 5.8c). However, there are a few discrepancies: (1) The U type walls present in both negative and positive

tigons cannot be explained by the model in Angus and Dyble (1975); (2) Some trigons have Y type walls consisting of two straight segments (Figure 3.10b), and some trigons with walls that I defined as Y type show combination of U and Y type walls (Figure 4.24f, 4.27e, 4.29c). These walls are different from the Y type walls with convex shape formed by single-kink mechanism (Figure 5.7a), or the Y type walls formed by mixed single-multiple kink mechanism showing upper walls with straight shape and lower walls with convex shape (Figure 5.7c); (3) Both negative and positive trigons can show complex forms such as multiple steps, and some positive trigons have curved bottoms or sides. These features are not predicted by the model in Angus and Dyble (1975). All the discrepancies indicate that the formation of trigons does not simply follow the kink mechanism.

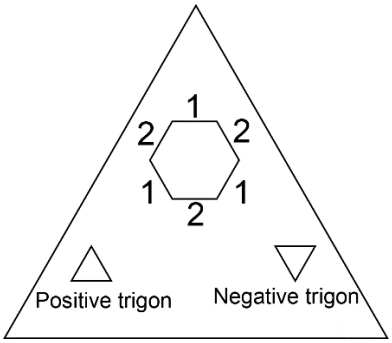

Figure 5.1 Step 1 and 2 on the {111} face of a diamond, reproduced from Yamaoka et al. (1980).

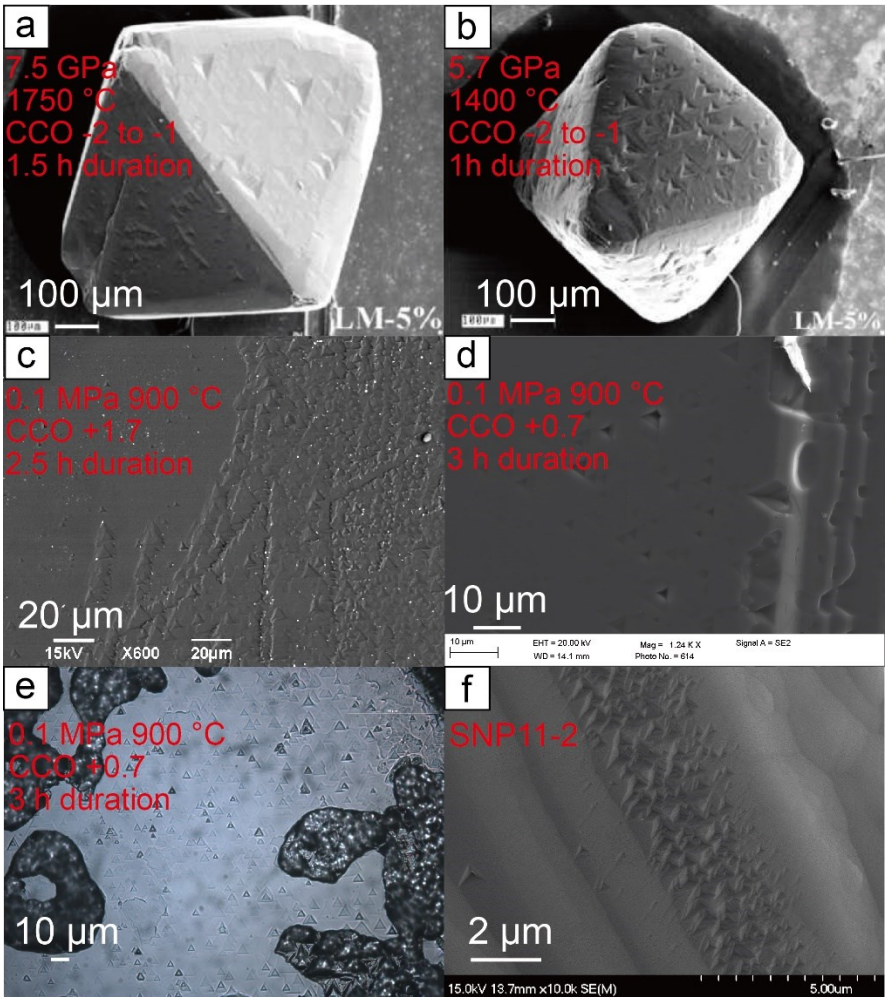

Figure 5.2 Comparison of positive trigons produced under high pressures (a, b) by Khokhryakov and Pal'yanov (2010) and atmospheric pressure (c-e) in this study, and natural positive trigons on Snap Lake diamond SNP11-2 (f).

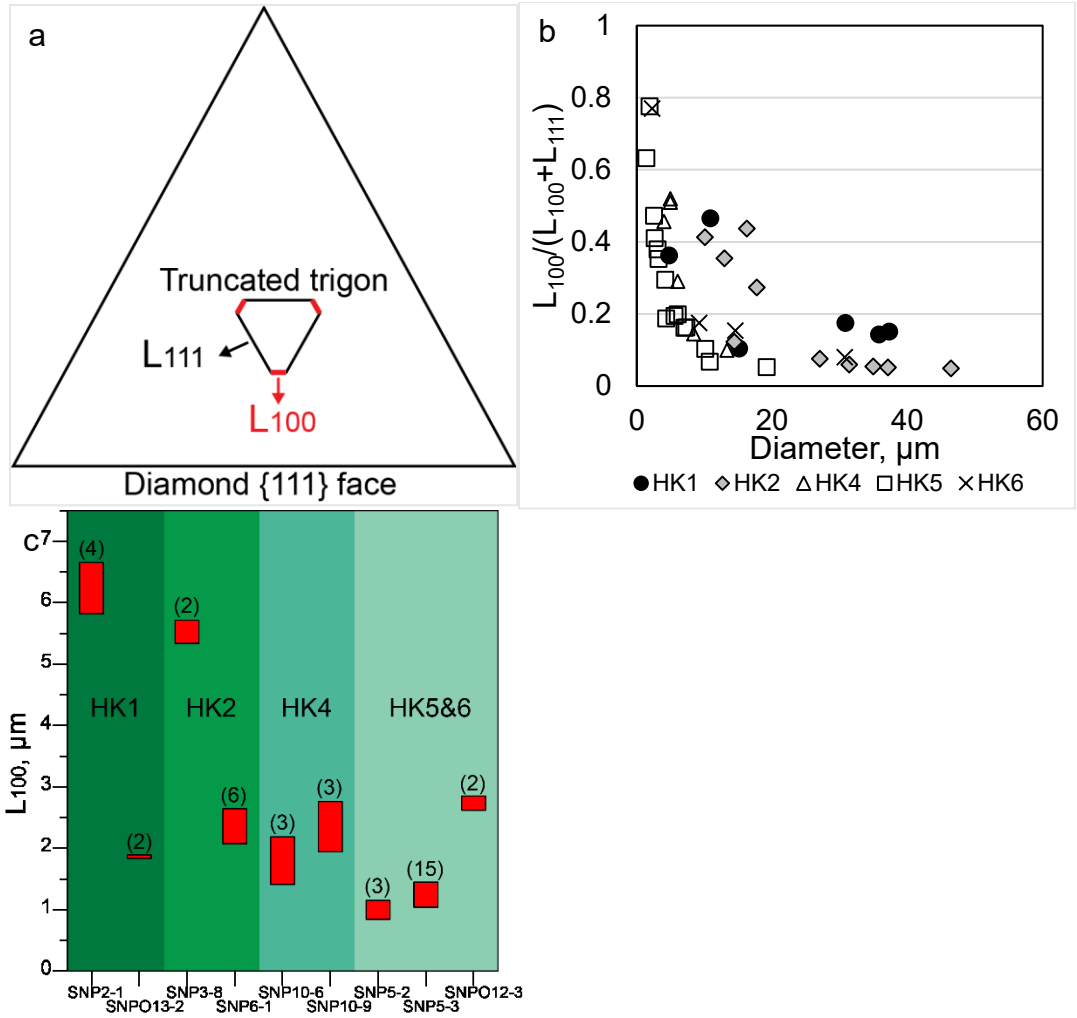

Figure 5.3 (a) Illustration of the length of sides measured as L_{100} (marked in red) and L_{111} (in black) of a truncated negative trigon; (b) The relationship between $L_{100}/(L_{100}+L_{111})$ and diameter of the measured etch pits on diamonds from different lithofacies. (c) The absolute L_{100} values of etch pits measured on diamonds from different lithofacies, the numbers of measured pits are shown in brackets.

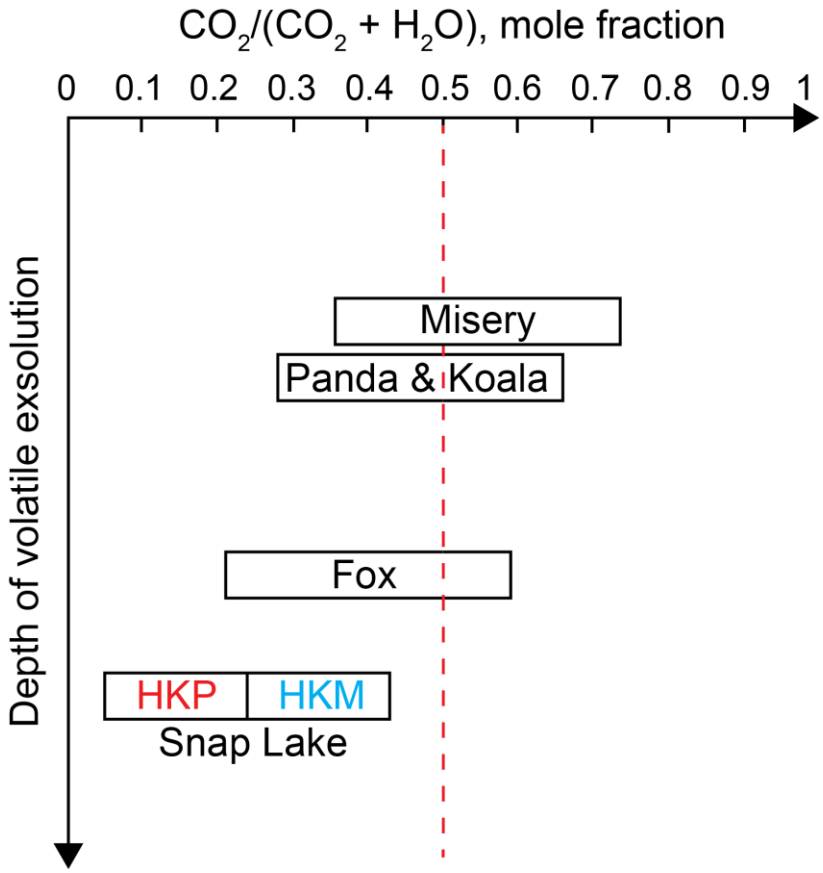

Figure 5.4 Relative depth of volatile exsolution and molar X_{CO2} of fluids for Snap Lake kimberlite and four studied Ekati kimberlites speculated from AFM study on trigons.

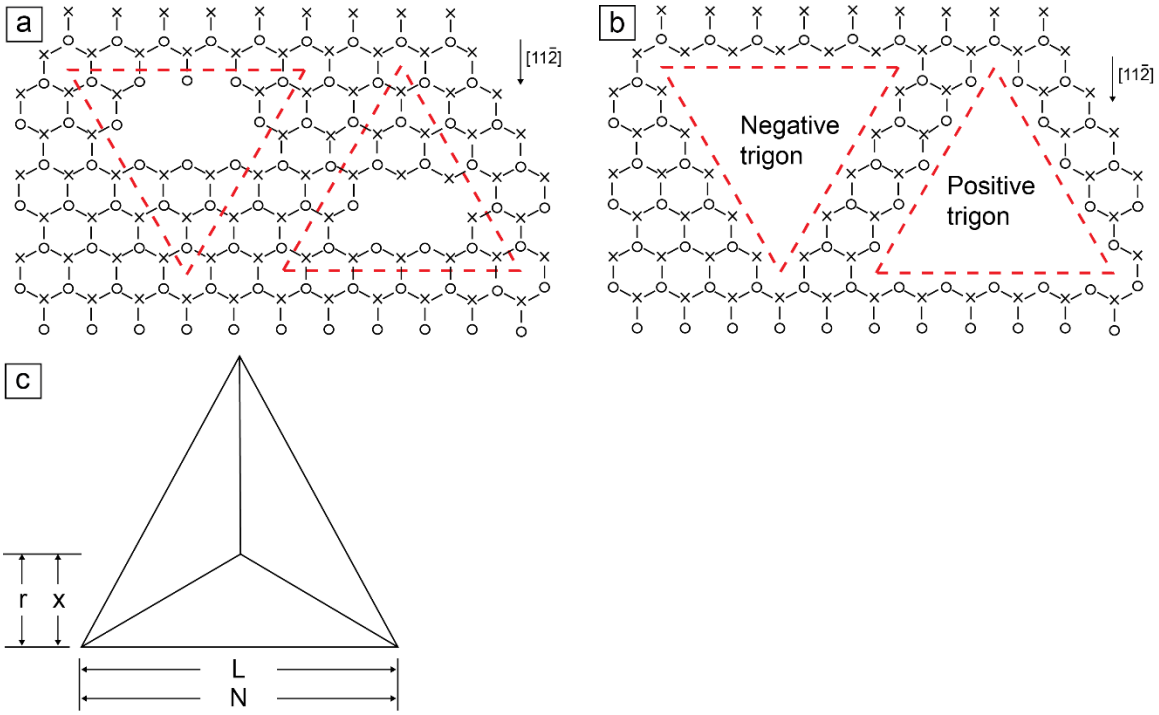

Figure 5.5 Atom removal processes from {111} diamond face. X is a top layer atom bonded to layer below. O is a top layer atom not bonded to a layer below. Image (a) shows arbitrary holes in the outer layer. Image (b) shows negative and positive trigons formed after removal of atoms inside the dashed line. Image (c) shows the geometry of a trigon. N = number of atoms, L = length of trigon edge; r = number of <$\bar{1}$10> rows of X-O-X-O atoms between trigon center and step; x = geometric distance between trigon center and step. The y axis (depth, as shown in Figure 4.6) is normal to the plane of the figure. Revised from Angus and Dyble (1975).

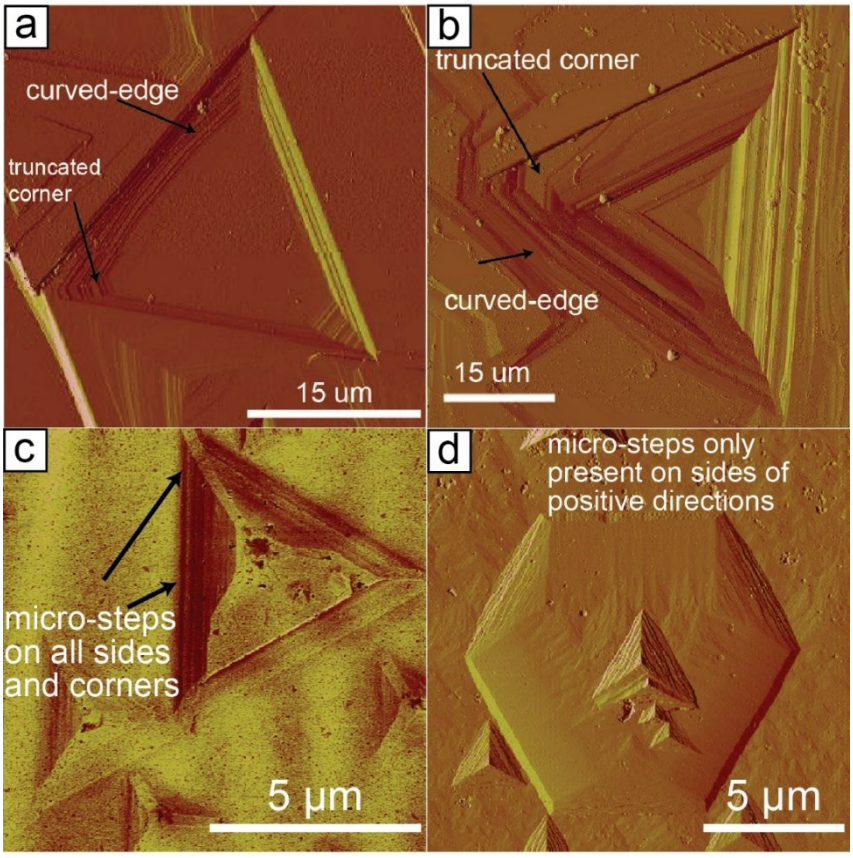

Figure 5.6 Comparison of truncated corners in trigons experimentally produced by Zhang (2016) (a, b), and natural trigons on diamonds from Grizzly pipe (c) and Snap Lake dyke (d).

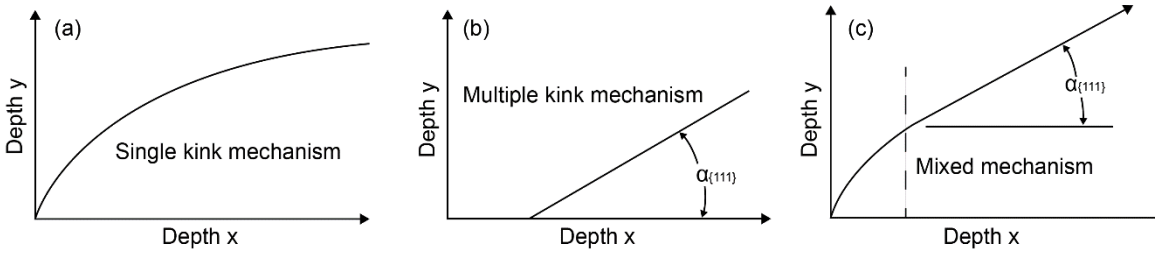

Figure 5.7 Cross-section views showing effect of kink mechanism on trigon wall slope proposed by Angus and Dyble (1975). (a) shows slope developed by single-kink mechanism, the $\alpha_{\{111\}}$ of the trigon wall will decrease as the distance from the centre of the trigon increases. (b) shows slope developed by multiple-kink mechanism, the $\alpha_{\{111\}}$ of the trigon wall will remain constant. (c) shows slope developed by mixed single-multiple mechanism. Modified after Angus and Dyble (1975).

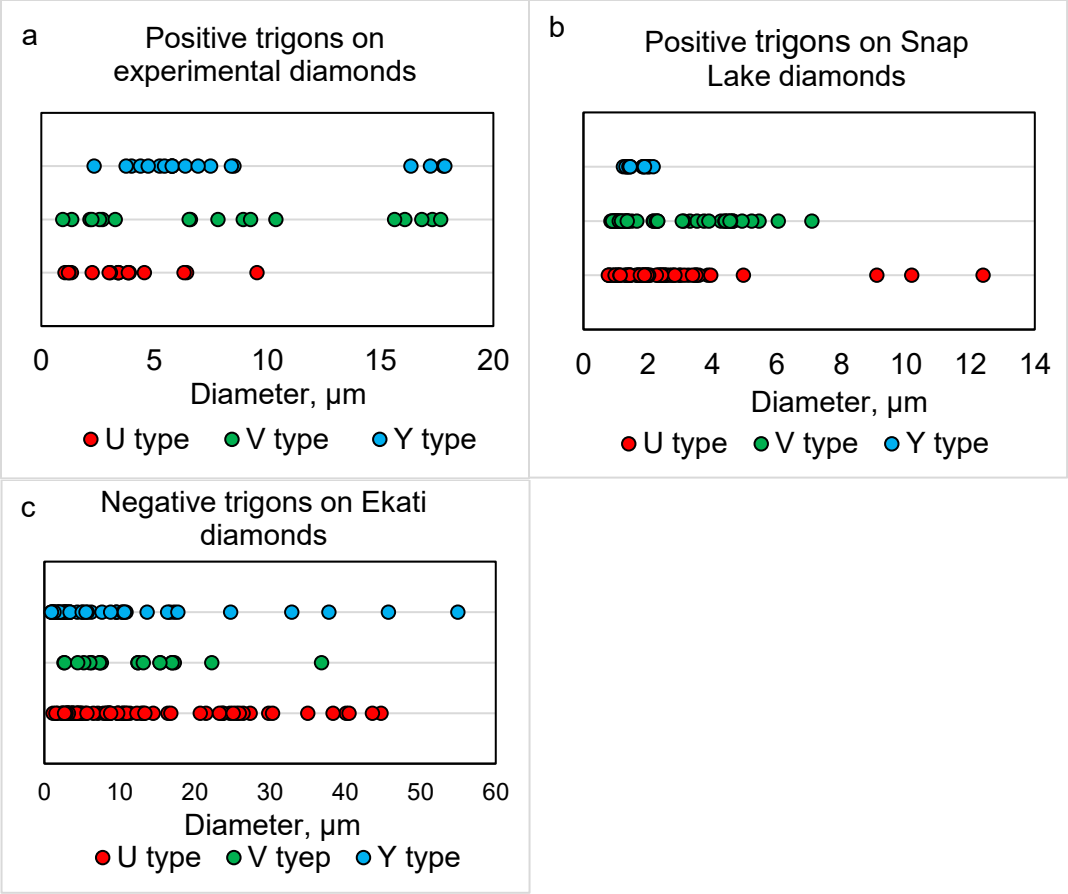

Figure 5.8 Diameters of positive trigons with U, V and Y type walls on experimental diamonds in this study (a), on Snap Lake diamonds (b), and negative trigons with U, V and Y type walls on Ekati diamonds.

CHAPTER 6. CONCLUSIONS

6.1 Use of AFM Measurements of Etch Pits to Reconstruct Kimberlite Emplacement Conditions

My study demonstrated that measurements of etch pits on diamonds can be used to reconstruct the kimberlite emplacement conditions, in terms of crystallization temperature and fO_2. By comparing the positive trigons on Snap Lake diamonds to trigons produced at 0.1 MPa and 900-1050 °C under controlled fO_2 of $\log fO_2$ = -9 to -16, I suggest that positive trigons on Snap Lake diamonds are produced by a late-stage resorption event, which occurred near to the surface at low pressure and in fluids with relatively high temperature of ~900-1000 °C. The development of positive trigons overprinted and added truncated corners to all the pre-existing negative trigons. Results of our oxidation experiments and other studies (Fedortchouk 2015; Forbes 2017) showed that positive trigons are enlarged with increasing temperature and fO_2. The size variation of positive trigons on Snap Lake diamonds from different lithofacies indicates that temperature was higher in HKM than in HKP during positive trigon formation, and possibly decreased from ~1000 °C in HK1 to < 900 °C in HK6. Oxygen fugacity may also have decreased from HK1 around CCO +0.5, to slightly above CCO in HK6.

Comparison of negative trigons on Ekati diamonds to trigons experimentally produced in H_2O or CO_2 fluids at 1GPa and 1150-1350 °C by Fedortchouk (2015) allows for relative estimation of crystallization temperatures during the formation of negative trigons. Fox had s relatively higher crystallization temperature than Misery. Panda and Koala had similar crystallization temperatures which were lower than those in Fox and Misery.

6.2 Contribution to Understanding Fluid System in Kimberlite Magma

The presence of diamonds showing aqueous resorption morphology (ditrigonal {111} faces, a few f/b negative trigons) and the dominance of f/b negative trigons detected by AFM revealed that fluids were H_2O-rich in the Snap Lake kimberlite. The diamonds from HKM show a higher O/THH ratio than stones from HKP, with negative trigons showing strong positive correlation between diameter and depth, which is similar to products from experiments in CO_2-rich fluid (Fedortchouk, 2015), while negative trigons on diamonds from HKP lack apparent correlation between diameter and depth. These features suggest that HKM and HKP vary had different fluid compositions, with fluids in HKP more H_2O-rich.

Examination of the geometry of negative trigons on Ekati diamonds from Fox, Panda, Koala, and Misery detected notable variation in CO_2/H_2O ratios in kimberlitic fluids between pipes, similar to the results of Fedortchouk (2015). The trigons on Panda and Koala diamonds show constant diameter with variable depth and the ubiquitous f/b trigons have simple forms resembling the trigons produced in H_2O fluid at 1150 °C by Fedortchouk (2015), suggesting low CO_2/H_2O ratio of the fluids in Panda and Koala. All four selected Misery diamonds have ditrigonal {111} faces with well-defined striations along the resorbed edges (Figure 2.6) indicating the kimberlitic fluid was H_2O-rich, while the strong positive correlation between diameter and depth of negative trigons, the prevalence of p/b trigons and resemblance of trigons to those produced in CO_2 fluid at 1150 and 1250 °C produced by Fedortchouk (2015), imply a higher CO_2/H_2O ratio of the fluid in Misery than the fluids in Koala and Panda. My limited AFM data and estimates from optical microscopy

show that negative trigons on Fox diamonds are generally shallower than those on diamonds from the other three pipes, and the trigons on Fox diamonds are most similar to those produced in H_2O fluid at 1250 and 1350 °C by Fedortchouk (2015). I infer that Fox may have had the kimberlitic fluid with the lowest CO_2/H_2O ratio, compared to the fluids in Panda, Koala and Misery.

The results of my study support the proposal by Skinner and Marsh (2004) that Class 1 and 3 kimberlites contain H_2O-rich fluids. The CO_2/H_2O ratio of fluids in Snap Lake kimberlite may have been lower than any of the four studied Ekati kimberlites, indicated by the dominance of f/b negative trigons on diamonds in the two Snap Lake parcels. The highly H_2O-rich Snap Lake kimberlite may have crystallized at depth and formed a dyke due to deeper exsolution of volatiles (Moussallam et al. 2016), while the Ekati kimberlites containing fluids with relatively higher CO_2/H_2O ratio tended to reach shallower depths and initiated pipe formation (Skinner and Marsh 2004).

6.3 Further Directions

To confirm my proposal that the presence of positive trigons is unique to diamonds from dykes, more samples from dykes and pipes of the same kimberlite body intruded into different geological settings need to be examined. If more diamonds with positive trigons are found from kimberlites with/without external source of fluid, it may help to clarify whether the fluid that produced positive trigons was magmatic or derived from adjacent carbonate as described by Kopylova et al. (2010). Also, more diamond oxidation experiments at pressure < 1 GPa are needed to quantify the depth of formation of positive trigons.

To clarify the evolution of etch pits, future work should focus on measuring trigons initiated at certain defect types during repeated etching under controlled P-T-X. For tracing the growth of pits from the embryonic stage, an AFM scanner of higher resolution (E scanner, maxim coverage 10 μm × 10 μm × 2.5 μm in x, y and z dimensions) is suggested. One can distinguish the trigons initiated at different defects with certainty by comparing their morphologies. Pits initiated at dislocations show point bottoms, and those initiated at surface defects or foreign particles show flat bottoms; pits initiated at point defects will be tiny (diameter < 0.2 μm) (de Theije et al. 2001). Further examination of pits with diameter > 10 μm can still use the J scanner as used in this study. The evolution of trigons formed at different defects in fluids with various CO_2/H_2O ratios may help to refine the semi-quantitative method of determining fluid composition proposed by Zhang (2016).

Hydrogen can be incorporated into lattice defects of olivine and bonded to oxygen to form OH^-. The concentration of OH^- in olivine is determined by water activity in the surrounding melt of fluid and can be measured by FTIR (Matveev et al., 2001). Thus, my

interpretation of fluid composition in Snap Lake and Ekati kimberlites can be tested by measuring the OH^- concentration in olivine from these kimberlites in future study. Also, apatite is a common mineral in kimberlite and incorporates trace elements and volatiles into its crystal structure, suggesting apatite composition can be used as a potential indicator of fluid composition in kimberlite melt (Milligan et al. 2015).

Further study of diamond resorption morphology also should focus on samples from Class 2 kimberlites. Skinner and Marsh (2004) proposed that the fluid in Class 2 kimberlites is CO_2-dominant so that they reach shallower levels before initiating phreatomagmatic eruptions. In this case, diamonds should show the corresponding carbonic or CO_2-resorption morphology, and the etch pits should resemble trigons produced in CO_2-rich fluid and the depth and diameter of the pits should be positively correlated.

REFERENCES

Afanasyev, A.A., Melnik, O., Porritt, L., Schumacher, J.C., and Sparks, R.S. 2014. Hydrothermal alteration of kimberlite by convective flows of external water. Contrib Mineral Petrol **168**(1): 1038.

Agashev, A.M., Pokhilenko, N.P., MacDonald, J.A., Takazawa, E., Vavilov, M.A., Sobolev, N.V., and Watanabe, T. 2001. A unique kimberlite–carbonatite primary association in the Snap Lake dyke system, Slave Craton: evidence from geochemical and isotopic studies. Slave–Kaapvaal Workshop Geological Survey of Canada, Merrickville, Ontario, Canada.

Angus, J.C., and Dyble, T.J. 1975. Etching models for {111} diamond surface: calculation of trigon slopes. Surface Science **50**: 157-177.

Arima, M. 1998. Experimental study of growth and resorption of diamond in kimberlitic melts at high pressures and temperatures. *In* 7th International Kimberlite Conference, Extended Abstracts. pp. 32-34.

Arima, M., and Kozai, Y. 2008. Diamond dissolution rates in kimberlitic melts at 1300–1500 °C in the graphite stability field. European Journal of Mineralogy **20**(3): 357-364.

Armstrong, J.P., Wilson, M., Barnett, R.L., Nowicki, T., and Kjarsgaard, B.A. 2004. Mineralogy of primary carbonate-bearing hypabyssal kimberlite, Lac de Gras, Slave Province, Northwest Territories, Canada. Lithos **76**(1-4): 415-433.

Aulbach, S., Griffin, W.L., Pearson, N.J., O'Reilly, S.Y., Kivi, K., and Doyle, B.J. 2004. Mantle formation and evolution, Slave Craton: constraints from HSE abundances and Re–Os isotope systematics of sulfide inclusions in mantle xenocrysts. Chemical Geology **208**(1-4): 61-88.

Aulbach, S., Griffin, W.L., Pearson, N.J., O'Reilly, S.Y., and Doyle, B.J. 2007. Lithosphere formation in the central Slave Craton (Canada): plume subcretion or lithosphere accretion? Contributions to Mineralogy and Petrology **154**(4): 409-427.

Aulbach, S., Stachel, T., Creaser, R.A., Heaman, L.M., Shirley, S.B., Muehlenbachs, K., Eichenberg, D., and Harris, J.W. 2009. Sulphide survival and diamond genesis during formation and evolution of Archaean subcontinental lithosphere: A comparison between the Slave and Kaapvaal cratons. Lithos **112S**: 747-757.

Aulbach, S., Stachel, T., Heaman, L.M., and Carlson, J.A. 2011. Microxenoliths from the Slave Craton: Archives of diamond formation along fluid conduits. Lithos **126**(3-4): 419-434.

Bank, C.G., Bostock, M.G., Ellis, R.M., and Cassidy, J.F. 2000a. A reconnaissance teleseismic study of the upper mantle and transition zone beneath the Archean Slave Craton in NW Canada. Tectonophysics **219**: 151-166.

Bank, C.G., Bostock, M.G., Ellis, R.M., and Cassidy, J.F. 2000b. A reconnaissance teleseismic study of the upper mantle and transition zone beneath the Archean Slave Craton in NW Canada. Tectonophysics **319**: 151-166.

Bartoshinsky, Z.V. 1983. Mineralogical calssification of natural diamonds. Mineral Journal **5**: 94-103.

Bowring, S.A., and Williams, I.S. 1999. Priscoan (4.00 ± 4.03 Ga) orthogneisses from northwestern Canada. Contributions to Mineralogy and Petrology **134**: 3-16.

Bowring, S.A., Williams, I.S., and Compstion, W. 1989. 3.96 Ga gneisses from the Slave Province, N.W.T., Canada. Geology **17**: 971-975.

Boyd, S.R., Kiflawi, I., and Woods, G.S. 1994. The relationship between infrared absorption and the A defect concentration in diamond. Philosophical Magazine B **69**(6): 1149-1153.

Boyd, S.R., Kiflawi, I., and Woods, G.S. 1995. Infrared absorption by the B nitrogen aggregate in diamond. Philosophical Magazine B **72**(3): 351-361.

Canil, D. 2004. Mildly incompatible elements in peridotites and the origins of mantle lithosphere. Lithos **77**(1-4): 375-393.

Canil, D., and Bellis, A.J. 2007. Ferric iron in $CaTiO_3$ perovskite as an oxygen barometer for kimberlite magmas II: applications. Journal of Petrology **48**: 231-252.

Carbno, G.B., and Canil, D. 2002. Mantle structure beneath the SW Slave Craton, Canada: constraints from garnet geochemistry in the Drybones Bay kimberlite. Journal of Petrology **43**: 129-142.

Card, K.D., and King, J.E. 1992. The tectonic evolution of the Superior and Slave provinces of the Canadian Shield: introduction. Canadian Journal of Earth Sciences **29**: 2059-2065.

Carlson, J.A., Ravenscroft, P.J., Lavoie, C., and Cunning, J. 2015. Ekati diamond mine: Northwest Territories, Canada NI 43-101 Technical Report. .

Chepurov, A.I., Khokhryakov, A.F., Sonin, V.M., and Pal'yanov, Y.N. 1985. Forms of dissolution of diamond crystals in silicate melts at high pressure. Doklady Academii Nauk SSSR, 285(1), 212–216 (in Russian).

Clement, C.R. 1982. A comparative geological study of some major kimberlite pipes in northern Cape and Orange Free State. PhD thesis (unpublished), University of Cape Town. p. 432.

Crawford, B.B., Porritt, L., Nowicki, T., and Carlson, J.A. 2006. Key geological characteristics of the Koala Kimberlite, Ekati Diamond Mine, Canada. In: Kimberlite Emplacement Workshop, Saskatoon, Canada.

Creaser, R.A., Grütter, H., Carlson, J., and Crawford, B. 2004. Macrocrystal phlogopite Rb–Sr dates for the Ekati property kimberlites, Slave Province, Canada: evidence for multiple intrusive episodes in the Paleocene and Eocene. Lithos **76**(1-4): 399-414.

Creighton, S., Stachel, T., McLean, H., Muehlenbachs, K., Simonetti, A., Eichenberg, D., and Luth, R. 2007. Diamondiferous peridotitic microxenoliths from the Diavik Diamond Mine, NT. Contributions to Mineralogy and Petrology **155**(5): 541-554.

Dalton, J.A., and Presnall, D.C. 1998. The Continuum of Primary Carbonatitic-Kimberlitic Melt Compositions in Equilibrium with Lherzolite: Data from the System CaO–MgO–Al_2O_3–SiO_2–CO_2 at 6 GPa. Journal of Petrology **39**: 1953-1964.

Davies, R.M., Griffin, W.L., O'Reilly, S.Y., and Doyle, B.J. 2004. Mineral inclusions and geochemical characteristics of microdiamonds from the DO27, A154, A21, A418, DO18, DD17 and Ranch Lake kimberlites at Lac de Gras, Slave Craton, Canada. Lithos **77**: 39-55.

Davis, W.J., and Bleeker, W. 1999. Time and plutonism, deformation, and metamorphism in the Yellowknife Domain, Slave Province, Canada. Canadian Journal of Earth Sciences **36**: 1169-1187.

Davis, W.J., Jones, A.G., and Grütter, H.S. 2003. Lithosphere development in the Slave Craton: a linked crustal and mantle perspective. Lithos **71(2-4)**: 575-589.

De Beers Analyst Seminar. 2014. Available from http://www.angloamerican.com/~/media/Files/A/Anglo-American-Plc/investors/presentations/2014pres/de-beers-seminar-london-nov-2014.pdf.

De Stefano, A., Kopylova, M.G., Cartigny, P., and Afanasiev, V. 2008. Diamonds and eclogites of the Jericho kimberlite (Northern Canada). Contributions to Mineralogy and Petrology **158**(295-315).

de Theije, F.K., van Veenendaal, E., van Enckevort, W.J.P., and Vlieg, E. 2001. Oxidative etching of cleaved synthetic diamond {111} surfaces. . Surface Science **492**: 91-105.

Diamond, L.W. 2003. Introduction to gas-bearing, aqueous fluid inclusions *In* Fluid inclusions: Anaylsis and interpretatio. *Edited by* I. Samson and A. Anderson and D. Marshall. Mineralogical Association of Canada, Vancouver, British Columbia. p. 374.

Dyck, D.R., Oshut, P.A., Carlson, J.A., Nowicki, T.E., and Mullins, M.P. 2004. Effective resource estimates for primary diamond deposits from the EKATI Diamond Mine™, Canada. Lithos **76**(1-4): 317-335.

Edgar, A.D., and Arima, M. 1983. Conditions of phlogopite crystallization in ultrapotassic volcanic rocks. Mineralogical Magazine **47**: 11-19.

Eggler, D.H. 1978. The stability of dolomite in a hydrous mantle, with implications for the mantle solidus. Geology **6**: 397-400.

Evans, T. 1976. Diamonds. Contemporary Physics **17**: 45-70.

Evans, T., and Phaal, C. 1961. The kinetics of the diamond–oxygen reaction. *In* Conference on Carbon, 5 PT. Pergamon Press, New York. pp. 147-153.

Evans, T., and Sauter, D.H. 1961. Etching of diamond surfaces with gases. Philosophical Magazine **6**(63): 429-440.

Fedortchouk, Y. 2015. Diamond resorption features as a new method for examining conditions of kimberlite emplacement. Contributions to Mineralogy and Petrology **170**(4): 1-19.

Fedortchouk, Y., and Canil, D. 2004. Intensive variables in kimberlite magmas, Lac de Gras, Canada and implications for diamond survival. Journal of Petrology **45**(9): 1725-1745.

Fedortchouk, Y., and Canil, D. 2009. Diamond oxidation at atmospheric pressure: development of surface features and the effect of oxigen fugacity. European Journal of Mineralogy: 623-635.

Fedortchouk, Y., Canil, D., and Carlson, J.A. 2005. Dissolution forms in Lac de Gras diamonds and their relationship to the temperature and redox state of kimberlite magma. Contributions to Mineralogy and Petrology **150**(1): 54-69.

Fedortchouk, Y., Canil, D., and Semenets, E. 2007. Mechanisms of diamond oxidation and their bearing on the fluid composition in kimberlite magmas. American Mineralogist **92**(7): 1200-1212.

Fedortchouk, Y., Manghnani, M.H., Hushur, A., Shiryaev, A., and Nestola, F. 2011. An atomic force microscopy study of diamond dissolution features: The effect of H_2O and CO_2 in the fluid on diamond morphology. American Mineralogist **96**(11-12): 1768-1775.

Fedortchouk, Y., Matveev, S., and Carlson, J.A. 2010. H_2O and CO_2 in kimberlitic fluid as recorded by diamonds and olivines in several Ekati Diamond Mine kimberlites, Northwest Territories, Canada. Earth and Planetary Science Letters **289**(3-4): 549-559.

Fersmann, A.V., and Goldschmidt, V. 1911. Der Diamant, Winter, Heidelberg, Germany. pp. 274.

Field, M., Gernon, T.M., Mock, A., Walters, A., Sparks, R.S.J., and Jerram, D.A. 2009. Variations of olivine abundance and grain size in the Snap Lake kimberlite intrusion, Northwest Territories, Canada: A possible proxy for diamonds. Lithos: 23-25.

Field, M., and Scott Smith, B.H. 1999. Contrasting Geology and Near-Surface Emplacement of Kimberlite Pipes in Southern Africa and Canada. *In* 7th International Kimberlite Conference. Red Roof Design, Cape Town, South Africa.

Forbes, N. 2017. Experimental study of positive trigons on diamonds; conditions of near-surface diamond resorption with application to emplacement condition of Snap Lake kimberlite. Honors thesis, Dalhousie University. p. 67.

Frank, F.C., and Puttick, K.E. 1958. Etch pits and trigons on diamond: II. Philosophical Magazine **3**(35): 1273-1279.

Frank, F.C., Puttick, K.E., and Wilks, E.M. 1958. Etch pits and trigons on diamond: I. Philosophical Magazine **3**(35): 1262-1272.

Frith, R.A., Loveridge, W.D., and van Breemen, O. 1986. U-Pb ages on zircon from basement granitoids of the western Slave Province, northwestern Canadian Shield. *In* Current research, part A. Geological Survey of Canada, Paper 86-1A. pp. 113-119.

Frost, B.R. 1991. Introduction to oxygen fugacity and its petrologic importance. Reviews in Mineralogy and Geochemistry **25**: 1-9.

Frost, D.J., and Wood, B.J. 1997. Experimental measurements of the fugacity of CO_2 and graphite/diamond stability from 35 to 77 kbar at 925 to 1650 °C. Geochimica et Cosmochimica Acta **61**(8): 1565–1574.

Gernon, T.M., Brown, R.J., Tait, M.A., and Hincks, T.K. 2012a. The origin of pelletal lapilli in explosive kimberlite eruptions. Nature Communications **3**: 832.

Gernon, T.M., Field, M., and Sparks, R.S.J. 2012b. Geology of the Snap Lake kimberlite intrusion, Northwest Territories, Canada: field observations and their interpretation. Journal of the Geological Society, London **169**: 1-16.

Griffin, W.L., Doyle, B.J., Ryan, C.G., Pearson, N.J., O'Reilly, S.Y., and Davies, R.M. 1999a. Layered Mantle Lithosphere in the Lac de Gras Area, Slave Craton: Composition, Structure and Origin. Journal of Petrology **40**: 705-727.

Griffin, W.L., Doyle, B.J., Ryan, C.G., Pearson, N.J., O'Reilly, S.Y., Natapov, L., Kivi, K., Kretschmar, U., and Ward, J. 1999b. Lithosphere structure and mantle terranes: Slave Craton, Canada. *In* Proceedings of the 7th International Kimberlite Conference. *Edited by* J.J. Gurney and S.R. Richardson. Cape Town: Red Roof Design. pp. 299-306.

Griffin, W.L., O'Reilly, S.Y., Doyle, B.J., Pearson, N.J., Coopersmith, H., Kivi, K., Malkovets, V., and Pokhilenko, N. 2004. Lithosphere mapping beneath the North American plate. Lithos **77**(1-4): 873-922.

Grütter, H.S., Apter, D.B., and Kong, J. 1999. Crust-mantle coupling: evidence from mantle-derived xenocrystic garnets. *In* Proceedings of the 7th Internationl Kimberlite Conference. *Edited by* J.J. Gurney and S.R. Richardson. Cape Town: Red Roof Design. pp. 307-312.

Gudfinnsson, G.H. 2005. Continuous Gradations among Primary Carbonatitic, Kimberlitic, Melilititic, Basaltic, Picritic, and Komatiitic Melts in Equilibrium with Garnet Lherzolite at 3-8 GPa. Journal of Petrology **46**(8): 1645-1659.

Gurney, J.J., Hildebrand, P.R., Carlson, J.A., Fedortchouk, Y., and Dyck, D.R. 2004. The morphological characteristics of diamonds from the Ekati property, Northwest Territories, Canada. Lithos **77**(1-4): 21-38.

Halperin, A. 1954. The formation of trigons on diamond. Proceedings of the Physical Society. Section B **67**: 539-545.

Harrison, E.R., and Tolansky, S. 1964. Growth history of a natural octahedral diamond. Proceedings of the Royal Society of London. Series A, Mathematical and Physical Sciences **279**: 490-496.

Hawthorne, J.B. 1975. Model of kimberlite Pipe. Proc. 1st Int. Kimb. Conf. Phys. Chem, Earth **9**: 1-15.

Heaman, L.M., Kjarsgaard, B.A., and Creaser, R.A. 2003. The timing of kimberlite magmatism in North America: implications for global kimberlite genesis and diamond exploration. Lithos **71**: 153-184.

Heaman, L.M., Kjarsgaard, B.A., and Creaser, R.A. 2004. The temporal evolution of North American kimberlites. Lithos **76**(1-4): 377-397.

Henderson, J.B., van Breemen, O., and Loveridge, W.D. 1987. Some U-Pb zircon ages from Archean basement, supracrustal and intrusive rocks, Yellowknife-Hearne Lake area, District of Mackenzie. *In* Radiogenic age and isotopic studies, report 1. Geological Survey, Paper 87-2. pp. 111-121.

Jones, A.G., Ferguson, I.J., Chave, A.D., Evans, R.L., and McNeice, G.W. 2001. Electric lithosphere of the Slave Craton. Geology **29(5)**: 423-426.

Keltie, E. 2016. Diamond dissolution in Na_2CO_3, Na_2CO_3-NaCl, and Na_2CO_3-NaF melts at 950ºC and 0.1 MPa. Honors thesis, Dalhousie University. p.63.

Ketchum, J.W.F., and Bleeker, W. 2001. 4.03-2.85 Ga growth and modification of the Slave protocraton, NW Canada. Abstracts, the Slave-Kaapvaal Workshop, September 2001, Merrickville.

Khmelnitsky, R.A., and Gippius, A.A. 2014. Transformation of diamond to graphite under heat treatment at low pressure. Phase Transitions **87**: 175-192.

Khokhryakov, A.F., and Pal'yanov, Y.N. 2007a. The evolution of diamond morphology in the process of dissolution: Experimental data. American Mineralogist **92**(5-6): 909-917.

Khokhryakov, A.F., and Pal'yanov, Y.N. 2010. Influence of the fluid composition on diamond dissolution forms in carbonate melts. American Mineralogist **95**(10): 1508-1514.

Khokhryakov, A.F., Pal'yanov, Y.N., and V., S.N. 2002. Crystal morphology as an indicator of redox conditions of natural diamond dissolution at the mantle PT parameters. Doklady Earth Sciences **385**: 534-537.

Khokhryakov, A.F., and Palyanov, Y.N. 2006. Revealing of dislocations in diamond crystals by the selective etching method. Journal of Crystal Growth **293**(2): 469-474.

Kjarsgaard, B.A. 2001. Lac de Gras Kimberlite Field, Slave Province, 1:250,000 geology map and descriptive notes. Geological Survey of Canada, Open File Map 2739, scale 1:50,000.

Kjarsgaard, B.A. 2007. Kimberlite pipe models: significance for exploration. In Proc. Decenn. Int. Conf. Miner. Explor. pp. 667-677.

Kjarsgaard, B.A., Pearson, D.G., Tappe, S., Nowell, G.M., and Dowall, D.P. 2009. Geochemistry of hypabyssal kimberlites from Lac de Gras, Canada: Comparisons to a global database and applications to the parent magma problem. Lithos **112**: 236-248.

Kjarsgaard, B.A., Wilson, M.R., and Taylor, B.E. 2006. Stable isotope composition of magmatic and deuteric carbonate phases in hypabyssal kimberlite, Lac de Gras field, NWT, Canada: implications for the composition of fluids in equilibrium with kimberlite magma and the origin of serpentine–calcite segregations. Extended Abstract, Kimberlite Emplacement Workshop, Saskatoon, SK, September 7–12, 2006.

Kopylova, M.G., and Caro, G. 2004. Mantle Xenoliths from the Southeastern Slave Craton: Evidence for Chemical Zonation in a Thick, Cold Lithosphere. Journal of Petrology **45**: 1045-1067.

Kopylova, M.G., Matveev, S., and Raudsepp, M. 2007. Searching for parental kimberlite melt. Geochimica et Cosmochimica Acta **71**(14): 3616-3629.

Kopylova, M.G., Mogg, T., and Smith, B.H.S. 2010. Mineralogy of the Snap Lake kimberlite, Northwest Territories, Canada, and compositions of phlogopite as records of its crystallization. The Canadian Mineralogist **48**: 549-570.

Kozai, Y., and Arima, M. 2005. Experimental study on diamond dissolution in kimberlitic and lamproitic melts at 1300–1420 °C and 1 GPa with controlled oxygen partial pressure. American Mineralogist **90**(11-12): 1759-1766.

Krogh, T.E., and Gibbins, W.A. 1978. U-Pb isotopic ages of basement and supracrustal rocks in the Point Lake area of the Slave Structural Province, Canada. Geological Association of Canada, Program with Abstracts. p. 438.

Lambert, M.L., and van Breemen, O. 1991. U-Pb zircon ages from the Sleepy Dragon Comples and a new occurrence of basement rocks within the Meander Lake Plutonic Suits, Slave Province, N.W.T. *In* Radiogenic age and isotopic studies, report 4. Geological Survey of Canada, Paper 90-2. pp. 79-84.

LeCheminant, A.N., and van Breemen, O. 1994. U–Pb ages of Proterozoic dyke swarms, Lac de Gras area, N.W.T.: evidence for progressive break-up of an Archean supercontinent. *In* GAC/MAC, Program with Abstracts. p. A62.

Lockhart, G., Grütter, H., and Carlson, J.C. 2004. Temporal, geomagnetic and related attributes of kimberlite magmatism at Ekati, Northwest Territories,Canada-NWT. Lithos **77**: 665-682.

Lüttge, A. 2006. Crystal dissolution kinetics and Gibbs free energy. Journal of Electron Spectroscopy and Related Phenomena **150**(2-3): 248-259.

Matveev, S., O'Neill, H.S.C., Ballhaus, C., Taylor, W.R., and Green, D.H. 2001. Effect of silica activity on OH-IR spectra of olivine: implications for low-aSiO_2 mantle metasomatism. Journal of Petrology 42: 721–729.

McBean, D., Kirkley, M., and Revering, C. 2003. Structural controls on the morphology of the Snap Lake kimberlite dyke. *In* 8th International Kimberlite Conference, Extended Abstracts, Victoria, Canada. pp. 69–74.

McCollom, T.M., and Seewald, J.S. 2013. Serpentinites, Hydrogen, and Life. Elements **9**(2): 129-134.

McElroy, R., Nowicki, T., Dyck, D., Carlson, J., Todd, J., and Roebuck, S. 2003. The geology of the Panda kimberlite, Ekati Diamond Mine, Canada. Long Abstracts, 8th International Kimberlite Conference, Victoria, Canada.

Mendelssohn, M.J., and Milledge, H.J. 1995. Morphological characteristics of diamond populations in relation to temperature-dependent growth and dissolution rates. International Geology Review **37**(4): 285-312.

Milligan, R., Fedortchouk, Y., Normandeau, P.X., and Fulop, A. 2015. Comparative study of composition and occurrence of apatite in Snap Lake and Ekati kimberlites. Yellowknife Geoscience Forum.

Mitchell, R.H. 1986. Kimberlites: Mineralogy, Geochemistry and Petrology. Plenum Press, New York. pp. 442.

Mitchell, R.H. 2004. Experimental studies At 5–12 GPa of the Ondermatjie hypabyssal kimberlite. Lithos **76**(1-4): 551-564.

Mitchell, R.H. 2008. Petrology of hypabyssal kimberlites: Relevance to primary magma compositions. Journal of Volcanology and Geothermal Research **174**(1-3): 1-8.

Mogg, T., Kopylova, M.G., Smith, B.H.S., and Kirkley, M. 2003. Petrology of the Snap Lake kimberlite. *In* 8th International Kimberlite Conference Long Abstract.

Moore, M., and Lang, A.R. 1974. On the origin of the rounded dodecahedral habit of natural diamond. Journal of Crystal Growth **26**(1): 133-139.

Moussallam, Y., Morizet, Y., and Gaillard, F. 2016. H_2O–CO_2 solubility in low SiO_2-melts and the unique mode of kimberlite degassing and emplacement. Earth and Planetary Science Letters **447**: 151-160.

Moussallam, Y., Morizet, Y., Massuyeau, M., Laumonier, M., and Gaillard, F. 2015. CO_2 solubility in kimberlite melts. Chemical Geology **418**: 198-205.

Mustafa, J., Nowicki, T., Oshust, P., Dyck, D., Crawford, B., and Harrison, S. 2003. The geology of the Misery kimberlite, Ekati Diamond Mine™. *In* 8th International Kimberlite Conference Long abstract, Victoria, Canada.

Nowicki, T.E., Crawford, B., Dyke, D., Carlson, J., McElroy, R., Oshust, P., and Helmstaedt, H. 2004. The geology of kimberlite pipes of the Ekati property, Northwest Territories, Canada. Lithos **76**(1-4): 1-27.

Nowicki, T.E., Porritt, L., Crawford, B., and Kjarsgaard, B. 2008. Geochemical trends in kimberlites of the Ekati property, Northwest Territories, Canada: Insights on volcanic and resedimentation processes. Journal of Volcanology and Geothermal Research **174**(1-3): 117-127.

Ogilvie-Harris, R.C., Sparks, R.S.J., Field, M., and Gernon, T.M. 2009. The Geochemistry of the Snap Lake kimberlite dyke, NW Territories, Canada: Phlogopite and Spinel. 2009 Joint Assembly, Abstract V33D-01

Orlov, Y.L. 1977. The mineralogy of diamond. John Wiley, New York. pp. 235.

Padgham, W.A., and Fyson, W.K. 1992. The Slave Province: a distinct Archean craton. Canadian Journal of Earth Sciences **29**: 2072-2086.

Papale, P., and Polacci, M. 1999. Role of carbon dioxide in the dynamics of magma ascent in explosive eruptions. Bulletin of Volcanology **60**(8): 583-584.

Porritt, L.A., Cas, R.A.F., and Crawford, B.B. 2008. In-vent column collapse as an alternative model for massive volcaniclastic kimberlite emplacement: An example from the Fox kimberlite, Ekati Diamond Mine, NWT. Journal of Volcanology and Geothermal Research **174**: 90-102.

Price, S.E., Russell, J.K., and Kopylova, M.G. 2000. Primitive Magma From the Jericho Pipe, N.W.T., Canada: Constraints on Primary Kimberlite Melt Chemistry. Journal of Petrology **41**: 789-808.

Robertson, R. 2001. Snap Lake underground mine takes shape under De Beers. The Northern Miner, available from http://www.northernminer.com.

Robinson, D.N. 1979. Surface features and other features of diamonds PhD thesis, University of Cape Town. p. 418.

Sarkar, C., Heaman, L.M., and Pearson, D.G. 2015. Duration and periodicity of kimberlite volcanic activity in the Lac de Gras kimberlite field, Canada and some recommendations for kimberlite geochronology. Lithos **218-219**: 155-166.

Scott Smith, B.H. 2008. Canadian kimberlites: Geological characteristics relevant to emplacement. Journal of Volcanology and Geothermal Research **174**(1-3): 9-19.

Scott Smith, B.H., Nowicki, T.E., Russell, J.K., Webb, K.J., Mitchell, R.H., Hetman, C.M., Harder, M., Skinner, E.M.W., and Robey, J.A. 2013. Kimberlite Terminology and Classification. *In* Proceedings of 10th International Kimberlite Conference. pp. 1-17.

Skinner, E.M.W., and Marsh, J.S. 2004. Distinct kimberlite pipe classes with contrasting eruption processes. Lithos **76**(1-4): 183-200.

Smart, K.A., Chacko, T., Stachel, T., Muehlenbachs, K., Stern, R.A., and Heaman, L.M. 2011. Diamond growth from oxidized carbon sources beneath the Northern Slave Craton, Canada: A δ13C–N study of eclogite-hosted diamonds from the Jericho kimberlite. Geochimica et Cosmochimica Acta **75**(20): 6027-6047.

Snyder, D.B., Hillier, M.J., Kjarsgaard, B.A., de Kemp, E.A., and Craven, J.A. 2014. Lithospheric architecture of the Slave Craton, northwest Canada, as determined from an interdisciplinary 3-D model. Geochemistry, Geophysics, Geosystems **15**(5): 1895-1910.

Sparks, R.S.J., Baker, L., Brown, R.J., Field, M., Schumacher, J., Stripp, G., and Walters, A. 2006. Dynamical constraints on kimberlite volcanism. Journal of Volcanology and Geothermal Research **155**(1-2): 18-48.

Sparks, R.S.J., Brooker, R.A., Field, M., Kavanagh, J., Schumacher, J.C., Walter, M.J., and White, J. 2009. The nature of erupting kimberlite melts. Lithos **112**: 429-438.

Stachel, T. 2003. Peridotitic diamonds from the Slave and the Kaapvaal cratons—similarities and differences based on a preliminary data set. Lithos **71**(2-4): 489-503.

Stachel, T., Banas, A., Muehlenbachs, K., Kurszlaukis, S., and Walker, E.C. 2006. Archean diamonds from Wawa (Canada): samples from deep cratonic roots predating cratonization of the Superior Province. Contributions to Mineralogy and Petrology **151**(6): 737-750.

Stepanov, A.S.S., V.S. Zedgenizov, D.A. Sobolev, N.V. 2007. Causes of variations in morphology and impurities of diamonds from the Udachnaya Pipe eclogite. Russian Geology and Geophysics **48**: 758-769.

Stubley, M.P. 2000. Geology of the Northern Snap Lake area. De Beers Canada Mining, internal report prepared for Winspear Resources, with accompaning 1:10,000 scale map.

Sunagawa, I. 1984. Morphology of natural and synthetic diamond crystals. *In* Material Science of the Earth's Interior. *Edited by* I. Sunagawa. Terra Scientific, Tokyo. pp. 303–330.

Tappert, R., Stachel, T., Harris, J.W., and Brey, G.P. 2005. Mineral inclusions in diamonds from the Panda kimberlite, Slave Province, Canada. European Journal of Mineralogy **17**: 423-440.

Tappert, R., and Tappert, M.C. 2011. Diamonds in Nature: A Guide to Rough Diamonds.

Taylor, W.R., Jaques, A.L., and Ridd, M. 1990. Nitrogen-defect aggregation characteristics of some Australasian diamonds: Time-temperature constraints on the source regions of pipe and alluvial diamonds. American Mineralogist 75: 1290-1310.

Thorpe, R.I., Cumming, G.L., and Mortensen, J.K. 1992. A major Pb-isotope boundary in the Slave Province and its probable relation to ancient basement of the western Slave. Canada-NWT MDA Summary Volume. Geological Survey of Canada, Open File 2484: 179-184.

Tolansky, S. 1968. Graphitized natural diamond. Diamond Research: 8-10.

van Breemen, O., Davis, W.J., and King, J.E. 1992. Temporal distribution of granitoid plutonic rocks in the Archean Slave Province, Northwest Canadian Shield. Canadian Journal of Earth Sciences **29**: 2186-2199.

Varma, C.K.R. 1967. Trigons on diamond. Philosophical Magazine **16**(143): 959-974.

Viljoen, K.S., Dobbe, R., Smit, B., Thomassot, E., and Cartigny, P. 2004. Petrology and geochemistry of a diamondiferous lherzolite from the Premier diamond mine, South Africa. Lithos **77**(1-4): 539-552.

Viljoen, K.S., Swash, P.M., Otter, M.L., Schulze, D.J., and Lawless, P.J. 1992. Diamondiferous garnet harzburgites from the Finsch kimberlite, Northern Cape, South Africa. Contributions to Mineralogy and Petrology **110**: 133-138.

Wagner, P.A. 1914. Note on graphite-coated diamonds from the Premier Min. Trans. Geol. Soc. S. Afr. **17**: 29-30.

Walters, A.L., Phillips, J.C., Brown, R.J., Field, M., Gernon, T., Stripp, G., and Sparks, R.S.J. 2006. The role of fluidisation in the formation of volcaniclastic kimberlite: Grain size observations and experimental investigation. Journal of Volcanology and Geothermal Research **155**(1-2): 119-137.

Westerlund, K.J., Shirey, S.B., Richardson, S.H., Carlson, R.W., Gurney, J.J., and Harris, J.W. 2006. A subduction wedge origin for Paleoarchean peridotitic diamonds and harzburgites from the Panda kimberlite, Slave Craton: evidence from Re–Os isotope systematics. Contributions to Mineralogy & Petrology **152**: 275-294.

Wyllie, P.J. 1980. The origin of kimberlite. Journal of Geophysical Research **85**(B12): 6902.

Wyllie, P.J. 1987. Transfer of subcratonic carbon into kimberlites and rare earth carbonaties. *In* Magmatic Processes: Physicochemical Principles. Special Publication - Geochemical Society. *Edited by* B.O. Mysen. pp. 107-119.

Yamaoka, S., Kanda, H., and Setaka, N. 1980. Etching of diamond octahedrons at high temperatures and pressure with controlled oxygen partial pressure. Materials Science. **15**: 332-336.

Zhang, Z. 2016. Diamond resorption morphology as a fluid proxy in diamond-bearing environments: constraints from emprical and experimental studies. PhD thesis, Dalhousie University. p. 319.

Zhang, Z., Fedortchouk, Y., and Hanley, J.J. 2015. Evolution of diamond resorption in a silicic aqueous fluid at 1–3 GPa: Application to kimberlite emplacement and mantle metasomatism. Lithos **227**: 179-193.

Appendix A

Appendix A is available online at http://dalspace.library.dal.ca. They include general description (size, weight, morphology and color) of 251 Snap Lake diamonds in two parcels (Table EA1); AFM measurements of positive trigons, trigon-hexagons, and hexagons on experimental diamonds in this study (Table EA2); Morphological grouping and N data of diamonds from Snap Lake kimberlite (Table EA4); AFM measurements of positive trigons on Snap Lake diamonds (Table EA3); AFM measurements of negative trigons/trigon-hexagons and hexagons on Snap Lake diamonds (Table EA5) and negative trigons on Ekati diamonds from Fox, Panda, Koala and Misery kimberlites (Table EA5).